IDŐJÁRÁS

QUARTERLY JOURNAL
OF THE HUNGARIAN METEOROLOGICAL SERVICE

CONTENTS

****

http://www.met.hu/Journal-Idojaras.php

VOL. 111 * NO. 1 * JANUARY – MARCH 2007

IDŐJÁRÁS

Quarterly Journal of the Hungarian Meteorological Service

Editorial Office: P.O. Box 39, H-1675 Budapest, Hungary or
Gilice tér 39, H-1181 Budapest, Hungary
E-mail: bozo.l@met.hu or *antal.e@met.hu*
Fax: (36-1) 346-4809

Subscription by

mail: IDŐJÁRÁS, P.O. Box 39, H-1675 Budapest, Hungary;
E-mail: bozo.l@met.hu or *antal.e@met.hu*; *Fax: (36-1) 346-4809*

IDŐJÁRÁS

Quarterly Journal of the Hungarian Meteorological Service
Vol. 111, No. 1, January–March 2007, pp. 1–40

Greenhouse effect in semi-transparent planetary atmospheres

Ferenc M. Miskolczi

Holston Lane 3, Hampton VA 23664, U.S.A.
E-mail: fmiskolczi@cox.net

(Manuscript received in final form October 29, 2006)

Abstract—In this work the theoretical relationship between the clear-sky outgoing infrared radiation and the surface upward radiative flux is explored by using a realistic finite semi-transparent atmospheric model. We show that the fundamental relationship between the optical depth and source function contains real boundary condition parameters. We also show that the radiative equilibrium is controlled by a special atmospheric transfer function and requires the continuity of the temperature at the ground surface. The long standing misinterpretation of the classic semi-infinite Eddington solution has been resolved. Compared to the semi-infinite model, the finite semi-transparent model predicts much smaller ground surface temperature and a larger surface air temperature. The new equation proves that the classic solution significantly overestimates the sensitivity of greenhouse forcing to optical depth perturbations. In Earth-type atmospheres sustained planetary greenhouse effect with a stable ground surface temperature can only exist at a particular planetary average flux optical depth of 1.841. Simulation results show that the Earth maintains a controlled greenhouse effect with a global average optical depth kept close to this critical value. The broadband radiative transfer in the clear Martian atmosphere follows different principle resulting in different analytical relationships among the fluxes. Applying the virial theorem to the radiative balance equation, we present a coherent picture of the planetary greenhouse effect.

Key-words: greenhouse effect, radiative equilibrium

1. Introduction

Recently, using powerful computers, virtually any atmospheric radiative transfer problem can be solved by numerical methods with the desired accuracy without using extensive approximations and complicated mathematical expressions common in the literature of the theoretical radiative transfer. However, to improve the understanding of the radiative transfer processes, it is sometimes useful to apply reasonable approximations and to arrive at solutions in more or less closed mathematical forms which clearly reflect the physics of the problem.

Regarding the planetary greenhouse effect, one must relate the amount of the atmospheric infrared (IR) absorbers to the surface temperature and the total absorbed short wave (SW) radiation. In this paper we derive purely theoretical relationships between the above quantities by using a simplified one dimensional atmospheric radiative transfer model. The relationships among the broadband atmospheric IR fluxes at the boundaries are based on the flux optical depth. The atmospheric total IR flux optical depths are obtained from sophisticated high-resolution spectral radiative transfer computations.

2. *Radiative transfer model*

In *Fig. 1* our semi-transparent clear sky planetary atmospheric model and the relevant (global mean) radiative flux terms are presented.

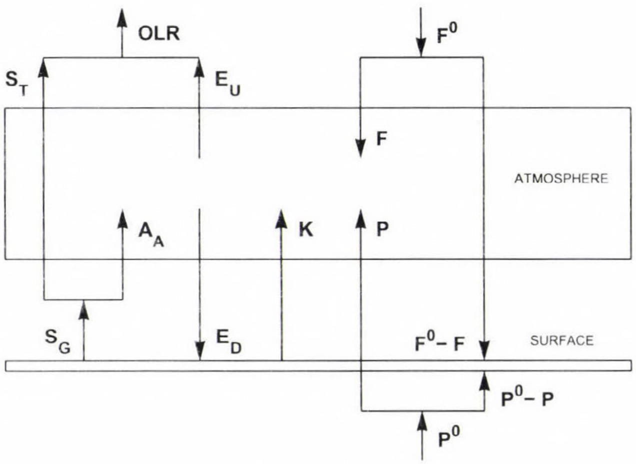

Fig. 1. Radiative flux components in a semi-transparent clear planetary atmosphere. Short wave downward: F^0 and F; long wave downward: E_D; long wave upward: OLR, E_U, S_T, A_A, and S_G; non-radiative origin: K, P^0 and P.

Here F^0 is the total absorbed SW radiation in the system, F is the part of F^0 absorbed within the atmosphere, E_D is the long wave (LW) downward atmospheric radiation, OLR is the outgoing LW radiation, E_U is the LW upward atmospheric radiation. S_G is the LW upward radiation from the ground: $S_G = \sigma t_G^4$, where t_G is the ground temperature and σ is the Stefan-Boltzmann constant. S_T and A_A are the transmitted and absorbed parts of S_G, respectively. The total thermal energy from the planetary interior to the surface-atmosphere system is P^0. P is the absorbed part of P^0 in the atmosphere. The net thermal energy to the atmosphere of non-radiative origin is K. The usual measure of the clear-sky atmospheric greenhouse effect is the $G = S_G - OLR$ greenhouse factor (*Inamdar* and *Ramanathan*, 1997). The normalized greenhouse factor is defined as the $G_N = G / S_G$ ratio. In some work the S_G / OLR ratio is also used as greenhouse parameter (*Stephens et al.*, 1993).

Our model assumptions are quite simple and general:

(a) — The available SW flux is totally absorbed in the system. In the process of thermalization F^0 is instantly converted to isotropic upward and downward LW radiation. The absorption of the SW photons and emission of the LW radiation are based on independent microphysical processes.

(b) — The temperature or source function profile is the result of the equilibrium between the IR radiation field and all other sinks and sources of thermal energy (latent heat transfer, convection, conduction, advection, turbulent mixing, short wave absorption, etc.). Note, that the K term is not restricted to strict vertical heat transfer. Due to the permanent motion of the atmosphere K represents a statistical or climatic average.

(c) — The atmosphere is in local thermodynamic equilibrium (LTE). In case of the Earth this is true up to about 60 km altitude.

(d) — The surface heat capacity is equal to zero, the surface emissivity ε_G is equal to one, and the surface radiates as a perfect blackbody.

(e) — The atmospheric IR absorption and emission are due to the molecular absorption of IR active gases. On the Earth these gases are minor atmospheric constituents. On the Mars and Venus they are the major components of the atmosphere.

(f) — In case of the Earth it is also assumed that the global average thermal flux from the planetary interior to the surface-atmosphere system is negligible, $P^0 = 0$. The estimated geothermal flux at the surface is less than 0.03 per cent of F^0 (*Peixoto* and *Oort*, 1992). However, in our definition P^0 is not restricted to the geothermal flux. It may contain the thermal energy released into the atmosphere by volcanism, tidal friction, or by other natural and non-natural sources.

(g) — The atmosphere is a gravitationally bounded system and constrained by the virial theorem: the total kinetic energy of the system must be half of the total gravitational potential energy. The surface air temperature, t_A, is linked to the total gravitational potential energy through the surface pressure and air density. The temperature, pressure, and air density obey the gas law, therefore, in terms of radiative flux $S_A = \sigma t_A^4$ represents also the total gravitational potential energy.

(h) — In the definition of the greenhouse temperature change keeping t_A and t_G different could pose some difficulties. Since the air is in permanent physical contact with the surface, it is reasonable to assume that, in the average sense, the surface and close-to-surface air are in thermal equilibrium: $t_S = t_A = t_G$, where t_S is the equilibrium temperature. The corresponding equilibrium blackbody radiatiation is $S_U = \sigma t_S^4$. For now, in *Fig. 1* S_G is assumed to be equal to S_U.

Assumptions (c), (d), (e), and (f) are commonly applied in broadband LW flux computations, see for example in *Kiehl* and *Trenberth* (1997). Under such conditions the energy balance equation of the atmosphere may be written as:

$$F + P + K + A_A - E_D - E_U = 0 . \qquad (1)$$

The balance equation at the lower boundary (surface) is:

$$F^0 + P^0 + E_D - F - P - K - A_A - S_T = 0 . \qquad (2)$$

The sum of these two equations results in the general relationship of:

$$F^0 + P^0 = S_T + E_U = OLR . \qquad (3)$$

This is a simple radiative (energy) balance equation and not related to the vertical structure of the atmosphere. For the Earth this equation simplifies to the well known relationship of $F^0 = OLR$. For long term global mean fluxes these balance equations are exact and they are the requirements for the steady-state climate. However, they do not necessarily hold for zonal or regional averages or for instantaneous local fluxes.

The most apparent reason of any zonal or local imbalance is related to the K term through the general circulation. For example, evaporation and precipitation must be balanced globally, but due to transport processes, they can add or remove optical depth to and from an individual air column in a non-balanced way. The zonal and meridional transfer of the sensible heat is another example.

When comparing clear sky simulation results of the LW fluxes, one should be careful with the cloud effects. Due to the SW effect of the cloud cover on F^0 and F, clear sky computations based on all sky radiosonde observations will also introduce deviations from the balance equations.

The true all sky outgoing LW radiation, OLR^A, must be computed from the clear OLR and the cloudy OLR^C fluxes as the weighted average by the fractional cloud cover: $OLR^A = (1-\beta)OLR + \beta OLR^C$, where β is the fractional cloud cover. Because of the large variety of cloud types and cloud cover and the required additional information on the cloud top altitude, temperature, and emissivity, the simulation of OLR^C is rather complicated.

The global average OLR^A may be estimated from the bolometric planetary equilibrium temperature. From the *ERBE* (2004) data product we estimated the five year average planetary equilibrium temperature as $t_E = 253.8$ K, which resulted in a global average $OLR^A = 235.2$ W m^{-2}. From the same data product the global average clear-sky OLR is 266.4 W m^{-2}.

3. *Kirchhoff law*

According to the Kirchhoff law, two systems in thermal equilibrium exchange energy by absorption and emission in equal amounts, therefore, the thermal energy of either system can not be changed. In case the atmosphere is in thermal equilibrium with the surface, we may write that:

$$A_A = S_U A = S_U(1-T_A) = E_D \,. \tag{4}$$

By definition the atmospheric flux transmittance T_A is equal to the S_T / S_U ratio: $T_A = 1 - A = \exp(-\tilde{\tau}_A) = S_T / S_U$, where A is the flux absorptance and $\tilde{\tau}_A$ is the total IR flux optical depth. The validity of the Kirchhoff law – concerning the surface and the inhomogeneous atmosphere above – is not trivial. Later, using the energy minimum principle, we shall give a simple theoretical proof of the Kirchhoff law for atmospheres in radiative equilibrium.

In *Fig.* 2 we present large scale simulation results of A_A and E_D for two measured diverse planetary atmospheric profile sets. Details of the simulation exercise above were reported in *Miskolczi* and *Mlynczak* (2004). This figure is a proof that the Kirchhoff law is in effect in real atmospheres. The direct consequences of the Kirchhoff law are the next two equations:

$$E_U = F + K + P, \tag{5}$$

$$S_U - (F^0 + P^0) = E_D - E_U. \tag{6}$$

The physical interpretations of these two equations may fundamentally change the general concept of greenhouse theories.

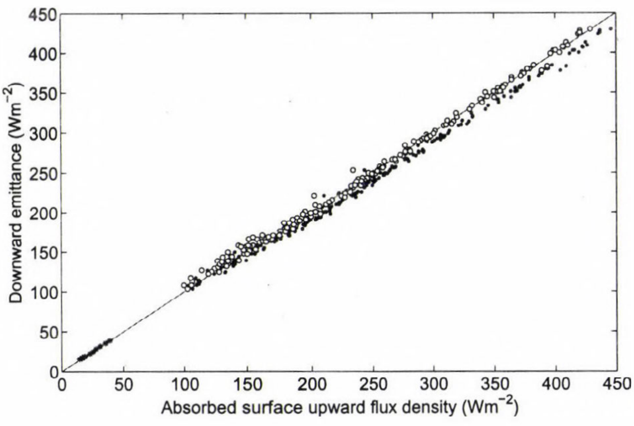

Fig. 2. Simulation results of A_A and E_D. Black dots and open circles represent 228 selected radiosonde observations with $\varepsilon_G = 1$ and $\varepsilon_G = 0.96$, respectively. Black stars are simulation results for Martian standard atmospheric profiles with $\varepsilon_G = 1$. We used two sets of eight standard profiles. One set contained no water vapor and in the other the water vapor concentration was set to constant 210 ppmv (approximately 0.0015 prcm H_2O).

3.1 Upward atmospheric radiation

Eq. (5) shows that the source of the upward atmospheric radiation is not related to LW absorption processes. The $F + K + P$ flux term is always dissipated within the atmosphere increasing (or decreasing) its total thermal energy. The $E_D = S_U - S_T$ functional relationship implies that $G - E_D = -E_U$, therefore, the interpretation of $G - E_D$ as the LW radiative heating (or cooling) of the atmosphere in *Inamdar* and *Ramanathan* (1997) could be misleading.

Regarding the origin, E_U is more closely related to the total internal kinetic energy of the atmosphere, which – according to the virial theorem – in hydrostatic equilibrium balances the total gravitational potential energy. To identify E_U as the total internal kinetic energy of the atmosphere, the $E_U = S_U/2$ equation must hold. E_U can also be related to G_N through the $E_U = S_U(A - G_N)$ equation. In opaque atmospheres $A = 1$ and the $G_N = 0.5$ is the theoretical upper limit of the normalized greenhouse factor.

3.2 Hydrostatic equilibrium

In Eq. (6) $S_U - (F^0 + P^0)$ and $E_D - E_U$ represent two flux terms of equal magnitude, propagating into opposite directions, while using the same F^0 and P^0 as energy sources. The first term heats the atmosphere and the second term maintains the surface energy balance. The principle of conservation of energy dictates that:

$$S_U - (F^0 + P^0) + E_D - E_U = F^0 + P^0 = OLR\,. \tag{7}$$

This equation poses a strict criterion on the global average S_U:

$$S_U = 3OLR/2 \quad \rightarrow \quad S_U - (F^0 + P^0) = R\,. \tag{8}$$

In the right equation R is the pressure of the thermal radiation at the ground: $R = S_U/3$. This equation might make the impression that G does not depend on the atmospheric absorption, which is generally not true. We shall see that under special conditions this dependence is negligible. Eq. (8) expresses the conservation of radiant energy but does not account for the fact, that the atmosphere is gravitationally bounded. Implementing the virial theorem into Eq. (8) is relatively simple. In the form of an additive S_V 'virial' term we obtained the general radiative balance equation:

$$S_U + S_T/2 - E_D/10 = 3OLR/2 \quad \rightarrow \quad S_U - (F^0 + P^0) = 6RA/5\,. \tag{9}$$

In Eq. (9) the $S_V = S_T/2 - E_D/10$ virial term will force the hydrostatic equilibrium while maintaining the radiative balance. From Eq. (9) follow the $3/5 + 2T_A/5 = OLR/S_U$ and the $E_U/E_D = 3/5$ relations. This equation is based on the principle of the conservation of energy and the virial theorem, and we expect that it will hold for any clear absorbing planetary atmosphere.

The optimal conversion of $F^0 + P^0$ to OLR would require that either $T_A \approx 0$ or $T_A \approx 1$. The first case is a planet with a completely opaque atmophere with saturated greenhouse effect, and the second case is a planet without greenhouse gases. For the Earth obviously the $T_A \approx 0$ condition apply and the $OLR^A/S_U^A = 3/5$ equation gives an optimal global average surface upward flux of $S_U^A = 392$ W m^{-2} and a global average surface temperature of 288.3 K. We know that – because of the existence of the IR atmospheric window – the flux transmittance must not be zero and the atmosphere can not be opaque. The Earth's atmosphere solves this contradiction by using the radiative effect of a partial cloud cover.

For atmospheres, where $E_D \approx 5 S_T$ or $T_A \approx 1/6$, Eq. (9) will take the form of Eq. (8). In optically thin atmospheres where, $E_D/10 << OLR$ or $S_T >> E_U$, Eq. (9) simplifies to:

$$S_U + S_T/2 = 3OLR/2 \quad \rightarrow \quad S_U - (F^0 + P^0) = R A . \qquad (10)$$

Eq. (10) implies the $2/3 + T_A/3 = OLR/S_U$ and $E_U/E_D = 2/3$ relations. Applying this equation for the Earth's atmosphere will introduce more than 10% error in the OLR.

3.2 Transfer and greenhouse functions

The relationships between the OLR and S_U may be expressed by using the concept of the transfer function. The transfer function converts the surface upward radiation to outgoing LW radiation. It is practically the OLR/S_U ratio or the normalized OLR. The greenhouse functions are analogous to the empirical G_N factor introduced in Section 2. From Eqs. (8), (9), and (10) one may easily derive the $f^+ = 2/3$, $f^\circ = 1 - 2A/5$, and $f^* = 1 - A/3$ transfer functions, and the $g^+ = 1/3$, $g^\circ = 2A/5$, and $g^* = A/3$ greenhouse functions, respectively. The g^+, g°, and g^* greenhouse functions will always satisfy the $S_U > F^0 + P^0$ relationship, which is the basic requirement of the greenhouse effect. On the evolutionary time scale of a planet, the mass and the composition of the atmosphere together with the F^0 and P^0 fluxes may change dramatically and accordingly, the relevant radiative balance equation could change with the time and could be different for different planets.

The most interesting fact is, that in case of Eq. (8) $g^+ = R/S_U = 1/3$ does not depend on the optical depth. G will always be equal to the radiation pressure of the ideal gas, and the atmosphere will have a constant optical depth $\tilde{\tau}_A^+$ which is only dependent on the sum of the external SW and internal thermal radiative forcings. In Eqs. (9) and (10) the dependence of G on A is expected. Planets following the radiation scheme of Eq. (8) can not change their surface temperature without changing the surface pressure – total mass of the atmosphere – or the SW or thermal energy input to the system. This kind of planet should have relatively strong absorption ($T_A \approx 1/6$), and the greenhouse gases must be the minor atmospheric constituents with very small effect on the surface pressure. Earth is a planet of this kind. In the Martian atmosphere E_U is far too small and in the Venusian atmosphere S_G is far too large to satisfy the $E_U \approx S_U/2$ condition, moreover, the atmospheric absorption on these planets significantly changes with the mass of the atmosphere – or with the surface pressure.

Our simulations show that on the Earth the global average transmitted radiative flux and downward atmospheric radiation are $S_T^E = 61$ W m^{-2} and $E_D^E = 309$ W m^{-2}. The $S_T^E \approx E_D^E/5$ approximation holds and Eq. (8) with the g^+ greenhouse function may be used. The global average clear sky S_U and OLR are $S_U^E = 382$ W m^{-2} and $OLR^E = 250$ W m^{-2}. Correcting this S_U^E to the altitude level where the OLR was computed (61.2 km), we may calculate the global average G_N as $G_N^E = (S_U^E - OLR^E)/S_U^E = 0.332$. In fact, G_N^E is in very good agreement with the theoretical $g^+ = 0.333$. The simulated global average flux optical depth is $\tilde{\tau}_A^E = -\ln(T_A^E) = 1.87$, where T_A^E is the global average flux transmittance. This simulated $\tilde{\tau}_A^E$ can not be compared with theoretical optical depths from Eq. (8) without the explicit knowledge of the $S_U(OLR, \tilde{\tau}_A)$ function. The best we can do is to use Eq. (9) – the $T_A = 1/6$ condition – to get an estimate of $\tilde{\tau}_A^+ \approx -\ln(1/6) = 1.79$, which is not very far from our $\tilde{\tau}_A^E$.

The popular explanation of the greenhouse effect as the result of the LW atmospheric absorption of the surface radiation and the surface heating by the atmospheric downward radiation is incorrect, since the involved flux terms (A_A and E_D) are always equal. The mechanism of the greenhouse effect may better be explained as the ability of a gravitationally bounded atmosphere to convert $F^0 + P^0$ to OLR in such a way that the equilibrium source function profile will assure the radiative balance ($F^0 + P^0 = OLR$), the validity of the Kirchhoff law ($E_D = S_U A$), and the hydrostatic equilibrium ($S_U = 2E_U$). Although an atmosphere may accommodate the thermal structure needed for the radiative equilibrium, it is not required for the greenhouse effect. Formally, in the presence of a solid or liquid surface, the radiation pressure of the thermalized photons is the real cause of the greenhouse effect, and its origin is related to the principle of the conservation of the momentum of the radiation field.

Long term balance between $F^0 + P^0$ and OLR can only exist at the $S_U = (F^0 + P^0)/(1 - 2A/5) \approx 3(F^0 + P^0)/2$ planetary equilibrium surface upward radiation. It worth to note that S_U does not depend directly on F, meaning that the SW absorption may happen anywhere in the system. F^0 depends only on the system albedo, the solar constant, and other relevant astronomical parameters.

In the broad sense the surface-atmosphere system is in the state of radiative balance if the radiative flux components satisfy Eqs. (3), (4), and (8). The equivalent forms of these conditions are the $E_D - E_U = S_U/3$ and $E_D - E_U = OLR/2$ equations. In such case there is no horizontal exchange of energy with the surrounding environment, and the use of a one dimensional or single-column model for global energy budget studies is justified.

Our task is to establish the theoretical relationship between S_U and OLR as the function of $\tilde{\tau}_A$ for semi-transparent bounded atmospheres assuming, that the radiative balance (Eqs. (8) and (9)) is maintained and the thermal structure (source function profile) satisfies the criterion of the radiative equilibrium. The evaluation of the response of an atmosphere for greenhouse gas perturbations is only possible with the explicit knowledge of such relationship.

4. Flux optical depth

To relate the total IR absorber amount to the flux densities, the most suitable parameter is the total IR flux optical depth. In the historical development of the gray approximation different spectrally averaged mean optical depths were introduced to deal with the different astrophysical problems (*Sagan*, 1969). If we are interested in the thermal emission, our relevant mean optical depth will be the Planck mean. Unfortunately, the Planck mean works only with very small monochromatic optical depths (*Collins*, 2003). In the Earth atmosphere the infrared monochromatic optical depth is varying many orders of magnitude, therefore, the required criteria for the application of the Planck mean is not satisfied.

This problem can be eliminated without sacrificing accuracy by using the simulated flux optical depth. Such optical depths may be computed from monochromatic directional transmittance by integrating over the hemisphere. We tuned our line-by-line (LBL) radiative transfer code (HARTCODE) for an extreme numerical accuracy, and we were able to compute the flux optical depth in a spherical refractive environment with an accuracy of five significant digits (*Miskolczi et al.*, 1990). To obtain this accuracy 9 streams, 150 homogeneous vertical layers, and 1 cm^{-1} spectral resolution were applied. These criteria control the accuracy of the numerical hemispheric and altitude integration and the convolution integral with the blackbody function, see Appendix A.

All over this paper the simulated total flux optical depths were computed as the negative natural logarithms of these high accuracy Planck weighted hemispheric monochromatic transmittance: $\tilde{\tau}_A = -\ln(T_A)$.

In a non-scattering atmosphere, theoretically, the dependence of the source function on the monochromatic optical depth is the solution of the following differential equation (*Goody* and *Young*, 1989):

$$\frac{d^2 H_\nu(\tau_\nu)}{d\tau_\nu^2} - 3H_\nu(\tau_\nu) = -4\pi \frac{dJ_\nu(\tau_\nu)}{d\tau_\nu}, \tag{11}$$

where $H_\nu(\tau_\nu)$ is the monochromatic net radiative flux (Eddington flux) and $J_\nu(\tau_\nu)$ is the monochromatic source function, which is – in LTE – identical with the Planck function, $J_\nu(\tau_\nu) = B_\nu(\tau_\nu)$. The vertically measured monochromatic optical depth is τ_ν. Eq. (11) assumes the isotropy of the radiation field in each hemisphere and the validity of the Eddington approximation.

For monochromatic radiative equilibrium $dH_\nu(\tau_\nu)/d\tau_\nu = 0$ and Eq. (11) becomes a first order linear differential equation for $B_\nu(\tau_\nu)$. Applying the gray approximation, one finds that there will be no dependence on the wave number, τ_ν will become a mean vertical gray-body optical depth, $\overline{\tau}$, and H will become the net radiative flux:

$$dB(\overline{\tau})/d\overline{\tau} = 3H/(4\pi). \tag{12}$$

The well known solution of Eq. (12) is:

$$B(\overline{\tau}) = (3/4\pi)H\overline{\tau} + B_0. \tag{13}$$

According to Eq. (13), in radiative equilibrium the source function increases linearly with the gray-body optical depth. The integration constant, B_0, can be determined from the Schwarzschild-Milne equation, which relates the net flux to the differences in the hemispheric mean intensities:

$$H(\overline{\tau}) = \pi(\overline{I}^+ - \overline{I}^-), \tag{14}$$

where $\overline{I}^+$ and $\overline{I}^-$ are the upward and downward hemispheric mean intensities, respectively. In the solution of Eq. (12) one has to apply the appropriate boundary conditions. In the further discussion we shall allow S_G and S_A to be different.

4.1 Semi-infinite atmosphere

In the semi-infinite atmosphere, the total vertical optical depth of the atmosphere is infinite. The boundary condition is usually given at the top of the atmosphere, where, due to the absence of the downward flux term, the net IR flux is known. Using the general classic solutions of the plane-parallel radiative transfer equation in Eq. (14), one sees that the integration constant will become $B_0 = H/(2\pi)$. Putting this B_0 into Eq. (13) will generate the classic semi-infinite solution for the $B(\tilde{\tau})$ source function:

$$B(\tilde{\tau}) = H(1+\tilde{\tau})/(2\pi), \tag{15}$$

where $\tilde{\tau}$ is the flux optical depth, as usually defined in two stream approximations, $\tilde{\tau}=(3/2)\bar{\tau}$. In astrophysics monographs Eq. (15) is referred to as the solution of the Schwarzschild-Milne type equation for the gray atmosphere using the Eddington approximation.

The characteristic gray-body optical depth, $\hat{\tau}_C$, defines the IR optical surface of the atmosphere: $\pi B(\hat{\tau}_C)=H$. The 'hat' indicates that this is a theoretically computed quantity. At the upper boundary, $\tilde{\tau}=0$, the source function is finite, and is usually associated with the atmospheric skin temperature: $\pi B_0=\pi B(0)=H/2$. Note, that in obtaining B_0, the fact of the semi-infinite integration domain over the optical depth in the formal solution is widely used. For finite or optically thin atmosphere Eq. (15) is not valid. In other words, this equation does not contain the necessary boundary condition parameters for the finite atmosphere problem.

Despite the above fact, in the literature of atmospheric radiation and greenhouse effect, Eq. (15) is almost exclusively applied to derive the dependence of the surface air temperature and the ground temperature on the total flux optical depth (*Goody* and *Yung*, 1989; *Stephens* and *Greenwald*, 1991; *McKay et al.*, 1999; *Lorenz* and *McKay*, 2003):

$$t_A^4=t_E^4(1+\tilde{\tau}_A)/2, \tag{16}$$

$$t_G^4=t_E^4(2+\tilde{\tau}_A)/2, \tag{17}$$

where $t_A^4=\pi B(\tilde{\tau}_A)/\sigma$, $t_G^4=t_A^4+t_E^4/2$, and $t_E^4=H/\sigma=OLR/\sigma$ are the surface air temperature, ground temperature, and the effective temperature, respectively. At the top of the atmosphere the net IR radiative flux is equal to the global average outgoing long wave radiation. As we have already seen, when long term global radiative balance exists between the SW and LW radiation, OLR is equal to the sum of the global averages of the available SW solar flux and the heat flux from the planetary interior.

Eq. (15) assumes that at the lower boundary the total flux optical depth is infinite. Therefore, in cases, where a significant amount of surface transmitted radiative flux is present in the OLR, Eqs. (16) and (17) are inherently incorrect. In stellar atmospheres, where, within a relatively short distance from the surface of a star the optical depth grows tremendously, this could be a reasonable assumption, and Eq. (15) has great practical value in astrophysical applications. The semi-infinite solution is useful, because there is no need to specify any explicit lower boundary temperature or radiative flux parameter (*Eddington*, 1916).

When considering the clear-sky greenhouse effect in the Earth's atmosphere or in optically thin planetary atmospheres, Eq. (16) is physically meaningless, since we know that the *OLR* is dependent on the surface temperature, which conflicts with the semi-infinite assumption that $\tilde{\tau}_A = \infty$. Eq. (17) is also not a prescribed mathematical necessity, but an incorrect assumption for the downward atmospheric radiation and applying the relationship of Eq. (16). As a consequence, Eq. (16) will underestimate t_A, and Eq. (17) will largely overestimate t_G (*Miskolczi* and *Mlynczak*, 2004).

There were several attempts to resolve the above deficiencies by developing simple semi-empirical spectral models, see for example *Weaver* and *Ramanathan* (1995), but the fundamental theoretical problem was never resolved. The source of this inconsistency can be traced back to several decades ago, when the semi-infinite solution was first used to solve bounded atmosphere problems. About 80 years ago Milne stated: "Assumption of infinite thickness involves little or no loss of generality", and later, in the same paper, he created the concept of a secondary (internal) boundary (*Milne*, 1922). He did not realize that the classic Eddington solution is not the general solution of the bounded atmosphere problem and he did not re-compute the appropriate integration constant. This is the reason why scientists have problems with a mysterious surface temperature discontinuity and unphysical solutions, as in *Lorenz* and *McKay* (2003). To accommodate the finite flux optical depth of the atmosphere and the existence of the transmitted radiative flux from the surface, the proper equations must be derived.

4.2 Bounded atmosphere

In the bounded or semi-transparent atmosphere $OLR = E_U + S_T$. In the Earth's atmosphere, the lower boundary conditions are well defined and explicitly given by t_A, t_G, and $\tilde{\tau}_A$. The surface upward hemispheric mean radiance is $B_G = S_G / \pi = \sigma t_G^4 / \pi$. The upper boundary condition at the top of the atmosphere is the zero downward IR radiance.

The complete solution of Eq. (12) requires only one boundary condition. To evaluate B_0 we can use either the top of the atmosphere or the surface boundary conditions since both of them are defined. Applying the boundary conditions in Eq. (14) at $H = H(0)$ and $H = H(\overline{\tau}_A)$ will yield two different equations for B_0. The traditional way is to solve this as a system of two independent equations for B_0 and B_G as unknowns, and arrive at the semi-infinite solution with a prescribed temperature discontinuity at the ground. In the traditional way, therefore, B_G becomes a constant, which does not represent the true lower boundary condition.

The source of the problem is, that at the lower boundary B_G is treated as an arbitrary parameter. In reality, when considering the Schwarzschild-Milne equation at $H = H(\overline{\tau}_A)$, we must apply a constraint for B_G. In the introduction we showed that this is set by the total energy balance requirement of the system: $OLR = S_G - E_D + E_U$. Using the above condition for solving Eq. (14) at $H = H(\overline{\tau}_A)$ will be equivalent to solving the same equation at $H = H(0)$. For mathematical simplicity now we introduce the atmospheric transfer and greenhouse functions by the following definitions:

$$f(\tilde{\tau}_A) = 2/(1+\tilde{\tau}_A + \exp(-\tilde{\tau}_A)), \tag{18}$$

and

$$g(\tilde{\tau}_A) = (\tilde{\tau}_A + \exp(-\tilde{\tau}_A) - 1)/(\tilde{\tau}_A + \exp(-\tilde{\tau}_A) + 1). \tag{19}$$

The f and g are special functions and they have some useful mathematical properties: $f = 1 - g$ and $dg / d\tilde{\tau}_A = -df / d\overline{\tau}_A = f^2 A/2$. Later we shall see that in case of radiative equilibrium, these functions partition the surface upward radiative flux into the OLR and $S_G - OLR$ parts. Using the above notations the derived B_0 takes the form:

$$\pi B_0 = \frac{H}{2A}\left[\frac{2}{f} - \tilde{\tau}_A A\right] - \pi B_G T_A / A. \tag{20}$$

For large $\tilde{\tau}_A$ this B_0 tends to the semi-infinite solution. Combining Eq. (20) with Eq. (13) we obtain the general form of the source function for the bounded atmosphere:

$$\pi B(\tilde{\tau}) = \frac{H}{2A}\left[\frac{2}{f} - (\tilde{\tau} - \tilde{\tau}_A)A\right] - \pi B_G T_A / A. \tag{21}$$

We call Eq. (21) the general greenhouse equation. It gives the fundamental relationship between $\tilde{\tau}$, $\tilde{\tau}_A$, B_G, H, and the IR radiation fluxes, and this is the equation that links the surface temperatures to the column density of absorber. This equation is general in the sense, that it contains the general boundary conditions of the semi-transparent atmosphere, and asymptotically includes the classic semi-infinite solution. For the validity of Eq. (21) the radiative equilibrium condition (Eq. (12)) must hold.

We could not find any references to the above equation in the meteorological literature or in basic astrophysical monographs, however, the importance of this equation is obvious, and its application in modeling the greenhouse effect in planetary atmospheres may have far reaching consequences.

For example, radiative-convective models usually assume that the surface upward convective flux is due to the temperature discontinuity at the surface. The fact, that the new B_0 (skin temperature) changes with the surface temperature and total optical depth, can seriously alter the convective flux estimates of previous radiative-convective model computations. Mathematical details on obtaining Eqs. (20) and (21) are summarized in Appendix B.

At the upper boundary $H = OLR$, and it is immediately clear that for large $\tilde{\tau}_A$ Eq. (21) converges to the semi-infinite case of Eq. (15). It is also clear that the frequently mentioned temperature discontinuity requirement at the surface has been removed by the explicit dependence of $B(\tilde{\tau})$ on B_G. The derivative of this equation is constant and equal to $3H/(4\pi)$, just like in the semi-infinite case, as it should be. According to Eq. (21), the surface air temperature and the characteristic optical depth depend on B_G and $\tilde{\tau}_A$:

$$\pi B(\tilde{\tau}_A) = (OLR/f - \pi B_G T_A)/A, \tag{22}$$

$$\hat{\tau}_C = 1 + \frac{2(1 - \pi B_G / OLR) + \tilde{\tau}_A}{1 - \exp(\tilde{\tau}_A)}. \tag{23}$$

Particularly simple forms of the OLR and E_U may be derived from Eq. (22):

$$OLR = f(S_A A + S_G T_A), \tag{24}$$

$$E_U = f S_A A - g S_G T_A. \tag{25}$$

In Eqs. (24) and (25) $S_A = \pi B(\tilde{\tau}_A) = \sigma t_A^4$. The upward atmospheric radiation clearly depends on the ground temperature and can not be computed without the explicit knowledge of S_G.

5. *Temperature discontinuity*

Now we shall again assume the thermal equilibrium at the surface: $t_S = t_A = t_G$. Inevitably, because the radiating ground surface is not a perfect blackbody, $S_U = S_A > S_G$, and $S_G = \varepsilon_G \sigma t_G^4 = \varepsilon_G \sigma t_S^4 = \varepsilon_G S_U$. From Eq. (24) one may easily express t_S:

$$t_S^4 = t_E^4 /(1 + T_A(\varepsilon_G - 1))/f. \tag{26}$$

For high emissivity and opaque areas the following approximations will hold:

$$t_S^4 = t_E^4 / f, \tag{27}$$

$$S_U = OLR / f. \tag{28}$$

The $E_U / S_U = (OLR - S_T)/ S_U = f - T_A$ relationship follows from Eq. (28). This function (normalized upward atmospheric radiation) has a sharp maximum at $\tilde{\tau}_A^U = 1.59$. It is worth noting, that in Eq. (26) the dependence of t_S on ε_G opens up a greenhouse feedback channel which might have importance in relatively transparent areas with low emissivity, for example at ice covered polar regions. Also, Eq. (26) must be the preferred equation to study radiative transfer above cloud layers. Assuming the global averages of $\varepsilon_G = 0.95$ and $T_A = 0.17$, Eq. (27) will underestimate t_S by about 0.9 per cent.

So far at the definition of ε_G we ignored the reflected part of the downward long-wave flux. The true surface emissivity is: $\varepsilon'_G = E_D T_A /(S_U - E_D)/ A$. ε'_G may be obtained from ε_G by applying the next correction: $\varepsilon'_G = \varepsilon_G T_A /(1 - \varepsilon_G A)$. The energy balance at the boundary is maintained by the net sensible and latent heat fluxes and other energy transport processes of non-radiative origin. Further on we shall assume that the $\varepsilon_G = \varepsilon'_G = 1$ approximation and Eqs. (27) and (28) are valid. Let us emphasize again, that these equations assume the thermal equilibrium at the ground.

5.1 Energy minimum principle

We may also arrive at Eq. (28) from a rather different route. The principle of minimum energy requires the most efficient disposal of the thermal energy of the atmosphere. Since in radiative equilibrium the quantity πB_0 is an additive constant to the source function, for a given OLR and S_G we may assume that in the atmosphere the total absorber amount (water vapor) will maximize B_0.

Mathematically, $\tilde{\tau}_A$ is set by the $dB_0 / d\tilde{\tau}_A = 0$ condition. It can be shown that this is equivalent to solve the $S_G = OLR / f$ transcendental equation for $\tilde{\tau}_A$, see the details in Appendix B. Comparing this equation with Eq. (28) follows the $S_G = S_U$ equation.

In other words, in radiative equilibrium there is a thermal equilibrium at the ground and the quantities S_G, OLR, and $\tilde{\tau}_A$ are linked together in such a way that $\tilde{\tau}_A$ will maximize B_0. The above concept is presented in *Fig. 3*. Here we show three πB_0 functions, with short vertical lines indicating the positions of their maxima. The thick solid curve was computed from Eq. (20) with the clear sky global averages of $OLR = 250$ W m^{-2} and $\pi B_G = 382$ W m^{-2}. The open circle at $\tilde{\tau}_A = 1.87$ represents the global average πB_0 of 228 simulations.

The position of the maximum of this curve is practically coincidental with the global average $\tilde{\tau}_A^E$. The location of the maximum may be used in a parameterized $H_2O(\tilde{\tau}_A)$ function for the purely theoretical estimate of the global average water vapor content. In such estimate our global average $\tilde{\tau}_A$ would result in about 2.61 precipitable centimeter (prcm) H_2O column amount.

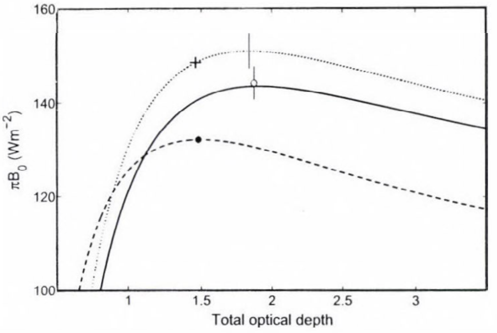

Fig. 3. $\pi B_0(\tilde{\tau}_A)$ functions computed from Eq. (20) for a realistic range of $\tilde{\tau}_A$. The solid line represents the clear-sky global average. The maximum of this curve is $\pi B_0 = 142$ W m^{-2} at $\tilde{\tau}_A = 1.86$. The open circle at $\pi B_0 = 143$ W m^{-2} and $\tilde{\tau}_A = 1.87$ is the global average of large scale line-by-line simulations involving 228 temperature and humidity profiles from around the globe. The broken line and the solid dot were computed for a zonal average arctic profile. The dotted line and the '+' symbol represent similar computations for the USST-76 atmosphere.

The broken line and the full circle show similar computations for a zonal mean arctic profile. For reference, the $\pi B_0(\tilde{\tau}_A)$ function of the U.S. Standard Atmosphere, 1976 (USST-76) is also plotted with a dotted line. In this case the actual optical depth $\tilde{\tau}_A^{US} = 1.462$ (indicated by the '+' symbol) is not coincidental with the position of tche maximum of the $\pi B_0(\tilde{\tau}_A)$ curve, meaning that this profile does not satisfy Eq. (28). Compared to the required equilibrium surface temperature of $t_A^{US} = 280.56$ K, the USST-76 atmosphere is warmer by about 7.6 K at the ground. Some further comparisons of the theoretical and simulated total optical depths are shown in *Fig. 4*.

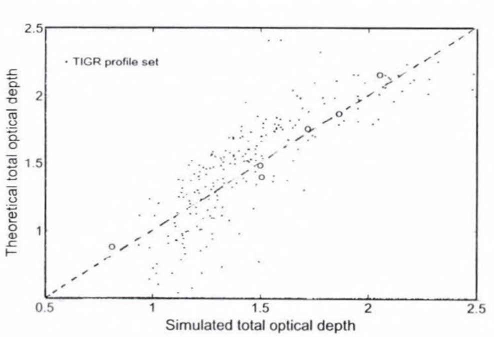

Fig. 4. Comparisons of the theoretical and simulated total flux optical depths. The inner four circles were computed for global and zonal mean temperature profiles, the leftmost circle were computed for an extremely cold arctic profile, the rightmost circle represents a mid-latitudinal summer profile. The dots show the results of 228 LBL simulations. The scatter of the dots are due to the fact that the temperature profiles were not in perfectradiative equilibrium.

The simulated data points were obtained by LBL computations using zonal mean temperature profiles at different polar and equatorial belts. The theoretical values – the solutions of Eq. (28) – are in fairly good agreement with the simulated $\tilde{\tau}_A$, the correlation coefficient is 0.989. The major conclusion of *Figs. 3* and *4* is the fact that for large scale spatial averages the finite atmosphere problem may be handled correctly with the different forms of Eqs. (24) or (28). For local or instantaneous fluxes (represented by the gray dots) the new equations do not apply because the chances to find an air column in radiative balance are slim.

5.2 Global average profiles

In *Fig. 5* we present our global average source function profile – which was computed from selected all-sky radiosonde observations – and the theoretical predictions of the semi-infinite and semi-transparent approximations.

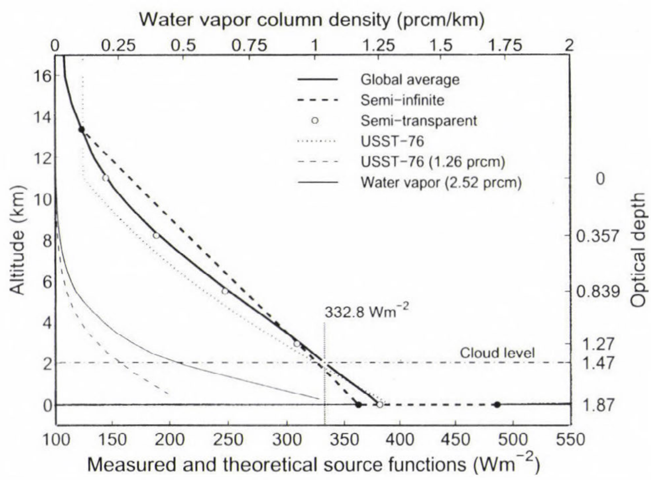

Fig. 5. Theoretical and measured source function profiles, and the global average H_2O profile. The solid lines were computed from 228 selected all sky radiosonde observations. The black dots and the dashed line represent the semi-infinite approximation with the temperature discontinuity at the ground. The open circles were computed from Eq. (21). The optical depth values of 0.357, 0.839, 1.28, 1.47, and 1.87 correspond to $\hat{\tau}_{E_U}$, $\hat{\tau}_C$, $\hat{\tau}_{E_D}$, $\bar{\tau}_A^C \approx \bar{\tau}_A^{US}$, and $\bar{\tau}_A^E$, respectively. The dash-dot line is the approximate altitude of an assumed cloud layer where the $OLR^A = E_D = OLR$.

The source function profile of the USST-76 model atmosphere is also plotted with a dotted line. The global average tropospheric source function profile is apparently a radiative equilibrium profile satisfying Eq. (21) or the

$B(\tilde{\tau}) = OLR\,\tilde{\tau}/2 + B_0$ equation, where $B_0 = 146$ W m^{-2}. Up to 10 km altitude the $B(z) \approx OLR^A\,(1 - z/10) + B_0$ approximation may be used, where the global average OLR^A is: $OLR^A \approx OLR\,\tilde{\tau}_A^E/2$.

Clearly the new equations give a far better representation of the true average tropospheric source function profile than the one obtained from the opaque semi-infinite equation. Our source function profile corresponds to a temperature profile with an average tropospheric lapse rate of 5.41 K km^{-1}. The flux densities S_U^E and OLR^E with $\tilde{\tau}_A^E$ closely satisfy Eqs. (8), (9), and (28). This optical depth is consistent with the observed global average water vapor column amount of about 2.5 prcm in *Peixoto* and *Oort* (1992).

In *Fig. 5* the thin solid and broken lines – and the top axis – show the water vapor column density profiles of our global average and the USST-76 atmospheres respectively.

Since the Earth-atmosphere system must have a way to reduce the clear sky OLR^E to the observed OLR^A we assume the existence of an effective cloud layer at about 2.05 km altitude. The corresponding optical depth is $\tilde{\tau}_A^C = 1.47$. *Fig. 6* shows the dependences of the OLR and E_D on the cloud top altitude and E_U on the cloud bottom altitude. At this cloud level the source function is $S^C = 332.8$ W m^{-2}. We also assume that the cloud layer is in thermal equilibrium with the surrounding air and radiates as a perfect black-body. Clear sky simulations show that at this level the $OLR \approx OLR^A \approx E_D$ and the layer is close to the radiative equilibrium. Cloudy computations also show that E_U – and consequently K – has a maximum around this level, which is favorable for cloud formation.

In cloudy areas the system loses the thermal energy to space at a rate of OLR^A which is now covered by the absorbed SW flux in the cloudy atmosphere. According to the Kirchhoff law, the downward radiation to the cloud top is also balanced. Below the cloud layer, the net LW flux is close to zero. Clouds at around 2 km altitude have minimal effect on the LW energy balance, and they seem to regulate the SW absorption of the system by adjusting the effective cloud cover β.

The $OLR^A - 2S_U^E/3 \approx -15$ W m^{-2} is a fairly good estimate of the global average cloud forcing. The estimated $\beta \approx 0.6$ is the required cloud cover (at this level) to balance OLR^A, which looks realistic. We believe that the β parameter is governed by the maximum entropy principle, the system tries to convert as much SW radiation to LW radiation as possible, while obeying the $2OLR/(3f) = F^0 + P^0$ condition. The cloud altitude, where the clear-sky $OLR = OLR^A = E_D$ depends only on the SW characteristics of the system (surface and cloud albedo, SW solar input) and alone, is a very important climate parameter.

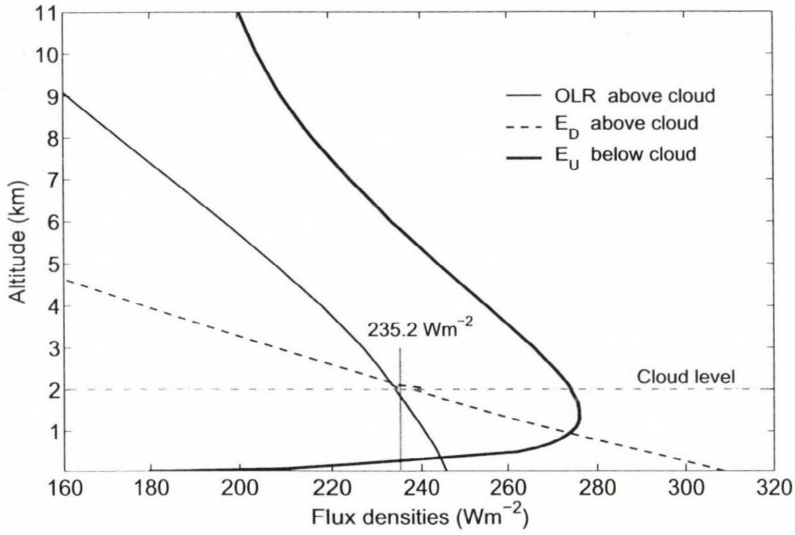

Fig. 6. Cloudy simulation results using the global average temperature and water vapor profiles. For the OLR and E_D curves the altitude is the cloud-top level. For the E_U curve the altitude is the level of the cloud-bottom. Simulations were performed at eleven cloud levels between the 0 and 11 km altitudes. The gray vertical line is the all-sky OLR^A.

In *Kiehl* and *Trenberth* (1997) the USST-76 atmosphere was used for the estimation of the clear-sky global mean E_D and OLR. To make their computed OLR consistent with the ERBE clear-sky observations, they reduced the tropospheric water vapor amount by 12%, to about 1.26 prcm. Our LBL simulation using the same profile indicates that $\tilde{\tau}_A^{US}$=1.462 and $f(\tilde{\tau}_A^{US})=0.742$, and as we have seen already, Eq. (28) is not satisfied. The expected equilibrium transfer function is $f=260.8/391.1=0.6668$, which corresponds to a global average water vapor column amount of 2.5 prcm. This value is about double of the actual amount.

Due to the low water vapor column amount in the USST-76 atmosphere the clear-sky estimates of the global average S_T, E_D, and E_U are irrealistic. The flux transmittance is over estimated by 33% and for example E_D is under estimated by about 31 W m^{-2}. The ERBE clear-sky OLR may also have a 6.5% positive bias. Although Eqs. (4) and (8) are satisfied, this discrepancy indicates that the USST-76 atmosphere does not represent a real radiative equilibrium temperature profile and should not be used as a single-column model for global energy budget studies.

It follows from Eq. (28) that $\pi B_0 = OLR(1-T_A)/2 = OLR(1+\hat{\tau}_C/2)$ and the characteristic optical depth will be equal to the total flux absorptance A. Those optical depths where the source function is equal to E_U or E_D can also be easily derived: $\hat{\tau}_{E_U} = A - 2T_A / f$ and $\hat{\tau}_{E_D} = (2A/f) - T_A - 1$. Using large number of radiosonde observations, the global averages of πB_0, E_U, OLR, E_D, S_U, and their respective optical depths can be computed, and one can establish the dependence of optical depth on the z geometric altitude. In *Fig. 5*, on the right vertical axis, the 0, $\hat{\tau}_{E_U}$, $\hat{\tau}_C$, $\tilde{\tau}_A^C$, $\hat{\tau}_{E_D}$, and $\tilde{\tau}_A^E$ optical depths are also indicated. Note the close to linear relationship between the altitude and the optical depth. This relationship may be represented pretty well by the $\hat{\tau}(z) = \tilde{\tau}_A(1 - z/10)$ equation, where z is given in km. This linear function directly contradicts to the usual assumption of exponential decrease of $\tilde{\tau}(z)$ function, indicating the different nature of $\hat{\tau}(z)$. The optical depth computed from Eq. (21) is essentially the measure of the transfer of heat energy by non radiative processes and can be regarded as a kind of dynamical flux optical depth. Although $\hat{\tau}(0) = \tilde{\tau}_A$, the $\tilde{\tau}(z) = -\ln(T_A(z))$ is an exponential function and the $T_A(z)$ is a linear function. Let us mention that a linear $\hat{\tau}(z)$ function is consistent with the hydrostatic equation: $dp/d\hat{\tau} = g_a / \hat{k}$, where p is the atmospheric pressure, g_a is the gravity acceleration, and $\hat{k}$ is an effective absorption coefficient associated with $\hat{\tau}(z)$.

6. Error estimates

Eq. (28) was extensively validated against the results of large scale LBL simulations of the planetary flux optical depth and greenhouse effect, and selected satellite observations in *Miskolczi* and *Mlynczak* (2004). In *Fig. 7* we summarize the errors of the semi-infinite approximation using Eqs. (16) , (17), and (28). The comparison with Eq. (24) would be more complex, it involves real (or imposed) surface temperature discontinuity (through the term of S_G) and will be discussed elsewhere.

In the realistic range of the clear-sky $\tilde{\tau}_A$, Eq. (28) predicts 2–15% underestimates in the source function at the surface in Eq. (16), and about 25% overestimates in the surface upward radiation in Eq. (17). According to Eqs. (14) and (15), the response of the surface upward flux to a small optical depth perturbation, (CO_2 doubling, for example), is proportional to $\Delta\tilde{\tau}_A$. In the semi-transparent approximation $\Delta S_U(\tilde{\tau}_A) \approx \Delta\tilde{\tau}_A(1 - \exp(-\tilde{\tau}_A))$, which means that the semi-infinite approximation will seriously overestimate ΔS_U.

At a global average clear-sky optical depth the relative error is around 20%, but for smaller optical depth (polar areas) the error could well exceed 60%. Differences of such magnitude may warrant the re-evaluation of earlier greenhouse effect estimates. For the estimation of the greenhouse effect at some point all atmospheric radiative transfer model has to relate the flux optical depth (or absorber amount) to the source function, therefore one should be aware of the errors they might introduce to their results when applying the semi-infinite approximation. The above sensitivity estimates assume a constant *OLR*, therefore, they should be regarded as initial responses for small optical depth perturbations. Considering the changes in the *OLR* as well, the correct theoretical prediction is $\Delta S_U / \Delta \tilde{\tau}_A = (A/4)OLR$.

For example, a hypothetical CO_2 doubling will increase the optical depth (of the global average profile) by 0.0241, and the related increase in the surface temperature will be 0.24 K. The related change in the *OLR* corresponds to −0.3 K cooling. This may be compared to the 0.3 K and −1.2 K observed temperature changes of the surface and lower stratosphere between 1979 and 2004 in *Karl et al.*, (2006).

From the extrapolation of the 'Keeling Curve' the estimated increase in the average CO_2 concentration during this time period is about 22% (*National Research Council of the National Academies*, 2004). Comparing the magnitude of the expected change in the surface temperature we conclude, that the observed increase in the CO_2 concentration must not be the primary reason of the global warming.

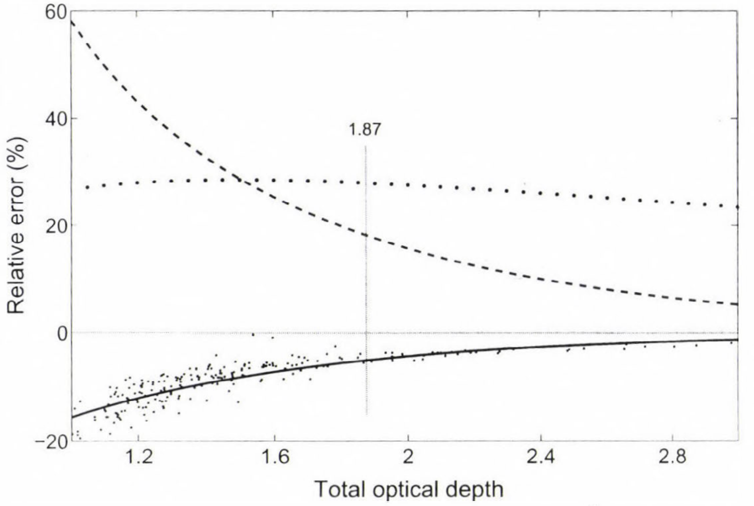

Fig. 7. The three relative error curves are: $f(\tilde{\tau}_A)[(1+\tilde{\tau}_A)/2 - 1/f(\tilde{\tau}_A)]$ (solid line), $f(\tilde{\tau}_A)[1+\tilde{\tau}_A/2 - 1/f(\tilde{\tau}_A)]$ (dotted line), and $1/(\exp(\tilde{\tau}_A)-1)$ (dashed line). These functions represent the relative differences using Eqs. (16) and (17) or Eq. (28) for the computation of $S_U(\tilde{\tau}_A)$ and $\Delta S_U(\tilde{\tau}_A)$, respectively. The vertical line is an estimate of the clear-sky global average $\tilde{\tau}_A$. The dots represent 228 LBL simulation results. The scatter of the dots is due to the fact that the temperature profiles were not in perfect radiative equilibrium.

7. Greenhouse parameters

The f and g functions may be used for the theoretical interpretation of some empirical greenhouse parameters: $G_1 = G_N = g$, and $G_2 = S_U / OLR = 1/f$. Here G_1 is Raval and Ramanathan's normalized greenhouse parameter, and G_2 is Stephens and Greenwald's greenhouse parameter (*Raval* and *Ramanathan*, 1989; *Stephens* and *Greenwald*, 1991). The sensitivity of the greenhouse function to optical depth perturbations is expressed by the derivative of g:

$$g_S = dg / d\tilde{\tau}_A = f^2 A / 2 . \qquad (29)$$

The g_S function has a maximum at $\tilde{\tau}_A^S = 1.0465$, therefore, positive optical depth perturbations in the real atmosphere are coupled with reduced greenhouse effect sensitivity. Here we note, that the $g_S^\circ = 2T_A/5$ and $g_S^* = T_A/3$ sensitivities are decreasing monotonously with increasing $\tilde{\tau}_A$. It is also important that, due to the compensation effect of the combined linear and exponential optical depth terms, the f and g functions have negligible temperature dependence. There is, however, a slight non-linear dependence on the surface temperature introduced by the weighting of the monochromatic flux transmittances with the spectral S_U. Note, that the f and g functions can not be related easily to the absorber amounts, and, for example, a simple linear parameterization of them with the water vapor column amount could be difficult and inaccurate (*Stephens* and *Greenwald*, 1991; *Miskolczi* and *Mlynczak*, 2004).

The greenhouse parameters are dependent only on the flux optical depth, therefore it is difficult to imagine any water vapor feedback mechanism to operate on global scale. The global average $\tilde{\tau}_A^E$ is set by the global energy balance requirement of Eqs. (8) and (9).

It follows from Eqs. (8) and (28) that $3OLR/2 = OLR/f$ and $f = 2/3 = f^+$, giving an equilibrium optical depth of $\tilde{\tau}_A^+ = 1.841$. Using Eq. (9) and (28) the equilibrium optical depth becomes $\tilde{\tau}_A^\circ = 1.867$. The $\tilde{\tau}_A^E = 1.87$ is consistent with these theoretical expectations and the estimate of 1.79 in Section 3. The excess optical depth $\tilde{\tau}_A^E - \tilde{\tau}_A^+ = 0.029$ corresponds to about 1.5 W m^{-2} imbalance in S_U, which may temporarily be compensated for example by 1.0 W m^{-2} net heat flow from the planetary interior or by small decrease in the SW system albedo. In case of Eq. (9) the optical depth difference is even smaller, $\tilde{\tau}_A^E - \tilde{\tau}_A^\circ = 0.003$.

Since the world oceans are virtually unlimited sources and sinks of the atmospheric water vapor (optical depth), the system - depending on the time constant of the different energy reservoirs - has many ways to restore the equilibrium situation and maintain the steady state global climate. For example, in case the increased CO_2 is compensated by reduced H_2O, then the general circulation has to re-adjust itself to maintain the meridional energy flow with less water vapor available. This could increase the global average rain rate and speed up the global water cycle resulting in a more dynamical climate, but still the energy balance equations do not allow the average surface temperature to rise. The general circulation can not change the global radiative balance although, changes in the meridional heat transfer may result in local or zonal warming or cooling which again leads to a more dynamical climate. Note that there are accumulating evidence of long term negative surface pressure trends all over the Southern Hemisphere (*Hines et al.*, 2000), which may be an indication of decreasing water vapor amount in the atmosphere.

The estimation of the absolute accuracy of the simulated global average $\tilde{\tau}_A^E$ is difficult. The numerical errors in the computations are negligible, and probably the largest single source of the error is related to the selection of the representative atmospheric profile set. To decide whether the indicated small optical depth differences are real, further global scale simulations are required.

In the view of the existence of the $\tilde{\tau}_A^+$ and $\tilde{\tau}_A^\circ$ critical optical depth, the runaway greenhouse theories have very little physical foundations. Greenhouse gases in any planetary atmosphere can only absorb the thermalized available SW radiation and the planetary heat flux. Keeping these flux terms constant, deviations from $\tilde{\tau}_A^+$ or $\tilde{\tau}_A^\circ$ will introduce imbalance in Eqs. (8) and (9), and sooner or later – due to the energy conservation principle – the global energy balance must be restored. On the long run the general energy balance requirement of Eq. (9) obviously overrules the IR radiative balance requirement of Eq. (28).

Based on Eq. (28) we may also give a simple interpretation of E_U: $E_U = S_U f - S_U T_A$. Since the total converted $F^0 + P^0$ to OLR is $S_U f$, and $S_U T_A$ is the transmitted part of the surface radiation, the $S_U f - S_U T_A$ difference is the contribution to the OLR from all other energy transfer processes which are not related to LW absorption: $E_U = F + K + P$. Substituting this last equation into the energy balance equation at the lower boundary, and using Eq. (3) we get: $E_D - A_A = 0$. This is the proof of the Kirchhoff law for the surface-atmosphere system. The validity of the Kirchhoff law requires the thermal equilibrium at the surface. Note, that in obtaining Eq. (28) the Kirchhoff law was not used (see Appendix B).

8. Zonal distributions

To explore the imbalance caused by optical depth perturbations, one has to use the differential form of Eq. (28):

$$\Delta f / f = \Delta OLR / OLR - \Delta S_U / S_U . \tag{30}$$

According to Eq. (30) the relative deviations from the equilibrium f, OLR, and S_U must be balanced. The validity of Eq. (30) is nicely demonstrated in *Fig. 8.*

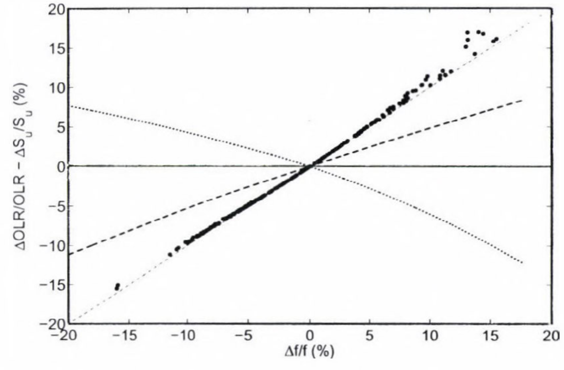

Fig. 8. Validation of the $\Delta f / f = \Delta OLR / OLR - \Delta S_U / S_U$ equation. Dots were computed from radiosonde observations and they represent the relative differences from the equilibrium f. The dashed and dotted lines are fitted to the $\Delta OLR / OLR$ and $\Delta S_U / S_U$ points, respectively.

The Δf can be related to the $\Delta \tilde{\tau}_A$ quantity through the $\Delta f = -\Delta \tilde{\tau}_A f^2 A / 2$ equation. The ΔOLR and ΔS_U quantities are defined by the next two equations: $\Delta OLR = -S_U \Delta \tilde{\tau}_A f^2 A / 4$ and $\Delta S_U = OLR \Delta \tilde{\tau}_A A / 4$. It can be shown that the $\Delta OLR / OLR + \Delta S_U / S_U = 0$, and $\Delta OLR = -f \Delta S_U$ equations also hold. In *Fig. 9* the dependence of ΔS_U on ΔOLR is presented. The open circles in this figure indicate small deviations from Eq. (30). At larger $|\Delta S_U|$ the true ΔOLR is slightly overestimated. *Figs. 8* and *9* show that the surface warming is coupled with reduced OLR, which is consistent with the concept of the stratospheric compensation.

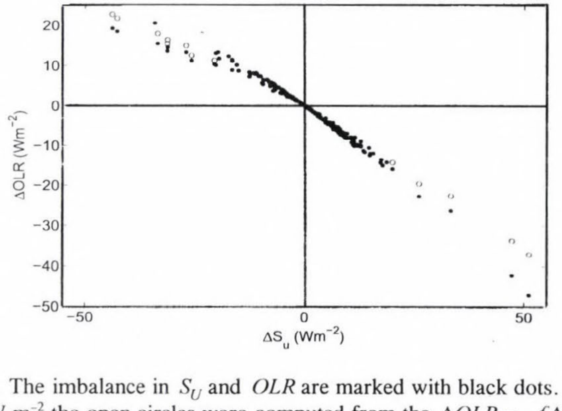

Fig. 9. The imbalance in S_U and OLR are marked with black dots. For the $|\Delta S_U| > 20$ W m^{-2} the open circles were computed from the $\Delta OLR = -f \Delta S_U$ equation.

Unfortunately, our static model can not deal with the dynamical factors represented by the variables K and F. The decomposition of E_U into its several components is beyond the scope of this study. Based on our large scale clear-sky simulations, in *Figs. 10, 11*, and *12* we present the meridional distributions of the zonal mean $\tilde{\tau}_A$, OLR, and S_U, and their deviations from Eqs. (8) and (28).

In *Fig. 10* the zonal average $\tilde{\tau}_A$ distributions are presented. At the equatorial regions up to about +/- 35 degree latitudes, the atmosphere contains more water vapor than the planetary balance requirement of $\tilde{\tau}_A^+$. This feature is the result of the combined effects of evaporation/precipitation processes and the transport of the latent and sensible heat by the general circulation. The reason of the differences between the actual and equilibrium zonal distributions is the clear-sky assumption. The global averages for both distributions are 1.87 representing about 2.61 prcm global average water vapor column amount.

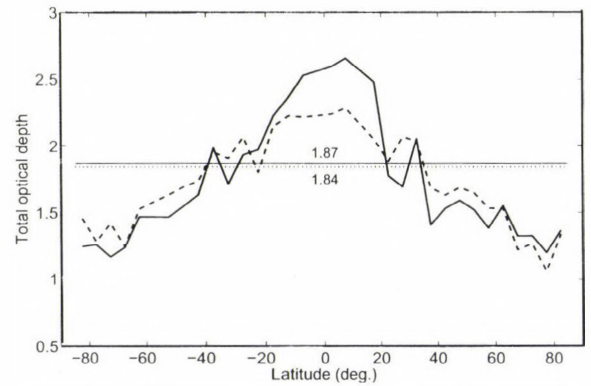

Fig. 10. Meridional distributions of the zonal mean clear sky $\tilde{\tau}_A$. Solid line is the actual $\tilde{\tau}_A$ computed from simulated flux transmittance. Dashed line is the required $\tilde{\tau}_A$ to satisfy the $2S_U / OLR - 1 = \tilde{\tau}_A + \exp(-\tilde{\tau}_A)$ equation. Thin solid horizontal line is the global average for both curves. Dotted line is the planetary equilibrium optical depth, $\tilde{\tau}_A^+$, obtained from Eqs. (6) and (26).

In *Fig. 11* the simulated OLR and the $f S_U$ theoretical curve show good agreement at higher latitudes, indicating that for zonal means the IR radiative balance holds. At the equatorial regions the simulations significantly overestimate $f S_U$. The reason is the un-accounted cloud cover at low latitudes. The dotted line is the required OLR to completely balance the zonal mean S_U and can be regarded as the zonal mean clear-sky F^0.

In *Fig. 12* again, the effect of the cloud cover at low latitudes is the reason of the theoretical overestimation of S_U. At high latitudes Eq. (28) approximately holds. The dots were computed using the semi-infinite model, and they show significant underestimation in the observed zonal mean S_U. According to *Figs. 11* and *12*, at higher latitudes the flux densities are almost balanced.

The quantitative analysis and the explanation of the imbalance at the equatorial regions requires further investigation involving large-scale simulations of cloudy atmospheres. It is also necessary to build a suitable theoretical broad band radiative transfer model for studying the different aspects of a complex multi-layer cloud cover. Using the new equations there is a hope that simple bulk formulation may be developed to deal with the planetary scale energetics of the cloud cover.

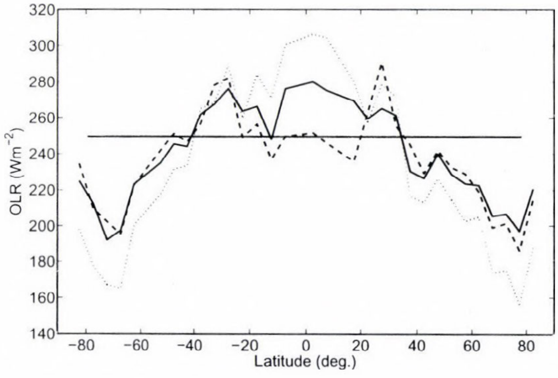

Fig. 11. Meridional distributions of the zonal mean OLR. Solid line is the actual clear-sky OLR computed from all sky radiosonde observations. Dashed line is the required OLR to satisfy the $OLR = fS_U$ equation. The horizontal line is the global average. Dotted line is the zonal mean equilibrium OLR computed as $2S_U/3$.

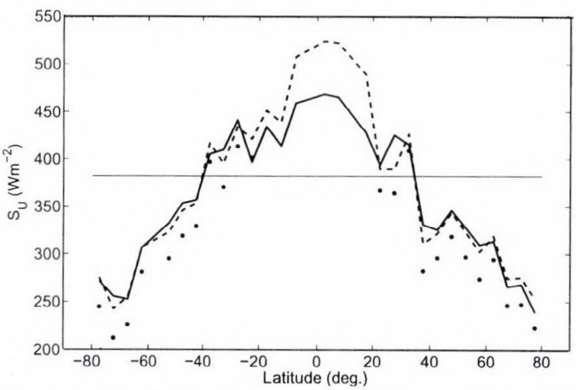

Fig. 12. Meridional distributions of the zonal mean surface upward flux densities. Thick solid line is the observed all sky S_U. Dashed line is the required S_U to satisfy the $S_U = OLR/f$ equation. Thin solid horizontal line is the global average. Dots represent the semi-infinite approximation of $S_U = OLR(1+\tilde{\tau}_A)/2$ for higher latitudes.

9. Planetary applications

The f, $f - T_A$, and g functions can be regarded as theoretical normalized radiative flux components representing OLR / S_U, E_U / S_U, and $(S_U - OLR) / S_U$ ratios, respectively. The f°, $f^{\circ} - T_A$, g°, and f^{*}, $f^{*} - T_A$, and g^{*} are similar functions representing Eqs. (9) and (10), respectively. The dependences of these functions and the g_S function on the optical depth are presented in *Fig. 13*. For reference, in this figure we also plotted the individual simulation results of E_U / S_U for the Earth and Mars, and the OLR / S_U only for the Mars. In the next sections we discuss some further characteristics of the broadband IR atmospheric radiative transfer of Earth and Mars.

At this time the Venusian atmosphere is not included in our study. The major problem with the Venusian atmosphere is the complete cloud cover and the lack of knowledge of the accurate surface SW and LW fluxes. The development of a comprehensive all-sky broadband radiative transfer model is in progress.

9.1 Earth

In *Fig. 13* the simulated global average normalized flux densities are very close to the theoretical curves, proving that the new equations reproduce the real atmospheric situations reasonably well. The horizontal scatter of the gray dots indicate the range of the optical depth that characteristic for the Earth's climate. Theoretically, the lower limit is set by the minimum water vapor amount and the CO_2 absorption. The upper limit is set by a theoretical limiting optical depth of $\tilde{\tau}_A^L = 2.97$, where the transfer and greenhouse functions becoming equal. This optical depth corresponds to about 6 prcm water vapor column amount, which is consistent with the observed maximum water vapor content of a warm and humid atmosphere.

The vertical scatter of the gray dots around the $f - T_A$ curve is the clear indication that locally the atmosphere is not in perfect radiative equilibrium and Eq. (28) is not perfectly satisfied. The obvious reason is the SW effect of the cloud cover and the more or less chaotic motion of the atmosphere. For the global averages Eqs. (8) and (28) represent strict radiative balance requirements. On regional or local scale this equation is not enforced by any physical law and we observe a kind of stochastic radiative equilibrium which is controlled by the local climate.

Over a wide range of optical depth around $\tilde{\tau}_A^U$, the $f - T_A$ curve is close to 0.5, which assures that E_U is approximately equal to $S_U / 2$ independently of the gravitational constraint (virial theorem). This explains why Eqs. (9) and (25) can co-exist at the same $\tilde{\tau}_A^E$. The USST-76 atmosphere seems to follow the radiation scheme of Eqs. (8), $OLR / S_U \approx 2/3$. At the $\tilde{\tau}_A^{US}$ the global radiative balance of the atmosphere is violated and the atmosphere can not be in radiative equilibrium either. The radiative balance and the radiative equilibrium can not co-exist at $\tilde{\tau}_A^{US}$. The radiative imbalance may be estimated from Eqs. (8) and (9) as $S_U(2/3-(1-2A/5)) \approx -10$ W m^{-2}. To retain the energy balance, the USST-76 atmosphere should lose about 10 W m^{-2} more IR radiation to space. The use of such atmospheres for global energy budget studies has very little merit.

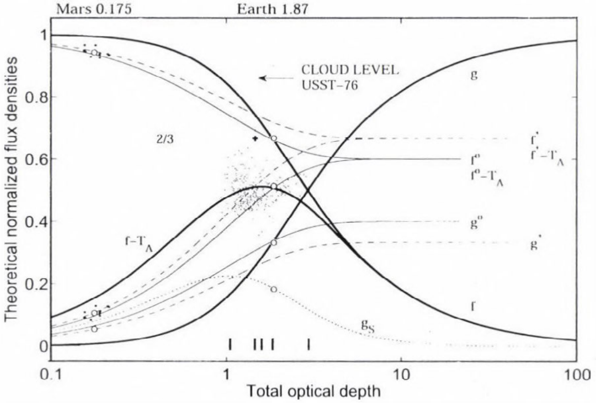

Fig. 13. Theoretical relative radiative flux ratio curves. Open circles are computed planetary averages from simulations. The individual simulation results of E_U/S_U are shown as gray dots for the Earth and black dots in the lower left corner for the Mars. The black dots in the upper left corner are the simulated OLR/S_U for Mars. The g_S curve is the theoretical greenhouse sensitivity function for the Earth. The five short vertical markers on the zero line at the positions of 1.05, 1.42, 1.59, 1.84, and 2.97 are (from left to right) the locations of $\tilde{\tau}_A^S$, $\tilde{\tau}_A^C \approx \tilde{\tau}_A^{US}$, $\tilde{\tau}_A^U$, $\tilde{\tau}_A^+ \approx \tilde{\tau}_A^\circ$, and $\tilde{\tau}_A^L$ optical depths, respectively.

This figure shows that the Earth has a controlled greenhouse effect with a stable global average $\tilde{\tau}_A^E = 1.87 \approx \tilde{\tau}^+ \approx \tilde{\tau}^\circ$, $g(\tilde{\tau}_A^E) = 0.33 \approx g^+ \approx g^\circ(\tilde{\tau}_A^E)$, and $g_S(\tilde{\tau}_A^E) \approx 0.185$. As long as the $F^0 + P^0$ flux term is constant and the system is in radiative balance with a global average radiative equilibrium source function profile, global warming looks impossible. Long term changes in the planetary radiative balance is governed by the $F^0 + P^0 = S_U(3/5 + 2T_A/5)$, $OLR = S_U f$ and $F^0 + P^0 = OLR$ equations. The system is locked to the $\tilde{\tau}_A^\circ$ optical depth because of the energy minimum principle prefers the radiative equilibrium configuration ($\tilde{\tau}_A < \tilde{\tau}_A^\circ$) but the energy conservation principle constrains the available thermal energy ($\tilde{\tau}_A > \tilde{\tau}_A^\circ$). The problem for example with the highly publicized simple 'bucket analogy' of greenhouse effect is the ignorance of the energy minimum principle (*Committee on Radiative Forcing Effects on Climate Change et al.*, 2005).

According to Eq. (9), a completely opaque cloudless atmosphere ($T_A \approx 0$) would accommodate a surface temperature of $\bar{t}_S = 288.3$ K, which is pretty close to the observed global average surface temperature. In this extent the LW effect of the cloud cover is equal to closing the IR atmospheric window and increasing the global average greenhouse effect by about 1.8 K, without changing the $\tilde{\tau}_A^E \approx \tilde{\tau}_A^{\circ}$ relation. The $\beta \approx 0.6$ cloud cover simultaneously assures the validity of the $OLR^A = \bar{S}_U(1 - 2\bar{A}/5) \approx 3\bar{S}_U/5$ radiation balance equation with $\bar{A} \approx 1$ and a global average $\bar{S}_U = 392$ W m^{-2}, and the radiative equilibrium clear-sky source function profile with $\tilde{\tau}_A^E = 1.87$. This could be the configuration, which maintains the most efficient cooling of the surface-atmosphere system.

9.2 Mars

We performed LBL simulations of the broadband radiative fluxes for eight Martian standard atmospheres. In *Fig. 14* the temperature and volume mixing ratio profiles are shown in the 0–60 km altitude range.

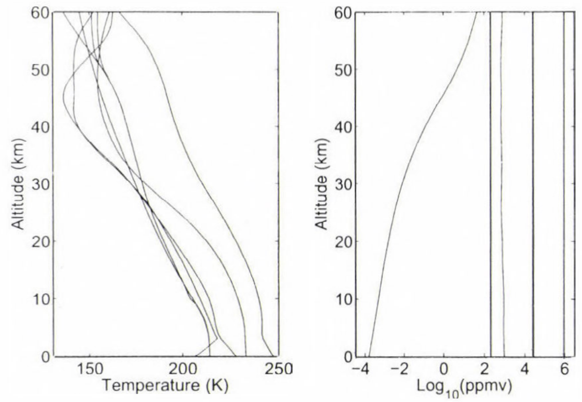

Fig. 14. Martian standard temperature and volume mixing ratio profiles. In the right plot the absorbers are (from left to right): O_3, H_2O, CO, N_2, and CO_2.

In *Fig. 15* dust-free clear-sky computed spectral *OLR* and S_U are presented for the coldest and warmest temperature profiles. The computations were performed in the 1–3490 cm^{-1} wavenumber range with 1 cm^{-1} spectral resolution. The single major absorption feature in these spectra is the 15 CO_2 band. The signatures of the 1042 cm^{-1} ozone band and several H_2O bands are present only in the upper (warmer) spectrum. Despite the almost pure CO_2 atmosphere, the clear Martian atmosphere is remarkably transparent. The average flux transmittance is $T_A = 0.839$ (just about equal to the flux absorptance on the Earth), and the OLR is largely made up from S_T.

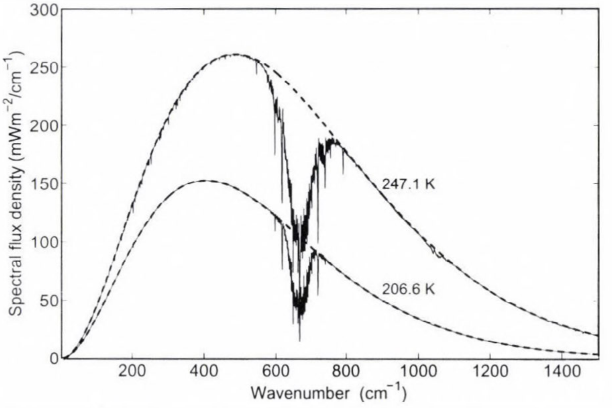

Fig. 15. LBL simulations of the spectral flux densities for a warm and a cold standard Martian atmospheric profile. The thin solid line is the spectral *OLR* and the thick dashed line is the blackbody function at the indicated surface temperatures.

In *Fig. 16* the relationships between S_U and S_T are shown for the Mars and Earth. In case of the Earth, S_T is almost independent of S_U, while in the Martian atmosphere the transmitted radiation depends linearly on the surface upward radiative flux. This fact is an indication that the broadband radiative transfer is fundamentally different on the two planets.

On Mars the optical depth has a strong direct dependence on the total mass of the atmosphere and consequently on surface pressure. The average flux optical depth is small, $\tilde{\tau}_A = 0.175 << \tilde{\tau}_A^+$. In *Fig. 13* the simulated OLR / S_U and E_U / S_U ratios systematically underestimate the theoretical f and $f - T_A$ functions. With the $P^0 \approx 0$ assumption, Mars does not satisfy the IR radiative equilibrium and the overall energy balance criteria at the surface.

For five model profiles the deviations from Eqs. (8) and (28) are presented in *Fig. 17.* The primary reason of the deviations related to the mechanism of the atmospheric heating by non IR radiative processes. On the Earth $K + F$ is large and sufficient to maintain the internal kinetic energy required by the surface pressure and the hydrostatic equilibrium ($E_U / S_U \approx 1/2$). The Martian atmosphere can not gain much energy through the K and F terms. The sublimation and condensation of CO_2 are mainly surface processes, no extended CO_2 cloud cover is observed. The visible and near IR absorption is also small, most of the SW flux is absorbed at the surface, consequently F is also small.

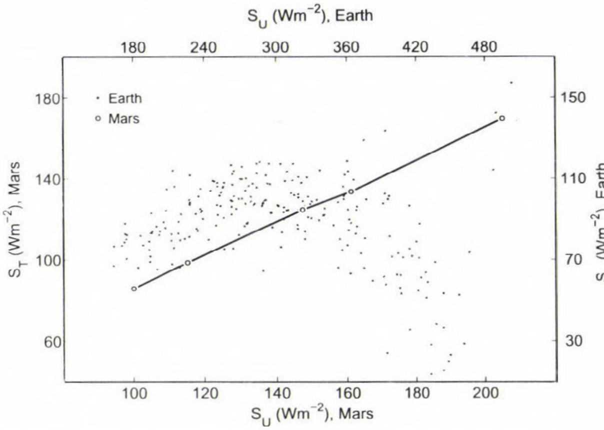

Fig. 16. Relationships between S_U and S_T. Data were obtained by LBL simulations using a set of Martian standard profiles and selected radiosonde observations from the TIGR radiosonde archive. In case of the Earth no significant linear correlation exists between S_U and S_T.

Simulation results show that the average E_U and S_U are 14.2 W m^{-2} and 134 W m^{-2}, respectively. The resulting $E_U/S_U \approx 0.1$ ratio is far too small to assure the hydrostatic equilibrium. In transparent atmospheres the $E_D/10$ term is usually small and may be ignored in Eq. (9). In case of Mars $E_D/10$ is about 1.5% of S_U, and apparentiy, the Martian atmosphere accommodates the radiative transfer scheme of Eq. (10).

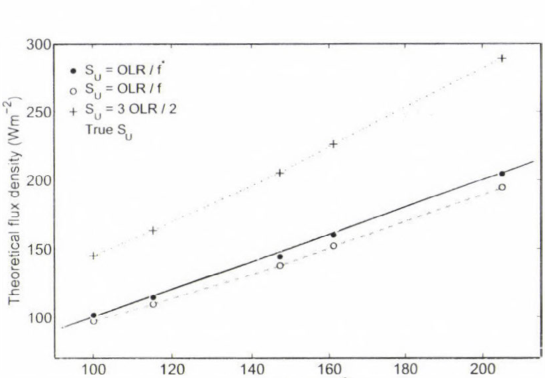

Fig. 17. Validation of the $f^* = 1 - A/3$ transfer function. The solid dots are the S_U fluxes computed with the new f^* transfer function. The 'true' S_U (solid line) were computed from the temperatures of the lowest levels of the standard Martian profiles via the Stefan-Boltzmann law. The 'o' and '+' symbols are the predictions of S_U using the f and the $S_U = 3OLR/2$ equations, respectively.

Using an average available absorbed SW radiation of 127 W m^{-2} Eq. (8) would require –56 W m^{-2} thermal energy to maintain the planetary energy balance. Simulation results show that S_T is 112.3 W m^{-2} and half of it could really restore the energy balance. Since the average E_U is small the $S_T/2$ flux term is the major contribution to the internal kinetic energy of the atmosphere. The wind blown atmospheric dust particles could have an important role in transferring this amount of thermal energy from the surface to the atmosphere. The f^* transfer function predicts both the true S_U in *Fig. 17* (solid dots) and the average relative *OLR* and E_U in *Fig. 13* (open circles) pretty well.

The linear dependence of $S_U f^*$ on $S_U T_A$ in *Fig. 16* explains why the band averaged spectral OLR/S_U ratio resolves the surface topography in the IR images in Chamberlain et al. (2006). The $f^* - T_A$ and g^* functions are also plotted in *Fig. 13*. The intersection of the f^* and f curves points to an optical depth of $\tilde{\tau}_A^* = 1.451$ where the atmosphere would be in radiative equilibrium with a linear average source function profile. At this $\tilde{\tau}_A^*$ the $E_D/10$ term in Eq. (9) becoming large, the approximation of Eq. (10) will not hold, and consequently the radiative balance can not exist. The error of Eq. (10) increases with increasing optical depth.

Regarding the range of the variability of the optical depth (or surface pressure) this situation can not occur in the clear Martian atmosphere. In the radiation scheme of Eq. (10) the runaway greenhouse effect is impossible, S_U will tend to $3OLR/2$ with increasing optical depth.

A further interesting consequence of Eq. (10) is the $2E_D - 3E_U = 0$ relationship. For the deeper understanding of these types of balance equations, in *Figs. 18* and *19* the spectral flux density differences are plotted around the central region of the 15 μm CO_2 absorption band.

In *Fig. 18* the band averaged differences of both the thick and thin solid curves are represented with a single dotted line at the zero position. We see that the spectral deviations of both the $S_U - OLR/f^*$ and $3OLR/2 - (S_U + S_T/2)$ spectral differences are almost perfectly compensated, assuring the validity of the respective balance equations. In *Fig. 19* similar explanation holds for the validity of the $2E_D - 3E_U = 0$ relationship. In this case the integral of the spectral $2E_D - 3E_U$ over the 1–3490 cm^{-1} range is 0.04 W m^{-2} only.

The average normalized greenhouse factor G_N is 0.0522, which is consistent with the $A/3 = 0.0536$ theoretical value. The $G = 7.1$ W m^{-2} greenhouse factor gives 3 K greenhouse enhancement to the planetary average surface temperature. The greenhouse sensitivity is $df^*/d\tilde{\tau}_A = T_A/3 = 0.23$ per unit optical depth and always decreasing with increasing $\tilde{\tau}_A$.

We may conclude, that Eq. (10) adequately describes the broadband radiative fluxes in the Martian atmosphere, but for planets with significantly larger optical depths Eq. (9) must be used.

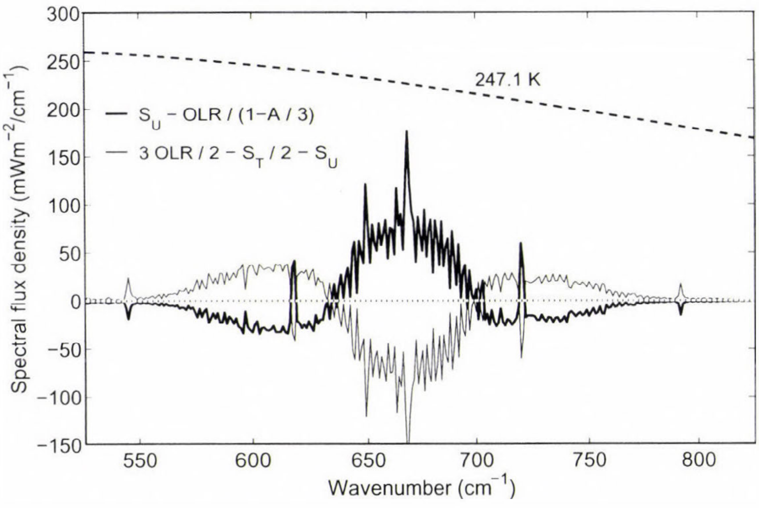

Fig. 18. Spectral flux differences in the 15 μm CO_2 band. The dotted line represents the averaged differences over the 1–3490 cm^{-1} spectral range for both curves. The dashed line is the spectral blackbody radiation at the indicated surface temperature. The spectral differences are compensated over a relatively narrow wavenumber interval around the band center.

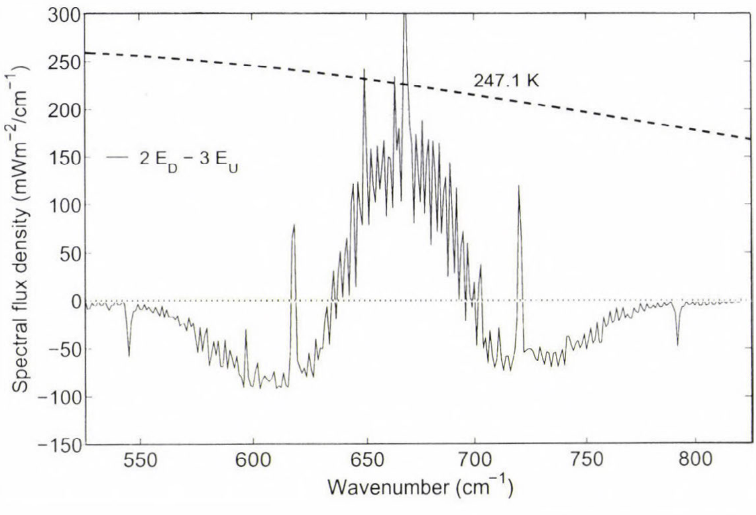

Fig. 19. Spectral differences in the $2E_D$ and $3E_U$ flux densities. The dotted line represents the averaged differences over the 1–3490 cm^{-1} spectral range. The dashed line is the spectral blackbody function at the indicated surface temperature. The spectral differences are largely compensated over the extent of the 15 μm CO_2 band.

10. Conclusions

The purpose of this study was to develop relevant theoretical equations for greenhouse studies in bounded semi-transparent planetary atmospheres in radiative equilibrium. In our terms the local radiative equilibrium is a unique instantaneous state of the atmosphere where the upward atmospheric radiation is balanced by the short wave atmospheric absorption and the net exchange of thermal fluxes of non-radiative origin at the boundary. In general, the thermal structure of the atmosphere assures that the absorbed surface upward radiation is equal to the downward atmospheric radiation. It seems that the Earth's atmosphere maintains the balance between the absorbed short wave and emitted long wave radiation by keeping the total flux optical depth close to the theoretical equilibrium values.

On local scale the regulatory role of the water vapor is apparent. On global scale, however, there can not be any direct water vapor feedback mechanism, working against the total energy balance requirement of the system. Runaway greenhouse theories contradict to the energy balance equations and therefore, can not work. We pointed to the importance of a characteristic altitude of about 2 km, where the cloud cover may control the SW input of the system without changing the global average OLR. To explain the observed increase in the global average surface temperature probably more attention should be paid to the changes in the net contribution from the F^0 and P^0 flux terms and changes in the global average water vapor content and cloud cover. Instead of the USST-76 atmosphere, further global energy budget studies should use appropriate zonal and global average atmospheres which satisfy the global radiative balance requirement and comply with the physics of the global greenhouse effect.

Eqs. (21) and its derivatives are theoretically sound and mathematically correct relationships between the fluxes, greenhouse parameters, and the flux optical depths, and they are good enough to give quantitative estimates with reasonable accuracy. One of the most important results is the derived $S_U = OLR/f$ functional relationship which replaces the mathematically incorrect $S_A = OLR(1+\tilde{\tau}_A)/2$ and $S_G = OLR(2+\tilde{\tau}_A)/2$ equations (classic Eddington solutions), and also resolves the surface temperature discontinuity problem. In radiative equilibrium the thermal equilibrium at the surface is the consequence of the energy minimum principle and it is an explicit requirement of the new equations.

We showed that, by applying the semi-infinite atmospheric model for clear or optically thin atmospheres, large errors may be introduced into the equilibrium surface temperatures. An other important consequence of the new equations is the significantly reduced greenhouse effect sensitivity to optical depth perturbations. Considering the magnitude of the observed global average surface temperature rise and the consequences of the new greenhouse equations, the increased atmospheric greenhouse gas concentrations must not be the reason of global warming. The greenhouse effect is tied to the energy conservation principle through the $S_U + S_T/2 - E_D/10 = 3(F^0 + P^0)/2 = 3S_U f/2$ equations and can not be changed without increasing the energy input to the system.

Applying the virial theorem new radiative balance equations were derived. We showed that the clear Martian model atmospheres are not in radiative equilibrium. The new transfer and greenhouse functions adequately describe the planetary greenhouse effect on the Mars and Earth. The formulation of the new theory for the completely cloudy Venusian atmosphere is in progress.

The basic limitations of our formulas are related to the Eddington, and LTE approximations, and – regarding the practical applications – the assumption of the radiative balance and radiative equilibrium. The simplicity and compactness of the formulas make the flux calculations easy and fast and make them good candidates for greenhouse effect parameterizations in sophisticated climate models. Reasonable global change assessment using GCMs is only possible by observing the basic physical principles governing the planetary greenhouse effect. Regarding the economical impact of the global warming the identification of the real causes of the warming should have the highest priority of the climate research. We believe that the fundamental physics of the greenhouse effect in semi-transparent planetary atmospheres is clearly reflected in the new equations and once the new greenhouse theory may even appear in textbooks on the atmospheric radiative transfer.

Acknowledgements—It is my privilege to publish this paper in the Időjárás. I wish to thank for the support and encouragement obtained from *G. Major, Sz. Barcza, Z. Tóth, M. Zágoni, L. Bozó, K. Sifrin, K. Rutledge, K. Vinnikov*, and *S. Gupta*. I am also very grateful to *M. Antal* for her help with the final editing of the manuscript.

Appendix A: Flux optical depth

The usual definition of the gray-body optical depth is the $d\bar{\tau} = \bar{k}\,du$ equation, where $\bar{k}$ is a properly averaged absorption coefficient over the wavenumber domain, and u is the total amount of a particular absorber along the optical path. Regarding an S_0 LW radiative flux passing through a homogeneous absorbing layer, it is expected that the transmitted part of S_0 satisfies the next equations: $S(\bar{\tau}) = S_0 \exp(-\bar{\tau}) = S_0 \exp(-\bar{k}u)$ and $S(0) = S_0$. In general, for a mixture of different kind of absorbers having complex overlapping rotational-vibrational band structures no such weighted average absorption coefficient (and effective absorber amount) can be computed a-priori. However, for an inhomogeneous layered atmosphere the exact flux optical depth may be obtained by using the LBL method. The first step is to compute the directional mean transmittances over a suitable short wavenumber interval:

$$\overline{T}_A(\Delta\nu,\mu)=\frac{1}{\Delta\nu}\int_{\Delta\nu}\exp\left[-\sum_{l=1}^{L}\sum_{i=1}^{N}\left[c^{i,l}+k_\nu^{i,l}\right]\frac{u^{i,l}}{\mu^l}\right]d\nu, \tag{A1}$$

where $\mu^l=\cos(\theta^l)$ and θ^l is the local zenith angle, $c^{i,l}$ and $k_\nu^{i,l}$ are the contributions to the total monochromatic absorption coefficient from the continuum type absorptions and all absorption lines relevant to the ith absorber and lth layer, respectively. $N=11$ is the total number of major absorbing molecular species and $L=150$ is the total number of the homogeneous atmospheric layers. In HARTCODE the wavenumber integration is performed numerically by 5th order Gaussian quadrature over a wavenumber mesh structure of variable length. At least $\Delta\nu=1\,\mathrm{cm}^{-1}$ spectral resolution is required for the accurate Planck weighting. The hemispheric spectral flux transmittance is obtained by integrating Eq. (A1) with respect the solid angle:

$$\tilde{T}_A(\Delta\nu)=\int_{2\pi}\overline{T}_A(\Delta\nu,\mu)d\omega\,. \tag{A2}$$

In the computation of the integral in Eq. (A2) nine streams (zenith angles) were used and the cylindrical symmetry of the radiation field was also assumed. The Planck-weighted hemispheric mean transmittances were computed from $\tilde{T}_A(\Delta\nu)$ by the following sum:

$$T_A=\frac{1}{\sigma t_A^4}\sum_{j=1}^{M}\pi B(\Delta\nu_j,t_A)\tilde{T}_A(\Delta\nu_j), \tag{A3}$$

where $M=3490$ is the total number of spectral intervals, t_A is the surface temperature, and $B(\Delta\nu_j,t_A)$ is the averaged Planck function over $\Delta\nu_j$. Since the sum in Eq. (A3) is obviously the total transmitted radiative flux from the ground, the exact flux optical depth may be expressed as:

$$\tilde{\tau}_A=-\ln(T_A)\,. \tag{A4}$$

The dependence of $\tilde{\tau}_A$ on the individual total absorber amounts still can not be computed directly, but using a pre-computed database the construction of a $\tilde{\tau}_A(u^1,u^2,\ldots,u^N)$ function is a matter of a multi-dimensional parameterization. Here $u^1,\ldots,u^N$ represent the column amounts of the different greenhouse gases. Such parameterization may also contain the effective temperature and pressure of the absorbers.

Appendix B: Source function profile in bounded atmosphere

We have seen that in a semi-transparent atmosphere the surface upward radiation is $B_G = \varepsilon_G \sigma t_G^4 / \pi$, and the upper boundary condition at the top of the atmosphere is the zero downward IR radiance. The upward and downward hemispheric mean radiance at the upper boundary using the general classic solution of the plane-parallel radiative transfer equation and the isotropy approximation are:

$$\overline{I}^+(0) = B_G e^{-\frac{3}{2}\overline{\tau}_A} + \frac{3}{2}\int_0^{\overline{\tau}_A} B(\overline{\tau}') e^{-\frac{3}{2}\overline{\tau}'} d\overline{\tau}' , \tag{B1}$$

and

$$\overline{I}^-(0) = 0 . \tag{B2}$$

Putting Eq. (B1) and Eq. (B2) into the $H(\overline{\tau}) = \pi(\overline{I}^+ - \overline{I}^-)$ equation, and substituting the source function with $B(\overline{\tau}) = 3H(\overline{\tau})/(4\pi) + B_0$ in the upward hemispheric mean radiance we get:

$$\frac{H}{\pi} = B_G e^{-\frac{3}{2}\overline{\tau}_A} + \frac{3}{2}\int_0^{\overline{\tau}_A} \frac{3H}{4\pi}\overline{\tau}' e^{-\frac{3}{2}\overline{\tau}'} d\overline{\tau}' + \frac{3}{2}\int_0^{\overline{\tau}_A} B_0 e^{-\frac{3}{2}\overline{\tau}'} d\overline{\tau}' . \tag{B3}$$

The two definite integrals in the second and third terms of the right hand side of Eq. (B3) must be evaluated:

$$\frac{3}{2}\int_0^{\overline{\tau}_A} \frac{3H}{4\pi}\overline{\tau}' e^{-\frac{3}{2}\overline{\tau}'} d\overline{\tau}' = -\frac{H}{4\pi}(2e^{-\frac{3}{2}\overline{\tau}_A} - 2 + 3\overline{\tau}_A e^{-\frac{3}{2}\overline{\tau}_A}), \tag{B4}$$

$$\frac{3}{2}\int_0^{\overline{\tau}_A} B_0 e^{-\frac{3}{2}\overline{\tau}'} d\overline{\tau}' = B_0(1 - e^{-\frac{3}{2}\overline{\tau}_A}). \tag{B5}$$

After putting back Eqs. (B4) and (B5) into Eq. (B3) we get:

$$\frac{H}{\pi} = B_G e^{-\frac{3}{2}\overline{\tau}_A} + \frac{H}{4\pi}(2e^{-\frac{3}{2}\overline{\tau}_A} - 2 + 3\overline{\tau}_A e^{-\frac{3}{2}\overline{\tau}_A}) + B_0(1 - e^{-\frac{3}{2}\overline{\tau}_A}). \tag{B6}$$

Rearranging Eq. (B6) and using the $\tilde{\tau}_A = (3/2)\bar{\tau}_A$ notation for the total flux optical depth, πB_0 can be expressed as:

$$\pi B_0 = \frac{\frac{H}{2}\left[1 + \tilde{\tau}_A e^{-\tilde{\tau}_A} + e^{-\tilde{\tau}_A}\right] - \pi B_G e^{-\tilde{\tau}_A}}{1 - e^{-\tilde{\tau}_A}}. \tag{B7}$$

This B_0 in the $B(\bar{\tau}) = 3H(\bar{\tau})/(4\pi) + B_0$ equation will give the general form of the source function profile:

$$\pi B(\tilde{\tau}) = \frac{\frac{H}{2}\left[1 + \tilde{\tau} + (\tilde{\tau}_A - \tilde{\tau} + 1)e^{-\tilde{\tau}_A}\right] - \pi B_G e^{-\tilde{\tau}_A}}{1 - e^{-\tilde{\tau}_A}}. \tag{B8}$$

Applying the $T_A = \exp(-\tilde{\tau}_A)$, $A = 1 - T_A$, and $f = 2/(1 + \tilde{\tau}_A + Tr_A)$ notations, Eq. (B8) will become identical with Eq. (21). The semi-infinite solution may be obtained exactly in the same way, but substituting $\tilde{\tau}_A$ with infinity in Eq. (B1), or simply by making these substitutions in Eq. (B8).

The most efficient cooling of the clear atmosphere requires a total optical depth that maximizes B_0. The derivative of Eq. (B7) with respect $\tilde{\tau}_A$ may be expressed as:

$$\pi \frac{dB_0(\tilde{\tau}_A)}{d\tilde{\tau}_A} = \frac{d}{d\tilde{\tau}_A}\left[\frac{\frac{OLR}{2}\left[1 + \tilde{\tau}_A + e^{\tilde{\tau}_A}\right] - \pi B_G}{e^{\tilde{\tau}_A} - 1}\right] \tag{B9}$$

From Eq. (B9) follows that:

$$\frac{\pi B_G e^{\tilde{\tau}_A} - \frac{OLR}{2}\left[1 + e^{\tilde{\tau}_A} + \tilde{\tau}_A e^{\tilde{\tau}_A}\right]}{\left(e^{\tilde{\tau}_A} - 1\right)^2} = 0. \tag{B10}$$

From Eq. (B10), assuming $\tilde{\tau}_A > 0$ we get:

$$\pi B_G = OLR \frac{1 + \tilde{\tau}_A + e^{-\tilde{\tau}_A}}{2} = \frac{OLR}{f}. \tag{B11}$$

Combining this equation with Eq. (28) we obtain the $\pi B_G = S_U$ equivalence requiring the thermal equilibrium at the ground surface. Note, that at real ground or sea surfaces the $\varepsilon_G \neq 1$ condition will result in the $S_G \neq S_A$ inequality, which is also apparent in *Fig. 2*.

References

Chamberlain, S.A., Bailey, J.A., and *Crisp, D.*, 2006: Mapping Martian atmospheric pressure with ground-based near infrared spectroscopy. *Publications of the Astronomical Society of Australia, 23*, 119-124.

Collins, G.W. II., 2003: *The Fundamentals of Stellar Astrophysics. Part II. Stellar Atmospheres.* WEB edition, 306 pp.

Committee on Radiative Forcing Effects on Climate Change, Climate Research Committee, and *National Research Council*, 2005: *Radiative Forcing of Climate Change: Expanding the Concept and Addressing Uncertainities*. The National Academies Press, USA.

Eddington, A.S., 1916: On the radiative equilibrium of the stars. *Monthly Notices of the Royal Astronomical Society*, LXXVII. I, 16-35.

ERBE, 2004: *ERBE Monthly Scanner Data Product*. NASA LRC, Langley DAAC User and Data Services. userserv@eosdis.larc.nasa.gov.

Goody, R.M. and *Yung, Y.L.*, 1989: *Atmospheric Radiation. Theoretical Basis*. University Press, Inc., Oxford, 392 pp.

Hines, K.M., Bromwich, D.H., and *Marshall, G.J.*, 2000: Artificial surface pressure trends in the NCEP-NCAR reanalysis over the southern ocean and Antarctica. *J. Climate 13*, 3490-3952.

Inamdar, A.K. and *Ramanathan, V.*, 1997: On monitoring the atmospheric greenhouse effect from space. *Tellus 49B*, 216-230.

Karl, T.R., Hassol, J.S., Miller, D.C., and *Murray, W.L.*, 2006: *Temperature Trends in the Lower Atmosphere*. U.S. Climate Change Science Program, Synthesis and Assessment Product 1.1, http://www.climatescience.gov.

Kiehl, J.T. and *Trenberth, K.E.*, 1997: Earth's annual global mean energy budget. *B. Am. Meteorol. Soc. 78*, 197-208.

Lorenz, R.D. and *McKay, C.P.*, 2003: A simple expression for vertical convective fluxes in planetary atmospheres. *Icarus*, 165, 407-413.

McKay, C.P., Lorenz, R.D., and *Lunine, J.I.*, 1999: Analytic solutions for the antigreenhouse effect: Titan and the early Earth. *Icarus*, 137, 56-61.

Milne, A.E., 1922: Radiative equilibrium: the insolation of an atmosphere. *Monthly Notices of the Royal Astronomical Society*, XXIV, 872-896.

Miskolczi, F.M. and *Mlynczak, M.G.*, 2004: The greenhouse effect and the spectral decomposition of the clear-sky terrestrial radiation. *Időjárás 108*, 209-251.

Miskolczi, F.M., Bonzagni, M., and *Guzzi, R.*, 1990: High-resolution atmospheric radiance-transmittance code (HARTCODE). In *Meteorology and Environmental Sciences: Proc. of the Course on Physical Climatology and Meteorology for Environmental Application*. World Scientific Publishing Co. Inc., Singapore.

National Research Council of the National Academies, 2004: *Climate Data Records from Environmental Satellites*. The National Academies Press, Washington DC.

Peixoto, J.P. and *Oort, A.H.*, 1992: *Physics of Climate*. American Institute of Physics, New York.

Raval, A. and *Ramanathan, V.*, 1989: Observational determination of the greenhouse effect. *Nature, 342*, 758-761.

Sagan, C., 1969: On the structure of the Venusian atmosphere. *Icarus*, 10, 274-289.

Stephens, G.L. and *Greenwald, T.J.*, 1991: The Earth's radiation budget and its relation to atmospheric hydrology 1. observations of the clear-sky greenhouse effect. *J. Geophys. Res. 96*, 15311-15324.

Stephens, G.L., Slingo, A., and *Webb, M.*, 1993: On measuring the greenhouse effect of Earth. *NATO ASI Series, Vol. 19*, 395-417.

Weaver, C.P. and *Ramanathan, V.*, 1995: Deductions from a simple climate model: factors governing surface temperature and thermal structure. *J. Geophys. Res. 100*, 11585-11591.

IDŐJÁRÁS

Quarterly Journal of the Hungarian Meteorological Service
Vol. 111, No. 1, January–March 2007, pp. 41–63

The Constitution Day storm in Budapest: Case study of the August 20, 2006 severe storm

Ákos Horváth[1*], **István Geresdi**[2], **Péter Németh**[3] and **Ferenc Dombai**[3]

[1]*Hungarian Meteorological Service, Storm Warning Observatory, Vitorlás u. 17, H-8600 Siófok, Hungary; E-mail: horvath.a@met.hu*

[2]*University of Pécs, Institute of Environmental Sciences, Ifjúság u. 6, H-7624 Pécs, Hungary; E-mail: geresdi@gamma.ttk.pte.hu*

[3]*Hungarian Meteorological Service, P.O. Box 39, H-1675 Budapest, Hungary; E-mails: nemeth.p@met.hu; dombai.f@met.hu*

(Manuscript received in final form March 5, 2007)

Abstract—In the evening of August 20, 2006 severe thunderstorms hit Budapest. The storm struck the downtown at the same time when the Constitution Day firework just started, killed five people and wounded hundreds of spectators crowded on the embankments of the river Danube. In this paper weather conditions from synoptic scale to storm scale are investigated to find the special circumstances, which led to formation of the devastating storm. Investigations show that a wave on a cold front, the mid level cold advection, the drift of jet stream above the warm sector, and an intense wet conveyor belt resulted in intense instability. Furthermore, the wind shear and the low level convergence also contributed to the formation of the fast moving squall line. Detailed Doppler-radar analysis proved that the thunderstorm, which crossed the downtown of Budapest, was a supercell. Comparison of the radar reflectivity and the lightning data of the investigated case with that of other severe storm cases shows that the Constitution Day storm was not an extreme event. The unique feature of this case was the extreme high speed of cell motions. High resolution numerical model (MM5) was applied to understand the dynamical structure and predictability of the storm. Model results show the importance of the layer on 3 km above ground level with high value of equivalent potential temperature and the active role of the cold front in the formation of the squall line. The model was able to simulate the structure and motion of the supercell proving the numerical predictability of this type of severe convective storms.

Key-words: squall line, supercell, MM5, severe convective storm, Doppler-radar

Corresponding author

1. Introduction

Late afternoon on August 20, 2006, a squall line coming from the north-west direction reached the western border of Hungary. Surface and radar observations showed, that thunderstorm cells moved fast and some of them were extremely intensive. The north part of the squall line arrived in Budapest at 19:00 UTC, when the traditional Constitution Day's firework had just started. In the centre of Budapest, more than half million people crowded on the embankments and bridges of the river, and numerous spectators watched the event from boots drifting on the Danube, too. The thunderstorm produced wind gusts reached 32.3 m/s in the centre of downtown (measured on the top of the building of the Hungarian Meteorological Service), and 34.1 m/s in the southern part of the downtown (measured on the top of the building of the University of Science). Broken trees and fragments from roof of houses hit into crowds causing injuries and panic. Five people were killed and hundreds were injured due to the extreme weather. The strong wind caused a loss of about 5 million USD in buildings and cars.

Severe thunderstorms and associated phenomena like stormy wind gusts, hailstorms, heavy rainfalls, sometimes tornadoes often occur in Hungary, especially in summer. The facts presented in this paper suggest that this storm was a supercell thunderstorm, one of the types of severe convective phenomena which are observed from time to time in Hungary (*Horváth* and *Geresdi*, 2003). Structure and development of severe convective phenomena have been investigated since the beginning of the 1950's. Among others, pioneering work of Fujita described the phenomenology of squall lines (*Fujita*, 1955), and the origin of thunderstorm pressure-heights (*Fujita et al.*, 1959). Meteorological satellites and radars have become the main tools for investigation and operative forecast of severe convection (*Reyonolds et al.*, 1979). These remote sensing equipments and the surface meso-networking observations allowed to develop comprehensive theories of the mesoscale convective system (MCS) such as long-lived squall lines (*Rotunno et al.*, 1988; *Houze et al.*, 1989). The most devastating mesoscale phenomena are the supercells which are mostly associated with MCS. The presently accepted theory about the dynamics and necessary conditions of supercell formation was published by *Klemp* (1987). Most of the MCSs and supercells form in the unstable region of cyclones and frontal systems. Prefrontal conditions – large convective available potential energy, horizontal and vertical wind shears (*Davies-Jones et al.*, 2001) – can produce favorable environment for the supercell formation. The convergence and vertical circulation of frontal system (*Hoskins*, 1972) also promote the MCS formation, especially if the MCS is connected with the circulation of the jet stream (*Shapiro*, 1982).

The first numerical experiments about the simulation of convective storms used twodimensional models in the 1960's (*Lilly*, 1962). The large computer capacity necessary for the three-dimensional simulation of thunderstorms (e.g., *Klemp*, 1978) was available by the late 70's. Supercells and squall lines are very complex atmospheric phenomena, so they can be simulated only with state-of art numerical models which involves non-hydrostatic version of equation of motion, detailed description of short and long wave radiation, processes occuring in the boundary layer, and formation of precipitation and cloud elements (*Wilhelmson*, 2001).

Early investigations of severe thunderstorms in Hungary were motivated by improving the efficiency of the storm warning at Lake Balaton (*Götz*, 1966; *Böjti et al.*, 1964; *Götz*, 1968). The hail suppressing system operated in the 1980's required the investigation of microphysical processes occuring in thunderstorms (*Zoltán* and *Geresdi*, 1984). Dynamical conditions of the formation of squall lines in the Carpathian Basin were investigated by *Horváth* and *Práger* (1985). *Bartha* (1987) worked out an empirical method to predict maximum wind gusts of thunderstorm cells. *Bodolainé* and *Tänczer* (2003) investigated flash flood causing mesoscale convective complexes in the Carpathian Basin. The nowcasting system of the Hungarian Meteorological Service gave a new tool for the ultrashort term forecast of severe weather (*Geresdi* and *Horváth*, 2000; *Horváth* and *Geresdi*, 2003; *Geresdi et al.*, 2004). Appearances of supercells and formation of tornadoes in Hungary was described first time by *Horváth* (1997). Due to the increased authenticity of radar in the weather radar network of Hungarian Meteorological Service (HMS) by the end of the 90's, more supercell cases were recognized (*Horváth*, 1997; *Horváth* and *Geresdi*, 2003). Not only the observation background has been improved, but a new tool for the numerical simulation of supercells and tornadoes became available by using limited area non-hydrostatic model MM5 (*Horváth et al.*, 2006).

In the first section of the paper the synoptic scale conditions of formation and development of the Budapest storm are shown by using ECMWF analysis and forecast. In the second section the development, movement, and other characteristics of the storm cells are analyzed by using radar data. In the third section results of MM5 model with high resolution are discussed. The general and special features, furthermore, the predictability of the Budapest storm are given in the conclusion.

2. Synoptic scale weather conditions

On August 20, 2006 a long and thermally sharp cold front crossed Central and Southern Europe moving to the east. On the 850 hPa pressure level the temperature difference between the warm sector and the postfrontal region was

10–12 °C. In the southern part of the long frontal system, between 00:00 and 12:00 UTC, a frontal wave developed. This wave – behaving like a temporary warm front – expanded to the Alps by 15:00 UTC (*Fig. 1*). The dotted line in *Fig. 1* represents the leading edge of a weak high level cold airmass, which moved above the warm sector. Signs of this high level cold advection can be seen in the figure of 500 hPa temperature and wind fields (*Fig. 2*). The high level cold air could move there, because the low level wave of the long cold frontal system did not affect upper streams, and they continued their drifting toward the east. In the cross section of potential vorticity field a positive local maximum can also be associated with the mid tropospheric cold advection (*Fig. 3*). The second important feature of the weather pattern is the extremely intense wet conveyor belt at the 700 hPa level (*Fig. 4*). In the layer of the wet conveyor belt the maximum values of relative humidity coincided with the significant wind maximum, which could be considered as the low level jet stream. The third characteristic is the upper level jet stream at the 300 hPa level (*Fig. 5*). The upper level strong wind results in vertical wind shear necessary for the formation of severe convective storm (*Holton*, 2004).

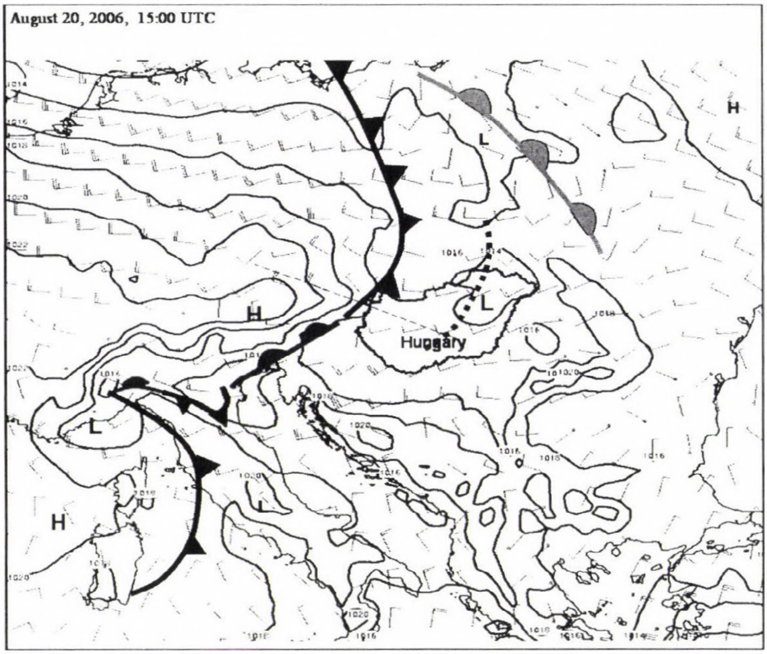

Fig. 1. ECMWF forecast of sea level pressure, 925 hPa wind, and fronts on August 20, 2006, 15:00 UTC. Dashed line shows the position of the direction of cross-section in Figs. 3 and 6.

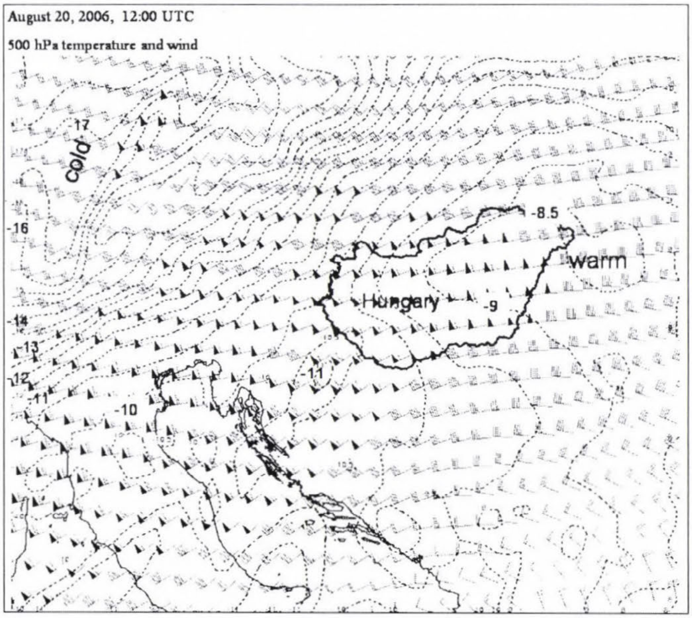

Fig. 2. 500 hPa wind and temperature (difference between the temperature isolines is 0.5 °C) on August 20, 2006, 12:00 UTC from the ECMWF analysis.

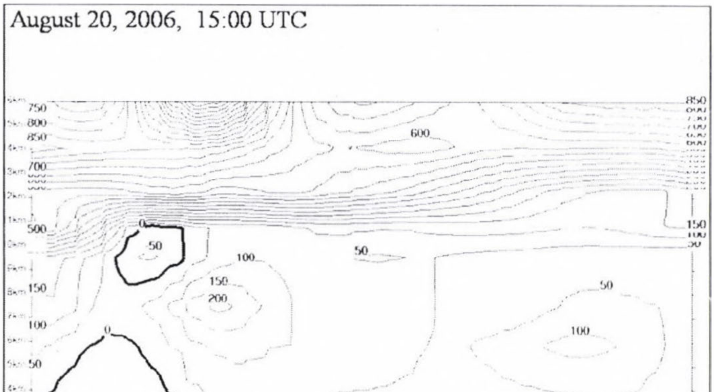

Fig. 3. Cross section of potential vorticity (10^{-5} s^{-1}) on August 20, 2006, 15:00 UTC from the ECMWF forecast. The direction of cross-section is denoted by dashed line in Fig. 1.

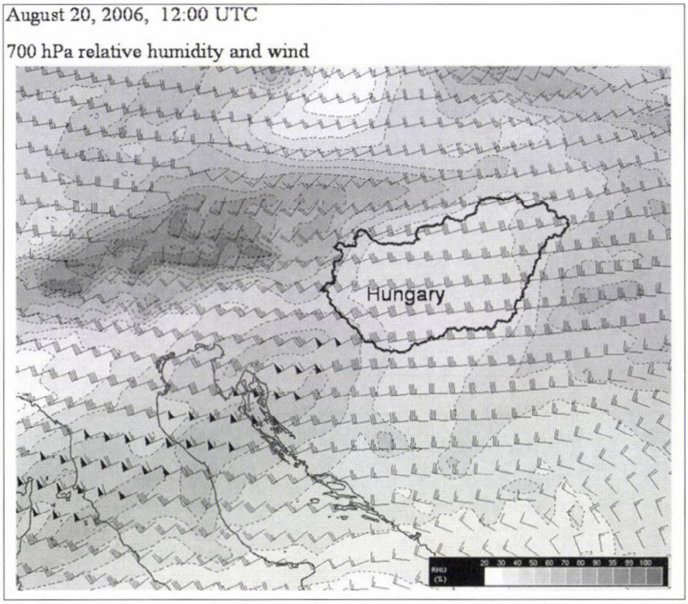

Fig. 4. 700 hPa wind and relative humidity on August 20, 2006, 12:00 UTC from the ECMWF analysis.

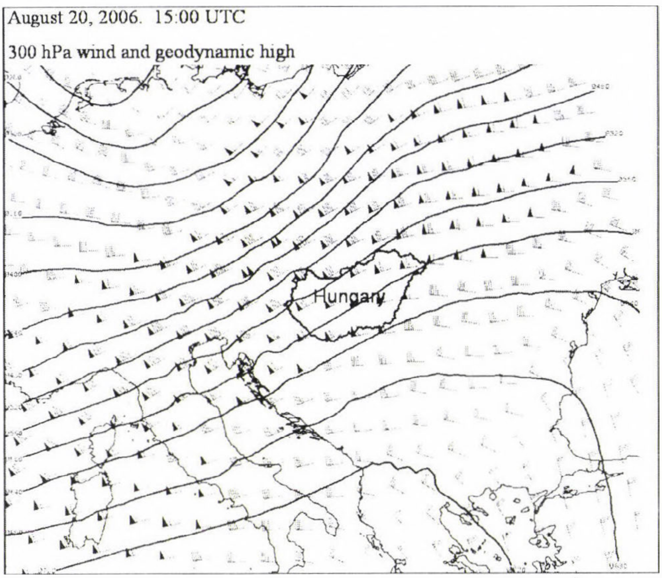

Fig. 5. 300 hPa wind and geopotentials on August 20, 2006, 15:00 UTC from the ECMWF forecast.

The direct role of the cold front in the formation of the Budapest storm is not obvious. Analysis of the ECMWF 12:00 UTC+6-hour forecast shows that the frontal system would not have reached Budapest by 19:00 UTC. The cross sections of potential vorticity and omega fields depict that the cold front reached the Hungarian border only at 18:00 UTC (*Fig. 6*). However observations show that the squall line was close to Budapest by this time.

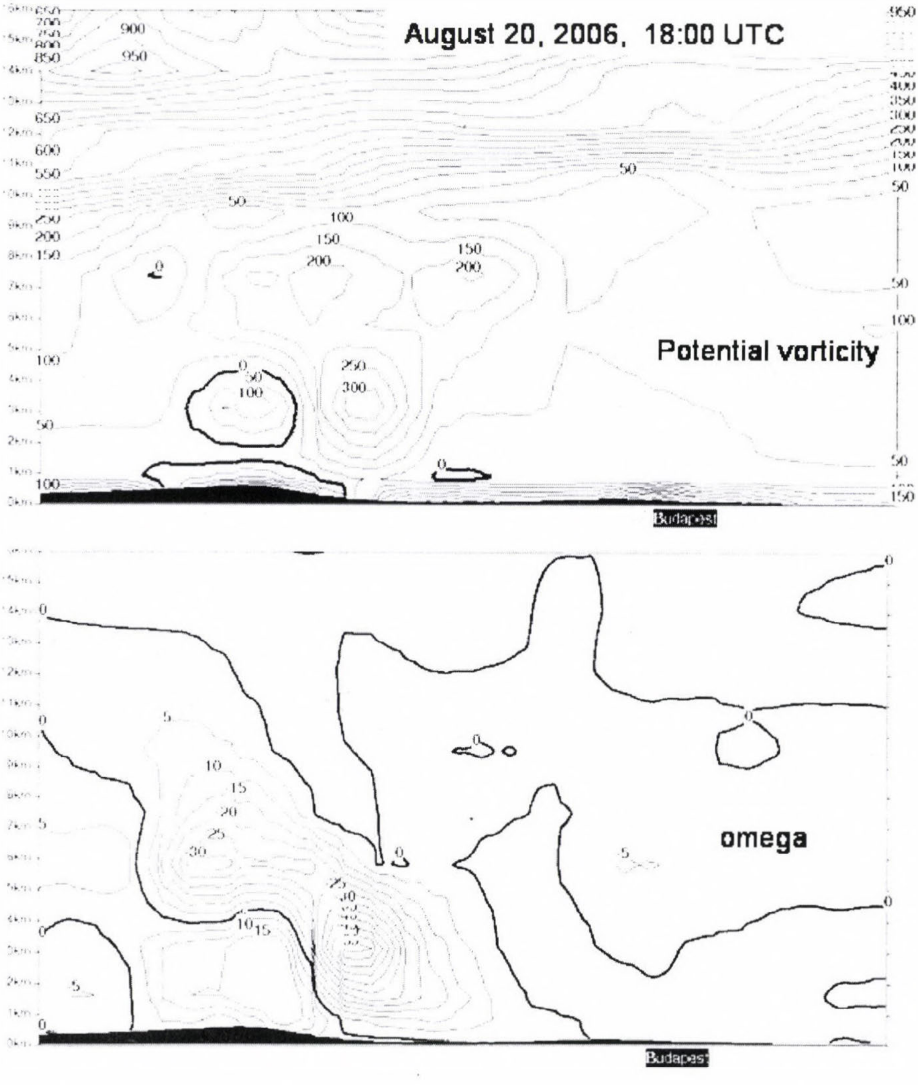

Fig. 6. Cross-section of potential vorticity (10^{-5} s^{-1}) and omega (10 Pa/h) at 18:00 UTC from the ECMWF forecast.

A possible explanation of the fact that thunderstorms arrived in Budapest 2 hours earlier than the modeled cold front is that a squall line separated from the front and run ahead. Because ECMWF forecast system is not suited for the simulation of convective scale processes, it was not able to predict the squall line. However it is notable that weather analysis could not distinguished different squall line and cold front in the time of Budapest storm.

Summing up the synoptic scale weather pattern in the investigated case one can state: (i) The wave of a sharp cold front formed an unstable warm sector, in which an intensive wet conveyor belt and strong high level jet stream resulted in favorable conditions for the formation of severe thunderstorms. (ii) After 15:00 UTC the effect of mesoscale convective processes became more dominant than that of the synoptic scale systems.

3. Observation of the Budapest storm

The HMS radar network detected the first significant radar echoes (R>40 dBZ) at the eastern part of the Alps at 13:00 UTC. The line structure of the position of the thunderstorms could be observed at 13:45 UTC, still in Austria. The squall line reached the Hungarian-Austrian border at 16:30 UTC (*Fig. 7a*). This time the observed wind gusts were below 20 m/s. At 17:45 UTC three main thunderstorm systems could be distinguished along the squall line: the first one was in the northern part, the second was in the center, and the third was in the southern part (*Fig. 7b*). Some of the weather stations reached by the squall line reported 22 m/s wind gusts at this time. By 18:15 UTC the most intensive thunderstorms appeared in the north part of the squall line, the maximum reflectivity was near 55 dBZ in this region. The thunderstorms in the central region became weaker, and the thunderstorms in the southern region fell behind the squall line (*Fig. 7c*). By 19:00 UTC the thunderstorms in the northerly part remained active, and their reflectivity maximum was near 60 dBZ (*Fig. 7d*). The north part of the squall line reached Budapest when the thunderstorms were very intensive in it. Time series of radar images show that three of thunderstorm-centers have long-lived (>2 hours) comma like cells, and presumably these cells were supercells. The presence of the wall cloud in the photograph of Budapest storm shows some similarity to the supercell features. The maximum observed wind gust in Budapest was 34.1 m/s, but extent of damage suggests even higher maximum wind speeds. An eyewitness reported funnel cloud, but it was not confirmed. The thunderstorm system moved to southeast direction, and at about 30 km southeast of Budapest a 38.3 m/s wind gust was measured. After leaving Budapest the system remained active as long as it reached the line of the river Tisza.

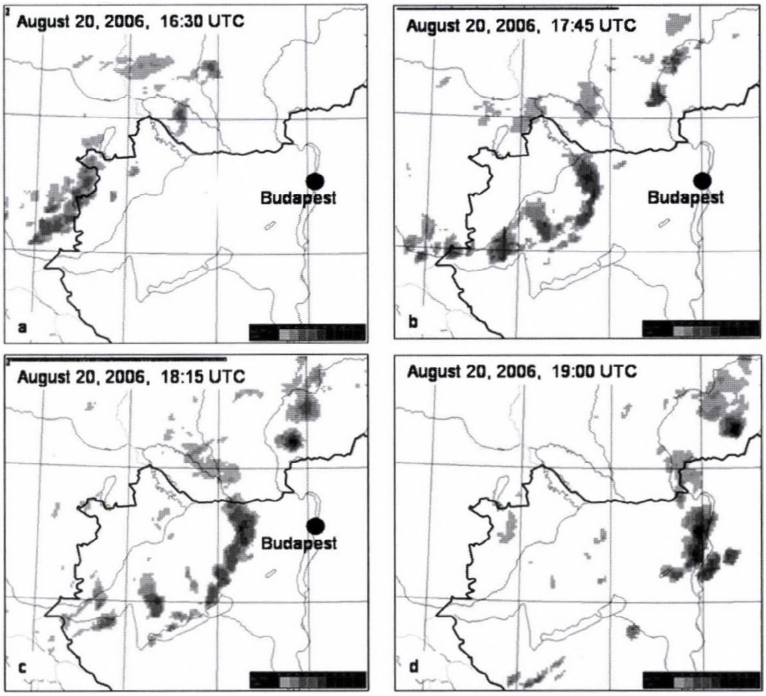

Fig. 7. Position of the squall line given by radar reflectivity.

3.1 Radar and lightening data

Thunderstorm formation and development were observed by the DWSR 2500 radar based weather radar network (3 radars) and SAFIR 3000 (7 sensors) based lightning location network of HMS. The data of these measurements were available in real time on the synoptic workstation of HMS all day. The basic radar and lightning characteristics were derived from the data of the routine observation, which include the national radar composites of CMAX dBZ values (maximum dBZ from 9 different elevations in every column) over a 800 km × 500 km region. The radar pictures were completed in every 15th minutes. The lightning events were recorded continuously this day providing data on IC and CG flashes. In our investigation these two data sets were carefully aligned in space and time. A site error compensation method was applied to reduce the large location errors of SAFIR system.

The radar and lightning data of the thunderstorms developed on August 20, 2006 did not show any unique or extreme characteristics. More intensive thunderstorms were observed on 7 days in this year. The total amount of flashes and precipitable water produced by the thunderstorms on August 20 can be considered as typical summer values in Hungary.

The main characteristics are summarized in *Table 1* for lightning data (comparing to an extreme active lightning day) and *Table 2* for radar data.

Table 1. General lightning characteristics for August 3, 2005 (an extreme active day) and August 20, 2006

Date	Daily total			Maximum (15 min)		
	Localization	IC Flash	CG Flash	Density km^{-2} h^{-1}	Area km^2	Flashes
08.03.2005	532,375	242,301	40,405	34.5	17,552	28,808
08.20.2006	28,270	14,580	964	7.5	3656	3170
Ratio	**18.8**	**16.6**	**41.9**	**4.6**	**4.8**	**9.1**

Table 2. General radar characteristics on August 3, 2005 and on August 20, 2006

Date	Daily total			Maximum (15 min)			
	Water million m^3 >15 dBZ	Water million m^3 >45 dBZ	Mean rain >15 dBZ	dBZ	Area km^2 >15 dBZ	Water million m^3 >15 dBZ	Water million m^3 >45 dBZ
08.03.2005	2040,14	44,76	1.83	57.0	98,924	350,0	28,0
08.20.2006	915,88	112,06	2.97	59.5	38,940	15,0	33,0
Ratio	**2.2**	**0.4**	**0.6**	**-2.5**	**2.5**	**2.3**	**0.8**

Computer programs were developed to calculate different kind of characteristics of thunderstorm cells from radar and lightning data. These codes provide minimum and maximum values of dBZ, area and center points of the cells, as well as rainfall intensity and precipitable water content of every radar cell. The contour of the cells could be defined with different reflectivity thresholds. The composite radar picture was generated in every 15th minute. The number and maximum density of flashes, areas, center points are also calculated for flash cells at different density thresholds. Altogether 9 radar cells and 5 flash cells were identified and tracked. The tracked radar cells were defined with 35 dBZ reflectivity threshold, and their main parameters are shown in *Fig. 8*.

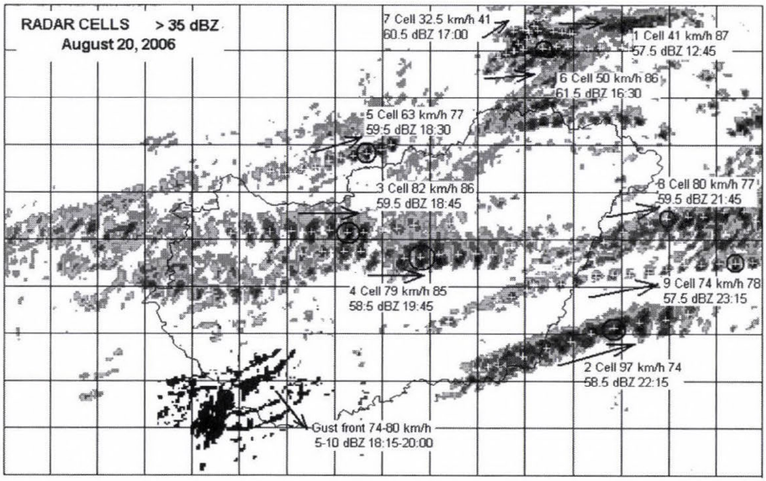

Fig. 8. The positions of the tracked radar cells in every 15th minute. The cells are defined with 35 dBZ reflectivity threshold. The main parameters are given: cell ID, mean velocity of motion, direction of motion (also with vectors), maximum reflectivity, and time of observation. The size of a grid is 50 × 50 km.

The main calculated parameters and features are shown in *Table 3* for radar cells and *Table 4* for flash cells. The cell ID used in figures and tables mark the same thunderstorm cells.

Table 3. Radar characteristics of thunderstorm cells on August 20, 2006

	Maximum reflectivity	Time	Max. area	Total water	Mean velocity	Mean direction	Max. area	Max. water production
	dBZ		km^2	million m^3	km/h	degree	km^2	million m^3 h^{-1}
Threshold			**15 dBZ**	**15 dBZ**	**35 dBZ**	**35 dBZ**	**35 dBZ**	**35 dBZ**
Cell ID								
1	57.5	12:45	788	21.9	40.7	86.8	428	13.7
2	58.5	22:15	9062	93.4	96.7	74.3	1404	44.4
3	59.5	18:45	2596	49.0	82.2	85.5	860	24.8
4	58.5	19:45	1153	50.9	78.5	84.3	738	30.1
5	59.5	18:30	805	23.0	62.7	76.9	689	13.6
6	61.5	16:30	759	26.2	50.1	86.0	496	19.0
7	60.5	17:00	532	14.7	32.5	41.2	280	12.2
8	59.5	21:45	2346	46.5	80.3	76.7	810	26.4
9	57.5	23:15	865	27.6	73.8	77.5	349	10.1

Table 4. Lightning characteristics of thunderstorm cells on August 20, 2006

	Max. flash density	Time	Max. area	Total flash	Mean velocity	Mean direction	Max. flash area	Max. flash activity
	$km^{-2}\ h^{-1}$		km^2		$km\ h^{-1}$	degree	km^2	h^{-1}
Threshold			$2 \times km^{-2}\ h^{-1}$		$2 \times km^{-2}\ h^{-1}$	$2 \times km^{-2}\ h^{-1}$	$2 \times km^{-2}\ h^{-1}$	
Cell ID								
2	28	21:15	1100	5187	96.6	92.4	668	5280
3	15	18:30	354	1313	81.7	86.7	216	1290
4	16	19:45	116	1156	91.6	106.0	64	560
5	12	18:15	176	429	62.0	71.6	76	492

In *Fig. 9* the water and flash production are shown for each tracked convective cells.

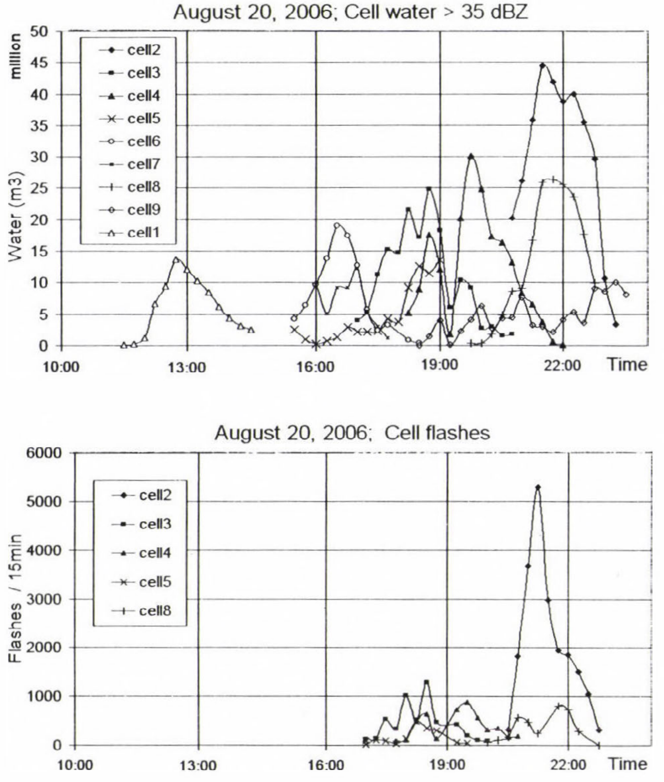

Fig. 9. The development of the water production (above) and the flash activity (below) in 15 minutes time intervals for each of tracked thunderstorm cell on August 20, 2006.

In *Table 5* the main radar and lightning characteristics of Budapest storm are summarized.

Table 5. Radar and lightning characteristics of Budapest thunderstorm cells on August 20, 2006

	Radar				**Lightning**			
	Max. dBZ	**Velocity**	**Direction**	**Area**	**Max. flash density**	**Velocity**	**Direction**	**Flash area**
	dBZ	**km h^{-1}**	**degree**	**km^2**	**km^{-2} h^{-1}**	**km h^{-1}**	**degree**	**km^2**
Thres.		**35 dBZ**	**35 dBZ**	**35 dBZ**		**2×km^{-2} h^{-1}**	**2×km^{-2} h^{-1}**	**2×km^{-2} h^{-1}**
Time								
17:00	43.0	0	0	388	6	0	0	60
17:15	50.5	83	82	268	4	172	123	102
17:30	52.5	79	90	538	7	88	85	276
17:45	52.5	86	87	648	4	92	71	196
18:00	53.5	89	75	648	10	144	99	444
18:15	55.5	77	89	780	9	28	146	274
18:30	55.0	74	101	802	15	80	85	354
18:45	59.5	76	84	860	7	64	76	188
19:00	57.0	81	93	598	SAFIR HMS stop			
19:15	46.5	screening		620	10	152	96	188
19:30	50.5	81	33	548	7	80	126	88

On the base of the radar and flash characteristics of tracked cells, the main features of the August 20 storm are the following:

- There was rapid eastward cell displacement this day. The velocity of the cells increased from 40 km/h (cell 1, at noon) to 82 km/h. The direction of motion turned slowly from the east to the north. Most of the thunderstorms involved two or more convective cells.
- The thunderstorm (cell 2) developed in the southeast region of the squall line and produced the maximum number of flashes at 21:15 UTC and precipitable water at 22:15 UTC. The total precipitable water was 94 million m^3, the maximum reflectivity was 58.5 dBZ, and the area of the largest cell was 9000 km^2.
- The most intensive thunderstorm (cell 3) moved almost eastward with a velocity of 82 km/h. The cell reached its maximum phase at 18:45 UTC with maximum reflectivity of 59.5 dBZ. This thunderstorm was composed of different convective cells producing about 49 million m^3 precipitation over a 2500 km^2 area.

- The Budapest storm was initiated by strong convection development at late afternoon in the west Hungary. This development resulted in a rapid gust front moving with about 74–80 km/h to the southeast. The observed reflectivity of the gust front was about 5-10 dBZ. The gust front was observed 1.5 hours ahead by the western radar of the network (Pogányvár C band radar).
- None of the radar cells, that have larger maximum radar reflectivity than 55 dBZ, showed observable flash activities.
- In every cell the flash activity reached its maximum value about 15-45 minutes earlier than the radar reflectivity and precipitable water production reached their maximum values.
- The velocity and the direction of motion of every cell were almost constant, or changed very slowly. This characteristic gave a chance for making forecasts of the cell positions 2–3 hours ahead.

In this research the existence of supercell was investigated by using objective methods. Doppler wind data were applied to find rotating cells using Rankine vortex theory (*Doviak* and *Zrnic*, 1993). The Rankine vortex (RV) model can be applied to recognize mesocyclones with characteristic size of 10 km. Tangential wind component (V_t) of the RV is given by the following equations:

$$V_t(r) = \frac{V_t^{\max}}{R_0} r \qquad \text{if} \quad r \le R_0,$$

$$V_t(r) = \frac{V_t^{\max}}{r} R_0 \qquad \text{if} \quad r > R_0,$$

where r is the distance from the center of RV, R_0 is the "radius" of the vortex, where the tangential wind has its maximum ($V_t^{\max}$).

Rankine vortex theory allows radial inflow or outflow (V_r) of the vortex:

$$V_r(r) = \frac{V_r^{\max}}{R_0} r \qquad \text{if} \quad r \le R_0,$$

$$V_r(r) = \frac{V_r^{\max}}{r} R_0 \qquad \text{if} \quad r > R_0,$$

where $V_r^{\max}$ is the maximum radial wind of the vortex at R_0. The vortex could be determined unambiguously, if the coordinates of the center of RV, $V_t^{\max}$ and $V_r^{\max}$, and R_0 were known. For the reason of simplicity, transformation of radar measured Doppler wind field into storm relative coordinate system is applied. Rankine vortices between diameters of 2 and 10 km were searching in such a way, that all points were tested as a possible center of an RV. A real vortex has to satisfy the following conditions:

(i) Inside the vortex $\frac{\partial V_r}{\partial r} \geq 2.5 \frac{\text{m s}^{-1}}{\text{km}}$.

(ii) $2R_0$ is between 2 and 10 km.

(iii) The explained variance of the tested vortex and the Doppler wind in the storm relative coordinate system has to be higher than 80%.

The most significant RV structures of the Budapest storm were found at 19:11 UTC when Doppler radar scanned at 1° elevation angle (*Fig. 10*). One of the cyclonic rotation center was exactly above the downtown where the Constitution Day firework occurred.

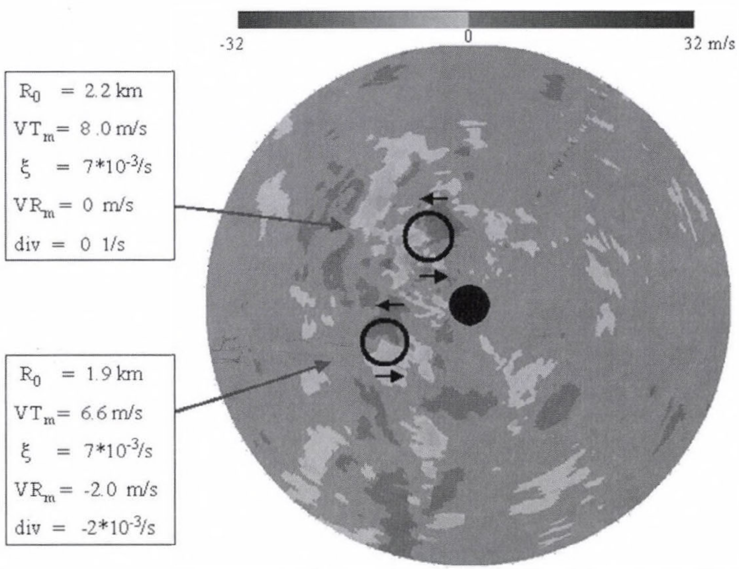

Fig. 10. Doppler wind field in storm relative coordinate system in 30 km radius of Budapest radar on August 20, 2006, 19:11 UTC. Circles show the indicated Rankine vortices with their parameters (ξ: vorticity; R_0: radius of the Rankine vortex; V_{tm}: tangential wind component of the vortex; V_{rm}: radial wind component of the vortex; div: divergence of the vortex). The northern vortex was above the downtown of Budapest.

4. Numerical simulation of the Budapest storm

The aim of the numerical model experiments was to understand the dynamics of thunderstorms like the Budapest storm and to investigate their predictability. The numerical simulations were made by the MM5 Version 3 (NCAR-PSU Mesoscale Model) (*Dudhia*, 1993). The high horizontal resolution (1.5 km) allowed us to run the model without cumulus parameterization. To describe microphysical processes, Reisner microphysical scheme (with five different types of hydrometeors) is applied (*Reisner et al.*, 1998). The planetary boundary layer (PBL) is described by the non-local PBL scheme based on *Troen* and *Mahrt* (1986). Land-surface processes are simulated by the Oregon State University Land-surface Model (*Chen* and *Dudhia*, 2001). For this study, the model was integrated with horizontal resolutions of 1.5 km, with 28 vertical levels on 400 × 500 horizontal grid points. 100 hPa was chosen as the upper level of the model. The model domain was chosen in such a way that the cold front was in the inner part of the model territory at 12:00 UTC initial time. A Lambert-conformal projection was applied with 48.0° latitude and 16.4° longitude central values. An experimental model run with 12 hours forecast needed 4 hours computer time on 64 processors of an ALTX 3700b computer.

The initial and lateral conditions for the MM5 were taken from the ECMWF deterministic model run of 12:00 UTC, on August 20. The ECMWF data set has 0.25 degree resolution. The MM5 model run initiated at 12:00 UTC used the 12:00 UTC ECMWF analysis. The other runs initiated at 13:00 and 14:00 UTC used +1 and +2 hours ECMWF forecast for initial conditions. Input data for MM5 initial condition (mean sea level pressure, three-dimensional temperature, humidity, wind fields, soil temperature and soil humidity values) were taken from the ECMWF analysis.

During model experiments at model run of 14:00 UTC, reflectivity of HMS radar network were also assimilated into initial conditions using the Robust Radar Impact (RRI) method (*Horváth*, 2006). The RRI method is based on theory and numerical experiments which show that the vertical profile of equivalent potential temperature (EPT) can be considered as a nearly constant value, especially in the cases of severe thunderstorms. Supposing that the air in thunderstorms is saturated (relative humidity profile is 100%), it is possible to retrieve a pressure-temperature profile which is valid only in the updraft regions of thunderstorms. In this way thunderstorms appear like warm and wet bubbles isolated from their environment. Case studies were made to determinate the most efficient way to calculate the characteristic EPT value. It was found that EPT of the most unstable layer of the lowest 1000 meters can be considered characteristic for air mass thunderstorms.

A new subprogram which calculates the reflectivity of the precipitation elements (rain, snow, and hail/graupel) was attached to the original code of the MM5. The calculated radar reflectivity field allows us to make a more direct comparison with the radar observation. (The quantitative comparison between the simulated precipitation intensity and the precipitation intensity derived from the reflectivity is very limited, because the calculation of precipitation field from the radar data bases on crude approximations.) The difficulty of the reflectivity calculation can be handled by supposing that the size of the precipitation elements is small enough to fall into the Rayleigh scattering region, and that the size distributions of these particles are given by an exponential function with fixed intersection parameters. According to *Smith et al.* (1975) the effect of the Mie-theory can be neglected, because the concentration of the hail stones larger than the radar wavelength (3–10 cm) is very small. The dielectric factor of 0.93 and 0.21 were used for the water drops and dry ice particles, respectively. If the temperature is larger than 0°C, the dielectric factor of the ice particles is the same as that of the water drops, because in this case a thin water layer formed on the surface of the ice particles.

3.1 Results of numerical experiments

Several numerical model experiments were made to determinate the optimal model domain and initiation time. A simulation was considered to be successful, if a thunderstorm with mesoscale rotation (mesocyclone) appeared during the simulation. All simulations predicted the cold front passage between 18:00 and 21:00 UTC in Budapest, but severe convective phenomena and associated mesocyclones appeared only in the cases, when at the start of the simulation the cold front was inside the model domain. In cases when the cold front only drifted into the model domain due to the lateral conditions (given by the ECMWF forecast), the model was not able to forecast mesocyclones. In runs with initial times later than 15:00 UTC, the model was not able to develop mesocyclones by 19:00 UTC.

The model run with 12:00 UTC initial time forecasted the squall line and some mesocyclones appeared in the line. However, the dominant supercell moved south of Budapest, and the simulated squall line reached the Danube one hour earlier than in real case. In this case the RRI method was useless, because at the initial time the radar echoes were weak. The most successful model run was when 14:00 UTC initiation was applied. In this case the RRI method helped the model to involve triggers to the appropriate places and passage, and the development of the squall line were closest to reality. Hereafter the results of the 14:00 UTC model run are discussed.

The calculated radar reflectivity seemed to be a good parameter to compare the model simulation with the measured radar data. The model retrieved a realistic image of the real squall line by 15:00 UTC (1 hour forecast), which means that the spin up time was less than one hour. The modeled squall line reached the Austrian-Hungarian border at the same time when the real squall line did. At 17:45 UTC three main calculated reflectivity maxima can be seen in *Fig. 11a*. Detailed analysis indicates that all of the three centers had mesocyclone. At this time the southern center had the strongest mesocyclone. At 18:15 UTC already the northern center had the highest reflectivity values and the southern center dropped behind (*Fig. 11b*), while at 18:45 UTC the northern center became obviously the dominant system (*Fig. 11c*). The squall line reached the Danube at 19:15 UTC only 15 minutes later than the real storm did (*Fig. 11d*). A detailed picture of the wind field and the calculated radar echoes show the center of the mesocyclone, which is only a few kilometers from the downtown of Budapest (*Fig. 12*).

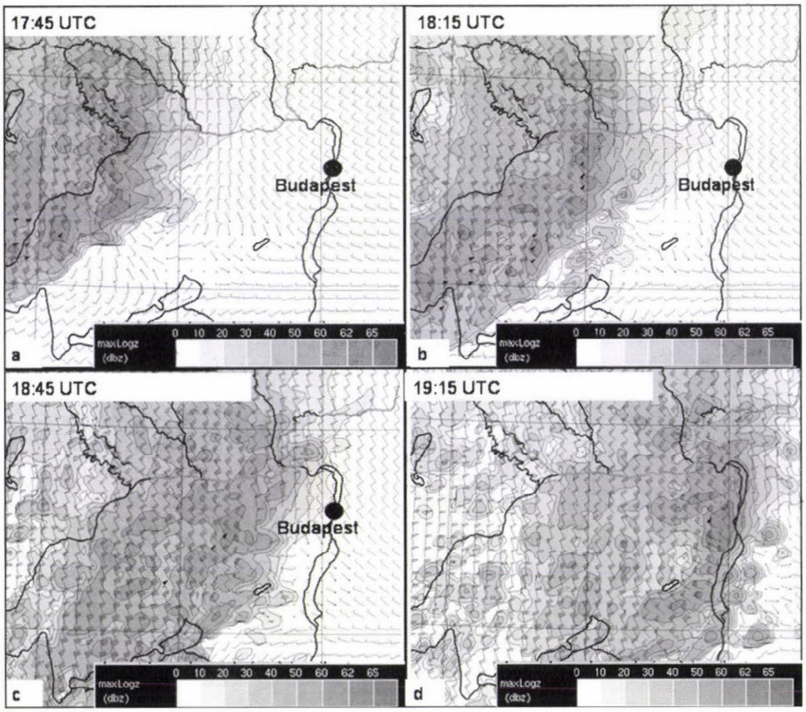

Fig. 11. MM5 simulated radar reflectivity (shadowed fields) and 925 hPa wind field of the squall line passage.

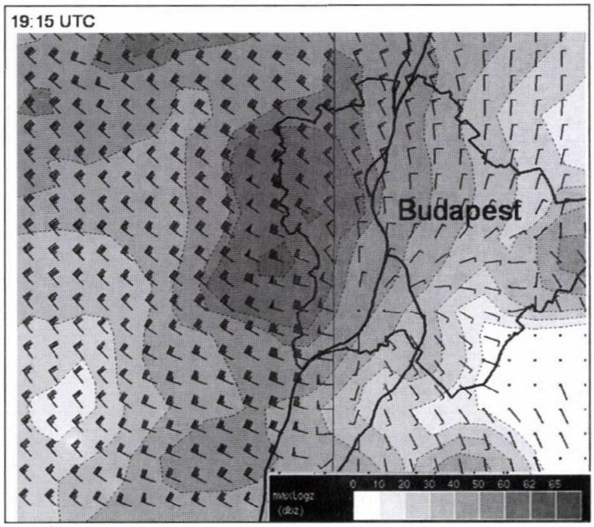

Fig. 12. MM5 simulated radar reflectivity and 925 hPa wind field at 19:15 UTC.

The low level thermodynamic characteristics of the squall line are shown by wind and equivalent potential temperature (EPT) fields of the 925 hPa level (*Fig. 13a, b*). The first conspicuous feature is that EPT values rise up behind the leading edge of the squall line. This behavior is opposite to that was found in an earlier investigated supercell occurred in Hungary (*Horváth et al.*, 2006). In this case the thunderstorms collected low level unstable air from areas in front of the thunderstorm line, and behind the thunderstorms EPT field formed a cold pool. At the present case the low level pattern of EPT suggests that low level prefrontal instability did not play an important role in supplying of the squall line. Missing of significant cold pools behind the squall line also supports this assumption.

The low level thermodynamic characteristics of the squall line are shown by wind and equivalent potential temperature (EPT) fields of the 925 hPa level (*Fig. 13a, b*). The first conspicuous feature is that EPT values rise up behind the leading edge of the squall line. This behavior is opposite to that was found in an earlier investigated supercell occurred in Hungary (*Horváth et al.*, 2006). In this case the thunderstorms collected low level unstable air from areas in front of the thunderstorm line, and behind the thunderstorms EPT field formed a cold pool. At the present case the low level pattern of EPT suggests that low level prefrontal instability did not play an important role in supplying of the squall line. Missing of significant cold pools behind the squall line also supports this assumption.

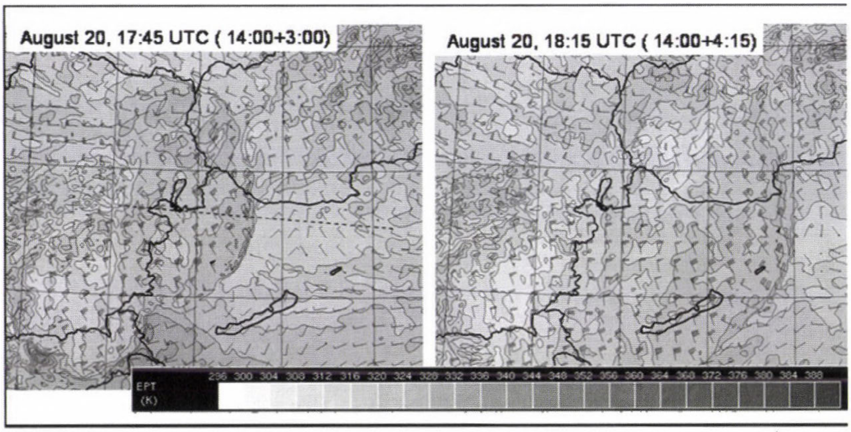

Fig. 13. MM5 simulated equivalent potential temperature and wind field on the 925 hPa level. Dashed line shows the position of cross-section in Fig. 14.

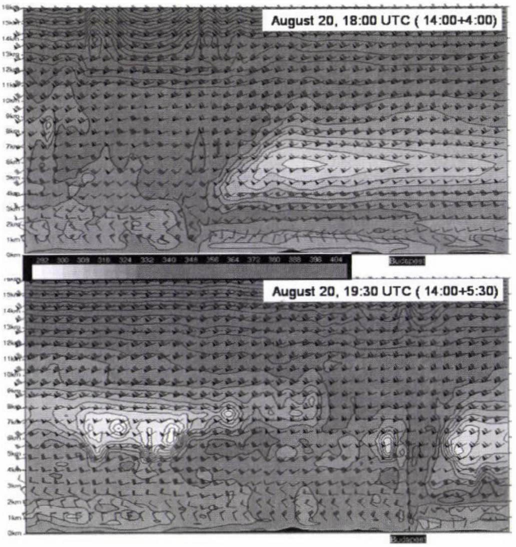

Fig. 14. Cross-section of MM5 simulated equivalent potential temperature and wind field during the squall line passage. The direction of the squall line is shown in Fig. 13.

Vertical cross sections of the squall line suggest that the unstable air mass which supplied the line of thunderstorms is between 1.5 and 4 km AGL (*Fig. 14a*). This unstable layer is generated by an active wet conveyor belt on the

700 hPa level. (More details about the wet conveyor belt are given at synoptic conditions in Section 2). The cold layer between the 5 and 7 km heights was a consequence of high level cold advection. This layer was responsible for the prefrontal conditional instability. The cold advection on the 500 hPa level was presented at discussion of the synoptic conditions in Section 2. The squall line can be identified by the towering maximum of EPT up to the troposphere and by lower level directional wind shear (*Fig. 14a, b*). Several parameters were used to analyze the cold front and to separate the front from the squall line. The cross section in *Fig 14b* shows low level cold advection behind the squall line, but there is no significant wind shear (both direction and speed) which would unambiguously indicate the cold front. An option is that the squall line probably blurred the cold front behind itself. The other option is that the squall line accelerated the front, and the separating line between the cold and warm air mass, and the squall line were identical.

5. Conclusion

The Budapest storm was not a classical self propagation squall line, where the cold pool and the low level wind shear play the main role in the formation of line of thunderstorms (*Rotunno*, 1982). The storm can not be place into the certain category of cold front aloft, where high level cold front is responsible for line organized convective storms (*Stoelinga et al.*, 2003). However, the situation was similar to a certain degree.

Basic conditions for convective instability were provided by synoptic scale events and weather patterns. The long frontal system extending across the continent provided good conditions for producing a significant prefrontal wet conveyor belt on the 700 hPa level. This layer supplied convective energy, instead of relative cold and stable lower air, allowing the formation of nocturnal thunderstorms. The frontal wave formed at the southeast Alps caused the air masses to slow down at low level and to run ahead at high level, above the warm sector. Also that wave was responsible for wind shear favorable for supercell formation.

In the unstable prefrontal warm sector a squall line developed and the thunderstorms which hit Budapest were parts of the squall line. The squall line had three main storm centers and by the time of reaching Budapest, the northerly center became the strongest.

Concerning radar reflectivity and lightning activity, the storm and the squall line were not extreme strong events, however, cell motions were very fast. Detailed Doppler wind analysis showed that among cells, which hit Budapest, there were supercells. In spite of the existence of supercells, the typical left or right deviation from the leading squall line direction was not recognized by detailed cell tracking analysis. The extreme fast motion was not favorable for supercell splitting.

High resolution, non-hydrostatic model experiments successfully simulated the squall line and the rotating thunderstorms in time and space. Model results show that thunderstorms got air masses with high equivalent potential temperature from layers between 2–4 km AGL. The air mass near the surface layers were stable, and did not supplied thunderstorms.

The fast moving squall line resulted in that the storm arrived in Budapest about a few hours earlier than the synoptic scale cold front was predicted. Even detailed analysis can not answer obviously, whether the squall line was a prefrontal phenomenon or the cold front became faster because of strong convection, but the direct role of the cold front at the Budapest storm is evident.

Acknowledgement—This research was supported by the NKFP 0022/2005 (Jedlik Ányos) project.

References

Bartha, I., 1987: An objective decision procedure for prediction of maximum wind gusts associated with Cumulonimbus clouds. *Időjárás 91*, 330-346.

Bodolainé, J.E. and *Tänczer, T.*, 2003: *Mesoscale Convective Systems - Triggering Off Flash Floods* (in Hungarian). Országos Meteorológiai Szolgálat, Budapest.

Böjti, B., *Bodolainé, J.E.*, and *Götz, G.*, 1964: Instability lines in Hungary (in Hungarian). *Beszámolók az 1964-ben végzett tudományos kutatásokról*. Országos Meteorológiai Szolgálat, Budapest, 139-165.

Chen, F. and *Dudhia, J.*: 2001: Coupling and advanced land surface-hydrology model with the Penn State-NCAR MM5 modeling system. Part I. Model implementation and sensitivity. *Mon. Weather Rev. 129*, 569-585.

Davies-Jones, R., *Trapp, R.J.*, and *Bluestein, H.B.*, 2001: Tornadoes and tornadic storms. In *Severe Convective Storms* (ed.: *C.D. Doswell*). *AMS Meteorological Monographs 28*, No. 50, 167-221.

Doviak, R.J. and *Zrinic, D.S.*, 1993: *Doppler Radar and Weather Observations*. Academic Press, 335-340.

Dudhia, J., 1993: A non-hydrostatic version of the Penn State-NCAR Mesoscale Model: Validation tests and simulation of an Atlantic cyclone and cold front. *Mon. Weather Rev. 121*, 1493-1513.

Fujita, T.T., 1955: Results of detailed synoptic studies of squall lines. *Tellus 7*, 405-436.

Fujita, T.T., 1959: Precipitation and cold air production in mesoscale thunderstorm systems. *J. Meteor. 15*, 454-466.

Geresdi, I. and *Horváth, Á.*, 2000: Nowcasting of precipitation type. Part I: Winter precipitation. *Időjárás 104*, 241-252.

Geresdi, I., *Horváth, Á.*, and *Mátyus, Á.*, 2004: Nowcasting of the precipitation type Part II: Forecast of thunderstorms and hailstone size. *Időjárás 108*, 33-49.

Götz, G., 1966: *Sturmwarnung am Balatonsee* (in German). Országos Meteorológiai Szolgálat, Budapest.

Götz, G., 1968: Hydrodynamic relationships between heavy convection and the jet stream. *Időjárás 72*, 157-165.

Holton, J.R., 2004: *An Introduction to Dynamic Meteorology*. Elsevier Academic Press.

Horváth, Á.,1997: Tornado (in Hungarian). *Légkör 62*, 2-9.

Horváth, Á., 2006: Numerical studies of severe convective phenomena using robust radar impact method. In *Proceedings of ERAD 2006*. Barcelona, 19-22 September, 557-558.

Horváth, Á. and *Práger, T.*, 1985: Study of dynamic and predictability of squall lines (in Hungarian). *Időjárás 89*, 141-160.

Horváth, Á. and *Geresdi, I.*, 2003: Severe storms and nowcasting in the Carpathian Basin. *Atmos. Res. 67-68*, 319-332.

Horváth, Á., Geresdi, I., and *Csirmaz, K.*, 2006: Numerical simulation of a tornado producing thunderstorm: A case study. *Időjárás 104*, 279-297.

Hoskins, B.J. and *Bretherton, F.P.*, 1972: Atmospheric frontogenesis models: Matematical formulation and solution. *J. Atmos. Sci. 29*, 11-37.

Houze, R.A., Rutledge, S.A., Biggerstaff, M.I., and *Sull, B.F.*, 1989: Interpretation of Doppler weather radar displays in middle latitude mesoscale convective systems. *B. Am. Meteorol. Soc. 70*, 608-619.

Klemp, J.B. and *Wilhelmson, R.*, 1978: The simulation of three dimensional convective storm dynamics. *J. Atmos. Sci. 35*, 1070-1096.

Klemp, J.B., 1987: Dynamics of tornadic thunderstorms. *Ann. Rev. Fluid Mech. 19*, 369-402.

Lilly, D.K., 1962: On the numerical simulation of buoyant convection. *Tellus XIV*, 148-172.

Reisner, J., Rasmussen, R.M., and *Bruintjes, R.T.*, 1998: Explicit forecasting of supercooled liquid water in winter storms using the MM5 mesoscale model. *Q. J. Roy. Meteor. Soc. 124*, 1071-1107.

Reynolds, D.A. and *Smith, E.*, 1979: Detailed analysis of composited digital radar and satellite data. *B. Am. Meteorol. Soc. 60*, 1024-1037.

Rotunno, R., Klemp, J.B., and *Weisman M.L.*, 1988: A theory for long living squall lines. *J. Atmos. Sci. 45*, 463-485.

Shapiro, M.A., 1982: *Mesoscale Weather Systems of the Central United State*. University of Colorado, Boulder, Co.

Smith, P.L., Jr., Myers, C.G., and *Orville, H.D.*, 1975: Radar reflectivity factor calculations in numerical cloud models using bulk parameterization of precipitation. *J. App. Meteorol. 14*, 1156-1165.

Stoelinga, M.T., Locatelli, J.D., Schwartz, D.R., and *Hobbs, P.V.*, 2003: Is a cold pool necessary for the maintenance of a squall line produced by a cold front aloft? *Mon. Weather Rev. 131*, 95-115.

Troen, I. and *Mahrt, L.*, 1986: A simple model of the atmospheric boundary layer: Sensitivity to surface evaporation. *Bound.-Lay. Meteorol. 37*, 129-148.

Wilhelmson, R.B. and *Wicker, L.J.*, 2001. Numerical modeling of severe local storms. In *Severe Convective Storms* (ed.: *C.D. Doswell*). *AMS Meteorological Monographs 28*, No. 50. 123-166.

Zoltán, Cs. and *Geresdi, I.*, 1984: A one-dimensional steady-state jet model for thunderclouds. *Időjárás 88*, 21-31.

IDŐJÁRÁS
Quarterly Journal of the Hungarian Meteorological Service
Vol. 111, No. 1, January–March 2007, pp. 65–77

Crop growing periods and irrigation needs of corn crop at some stations in Northeast Brazil

K. Karuna Kumar* and **T.V. Ramana Rao**

Department of Atmospheric Sciences, Federal University of Campina Grande
58.109-970 - Campina Grande – PB, BRAZIL
E-mail: karuna@dca.ufcg.edu.br

(Manuscript received in final form October 23, 2006)

Abstract—Results of a climatological study of soil moisture under corn crop at six stations in the semiarid region of Northeast Brazil are reported in this paper. Daily values of available soil moisture during the wet season are evaluated using a six-zone versatile soil moisture budget (VSMB) model. A first order Markov chain model is applied to the daily soil moisture data. Soil moisture averages and probabilities are used to identify the optimum growing periods for corn crop at the stations, and the irrigation needs during these periods are evaluated. The effect of soil hydro physical properties in the VSMB model is discussed. The use of mean daily precipitation values in the model in place of actual precipitation data is briefly discussed.

Key-words: versatile soil moisture budget, available soil moisture, crop growing periods, irrigation needs, Markov chain probabilities

1. Introduction

Soil moisture is an important parameter in agriculture, forestry, and hydrology. It plays a significant role in determining crop yields and in the hydrological balance of a region. Since it is impractical to measure soil moisture on the time and space scales required for agro-climatological studies, several models have been developed in the past for its estimation (*Thornthwaite* and *Mather*, 1955; *Holmes* and *Robertson*, 1959; *Baier* and *Robertson*, 1966; *De Jong* and *Shaykewich*, 1981; *Robertson*, 1985). The versatile soil moisture

*Address for correspondence: R. Rodrigues Alves 1183, Apt 203, Prata Campina Grande – 58101-291 (PB), BRAZIL

budget (VSMB) originally developed by *Baier* and *Robertson* (1966) takes into consideration the rooting depth of the crop, root concentration in different soil zones, and water holding and water release characteristics of each zone. In addition, allowance can be made for the changes in root concentration, as the crop develops towards maturity.

De Jong (1988) compared the soil moisture estimates from the VSMB and SPAW (soil-, plant-, air-water) models with measured data in the semiarid region of Saskatchewan. He found that both models gave equally good results, and that the VSMB model required less crop and soil information as input than the SPAW model. *Boisvert et al.* (1992) used the VSMB model to predict the water table depth. It has also been used to study the soil moisture conditions in the Canadian prairies (*De Jong et al.*, 1992). The VSMB model has been used to estimate soil moisture under palm plantations in Malaysia (*Robertson* and *Foong*, 1977), to calculate soil moisture in arid soils in India (*Robertson*, 1977), and to predict summer drought conditions under grass land in South Africa (*Dyer* and *De Jager*, 1986). Recent developments in soil water modeling including the VSMB model were reviewed by *De Jong* and *Bootsma* (1996) and *Baier* and *Bootsma* (1999).

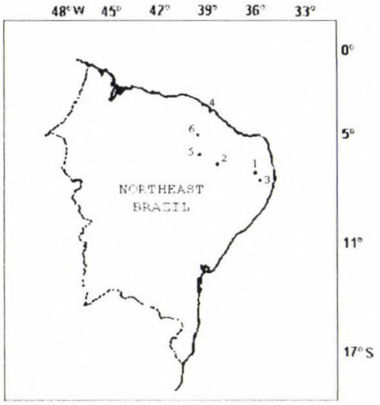

Fig. 1. Location of stations. 1. Campina Grande; 2. São Gonçalo; 3. Umbuzeiro; 4. Fortaleza; 5. Iguatu; 6. Quixeiramobim.

The present paper is based on a study of soil moisture conditions under corn crop at six stations in the semiarid zone of Northeast Brazil (*Fig. 1*). Northeast Brazil comprises an area of about 1.5 million km^2 and consists about 30% of the country's population. In the coastal areas rainfall can be up to 2000 mm per year. About 35% of the region lies in the zone of equatorial climate and 65% in the zone of subtropical climate. The highest and lowest recorded temperatures are 41.5 °C and 11.6 °C, respectively. About 10% of the region receives less than 250 mm of annual rainfall and about 60% receives more than

600 mm. Apart from the generally low amount of rainfall, the highly irregular nature of rainfall during the year is responsible for the frequent occurrence of droughts in this region. In most years about 90% of annual rainfall occurs from December to April or May. The duration of the rainy season is fairly constant, but its starting point, which generally coincides with the sowing time, may vary between 60 to 90 days.

The semiarid zone occupies 60% of Northeast Brazil and contains 40% of its population. The main climatic characteristics are: annual rainfall of 400–800 mm with a high coefficient of variability, high air temperatures, and high potential evapotranspiration rates (averaging 2000 mm). The crops grown in the semiarid zone are cotton, corn, and beans.

In the semiarid zone the main constraint to crop production is rainfall and its extreme variability. Studies of soil moisture conditions under agricultural crops are thus a matter of much importance in this region.

2. *Methodology*

In the present study, long term mean decadal (ten day periods) potential evapotranspiration (*PE*) values derived from Thornthwaite's procedure (*Thornthwaite*, 1948, *Thornthwaite* and *Mather*, 1957) are used to obtain daily *PE* values, and these together with daily precipitation data are used to evaluate daily soil moisture values. A versatile soil moisture budget model is used for this purpose, and the computations are carried out for a minimum period of 25 years. Values of 75, 100, 150, and 200 mm are assigned to the available moisture capacity (*AWC*) of the root zone of the soil. The *AWC* is defined as the difference between the field capacity and the permanent wilting point. The soil root depth is divided into six zones and approximately 5, 7.5, 12.5, 25, 25, and 25% of the total *AWC* are attributed to zones one to six respectively.

The contribution of each zone to the total actual evapotranspiration (*AE*) is evaluated from following expression:

$$PAE_{j,x} = K_{i,j}\left(WS_{j,x-1} / WC_j\right)Z_{j,x}PE_x, \tag{1}$$

where $PAE_{j,x}$ = partial evapotranspiration from the jth zone on day x;
$K_{i,j}$ = crop coefficient for the jth zone in growth stage i;
$WS_{j,x-1}$ = available moisture content of the jth zone at the end of day x-1;
WC_j = available moisture capacity of jth zone;
PE_x = potential evapotranspiration on day x;
Z = factor depending on soil dryness characteristics.

A set of 100 values between 0.0 and 1.0 are assigned to Z corresponding to 100 values between 0.0 and 1.0 of WS/WC on the assumption, that the ratio AE/PE remains equal to unity until relative available moisture content WS/WC decreases to 0.7 and then decreases linearly with WS/WC. Such an assumption is a reasonable first approximation for most medium textured soils.

The K coefficients reflect the root activity at different depths during different growth stages of the crop. The corn crop-growing period is divided into three principal stages, and in each stage different K values are assigned to the six zones. When the upper zones of the soil are dry, relatively more moisture is removed from the lower zones than in the case of uniformly wet soil. To take this aspect into consideration, the K coefficients for each zone below the first are increased as a function of the moisture content of the respective upper zones.

$$K'_j = K_j + K_j \left[\sum_{m=1}^{j-1} K_m \left(1 - \frac{WS_m}{WC_m} \right) \right], \tag{2}$$

where K'_j = adjusted K coefficient for the jth zone;
WS_m = available moisture content in the mth zone;
WC_m = available moisture capacity of the mth zone;

The available moisture content and the moisture loss from each zone are obtained from the following expressions:

$$\begin{aligned} WS_{j,x} &= WS_{j,x-1} - PAE_{j,x}, \\ WS_{j,x} &= 0 \ \text{ if } \ PAE_{j,x} > WS_{j,x-1}, \end{aligned} \tag{3}$$

where $WS_{j,x}$ is the available moisture in the jth zone at the end of day x.

$$\begin{aligned} AE_{j,x} &= PAE_{j,x} \ \text{ if } \ PAE_{j,x} \leq WS_{j,x-1}, \\ AE_{j,x} &= WS_{j,x-1} \ \text{ if } \ PAE_{j,x} > WS_{j,x-1}. \end{aligned} \tag{4}$$

The sum of $AE_{j,x}$ for the six zones gives the actual evapotranspiration (AE) on day x. The sum of $WS_{j,x}$ for the six zones represents the available moisture content of the root zone of the soil on day x, if no precipitation occurs on that day. If precipitation occurs the values of $WS_{j,x}$ for some or all the six zones will increase.

On days with precipitation it is assumed, that moisture loss due to evapotranspiration occurs before precipitation. Precipitation enters the first zone and if this zone reaches its moisture holding capacity, the excess water enters the second zone, and so on. Excess water leaving the sixth zone is considered the water surplus on that day.

In each year the computations are carried out for different four-month corn growing periods for the four *AWC* values assumed.

Each month is divided into three decades, the last decade having 8, 9, 10, or 11 days depending on the month. Based on the daily soil moisture data for the study periods, mean decadal available moisture contents are obtained. A first order Markov chain model is applied to the daily soil moisture data, and the initial and conditional probabilities of dry and wet days are computed. The critical moisture content separating a wet day from a dry day is taken to be half of the assumed *AWC* value. For each decade during the growing period, the probability of occurrence of five consecutive wet days, $P(5W)$ is evaluated using the above probabilities. Soil moisture averages and probabilities are used to determine the optimum growing periods for corn at the stations.

The soil moisture model described above is also used to evaluate the irrigation needs for corn crop at the stations. The computations for *AWC* values of 100, 150, and 200 mm are repeated with the modification, that each time the available moisture content decreases to a predetermined value, the moisture content on that day is replaced with that corresponding to 95% of the *AWC*. In practical terms this means, that each time the soil moisture is depleted to a preselected value, irrigation is applied to bring it back to a safe level. This part of the study is carried out assuming three limiting soil moisture levels (50%, 70%, and 90% of the *AWC*). The number of irrigation applications during the four-month (optimum) growing period and the mean interval between irrigations are obtained for each year, and from these numbers the mean values for the study period are derived.

3. Results and discussion

Mean decadal values of available moisture content at Campina Grande are evaluated for different growing periods during the wet season for the four *AWC* values considered and results for AWC_{200} are shown in *Fig. 2*. It is found that in general, the available moisture content as a fraction of *AWC* decreases with the increase in *AWC* value from 75 to 200 mm. During the period May–August, available moisture content was almost always more than 50% of the *AWC* even though the climatic water balance based on Thornthwaite's procedure (*Thornthwaite*, 1948; *Thornthwaite* and *Mather*, 1957) shows large water deficiency during the months August-September. Based on mean decadal values of available moisture content, the period May–August is found to be the optimum growing period for corn at Campina Grande. Values of probability of occurrence of five consecutive wet days, $P(5W)$ are evaluated for each of the twelve decades in successive four-month periods. The results once again indicate that the period May–August is the best of the three growing periods considered. The same conclusion is drawn on the basis of *Table 1*, which shows the available moisture content, exceeded at different probability levels. However, even during the period May–August, supplementary irrigation is found necessary for corn growth.

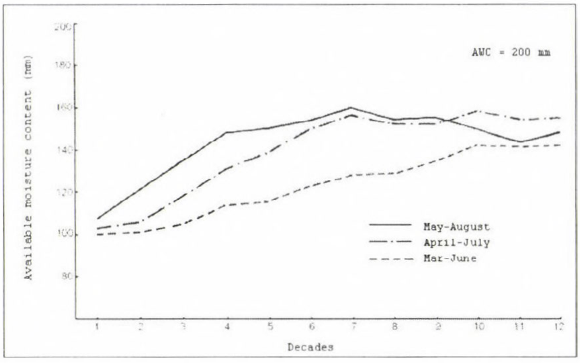

Fig. 2. Available soil moisture at Campina Grande in different growing periods.

Mean decadal values of *AE* for the months February–May for the 25-year study period at Teresina are compared with the corresponding *PE* values. During February, March, and May, *AE* is much smaller than *PE*. In April the moisture content in the root zone is quite high, and the sum of the *K* coefficients for the six soil layers is more than unity. Hence, *AE* during the three decades in April exceeds the *PE*. Under well watered conditions, *AE* estimates from the VSMB model exceed *PE* during a part of the growing cycle (*Dyer* and *Mack*, 1984). This in turn implies values of crop coefficient K_c, which relates evapotranspiration to reference crop evapotranspiration (*Doorenbos* and *Pruitt*, 1977) higher than 1. Values of K_c for corn between 1.0 and 1.2 during certain growth stages have been reported by *Allen et al.* (1998) and *Doorenbos* and *Kassam* (1979).

One of the parameters of the VSMB model is the *Z* factor, which is the ratio between *AE/PE* and *WS/AWC*. Much controversy surrounds the relationship between these two ratios, and the use of incorrect relationship in the model may lead to erroneous soil moisture estimates. To study this aspect, daily values of available moisture at Campina Grande are computed for 25 years using *Z* tables corresponding to the different curves of *Fig. 3*. The results are shown in *Fig. 4a* and *b*.

Table 1. Estimated soil water content (mm) exceeded at given probabilities

Probability	March–June			April–July			May–August		
Decade	25%	50%	75%	25%	50%	75%	25%	50%	75%
1	98	94	89	110	98	93	112	101	96
2	122	85	79	125	106	85	147	110	94
3	131	89	74	138	114	91	177	129	96
4	149	96	80	172	132	99	190	151	111
5	149	109	73	179	144	105	191	165	109
6	169	105	84	187	162	118	196	176	111
7	168	120	87	192	164	141	196	174	124
8	164	132	94	188	172	126	189	171	123
9	169	138	102	189	169	132	186	168	132
10	176	145	126	196	178	138	175	158	142
11	182	148	115	190	174	129	174	151	125
12	187	144	104	187	166	146	175	142	121

Station: Campina Grande Available water capacity: 200 mm

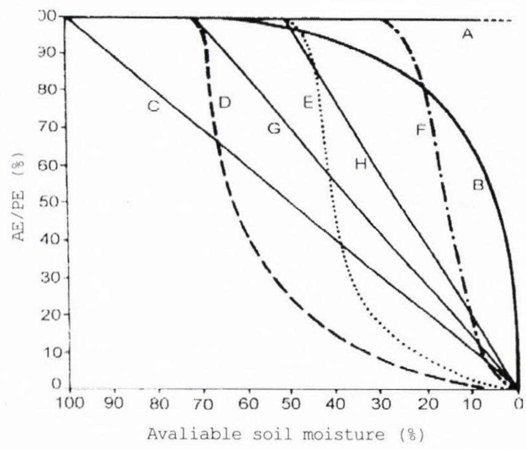

Fig. 3. Relationship between *AE/PE* and available soil moisture content (*Baier* and *Robertson*, 1966).

The lowest values of moisture content are observed when curve A is used in the model. This curve is based on the assumption, that moisture is equally available to plants for evapotranspiration over the range from field capacity to the permanent wilting point. According to *Baier et al.* (1979), this assumption is probably valid for sandy soils well permeated with roots.

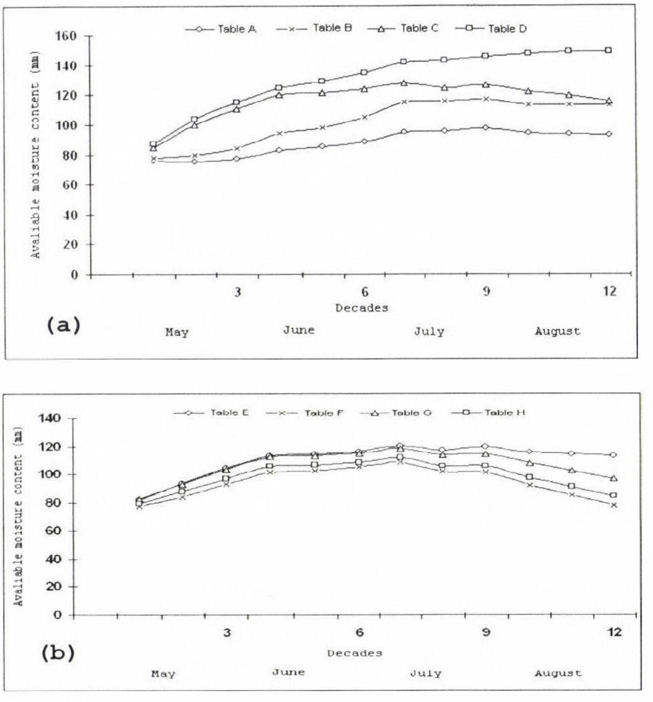

Fig. 4. Available soil moisture at Campina Grande based on different *Z* tables.

According to curve B, no significant decrease in evapotranspiration occurs except in very dry soil. This concept was suggested by *Pierce* (1958) and was used by *Gardner* (1960) for a sandy soil. Curve C assumes a linear relationship between the *AE*/*PE* ratio and the soil moisture percentage. Such a relation was supported by various authors (*Denmead* and *Shaw*, 1962; *Gardner* and *Ehlig*, 1963; *Smith*, 1959). Curves D, E, and F assume no reduction in the *AE*/*PE* ratio over the range of available moisture from 100 to 70% (curve D), to 50% (curve E), and to 30% (curve F). Beyond these limits the *AE*/*PE* ratio decreases rapidly with the drying of the soil. Curve G assumes no reduction in *AE*/*PE* over the range from 100 to 70% of available moisture and a linear decrease below 70%. This curve is recommended for most medium textured non-irrigated soils. Curve H is similar to curve G, except that no reduction in *AE*/*PE* ratio is assumed over the range from 100 to 50% of available soil moisture.

Soil moisture estimates based on curves B and E are quite similar, while the highest values of soil moisture are obtained with the use of curve D. Soil moisture values based on curves E, F, G, and H are very close to each other over a large part of the four-month growing period. The results based on curve C are quite close to those obtained from all other curves except curve A. This is in agreement with *Baier*'s (1969) suggestion, that if soil moisture observations are not available for comparison, curve C provides a reasonable approximation.

If daily precipitation data over a long time period is not available, mean daily precipitation values derived from climatic monthly mean values can perhaps be used in the VSMB model to obtain an estimate of actual evapotranspiration. This aspect is studied using data for Campina Grande. *Brook*'s (1943) sine curve interpolation technique is used to derive daily precipitation values from climatic monthly means, and the resulting daily values are used together with the daily *PE* values to obtain daily values of *AE* during the growing season. From the 122 daily values, mean values for each decade are derived. These values are compared with mean decadal *AE* values obtained from the use of actual daily precipitation data for 25 years in the model (*Fig. 5*). Actual evapotranspiration obtained using mean daily precipitation data is always higher than that based on daily precipitation data. Use of mean precipitation data also shows the surface soil layers wetter and water surplus lower than in the case of using daily precipitation data. Actual evapotranspiration during the crop-growing season is an important parameter, and the close agreement between the two curves is quite encouraging.

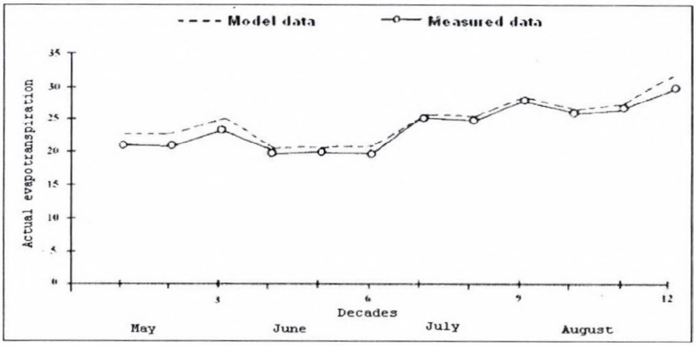

Fig. 5. Actual evapotranspiration (mm/decade) at Campina Grande obtained from the VSMB model using (1) mean daily precipitation data and (2) actual precipitation data.

Results of irrigation computations for Fortaleza for a limiting moisture value (*VC*) of 105 mm are given in *Table 2*. A summary of the results for all the stations is presented in *Table 3*.

As it is expected, the number of irrigations increases and the mean interval between irrigations decreases as the limiting moisture level increases. However, the change in the total water need is not very pronounced, since at higher *VC* values less water is applied in each irrigation. Comparison of water surplus data under irrigated and unirrigated conditions shows that, in general, the fraction of irrigation water that is lost as water surplus increases as the limiting moisture level increases.

Table 2. Irrigation requirements at Fortaleza.
AWC=150 mm, *VC*=105 mm. Period: April–July

Year	Number of irrigations	Mean interval between irrigations (days)	Number of days with available moisture content (mm) between		
			105–120	120–135	135–150
25	6	22	29	40	53
26	5	28	26	36	60
27	5	29	25	38	59
28	7	19	32	40	50
29	5	28	21	31	70
30	4	37	33	35	54
31	6	22	28	43	51
32	8	17	39	51	32
33	6	23	30	35	57
34	6	24	21	19	82
35	4	38	16	26	80
36	7	19	38	35	49
37	4	40	19	28	75
38	4	40	20	41	61
39	5	26	26	37	59
40	4	37	13	29	80
41	7	19	35	50	37
42	7	20	44	39	39
43	7	19	37	34	51
44	6	22	24	30	68
45	3	58	8	24	90
46	5	28	23	37	62
47	5	29	26	28	68
48	3	59	24	36	62
49	5	30	17	21	84
50	6	23	27	24	71
51	5	30	37	37	48
52	6	23	28	34	60
53	6	23	21	39	62
54	6	24	29	29	64
55	6	23	26	33	63
56	7	19	31	50	41
57	7	19	35	35	52

Table 3. Irrigation needs at the stations. AWC = 150 mm

Station	Crop growing period	Limiting soil moisture level (mm)	Number of irrigations	Mean interval between irrigations (days)	Irrigation amount (mm)
Iguatu	Mar – Jun	75	2	90	135
		105	4	37	150
		135	25	5	190
Fortaleza	Apr – Jul	75	3	74	200
		105	5	28	190
		135	29	5	220
Quixeramobim	Apr – Jul	75	3	55	200
		105	7	20	260
		135	37	3	280
São Gonçalo	Feb – May	75	2	94	135
		105	4	41	150
		135	27	5	200
Umbuzeiro	Jun – Sep	75	2	106	135
		105	3	72	110
		135	16	9	120
Campina Grande	May – Aug	75	1	116	70
		105	2	78	75
		135	13	10	100

The climatic water balance table for Sao Gonçalo based on Thornthwaite's procedure (*Thornthwaite* and *Mather*, 1957) for AWC value of 250 mm indicates the following values for the period February–May: PE = 507 mm, AE = 499 mm, P = 678 mm. It may be mentioned here, that this procedure is based on the relationship between *AE/PE* and *WS/AWC* given by curve C of *Fig. 3*.

Table 4. Potential evapotranspiration (*PE*), actual evapotranspiration (*AE*), and precipitation (*P*) during the growing periods based on Thornthwaite's procedure

Station	Campina Grande	Umbuzeiro	Iguatu	Fortaleza	Quixeramobim	São Gonçalo
Period	**May – Aug**	**Jun – Sep**	**Mar – Jun**	**Apr – Jul**	**Apr – Jul**	**Feb – May**
PE	304	284	492	511	543	507
AE	294	261	403	492	344	499
P	367	317	465	668	331	679

Results of the present study show, however, that even to maintain the moisture content above 50% of AWC irrigation is needed in each year of the 36-year study period. Comparison of data presented in *Table 4* with irrigation needs at the stations (*Table 3*) indicates, that climatic water balance data may not be of much use in evaluating the agricultural potential of a region. Irrigation needs are evaluated at Campina Grande for AWC values of 100 and 200 mm and a VC level of 85%. The results show that to maintain similar moisture levels in the soil, more irrigation is necessary in the case of AWC_{100} than for AWC_{200}. Similar result was reported by *De Jong* (1985).

References

Allen, R.G., Pereira, L.S., Raes, D., and *Smith, M.*, 1998: Crop evapotranspiration. Guidelines for computing crop water requirements. *FAO Irrigation and drainage paper 56*. FAO, Rome, Italy. 301 pp.

Baier, W., 1969: Concepts of soil moisture availability and their effects on soil moisture estimates from a meteorological budget. *Agr. Meteorol. 6*, 165-178.

Baier, W. and *Robertson, G.W.*, 1966: A new versatile soil moisture budget. *Can J. Plant Sci. 46*, 299-315.

Baier, W., Dyer, J.A., and *Sharp, W.R.*, 1979: The versatile soil moisture budget. *Tech. Bull. 87,* Agrometeorology Section, Research Branch, Agriculture Canada, Ottawa, Ont. 52 pp.

Baier, W. and *Bootsma, A.*, 1999: Climate input requirements of soil-crop-weather models for climate change assessments. Agriculture and Agri-Food Canada, Research Branch, Eastern Cereal and Oilseed Research Center contribution No 981348,*Tech. Bull.* 33 pp.

Boisvert, J.B., Dyer, J.A., Lagace, R., and *Dube, P.A.*, 1992: Estimating water table fluctuations with a daily weather-based water budget approach. *Can. Agr. Eng. 34*, 115-124.

Brooks, C.E.P., 1943: Interpolation tables for daily values of meteorological elements. *Q. J. Roy. Meteor. Soc. 69*, 160-162.

Denmead, O.T. and *Shaw, R.H.*, 1962: Availability of soil water to plants as affected by soil moisture content and meteorological conditions. *Agron. J. 54*, 385-390.

De Jong, R., 1985: Soil water modelling using daily and mean daily data derived from historical monthly values. *Atmos.-Ocean 23*, 254-266.

De Jong, R., 1988: Comparison of two-soil water models under semi-arid growing conditions. *Can. J. Soil.Sci. 68*, 307-321.

De Jong, R. and *Bootsma, A.*, 1996: Review of recent developments in soil water simulation models. *Can. J. Soil. Sci. 76*, 263-273.

De Jong, R. and *Shaykewich, C.F.*, 1981: A soil water budget model with a nearly impermeable layer. *Can. J. Soil. Sci. 61*, 361-371.

De Jong, R., Bootsma, A., Dumanski, J., and *Samuel, K.*, 1992: Characterizing the soil water regime of the Canadian prairies. *Tech. Bull. 1992-2E.* Center for Land and Biological Research, Agriculture Canada. Ottawa, ON, 15 pp.

Doorenbos, J. and *Kassam, A.H.*, 1979: Yield response to water. *FAO Irrigation and Drainage Paper,* No. 33. FAO, Rome, Italy. 193 pp.

Doorenbos, J. and *Pruitt, W.O.*, 1977: Guidelines for prediction of crop water requirements. *FAO Irrigation and Drainage Paper*, No. 24. FAO, Rome, Italy. 156 pp.

Dyer, J.A. and *De Jager, J.M.*, 1986: Assessment of recent drought severity for natural grassland at three locations. *S.A.J. Plant. Sci. 3*, 80-82.

Dyer, J.A. and *Mack, A.R.*, 1984:Tthe versatile soil moisture budget - version three. *LRRI Contribution No. 82-3,* Agriculture Canada, Ottawa, Ontario, Canada, 24 pp.

Gardner, W.R., 1960: Dynamic aspects of water availability to plants. *Soil Sci. 89*, 63-73.

Gardner, W.R. and *Ehlig, C.F.*, 1963: The influence of soil water on transpiration by plants. *J. Geophys. Res. 68*, 5719-5724.

Holmes, R.M., and *Robertson, G.W.*, 1959: A modulated soil moisture budget. *Mon. Weather Rev. 87*, 101-106.

Pierce, L.T., 1958: Estimating seasonal and short-term fluctuations in evapotranspiration from meadow crops. *B. Am. Meteorol. Soc. 39*, 73-78.

Robertson, G.W., 1977: A versatile soil moisture budget for drought prone regions and dryland farming areas in India. Prepared as part of *FAO/TF/IND/136*. Drought prone areas project. Dryland Agriculture Center, Hyderabad 500012, India, 50 pp.

Robertson, G.W., 1985: Multiple-crop multiple-layer soil-water budget: *A computer program documentation*. Supply and Services Canada. Ottawa. 41 pp.

Robertson, G.W. and *Foong, Sang Foo*, 1977: Weather based yield forecast for oil palm fresh fruit bunches. *Proc. of the Malaysian International Oil Palm Conference, 1976*. The Incorporated Society of Planters, 695-709.

Smith, G.W., 1959: The determination of soil moisture under a permanent grass cover. *J. Geophys. Res. 64*, 477-483.

Thornthwaite, C.W., 1948: An approach toward a rational classification of climate. *Geogr. Rev. 38*, 55-94.

Thornthwaite, C.W. and *Mather, J.R.*, 1955: The water balance. *Publ. Climatol. 8* (1). Lab of Climatology. N.J., 1-104.

Thornthwaite, C.W. and *Mather, J.R.*, 1957: Instructions and tables for computing potential evapotranspiration and the water balance. *Publ. Climatol. 10* (3). Lab of Climatology. N.J., 185-311.

GUIDE FOR AUTHORS OF *IDŐJÁRÁS*

The purpose of the journal is to publish papers in any field of meteorology and atmosphere related scientific areas. These may be

- research papers on new results of scientific investigations,
- critical review articles summarizing the current state of art of a certain topic,
- short contributions dealing with a particular question.

Some issues contain "News" and "Book review", therefore, such contributions are also welcome. The papers must be in American English and should be checked by a native speaker if necessary.

Authors are requested to send their manuscripts to

Editor-in Chief of IDŐJÁRÁS

P.O. Box 39, H-1675 Budapest, Hungary

in three identical printed copies including all illustrations. Papers will then be reviewed normally by two independent referees, who remain unidentified for the author(s). The Editor-in-Chief will inform the author(s) whether or not the paper is acceptable for publication, and what modifications, if any, are necessary.

Please, follow the order given below when typing manuscripts.

Title part: should consist of the title, the name(s) of the author(s), their affiliation(s) including full postal and e-mail address(es). In case of more than one author, the corresponding author must be identified.

Abstract: should contain the purpose, the applied data and methods as well as the basic conclusion(s) of the paper.

Key-words: must be included (from 5 to 10) to help to classify the topic.

Text: has to be typed in single spacing with wide margins on one side of an A4 size white paper. Use of S.I. units are expected, and the use of negative exponent is preferred to fractional sign. Mathematical formulae are expected to be as simple as possible and numbered in parentheses at the right margin.

All publications cited in the text should be presented in a *list of references*, arranged in alphabetical order. For an article: name(s) of author(s) in Italics, year, title of article, name of journal, volume, number (the latter two in Italics) and pages. E.g., *Nathan, K.K.,* 1986: A note on the relationship between photo-synthetically active radiation and cloud amount. *Időjárás 90,* 10-13. For a book: name(s) of author(s), year, title of the book (all in Italics except the year), publisher and place of publication. E.g., *Junge, C.E.,* 1963: *Air Chemistry and Radioactivity.* Academic Press, New York and London. Reference in the text should contain the name(s) of the author(s) in Italics and year of publication. E.g., in the case of one author: *Miller* (1989); in the case of two authors: *Gamov* and *Cleveland* (1973); and if there are more than two authors: *Smith et al.* (1990). If the name of the author cannot be fitted into the text: *(Miller,* 1989); etc. When referring papers published in the same year by the same author, letters a, b, c, etc. should follow the year of publication.

Tables should be marked by Arabic numbers and printed in separate sheets with their numbers and legends given below them. Avoid too lengthy or complicated tables, or tables duplicating results given in other form in the manuscript (e.g., graphs)

Figures should also be marked with Arabic numbers and printed in black and white in camera-ready form in separate sheets with their numbers and captions given below them. JPG, GIF, or XLS formats should be used for electronic artwork submission.

The text should be submitted both in manuscript and in electronic form, the latter on disks or in e-mail. Use standard 3.5" MS-DOS formatted diskette or CD for this purpose. MS Word format is preferred.

Reprints: authors receive 30 reprints free of charge. Additional reprints may be ordered at the authors' expense when sending back the proofs to the Editorial Office.

Information on the last issues: http://www.met.hu/Journal-Idojaras.php

Published by the Hungarian Meteorological Service

Budapest, Hungary

INDEX: 26 361

HU ISSN 0324-6329

IDŐJÁRÁS

QUARTERLY JOURNAL
OF THE HUNGARIAN METEOROLOGICAL SERVICE

Special Issue: Workshop on Environmental Fluid Mechanics as Elements in Agrometeorological Modeling

Guest Editors: **Tor Håkon Sivertsen** and **Peder A. Tyvand**

CONTENTS

****

http://www.met.hu/Journal-Idojaras.php

VOL. 111 * NO. 2-3 * APRIL – SEPTEMBER 2007

IDŐJÁRÁS

Quarterly Journal of the Hungarian Meteorological Service

Editor-in-Chief
LÁSZLÓ BOZÓ

Executive Editor
MARGIT ANTAL

Editorial Office: P.O. Box 39, H-1675 Budapest, Hungary or
Gilice tér 39, H-1181 Budapest, Hungary
E-mail: bozo.l@met.hu or *antal.e@met.hu*
Fax: (36-1) 346-4809

Subscription by

mail: IDŐJÁRÁS, P.O. Box 39, H-1675 Budapest, Hungary;
E-mail: bozo.l@met.hu or *antal.e@met.hu*; *Fax: (36-1) 346-4809*

This special issue contains the proceedings from a workshop arranged at Ås in Norway in June 2006, called 'Workshop on environmental fluid mechanics as elements in agrometeorological modeling'.

Agrometeorology is a field of applied science aiming to develop operational systems for decision support in crop production and horticultural production. Both support of strategic decisions on what crops to grow at a certain farm or in a certain region, and support of tactical decisions on protecting the field crops against pests and disease, on timing the harvest, on irrigation scheduling etc. are covered by agro meteorological models. Furthermore, analyzing the environmental results of agricultural crop production is dependent on agrometeorological knowledge.

The models of agrometeorology contain results from the fields of physical meteorology, fluid dynamics, crop science, and biological sciences connected to operational crop protection. One major aim of this workshop has been to look into the sub-models of agrometeorology related to fluid dynamics and dynamical meteorology.

Norway once was a pioneering country for meteorology. Vilhelm Bjerknes (1862–1951) had important influence on the development of operational meteorology into a deterministic science based on the principles of hydrodynamics and synoptic systems for making observation. Before Bjerknes started his pioneering work in the beginning of the 20th century, there was no deterministic meteorology used operationally. The weather prognoses were mainly based on the combination of climate data, weather signs, and statistical inference. It was a great progress to be able to use deterministic weather forecasts instead of vague statistical prognoses. Life and death may depend on knowledge in advance, if a disastrous winter storm is heading for the western coast of Norway.

Today large-scale meteorology is established as a deterministic science, and numerical weather forecasts based on fluid dynamics as an important tool.

Agrometeorology is a special branch of physical meteorology. It works on the smallest length scale, where there is no direct influence of the Earth's rotation. The large-scale weather forecasts are sometimes used as input data in agrometeorological forecasts. In large-scale meteorology the horizontal transport of mass and energy is of primary importance. In small-scale meteorology the vertical fluxes play a dominant role. In order to understand and control the conditions for healthy growth of a plant crop, one needs to measure and model the vertical flow of energy and mass in the system of soil, water, air, and plants.

Agrometeorology is being developed at a crossroad between deterministic and statistical science. Plant growth and plant health inevitably bring statistical elements into the models of agrometeorology. Other elements of statistical uncertainty are leaf area, transpiration, humidity, albedo, and turbulent transport coefficients. It is a scientific goal to make agrometeorology models as deterministic as possible. However, the smaller the time and length scales involved, the statistical deviations will be relatively greater. Therefore, a model that works on the shortest length scales can never be fully deterministic in all aspects.

In this special issue of IDŐJÁRÁS *we are presenting some of the results from the workshop for an international audience. The issue contains one paper on the subject of administrating meteorological and biological data to be used operationally as input to models. Another paper on agroclimatic modeling, meant for decision support on strategic issues is included. Three papers are dealing with local meteorological features connected to the fluid dynamical concepts of plumes and internal gravity waves in the atmosphere. At the small special session on gravity waves an interesting contribution on the history of Fridtjof Nansen and gravity waves in the ocean, as well as theory on internal waves and* *boundary layers was presented, and this is one of the contributions in the proceedings. Numerical modeling of fluxes of particles and heat in the boundary layer near the ground are dealt with in this issue. Furthermore, two papers connected to fluid dynamical instabilities in films of fluid are included.*

The important theme of 'representativeness' of input data to operational biometeorological models is the theme of one paper. Finally, we will mention an essay dealing with the non-linearity and chaotic behavior of the seemingly simple energy balance equation in the vicinity of the soil surface.

Looking into the future we think it is worthwhile to continue this discussion between biologists and researchers in the field of fluid dynamics to clarify the content and the scope of black boxes used operationally, and try to interpret complicated formulas using ordinary language. Two important related problems connected to operational models will be more and more relevant to deal with in the future: (a) determining the scope of qualitative modeling techniques, (b) developing methods for integrating data from different sources (automated networks of meteorological stations, weather radars, satellites, and manual observations) to be used in an optimal and intelligible way.

Acknowledgements

We would like to thank IDŐJÁRÁS *for giving us the opportunity to publish the proceedings from this workshop in a special issue. We also would like to thank Norwegian Institute for Agricultural and Environmental Research (both the Director of Research and the project 'Agrometorological Service of Norway'), the Norwegian Institute for Life Sciences (both the Director of Research and the Department of Mathematical Sciences and Technology), and Nordic Association of Agricultural Sciences for making it economically possible to arrange this workshop and publish the proceedings.*

Especially we will to thank the secretaries Karin K. Lyngmo and Signe Kroken for helping us with the arrangement and typewriting.

Tor Håkon Sivertsen[1] *and Peder A. Tyvand*[2]
Guest editors

[1]*Norwegian Institute for Agricultural and Environmental Research*
[2]*Norwegian University of Life Sciences*

IDŐJÁRÁS

Quarterly Journal of the Hungarian Meteorological Service
Vol. 111, No. 2–3, April–September 2007, pp. 79–89

Discussing a web-based system for administration, evaluation, and correction of meteorological and biological data in a perspective of actor-network theory

Tor Håkon Sivertsen[1] and Janis Gailis[2]

[1]*Norwegian Institute for Agricultural and Environmental Research, Høgskoleveien 7, N-1432 Ås, Norway; E-mail: thsivert@online.no*

[2]*Agder University College, Service Box 422, N-4604 Kristansand, Norway; E-mail: janis.gailis@hia.no*

(Manuscript received in final form January 29, 2007)

Abstract—The history of a web-based system for administrating data from a network of agrometeorological stations is shortly presented, and the module of this system containing the documentation of the instruments in this network is discussed in detail. The quality concept of meteorological data is the starting point for this discussion. The way of coupling the instruments and parameters on each meteorological station is shown, as well as the use of this information by controlling and correcting meteorological data.

Ideas of actor-network theory are discussed connected to the future challenges of data integration and use of data from different sources in applications.

Key-words: meteorological data, instruments, controlling data, documentation system, correcting meteorological data, actor-network theory

1. Introduction

The agrometeorological service of Norway is the owner of a network of agrometeorological stations, and during the growing season of 2006 the number of stations was 80. In 1998 and 1999 a web-based system for administration of this network of stations was developed, and this system was used operationally from May 2000 until March 2006. Documentation of the system, both the technical as well as theoretical parts, was published in an internal report at the Plant Protection Centre of The Norwegian Crop Research Institute in November 2002 (*Sivertsen* and *Gailis,* 2002), in Norwegian. The development of the software was based on ideas on object oriented analysis of the operational use of the results, put up by (*Brown,* 1997).

In January 2005 a description of the main theoretical elements of the system was published together with several ideas for refinement of the system to include methods for making measurements of meteorological parameters (networks of meteorological stations, weather radars, etc., as well as output from different models, meteorological prognoses on different spatial and temporal scales) (*Sivertsen,* 2005a).

Ideas for extending this system to include biological data, both long time series of measurements and model calculations were published in 2005 (*Sivertsen*, 2005b), together with technical information on constructing the most important tables of the database.

This system for administrating the stations contain a documentation system for meteorological parameters (*Sivertsen,* 2004, 2005a, c and d), and a documentation of instruments giving unique identification of each instrument at every station. In Section 2 the documentation of instruments, as well as the way the instruments and parameters are coupled, are described. The coupling of instrumentation and parameters is used for controlling the values of the meteorological parameters. Furthermore, routines for automated corrections of meteorological data, connected to the specific types of instruments is a part of this system.

The responsibility of the agrometeorological service of the Norwegian Institute for Agricultural and Environmental Research is to run the network of agrometeorological stations as well as to gather, store, control, and use meteorological and biological data originated from the stations and other sources to be used in applications for plant protection (for tactical and strategical decisions) and in research purposes on agricultural and environmental issues. Important future challenges are connected to the integration and use of data from different sources in an intelligent and optimal manner (*Sivertsen,* 2006).

A few elements of actor-network theory (*Latour*, 2005) are discussed in this paper. The ideas of this theory may be applied in inquiry of the exchange of data and applications on the internet by a heterogenous system of actors. Norwegian Institute for Agricultural and Environmental Research ought to act in this heterorgeneous world wide network according to the responsibility of the organization. When the institute is gathering data and information, this ought to be done according to an evaluation of what is needed for each specific task. The organization may demand specific quality on the data gathered and only use the data according to the known quality level of the data. When submitting data to other organizations and to the public, the Norwegian Institute for Agricultural and Environmental Research may explicitely document the quality and scope of these data. The institute may suggest in which context the information should be used and in which context the information should not be used.

Specifically, the Norwegian Institute for Agricultural and Environmental Research has been be engaged in standarazing formats for exchange of meteorological and biological data (*Sivertsen,* 2005c; *Mestre,* 2006). Such work is a task logically connected to the responsibility of the organization.

2. *Connecting measurable quantities to the scientific principle*

2.1. *The concept of a parameter and the quality of data*

When any physical, meteorological, or biological phenomenon is described by attaching quantitative attributes to it, this is called 'parameterization' in this paper (*Sivertsen*, 2004, 2005c and e). The main attributes of documenting measured parameters and parameters of models are given in the following manner (*Sivertsen*, 2005a and b) and (*Mestre*, 2006):

Measured parameters:

Name of the parameter
Unit
Definition
Method(s) for measuring the parameter
Representativeness for certain phenomena (models).

Parameters in models:

Name of the parameter
Unit
Definition of the parameter
Representativeness for certain phenomena in other models.

The term quality is derived from the Latin word 'qualitas' meaning the nature (good or bad), properties, or condition of something. If we know the nature and sources of meteorological and biological data, the value of the data is known.

The quality of the meteorological data may in a very short manner be described in this way (*Sivertsen,* 2005b):

(a) Connection of the data to the objects of nature (*Sivertsen,* 2005d);
(b) Properties, conditions, and quantitative values of the data, including completeness and representativeness;
(c) Identity of the data that is linked to the social system producing the data (giving the data authority);
(d) Availability of the data; and
(e) Presentation and use of the data including the context of the presentation.

The meteorological data of interest for the use in models, etc., of course are the numerical values of the parameters. Nevertheless, for discussions connected to the scope of the model systems, contained in the interpretation of the scientific principle given in *Fig. 1* (*Sivertsen*, 2005e), the knowledge of the definition of the parameters, technical details of the measurements, and other attributes of the metadata are of interest. Thus, the points (a), (b), and (c) above connected to the quality of the data are of relevance for the discussion in this paper.

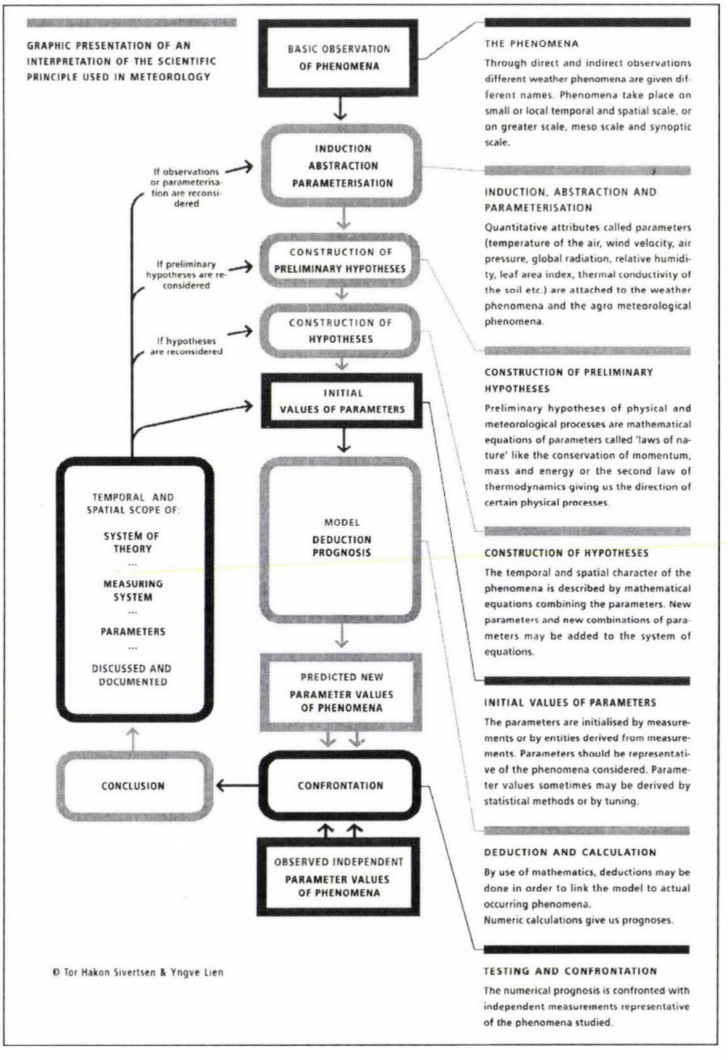

Fig. 1. Graphical representation of an interpretation of the scientific principle.

2.2. Documentation of the instruments

The instruments are documented in a hierarchy, and the four levels in this hierarchy have got the following names: (a) InstrumentType: the type name used by the producer of the instrumen, (b) SensorType: type of sensors connected to each type of instrument, (c) SensorGroupType: defined group of sensors connected to a certain type of instrument, and it may consist of only one type of sensor, (d) SensorGroup: the actual group of sensors connected to a type of instrument and a certain logger. This group of sensors (one sensor or several sensors) is used to measure one or several parameter values.

The highest level is the InstrumentType. This is a rather short description of the types of instruments used in the web-system. The instrument type is defined as the production name used by the company producing the instrument. Also the name of the producer, the country of the producing company, and a short description of the instrument are given as attributes in this table.

The second highest level is the SensorType. This level contains description of the different types of sensors connected to a certain type of instrument. An important part of the description, and the key of the table, is a short name, a symbolic name, constructed to give a very short description of the physical principle of the sensor. Here is a list of some short names used (the type of instrument and the producer's name are also given to clarify the system):

PHEV (photo electric vane) WAV15, Vaisala Oy, Finland

P2 (Pt 100) MP-100, Rotronic AG, Germany

CP (sensor measuring electric capacity of air) MP-100, Rotronic AG, Germany

TIPB (tipping bucket) ARG 100, Campbell Scientific, USA

P3 (Pt1000) HMP45A, Vaisala Oy, Finland

CPaa2 (sensor measuring electric capacity of air, second type) HMP45A, Vaisala Oy, Finland

TIPBH (tipping bucket, heated) ARG 100Heated, Campbell Scientific Ltd, USA

TIPBaa2 (tipping bucket, second instrumenttype) Rainmatic, Pronamic, Denmark

3CUP (3 cup anemometer) A100R, Vector Instruments, United Kingdom

3CUPH (3 cup anemometer, heated) WAA15, Vaisala Oy, Finland

3CUPHaa2 (3 cup anemometer, heated, second type) 432 Anemometer, Theodor Fiedrichs & Co, Germany

3CUPaa2 (3 cup anemometer, second type) Wind Speed Sensor 2740, Aanderaa Instrumnents, Norway.

In addition the calibration procedure of the sensor, the temperature range of usefulness, the measuring range, the precision of the measurement, if it can be used in darkness and if it is useful below 0 degrees Celsius, are given as attributes of the SensorType.

The third highest level is called SensorGroupType. This is a table of shortnames. Usually a few letters are added to the SensorType shortname or to a combination of SensorType short names to give an indication of which meteorological parameter are most usually recorded by an actual instrument with this SensorGroupType.

Below a few examples are presented:

ALBSN (measuring 'albedo') consists of the sensor types TCUPaa4 and TCDO

GRPHDD (measuring 'global radiation') consists of the sensor type PHDD

GRTCUP (measuring 'global radiation') consists of the sensor type TCUP

LWARTL (measuring 'leaf wetness') consists of the sensor type ARTL

PBUSTRI (measuring 'precipitation') consists of the sensor type BUSTRI

TP2 (measuring 'the temperature of the air') consists of the sensor type P2.

The lowest level in the description and classification of the instruments is the SensorGroup, which is a unique registration of one particular group of sensor on one particular logger. Most of the loggers are permanently placed on a certain site. We, therefore, always add three unique letters to the 'SensorGroupType' short name to tell at which site the 'SensorGroup' is placed.

An example is given below:

GRTCUPUDN is the SensorGroup measuring global radiation on the logger number 14 placed at Udnes.

In the case of certain SensorGroups, for example sensor groups measuring the temperature of the soil in different depths, the name of the sensor group also indicates in which depth the instrument is placed.

Two examples are given below:

JT10TTHERMUDN is the SensorGroup belonging to the SensorGroupType TTHERM measuring soil temperature in 10 cm depth on the logger number 14 at Udnes.

JT20TTHERMUDN is the SensorGroup belonging to the SensorGroupType TTHERM measuring soil temperature in 20 cm depth on the logger number 14 at Udnes.

2.3. *Coupling of instruments and parameters*

Through a user interface the different meteorological parameters may be coupled to the SensorGroups defined on each logger, and each parameter is also defined by a shortname:

One example:

The SensorGroup TP2UDN is connected to four parameters:

TM: The hourly mean air temperature 2m above the soil surface.

TN: The hourly minimum air temperature 2m above the soil surface.

TX: The hourly maximum air temperature 2m above the soil surface.

TT: The instantaneous air temperature 2m above the soil surface in the end of the hourly interval considered.

2.4. *Data controlling and correction*

One special feature of the system is the development and implementation of the unique characteristics and naming of each instrument at every station, and the unique coupling of the instrument, denoted to a SensorGroup, to every parameter measured at the station. Six different types of tests and corrections exist:

R-test: This range test of parameter values is often connected to the climate at the different sites.

J-test: Jump test (this is a temporal test comparing the values of a parameter at one recorded measurement and the previous recorded measurement (usually connected to climate and season of the year).

L-test: Consistency test connected to the parameters of one single SensorGroup. An example is testing the logical consistency of four hourly values of air temperature, TM (average temperature), TN (minimum temperature), TX (maximum temperature), and TT (temperature measured in the last minute of the hour).

LT-test: Consistency test connected to the parameters of two different SensorGroups. An example is comparing leaf wetness duration, BT, and precipitation, RR. Two different sensors are used. When it is raining, the sensor for measuring leaf wetness shall indicate leaf wetness.

CI-correction: This is an automated test of the parameters of one SensorGroup, followed by an automated correction, specific for the unique SensorGroupType in question. An example is correcting different types of gauge for measuring precipitation, using different physical principles. The sensors, using the tipping bucket system, are existing functions only in the warm season with no snow or other types of hydrometeors precipitating from the clouds. These instruments normally need no corrections. At several sites the GEONOR instrument, using the principle of weigthing the snow or rain that is falling, is used. This instrument is functioning at all seasons, but the outcome will also have spurious small positive and negative values that ought to be corrected.

CTI-correction: This is an automated test of the parameters of two different SensorGroups, where the result from one group indicates the relevance of the results from the other. An example is: If the temperature of the air is below 0 degrees Celsius, this indicates that the parameter value of precipitation from the tipping bucket-systems are not correct.

The actual R, J, L, and LT tests are not very different from the tests used at other Nordic institutions in charge of running networks of meteorological stations (*Vejen et al.*, 2002). The main difference is that in the system described above, a test is defined as a test of the functioning of a SensorGroup, using values of the parameters connected to the SensorGroup as input. The knowledge of type of instrument also makes it easy to validate the results of the tests. The construction also makes it possible to implement the corrections named CI and CTI relatively easy.

3. Reflections on actor-network theory

The information system for administration of meteorological data, discussed in this paper was developed according to traditional (mainly object-oriented) methodologies (*Brown,* 1997). The whole concept is confined to the responsibility of the institute and the possible use of meteorological and biological models and data on the field of plant protection in the commercial agriculture of Norway.

Information technology provides an arena for network building in the global sense. The cooperation in such networks is essential for innovation. According to actor-network theory, the society consists of networks of heteorogeneous actors, both human and non-human. "Agents, texts, devices, architectures are all generated in forming part of, and are essential to, the network of the social" (*Law,* 1992).

In the Wikipedia one can read: "Actor-network theory is useful in exploration of why technologies, scientific theories, and/or social endeavours succeed or fail as the direct result of changes in their network integrity, in such an analysis the technologies or theory is positioned as token."

The network of agrometeorological stations considered and the data produced by using the measurements are fully financed by the Norwegian Ministry of Agriculture and Food. The Norwegian Institute for Agricultural and Environmental Research may be considered one of the most important stakeholders of this system for managing and producing information beneficial for the Norwegian society. To a certain measure, stakeholders want to keep a network punctualized, where punctualization means that when a problem or issue is presented, the answer should be given inside the actual frame of the question. If the system is de-punctualized, the result may end in conflicts because stakeholders are loosing control. But a stakeholder do not have to define himself as a controlling agency. He merely may try to keep order in his relations in the processes of bringing up the problems and solving the problems, also through mobilisation of allies. But never the less it is in fact very difficult in the long run to act with integrity for any stakeholder. Integrity can not be retained without compassionate understanding of all the different relations.

4. Future challenges on integration of meteorological and biological data

When designing a system for administration of meteorological and biological data in the future, the requirements ought to be evaluated and presented by the Norwegian Institute for Agricultural and Environmental Research. The challenges seems to be the ability of creating a flexible and extendable system for administrating the data, containing the possibility of integrating, and utilizing data from different sources. In order to assure effective retrieval of data, cooperation with other organizations nationally and on the international level have to be organized. The processes/tasks of exchange of data from different sources as well as exchange of applications have to be organized through cooperation. The scientific and practical scope of the system may be discussed, also by allowing conceptual discussions.

Also the Norwegian Institute for Agricultural and Environmental Research may organize its own controlling system of data and document, the quality of the data produced by this organization, and the institute may make demands on the quality of the data produced by other organizations to define the usefulness of data from any source.

The exchange of meteorological data is formalized and may be further formalized through defining and using standardized schemes for exchange (*Sivertsen,* 2005e).

5. Conclusions

A documenting system of instruments may be used as a very effective feed back to the part of the organization in charge of the technical maintenance of the instrumentation.

Furthermore, meteorological data from agrometeorological networks of stations is used in many different meteorological and biological models. The models are often used for practical decisions, and they normally need correct and complete time series of data. Documenting the data is then a tool for deciding the scope of the use of the data. So, the first step is to construct a system telling the status of the data in the database. The next step is to construct relevant sets of data for each model when specific data from the systems for making measurement is lacking. The system described in this paper is mainly a presentation of how incorrect or questionable data may be indicated. A few additional corrections specific for certain types of instruments may be relatively easily implemented by using the system.

The further steps of constructing complete time series when data is lacking may be organized in two somewhat different ways. One way of doing this is that the people in charge of running a model is asking the people in charge of producing the data to deliver them complete time series of data. Another way of constructing complete time series is that the model-people themselves make the corrections of the input data. The second way is often the most practical one, and probably the input part of each model ought to contain a module containing corrections of the input data (or alternative data is used when data is lacking).

The responsibility of the agrometeorological service of the Norwegian Institute for Agricultural and Environmental Research is to manage a network of agrometeorological stations as well as gathering, storing, controlling, and using data from the stations and from other sources to be used in applications for plant protection and research purposes. Important future challenges are connected to the integration and use of data from different sources in an intelligent and optimal manner.

References

Brown, D., 1997: *An Introduction to Object/Oriented Analysis.* John Wiley & Sons Inc., 700 pp.

Latour, B., 2005: *Resembling the Social. An introduction to Actor-Network Theory.* Oxford University Press Inc., New York.

Law, J., 1992: Notes on the theory of the actor-network: Ordering, strategy and heterogeneity. In *Systemic Practice and Action Research.* Springer, Netherlands, 379-393.

Mestre, A., 2006: Meteorological Information as input in agrometeorological models; analysis of the potential use of data from numerical weather models in agrometeorology. In COST ACTION 718 *Meteorological Applications for Agriculture* (eds.: *G. Maracchi, A. Mestre, L. Toulios, L. Kajfez-Bogataj*, and *A.A. Hocevar*). COST OFFICE, 2006.

Sivertsen, T.H., 2004: Invitation to Conceptual Discussions Concerning the Scope of the Scientific Method and Classification Systems of Meteorological Phenomena and Meteorological Parameters, Selected Papers of the International Conference "Fluxes and Structures in Fluids". St. Petersburg, Russia, June 23-26, 2003. Moscow. IPM RAS. 2004, 6 p.

Sivertsen, T.H., 2005a: Discussing the scientific method and a documentation systems of meteorological and biological parameters, Physics and Chemistry of the Earth Special Issue: *Agrometeorology*, 2003, *30* (1-3), 35-43.

Sivertsen, T.H., 2005b: Implementation of a General Documentation System for web-based administration and use of historical series of meteorological and biological data, Physics and Chemistry of the Earth Special Issue: *Agrometeorology*, 2003, *30* (1-3), 217-222.

Sivertsen, T.H., 2005c: Discussing scientific methods and the quality of meteorological data. In *Use and Availability of Meteorological Information from Different Sources as Input in Agrometeorological Models.* COST ACTIONS 718, *Meteorological Applications for Agriculture* (eds.: *G. Maracchi, A. Mestre, L. Toulios,* and *B. Gozzin).*

Sivertsen, T.H., 2005d: The Concept of Leaf Wetness used in Agro Meteorology. In *Leaf Wetness Duration: Analysis of the Agrometeorological requirements and Evaluation of New Estimation Methods.* COST ACTIONS 718 *Meteorological Applications for Agriculture* (eds.: *G. Maracchi, L. Kajfez Bogataj, S. Orlandini, A. Dalla Marta,* and *F. Rossi*).

Sivertsen, T.H., 2005e: *Reflections on the Theme of Classifying.* Documenting and Exchanging Meteorological Data. *Atmospheric Science Letters.* John Wiley & Sons.

Sivertsen, T.H., 2006: Quality considerations on meteorological parameters to be used for modelling UV-radiation. Proceedings from the session *Remote Sensing of Clouds and the Atmosphere.* Arranged by The International Society for Optical Engineering (SPIE), Stockholm, September 2006.

Sivertsen, T.H. and *Gailis, J.*, 2002: Weather data project containing: Complete list of documents, attachments and references in the documentation. The vision and requirements of the project. System architecture document. Glossary and Diary for the documentation. Internal Report of The Plant Protection Centre of The Norwegian Crop Research Institute (in Norwegian).

Vejen, F., Jacobsson, C., Fredrikson, U., Moe, M., Andersen, L., Hellsten, E., Rissanen, P., Pálsdottir, T., and *Arason, T.*, 2002: Quality Control of Meteorological Observations. Automatic Methods used in the Nordic Countries. *Report 8,* 2002, The Norwegian Meteorological Institute.

IDŐJÁRÁS

Quarterly Journal of the Hungarian Meteorological Service
Vol. 111, No. 2–3, April–September 2007, pp. 91–99

Use of crop development models in agroclimatic mapping

Arne Oddvar Skjelvåg[1*], Ole Einar Tveito[2] and Inge Bjørdal[3]

[1]*Department of Plant and Environmental Sciences, Norwegian University of Life Sciences, P.O. Box 5003, N-1432 Ås, Norway; E-mail: arne.skjelvag@umb.no*

[2]*Norwegian Meteorological Institute, P.O. Box 43 Blindern, N-0313 Oslo, Norway; E-mail: ole.einar.tveito@met.no*

[3]*The Norwegian Forest and Landscape Institute, P.O. Box 115, N-1430 Ås, Norway; E-mail: inge.bjordal@skogoglandskap.no*

(Manuscript received in final form January 31, 2007)

Abstract—An example is given from a pilot project on a coherent application of soil and weather data to produce crop security estimates of barley. GIS was used to interpolate daily weather elements from a network of weather stations to individually mapped soil type units, on average less than 1 ha, of arable land. Other model tools are: a soil moisture model to estimate soil drying from the day of snow thaw until sowing date, temperature sum functions to estimate daily advance in phenological development to emergence, heading, and yellow ripeness, and thereafter, a grain moisture model for logging of combine harvesting days, taking also daily precipitation into account. The outcome is probability estimates of getting at least a given number of combining options within a given calendar day.

Key-words: weather, interpolation, soil types, phenology, barley, crop security

1. Introduction

Agroclimatic mapping has mostly defined and classified agroclimatic zones that differ in climatic conditions for crop production (*Mischenko,* 1984). Simple temperature indices have often been used as the sole parameter to characterize climatic conditions for agriculture in general, or for specific crops or cropping systems (*Samnordisk planteforedling,* 1992). However, a modern approach should be such designed that it is agronomically meaningful, which implies the use of more weather elements and terms such as yield level and crop security.

* Corresponding author

Hutchinson et al. (1992) have briefly reviewed the development of zonation for large area mapping purposes as related to plant growth for all the time since Köppen's attempt by use of monthly temperature and precipitation records until the recent use of simple crop growth models (*Köppen*, 1900). An early Nordic example on use of a crop growth model is the geographical distribution of first cut hay yield estimates in Sweden (*Angus et al.*, 1980).

Soil and climatic data have been combined with crop growth models for estimation of production potential on a large scale (e.g., *Netherlands Scientific Council*, 1992). During recent decades there has been a great development in geographical information systems (GIS), and new options have appeared in coherent application of both soil and weather data. Soil inventory data are now easily available on electronic media, at least for parts of the arable land. Weather records have got a much more adaptable application through new interpolation techniques that allow for making weather estimates to any location surrounded by more or less distant weather stations (*Tveito* and *Førland,* 1999; *Tveito* and *Schöner,* 2002). Soil and weather make up the natural resource base for crop production. Thus, by using such data in crop growth and development models, a detailed map of crop performance may be produced. The objective of this work has been to demonstrate the feasibility of such an approach reported in detail by *Aune et al.* (2004).

2. *Materials and methods*

The procedure followed in the present project, located in two Norwegian municipalities, Inderøy and Steinkjer, at about 64°N 11.5°E, is as follows: The cultivated land, altogether ca. 21 kha, was mapped into homogeneous soil type area units according to *FAO* (1998). There was a wide range of soil types from coarse sand to clays and organic soils, as indicated in *Fig. 1* by soil moisture capacity of the top soil. Each of these approximately 31,000 units in the entire study area (*Fig. 2*) was defined by midpoint geographical coordinates and altitude, using a digital terrain model.

Daily weather records for the years 1991 to 2000 were interpolated to each individual soil type area unit according to *Tveito et al.* (2005). Thus, temperature was spatially interpolated by residual kriging after application of covariables as terrain, longitude, and latitude. Wind speed, air humidity, and snow depth were dealt with by inverse distance weighting. Precipitation was interpolated by triangulation with terrain adjustment. After interpolation daily potential evapotranspiration was calculated for each unit by the Penman II method (*Shaw*, 1983). A network of 98 Norwegian weather stations located from 62.5 to 66°N, were applied as basis for the interpolation of global radiation and the mentioned parameters. Most of the stations (77) only observe precipitation and snow cover.

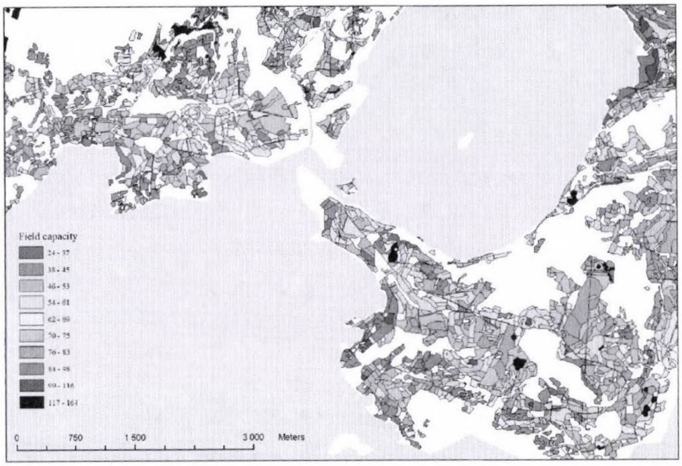

Fig. 1. Field capacity in mm of water of the 20 cm topsoil at soil type area units, on arable land northwest and southeast to the Straumen area of the Inderøy community.

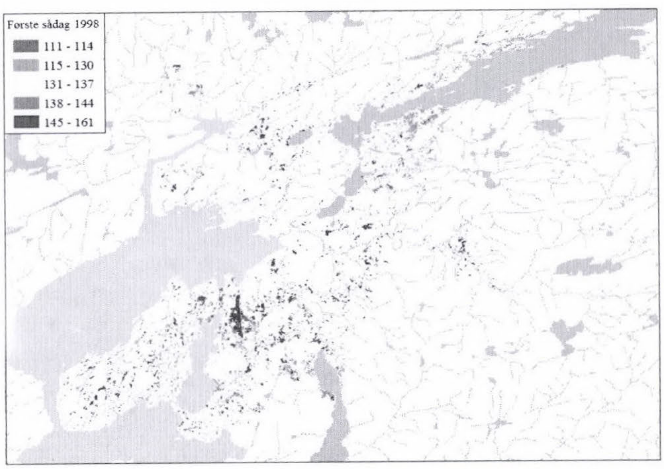

Fig. 2. First possible sowing date in 1998 on soil type area units covering all arable land in the Inderøy and Steinkjer communities. Day numbers of the year: 121 = May 1, 152 = June 1.

For each soil type area unit of the cultivated land, the first possible sowing date was determined on the basis of interpolated snow thaw time. Soil moisture at the first observed day of snowless ground was set to field capacity. Subsequently, estimates of top soil drying were made by the model of *Ritchie* (1972) until the required soil dryness for sowing day was met (*Skjelvåg,* 1986).

The daily advance in phenological development, (dP_i), was calculated by the formula

$$dP_i = (t_i - t_b) / ts_j, \qquad j = 1,2,3, \tag{1}$$

where t_i is the diurnal mean temperature, t_b is the base temperature, ts_j is the temperature sum, i is the number of days, and j is the number of phases. The formula is used with parameter values from the paper of *Bleken* (2001) when $t_i \geq t_b$, from sowing to emergence, further to heading, and in the third phase to yellow ripeness (40% grain moisture content) of 'Bamse' barley. Base temperatures were −1.57, −3.17, and 4.89 °C, and temperature sums were: 139, 685, and 383 °C of the three phases, respectively.

From yellow ripeness on, the daily calculations of grain moisture content was conducted by the model of *Stewart* and *Lievers* (1978), with coefficients and constants adjusted to 'Bamse' barley under Norwegian conditions (*Govasmark,* 2000). The driving variables are the potential evapotranspiration and precipitation.

Conditions for combine harvesting were evaluated daily from yellow ripeness until the end of the month of October for every individual soil type area unit. The requirement for being logged as a possible day for combining was an estimated grain moisture content less than or equal to a specified level starting at 20% on August 1, gradually increasing to 43% on October 1. Later it was increased to 45% on October 15 and kept at that level to the end of the month (*Aune et al.,* 2004). Furthermore, the recorded daily precipitation should be less than or equal to 2 mm.

The final result can be presented in various frequency statistics of number of possible days for combine harvesting of barley within certain dates. By defining requirements for number of combine harvesting days within given calendar time, one may calculate the probabilities to meet the specified performance for successful cropping at individual soil type area units.

3. Results

In addition to the snow cover observation and drying of the soil, sowing date is much determined by the soil moisture capacity of each soil type area unit. Within a small geographical area, the amount of soil moisture to be evaporated before sowing may vary considerably (*Fig. 1*). In this detailed segment there is a variation in field capacity of the 20 cm topsoil from about 25 mm of water to the sixfold of that.

As an example from the year 1998, three large and time spaced rainfalls interrupted soil drying and spring work. The combination of this with time of snow thaw and soil moisture capacity created a variation in the first possible sowing day of about seven weeks from the April 24 to June 10 (*Fig. 2*). In this marginal area of grain production, the latter is considered close to the last possible sowing day of an early barley cultivar to reach maturity in an average growing season.

In the other end of the growing season, number of days suitable for combine harvesting of the barley crop varied considerably. Within the end of September and on average of ten years, the range of threshing options varied from a couple of days to more than two weeks (*Fig. 3*).

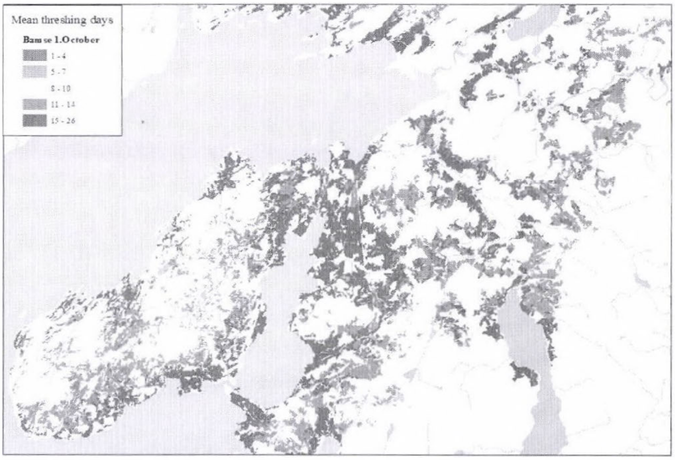

Fig. 3. Mean number of days with combine harvesting options within October 1 during the years 1991–2000 for 'Bamse' barley, at soil type area units in the Inderøy community and partly that of Steinkjer.

As may be seen from *Fig. 3*, much of the variation in number of calculated combining days is related to the distance from the sea. This is confirmed by *Fig. 4*, which shows a declining barley crop security with altitude. Up to 50 m a.s.l. on most of the soil type area units, one could expect six or seven years out of ten with at least five days with combining conditions within mid September. Very few area units came to eight, nine, and even ten years out of ten, whilst more units, though relatively few, reached only five, four, and three years. A large part of the arable land in the two communities is situated between 50 and 100 m a.s.l. (*Fig. 4*). In this altitudinal interval the distribution of soil type area units with varying crop security had a lower kurtosis, i.e., less peakish, than in the interval closer to sea level. The majority of field units could meet the requirement in four, five, or six years out of ten. However, equal numbers of area units fell under the classes three or seven years, and area units towards both ends of the entire range from nil to ten years were found.

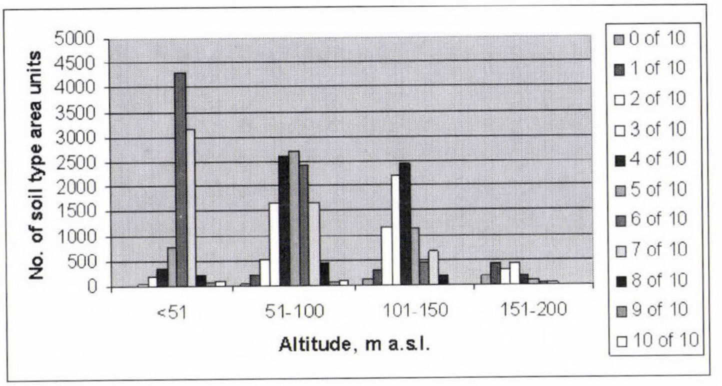

Fig. 4. Number of soil type area units with more than four combine harvesting options within September 15, in none to all years out of ten (1991–2000), in four altitudinal intervals.

In the interval 101 to 150 m a.s.l., the distribution of soil type area units was much similar to that of the interval below, but more than half of the number of field units fell into the categories in three and four years out of ten, and a clear majority in two to five. This shows the gradual decline in crop security with rising altitude. The picture is completed by proceeding to the higher elevation interval of 151–200 m a.s.l. In that height, most of the arable land could exhibit a probability that met the specified requirement in only one to three out of ten years.

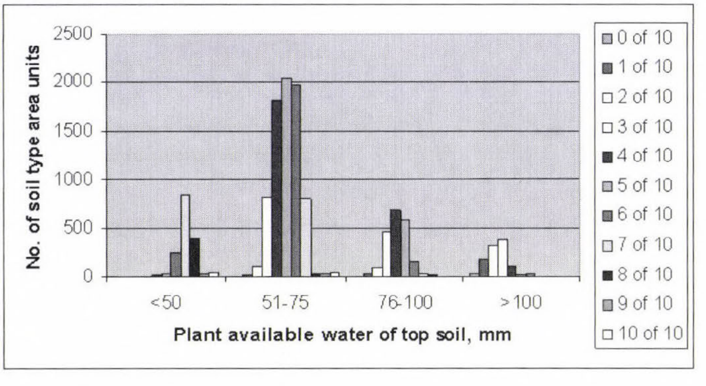

Fig. 5. Number of soil type area units in the altitude interval 51 to 100 m a.s.l., grouped according to intervals of topsoil moisture capacity, and their estimated classing with the requirement of more than 4 days suitable for combine harvesting within September 15, in none to all years during the period 1991–2000.

A certain part of the variation within altitude intervals in *Fig. 4* was due to differences in soil moisture capacity of the topsoil, and its implication for soil drying in spring. This is illustrated in *Fig. 2* with respect to sowing date. *Fig. 5* shows how an increasing soil moisture capacity of the topsoil was related to a declining ability to meet the requirement of at least five days of combine harvesting options within mid September. The median crop security classification of the four intervals of soil moisture capacity fell in class seven, five, four, and barely into three out of ten years, respectively.

4. Discussion

It is outside the scope of this short presentation to repeat a full discussion of methods, results, and possible applications as given by *Aune et al.* (2004) and *Tveito et al.* (2005). A coherent use of a series of disciplines creates many interfaces and needs for mutual adjustments, and only a few points may be emphasized. The approach depicts both the great annual variation in crop performance and also that originating from the interaction between soil type and weather.

Regional variation was included by use of the digital terrain model and the interpolation of weather elements. GIS has facilitated the use of all weather parameters and not only the simplest one, the temperature. However, the interpolation procedures have not yet included local effects of aspect, cold air drains, vicinity to open water, etc. The results are, therefore, more valid for somewhat larger areas than the individual soil type area units, and averages over larger areas, for instance altitude intervals, can easily be computed. Also on the agronomic side there are challenges. The sowing day estimates still lack a record of soil frost. Soil moisture capacity was calculated according to *Riley* (1996) on the basis of soil texture and content of organic matter. The functions are considered to be less precise for soils with a high content of organic matter. Sowing day is in practice dependent also on machine capacity, and all sowing can not be made on the very first day. The use of the same relative moisture level required for sowing day dryness of all soil types, is probably not optimal. On organic soils sowing may take place even with frost in deeper soil layers. In a rainy spring, when approaching the deadline for successful sowing time, farmers are expected to sow on a wetter soil than else preferred. Most of the various meteorological and agronomic shortcomings may be remedied, either by incorporating additional submodels or by strictly defining the preconditions specified for the calculations.

The phenological functions are considered to be fairly correct, and the same may be said about the grain moisture model. The logging of days suitable for combine harvesting needs improvement. Firstly, precipitation less than or equal to 2 mm is now recorded as a 24 h rainfall. It is very decisive, whether the rain has fallen during the day or during the night. This may be improved by using more detailed rainfall records. Secondly, the requirement for grain moisture content at various times during the autumn is very differently evaluated by farmers. The required level of grain moisture should rather be strictly defined and given as a precondition for the calculations. However, for special use, the flexibility of the model tool easily opens for runs with various choices. Furthermore, inclusion of additional subroutines to remedy more of the mentioned shortcomings is fairly simple.

5. Conclusions

The combined use of GIS techniques with access to weather and soil data makes it possible to quantify the natural basis for crop production in agronomically meaningful terms. The key instruments to reach such a goal are models at a suitable resolution level of soil moisture conditions and crop growth and development. As field crop production is continuously subjected to the vagaries of weather, probabilities for crop failure or success are useful characteristics of conditions for plant production. The basis for the present probability estimates has been: (1) a wide range in soil conditions over numerous area sites within a geographically small area, (2) site specific interpolated weather estimates, and (3) the above mentioned model tools. Probability estimates of this or similar types may find applications in public administration, advisory service in agriculture and management of natural resources, and in research and development.

References

Angus, J.F., Kornher, A., and *Torssell, B.W.R.,* 1980: A systems approach to Estimation of Swedish ley production. *Progress report* 1979/80. *Report 85.* Department of Plant Husbandry, Swedish University of Agricultural Sciences, 29 pp.

Aune, B., Aurbakken, E.A., Bjørdal, I., Tveito, O.E., and *Skjelvåg, A.O.,* 2004: *Project Soil Resource Map.* Combined use of soil, climate, and plant data for quantification of production potential. Report from a working group established by NIJOS (in Norwegian). Norwegian Institute of Land Inventory. *Report No. 16/2004,* 51 pp.

Bleken, M.A., 2001: KONOR. A model for simulation of cereal growth. Documentation. Agricultural University of Norway, *Report* No. 2/220, 33 pp.

FAO, 1998: World Reference Base for Soil Resources. *World Soil Resources Reports 84.* FAO, ISRIC og ISSS, Rome, 88 pp.

Govasmark, E., 2000: Modeling of grain moisture content in barley after yellow ripeness (in Norwegian). *MSc Thesis.* Agricultural University of Norway, Department of Horticulture and Crop Sciences, 80 pp.

Hutchinson, M.F., Nix, H.A., and *McMahon, J.P.,* 1992: Climate constraints on cropping Systems. In *Field Crop Systems* (ed.: *C.J. Pearson*), *Vol. 18 of Ecosystems of the World* (ed.: *D.W. Goodall*). Elsevier, Amsterdam, pp. 37-58

Köppen, W., 1900: Versuch einer Klassifikation der Klimate, vorzugsweise nach ihren Beziehungen zur Pflanzenwelt. *Geogr. Z. 6,* 593-611 and 657-679.

Mischenko, Z.A., 1984: Agroclimatic mapping of the continents. World Meteorological Organization. Agricultural Meteorology. *CAgM Report No 2,* 109 pp.

Netherlands Scientific Council for Government Policy, 1992: Ground for choices. Four perspectives for the rural areas in the European Community. *Reports to the Government 42,* 144 pp.

Riley, H., 1996: Estimation of physical properties of cultivated soils in southeast Norway from readily available soil information. *Norw. J. Agr. Sci. Supplement 2,* 51 pp.

Ritchie, J.T., 1972: Model for predicting evaporation from a row crop with incomplete cover. *Water Resour. Res. 8,* 1204-1213.

Samnordisk planteforedling, 1992: Agroclimatic mapping of Norden (in Norwegian). *Skrifter och rapporter nr 5,* 97 pp.

Shaw, E., 1983: *Hydrology in Practice*. Van Nostrand Reinhold, Wokingham, UK. 569 pp.

Skjelvåg, A.O., 1986: Estimation of the first sowing date from weather recors (in Norwegian). *Forskning og forsøk i landbruket 37,* 295-301.

Stewart, D.W. and *Lievers, K.W.*, 1978: A simulation model for the drying and rewetting processes of wheat. *Can. Agr. Eng. 20,* 53-59.

Tveito, O.E. and *Førland, E.*, 1999: Mapping temperatures in Norway applying terrain information, geostatistics and GIS. *Norsk geografisk Tidsskrift 53,* 202-212.

Tveito, O.E. and *Schöner, W.*, 2002: Application of spatial interpolation of climatological and meteorological elements by the use of geographical information systems (GIS). *Met. no Report 28/02 KLIMA*.

Tveito, O.E., *Bjørdal, I.*, *Skjelvåg, A.O.*, and *Aune, B.*, 2005: A GIS-based agro-ecological decision system based on gridded climatology. *Meteorol. Appl. 12,* 57-68.

IDŐJÁRÁS
Quarterly Journal of the Hungarian Meteorological Service
Vol. 111, No. 2–3, April–September 2007, pp. 101–108

A diffusive Boussinesq plume

Peder A. Tyvand

Department of Mathematical Sciences and Technology,
Norwegian University of Life Sciences,
P.O. Box 5003, 1432 Ås, Norway; E-mail: peder.tyvand@umb.no

(Manuscript received in final form January 31, 2007)

Abstract—An axisymmetric Boussinesq plume in a uniform ambient fluid is considered. The classical similarity solution of *Morton et al.* (1956) is modified to account for diffusive losses of buoyancy flux and momentum flux. This leads to a buoyancy flux and a momentum flux that both tend to zero at infinite height. The mass flux at infinity will tend to a finite value that depends on the diffusion parameters for buoyancy and momentum.

Key-words: buoyancy, Boussinesq, diffusion, heat source, plume

1. Introduction

Plumes are relatively slender vertical flows rising above concentrated buoyancy sources. Fire disasters produce strong buoyant plumes. Plumes are important in local meteorology, especially in connection with formation of cumulus clouds. Some basic mathematical solutions for plumes can be found when a singular heat source is taken as the driving mechanism. The most important of these is the celebrated similarity solution of *Morton et al.* (1956), hereafter called the MTT solution.

The MTT solution with the Boussinesq approximation is mathematically compact. It accounts for mass balance, and it preserves momentum and energy within the plume. However, its obvious shortcoming is that it possesses no physical length scale. Any similarity solution will assume that the plume rises to infinite height. According to a similarity solution, the plume velocity will ultimately tend to zero, but the upward mass flux will increase indefinitely. In spite of its mathematical convenience, a similarity solution lacks physical consistency in that it implies an indefinite amount of mass entrainment, up to infinite height. In reality, the entrainment of momentum from outside into the plume must vanish asymptotically at great heights, when the plume velocity slows down sufficiently. Opposing the entrainment, there will be diffusive losses of momentum and buoyancy, from the plume to the surrounding fluid. These diffusive losses introduce physical length scales in the vertical direction. A well-known example of such a length scale is the altitude of a cumulus cloud above the heated ground.

Convective flows in the atmosphere or ocean occur as recirculating convection cells. This means that a plume cannot be considered as an isolated phenomenon. All plumes in the atmosphere and ocean occur as parts of convection cells. This fact suggests another physical shortcoming of the MTT solution. It disregards the fact that a rising plume occupies only a narrow section of the convection cell that it belongs to. A narrow upwelling plume should therefore be surrounded by a broad and slow downwelling flow. However, in the course of this study it becomes clear that the present modifications of the MTT model are insufficient to construct a recirculating convection cell.

The MTT paper succeeded a seminal paper on plumes by *Batchelor* (1954), who also developed similarity solutions. After MTT a lot of papers have followed. To our knowledge, the physical validity of similarity solutions has not been addressed. A recent work by *Scase et al.* (2006) generalizes the axisymmetric MTT model in a fruitful way by starting from the basic hydrodynamic equations to take time-dependence into account.

2. The MTT model

We consider a rising axisymmetric plume in a fluid that would otherwise be at rest. The flow is generated by a singular heat source. The gravitational acceleration is denoted by g. The axisymmetric flow depends on the vertical coordinate z and the radial coordinate r. We define $z = 0$ by the concentrated heat source that drives the flow. We define the radial coordinate r as the horizontal distance from the vertical line through the heat source.

The classical MTT plume model assumes 'top-hat' profiles for the density $\rho(r,z)$

$$\begin{aligned} \rho(r,z) &= \rho(z), & r &\le b(z), \\ \rho(r,z) &= \rho_\infty, & r &> b(z), \end{aligned} \tag{1}$$

and the vertical velocity $w(r,z)$

$$\begin{aligned} w(r,z) &= w(z), & r &\le b(z), \\ w(r,z) &= 0, & r &> b(z). \end{aligned} \tag{2}$$

Here we have introduced the plume radius $b(z)$ and the density of the ambient fluid ρ_∞ We will consider only the simplest case, where ρ_∞ is taken constant so that the ambient fluid is assumed uniform. We take the Boussinesq approximation where density variation is included only in the buoyancy term of the momentum equation. The 'top-hat' description, Eqs. (1)–(2), assumes that the plume radius $b(z)$ can be sharply defined at each height z. Moreover, it replaces the density and velocity fields within the plume by their average values taken over the plume cross section at each given height z. In the MTT solution, the only communication with the fluid outside the plume is the entrainment of fluid by turbulent mixing into the plume. It is assumed that no loss of momentum or energy from the plume to the surrounding fluid will take place.

The entrainment constant α is introduced by the standard entrainment assumption

$$u_r\big|_{r=b(z)} = \alpha w, \tag{3}$$

where u_r is the inward radial velocity of the surrounding fluid at the boundary of the plume. This radial entrainment velocity u_r is thus assumed to be proportional to the vertical velocity in the plume at each vertical level z. In this theory, the radial velocity is significant only at the plume boundary. Once the entrained fluid has entered the plume, it is assumed to be thoroughly mixed so that the net average flow becomes vertical. In this averaging procedure one cannot include continuity in radial velocity across the plume boundary.

We introduce the mass flux πQ, the momentum flux πM, and the buoyancy flux πF for the steady plume. By definition we have

$$Q = b(z)^2 w(z)\rho(z), \tag{4}$$

$$M = b(z)^2 w(z)^2 \rho(z), \tag{5}$$

$$F = b(z)^2 w(z) g(\rho_\infty - \rho(z)). \tag{6}$$

This implies the relationships

$$w = M / Q,\ \ \rho = \rho_\infty g Q/(gQ+F),\ \ b = Q / \sqrt{M\rho},\ \ g' = g(\rho_\infty - \rho)/\rho = F / Q. \tag{7}$$

Here we have introduced the 'reduced gravity' g'. The conservation of mass, momentum, and energy in a steady plume is expressed by the equations

$$dQ / dz = 2\alpha\sqrt{\rho_\infty M}, \tag{8}$$

$$dM / dz = QF / M, \tag{9}$$

$$F = F_0 = constant, \tag{10}$$

respectively.

3. *Diffusive losses of buoyancy and momentum*

Since the buoyancy flux F_0 is constant in the MTT model described above, it parameterizes the singular hot spot in the origin. The energy equation is simply F = constant for a steady plume in homogeneous ambient fluid. Let us take into account a turbulent diffusive loss of energy by postulating the relationship

$$F(z) = F_0 \exp(-\gamma z), \tag{11}$$

where F_0 remains the buoyancy flux specified by the MTT solution, and a spatial decay parameter γ is introduced, assumed to be constant. With this modification, F_0 still parameterizes the hot spot in the origin. The energy equation that is implicitly assumed by the solution, Eq. (11) is

$$dF / dz = -\gamma F, \tag{12}$$

replacing the previous energy conservation equation dF/dz=0. The solution, Eq. (11) is a reasonable starting point, because it introduces a physical length scale $1/\gamma$. Since the MTT solution does not contain any length scale, γz immediately constitutes itself as a dimensionless vertical coordinate, which establishes a physical length scale.

A physically consistent description of a diffusive plume must also take into account a diffusive loss of momentum. We modify the momentum equation, Eq. (9) as follows

$$dM / dz = QF / M - \Gamma M, \tag{13}$$

where an additional spatial decay parameter Γ for momentum is introduced, assumed to be constant. Γ is introduced in analogy with the buoyancy decay parameter Γ introduced above. This is a simpler model of turbulent momentum loss than the averaged Navier-Stokes momentum equation with eddy viscosity. However, a Navier-Stokes equation cannot be formulated for the plume in the 'top-hat' description, since the relevant velocity gradients have already been eliminated by the averaging procedure.

We will now derive the plume solution following from the starting point of Eqs. (11) and (13). We still assume that mass is conserved within the plume, with the application of the entrainment hypothesis. We introduce dimensionless length, velocity, mass flux, momentum flux, and buoyancy flux, respectively, by the definitions

$$\hat{z} = \gamma z, \quad \hat{w} = w(\rho_\infty / (\gamma F_0))^{1/3}, \quad \hat{Q} = (\gamma^{5/3} Q)/(F_0^{1/3} \rho_\infty^{2/3}),$$
$$\hat{M} = (\gamma^{4/3} M)/(F_0^{2/3} \rho_\infty^{1/3}), \; \hat{F} = F / F_0.$$

From now on, we work with dimensionless quantities and drop the hat superscripts. From Eqs. (8) and (13) the governing equations are

$$dQ / dz = 2\alpha\sqrt{M}\,, \qquad dM / dz = QF / M - \beta M\,, \tag{14}$$

expressing conservation of mass and a diffusive loss of momentum. Here we have introduced a dimensionless parameter β defined as

$$\beta = \Gamma / \gamma\,, \tag{15}$$

which may be considered as a turbulent Prandtl number, expressing the relative rate of momentum diffusion compared with buoyancy diffusion. For strong turbulence (large Reynolds numbers), it is plausible that β will be of order unity.

The postulated loss of buoyancy flux is given by

$$F(z) = \exp(-z)\,. \tag{16}$$

In order to solve this set of governing equations we define

$$Q(z) = Q_S(z)\varphi(z)\,, \qquad M(z) = M_S(z)\mu(z)\,, \tag{17}$$

thereby introducing two unknown functions $\varphi(z)$ and $\mu(z)$ that represent the local relative deviations from the steady MTT solution. The MTT similarity solution is represented by $Q_S(z)$ and $M_S(z)$, given by

$$Q_S(z) = (6\alpha / 5)(9\alpha / 10)^{1/3} z^{5/3}\,, \;\; M_S(z) = (9\alpha / 10)^{2/3} z^{4/3}\,. \tag{18}$$

This is called a similarity solution since it assumes no other length scale than the vertical coordinate itself.

We will now compute the unknown functions $\varphi(z)$ and $\mu(z)$ in this diffusive plume problem. Their boundary conditions are simply

$$\varphi(0) = \mu(0) = 1\,, \tag{19}$$

since the solution coincides with the MTT solution near the source. The governing equations for $\varphi(z)$ and $\mu(z)$ are determined by inserting their definitions, Eq. (17) into Eq. (14). The resulting equations are

$$(3/5)z\varphi'(z) + \varphi(z) = \sqrt{\mu(z)}\,, \tag{20}$$

$$(3/4)z\mu'(z) + (1 + (3/4)\beta z)\mu(z) = \exp(-z)\varphi(z) / \mu(z)\,. \tag{21}$$

Eqs. (20) and (21) valid for all $z>0$ with the spatial 'initial' conditions, Eq. (19). It is worth noting that Eqs. (20)–(21) are independent of the entrainment constant α. The mathematical problem is thus a one-parameter problem in terms of the dimensionless momentum diffusion parameter β. The dependence of buoyancy diffusion is implicit through the definition of dimensionless variables.

This nonlinear system of two first-order Eqs. (20)–(21) will be solved numerically by MATHEMATICA. Because of the factor z accompanying the derivatives, we have to start the integration with a value of z slightly greater than 0. Some results are shown in *Fig. 1* and *2*. *Fig. 1* shows the functions $\varphi(z)$ and $\mu(z)$. *Fig. 2* gives the mass flux $Q(z)$ (upper graphs) and the momentum flux $M(z)$ (lower graphs). The case $\beta=1$ is represented by solid curves. The dotted curves represent $\beta=1/3$, while the dashed curves represent $\beta=1/3$. Since β is a kind of turbulent Prandt number, it should be of order unity.

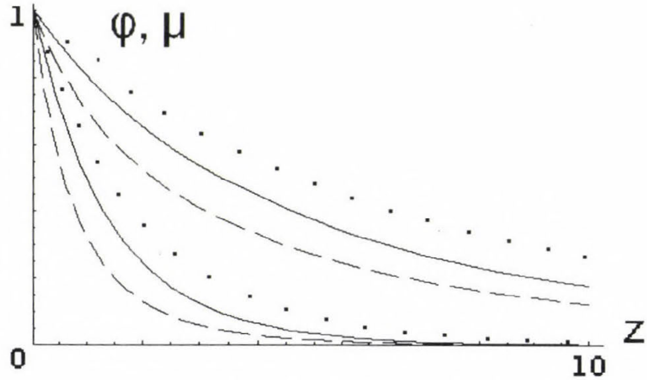

Fig. 1. The functions $\varphi(z)$ (upper curves) and $\mu(z)$ (lower curves). These functions are displayed for $\beta=1/3$ (dotted curves), $\beta=1$ (solid curves), and $\beta=3$ (dashed curves).

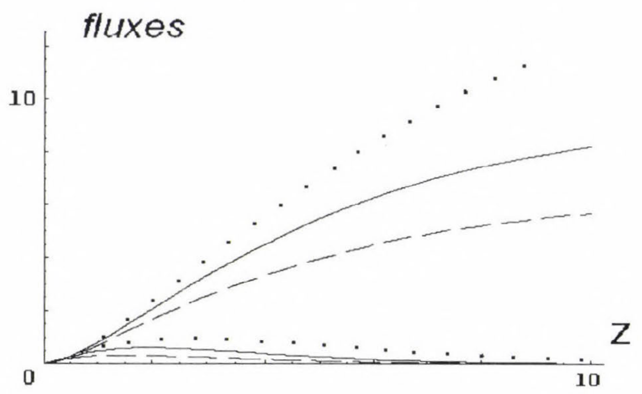

Fig. 2. The upper set of curves represent mass flux $(5/(6\ \alpha))(10/(9\ \alpha))^{1/3}Q(z)$. The lower set of curves represent momentum flux $(10/(9\ \alpha))^{2/3}M(z)$. The functions are displayed for $\beta=1/3$ (dotted curves), $\beta=1$ (solid curves), and $\beta=3$ (dashed curves).

From *Fig. 2* we see that the momentum flux $M(z)$ has a maximum value for a certain value of z, depending on β. On the other hand, there is no maximum value for the mass flux $Q(z)$. Further computations show that it increases with increasing z, and it reaches a constant asymptotic value, dependent on β when $z \to \infty$. In *Table 1* we show $Q(\infty)$ for various values of β, together with the maximal values for $M(z)$. There may be a certain amount of roundoff errors in this system where boundary conditions are specified only at $z=0$, and the numerical integrations for determining $Q(\infty)$ in *Table 1* have all been terminated at $z=50$. The present coupled system of first-order equations seems to defy analytical treatment, since the variables are not separable. *Table 1* shows that $z>1$ at the point of maximum momentum flux, even when the momentum diffusion is relatively strong. This is because the diffusive loss of momentum is compensated by the buoyancy source up to unit height above the heat source.

Table 1. The mass flux at infinite height and the maximum point for the momentum flux for various values of the dimensionless momentum diffusion parameter β

β	$(5/(6\alpha))(10/(9\alpha))^{1/3}Q(\infty)$	$(10/(9\alpha))^{2/3}M_{max}$	z at $M=M_{max}$
0.2	25.02	1.1237	3.141
0.5	12.77	0.8352	2.386
1	9.39	0.6188	1.926
2	7.34	0.4322	1.608
5	5.42	0.2523	1.356

The dimensionless expressions for the plume velocity and plume radius are

$$w(z) = (5/(6\alpha))(9\alpha/(10z))^{1/3}\,\mu(z)/\varphi(z), \tag{22}$$

$$b(z) = (6\alpha z/5)\varphi(z)/\sqrt{\mu(z)}. \tag{23}$$

In *Fig. 3* we show the radius of the plume as a function of the height, represented by $(5/(6\,\alpha))\,b(z)$, for some values of β. For comparison, the MTT solution is represented by an exact cone that gives the common tangent for these three curves at the apex in the origin.

Contrary to the motivation for this work, it proves impossible to construct an outer solution that gives a closed convection cell, since the mass flux does not tend to zero as $z \to \infty$. There is no balance between sources and sinks in the outer field, so the streamlines will not be closed curves.

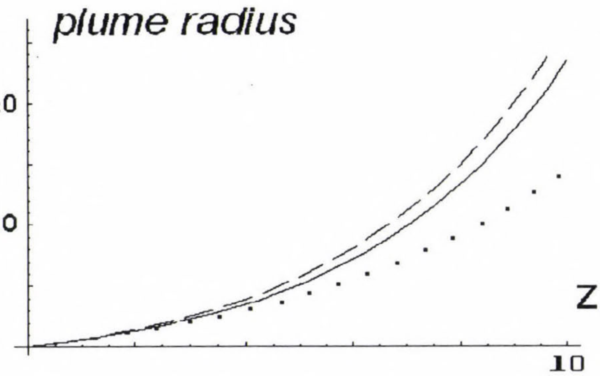

Fig. 3. The plume radius as a function of height represented by $(5/(6\ \alpha))b(z)$. It is displayed for $\beta=1/3$ (dotted curve), $\beta=1$ (solid curve), and $\beta=3$ (dashed curve).

4. Conclusions

An aim of the present work was to model consistently the inner and outer flow field of a plume. In order to achieve this, we included diffusive losses of momentum flux and buoyancy flux from the plume to the ambient fluid, which is assumed of constant density. In order to model the outer flow, it is necessary that the mass flux of the plume ultimately tends to zero with increasing height. The present work shows that this is impossible when the density of the ambient fluid is assumed to be constant. The mass flux in the plume will not tend to zero with increasing height, but it will settle at a constant value. Therefore, no recirculating convection cell can be described by the present type of modeling.

Any model of plume flow in a fluid must be irreversible in time. In the classical MTT solution, the only entropy producing mechanism is the mass entrainment into the plume. As a contrast, the present model takes into account three irreversible phenomena: (i) Turbulent entrainment from the ambient fluid, incorporated into the mass balance. (ii) Turbulent diffusive loss of momentum flux to the ambient fluid. (iii) Turbulent diffusive loss of buoyancy flux to the ambient fluid. While these three phenomena are still being modelled in a highly simplified way, their descriptions in the present work are mutually consistent.

References

Batchelor, G.K., 1954: Heat convection and buoyancy effects in fluids. *Q. J. Roy. Meteor. Soc. 80*, 339-358.

Morton, B.R., *Taylor, G.I.*, and *Turner, J.S.*, 1956: Turbulent gravitational convection from maintained and instantaneous sources. *Proc. Roy. Soc. London A 234*, 1-32. (Herein referred to as MTT.)

Scase, M.M., *Caulfield, C.P.*, and *Dalziel, S.B.*, 2006: Boussinesq plumes and jets with decreasing source strengths in stratified environments. *J. Fluid Mech. 563*, 463-472.

IDŐJÁRÁS

Quarterly Journal of the Hungarian Meteorological Service
Vol. 111, No. 2–3, April–September 2007, pp. 109–122

Curved free convection plume paths in porous media

Oliver J. Brambles and **D. Andrew S. Rees**

Department of Mechanical Engineering, University of Bath, Claverton Down, Bath, BA2 7AY, U.K.; E-mail: D.A.S.Rees@bath.ac.uk

(Manuscript received in final form January 31, 2007)

Abstract—This short paper presents some numerical simulations of how free convection plumes in a porous medium are affected by the presence of a neighboring boundary or a neighboring plume. It is found that they are drawn towards a vertical boundary with the 'centreline' following a curved path from the source to the boundary. Thus the boundary entrains the plume in a manner which is reminiscent of the well-known Coandă effect in aerodynamics where a fluid jet is drawn towards a solid surface. When two plumes are present in a horizontally unbounded porous medium, the plumes are drawn towards one another before rising vertically. In many cases where one plume is weaker or lower than the other, the former is affected greatly by the latter, but not vice versa.

Key-words: porous media, free convection, plume, entrainment

1. Introduction

Free convection plumes usually rise vertically. However, this is true only in certain circumstances, namely, when the flow domain is symmetric about a vertical line through the heat source. This situation was assumed by *Afzal* (1985), where a line source of heat was placed at the intersection of two plane surfaces bounding a wedge-shaped region of porous medium, but where the boundaries are at equal but opposite inclinations away from the vertical. *Afzal* (1985) provided a detailed high order boundary layer theory to determine the manner in which such boundaries affect the strength of the plume, thereby extending the analysis of *Wooding* (1963). A more general situation was considered by *Bassom et al.* (2000), where a porous wedge was allowed to have a centreline which is no longer vertical. In this case the centreline of the plume remains straight, at least according to boundary layer theory, but it no longer remains vertical. In general, the direction of the plume is somewhere between the vertical and the direction corresponding to the centreline of the wedge, and it is, therefore, a compromise between the effect of buoyancy (which induces vertical forces) and the need to entrain equal amounts of fluid from either side of the plume (which draws the plume towards the centreline of the wedge). *Bassom et al.* (2000) used boundary layer theory and presented an analytical expression for the direction taken by the plume in the terms of the inclinations of the bounding surfaces. Similar situations arise for anisotropic porous media (*Rees et al.*, 2002) and for clear fluids (*Rees* and *Storesletten*, 2002; *Kurdyumov*, 2006).

In the context of groundwater studies the presence of groundwater flow, together with other effects, such as heterogeneities and variable saturation, also serve to modify the path taken by contaminant plume in porous medium; see *Harter* and *Yeh* (1996a, b) for example. It is also a matter of common experience that a crosswind will modify the direction of chimney plumes. Deviations from straight path were also found by *Shaw* (1985) when considering plume flow in a cavity with an inlet and outlet at different horizontal locations.

In the present paper we consider (i) how a plume path is modified by presence of an adjacent insulated vertical surface and (ii) the merging of two plumes. This is a purely numerical study of the fully elliptic equations of motion, and it is, therefore, not a boundary layer study. Indeed, we regard this as an exploratory investigation into the behaviour which may be displayed by free convection plumes in porous media, and we intend to follow this work by a more detailed quantitative study in the near future.

As we have used a time-dependent solver to determine the eventual steady state solutions, we conclude that such plume flows are stable, at least to two-dimensional perturbations. We find that, when a localized heat source is placed away from a vertical surface, the plume curves towards the surface, and the point of attachment changes its location as the Rayleigh number varies. We also consider the interaction of two plumes, a situation which has been reviewed by *Gebhart* (1979) for plumes in clear fluids.

2. *Equations of motion and numerical scheme*

The equations governing two-dimensional convection in a porous medium are,

$$\frac{\partial \bar{u}}{\partial \bar{x}} + \frac{\partial \bar{v}}{\partial \bar{y}} = 0, \tag{1}$$

$$\bar{u} = -\frac{K}{\mu}\frac{\partial \bar{p}}{\partial \bar{x}}, \tag{2}$$

$$\bar{v} = -\frac{K}{\mu}\left[\frac{\partial \bar{p}}{\partial \bar{y}} - \rho g \beta (T - T_0)\right], \tag{3}$$

$$\sigma\frac{\partial T}{\partial \bar{t}}+\bar{u}\frac{\partial T}{\partial \bar{x}}+\bar{v}\frac{\partial T}{\partial \bar{y}}=\frac{k}{\rho C}\left(\frac{\partial^2 T}{\partial \bar{x}^2}+\frac{\partial^2 T}{\partial \bar{y}^2}\right)+\frac{q'''}{\rho C}, \tag{4}$$

where Darcy's law has been assumed to be valid for the momentum equation and the Boussinesq approximation holds. Here $\bar{x}$ and $\bar{y}$ are the horizontal and vertical coordinates, respectively, and the corresponding flux velocities are $\bar{u}$ and $\bar{v}$. In addition, $\bar{p}$ is the pressure and T is the temperature. Heat generation takes place within the porous medium with the rate q''', which represents a local source centreed at the horizontal distance L, from an insulated vertical surface. The other quantities, namely K, μ, ρ, g, β, k, C, and σ, take their usual meanings: permeability, dynamic viscosity, reference fluid density, gravity, coefficient of thermal expansion, thermal conductivity of the porous medium, specific heat of the fluid, and the ratio of thermal capacities of the porous medium and the fluid. Finally, T_0 is the ambient temperature of the porous medium.

Nondimensionalization takes place using the following transformations

$$(\bar{x},\bar{y})=L(x,y),\quad (\bar{u},\bar{v})=\frac{k}{L(\rho C)}(u,v),\quad \bar{p}=\frac{k\mu}{(\rho C)K}p,\quad T=T_0+\frac{QL^2}{k}, \tag{5}$$

where

$$Q=L^{-2}\int_0^\infty\int_0^\infty q'''\,d\bar{x}\,d\bar{y}. \tag{6}$$

On introduction of the streamfunction ψ, using

$$u=-\frac{\partial\psi}{\partial y},\qquad v=\frac{\partial\psi}{\partial x}, \tag{7}$$

the governing equations become

$$\frac{\partial^2\psi}{\partial x^2}+\frac{\partial^2\psi}{\partial y^2}=\mathrm{Ra}\frac{\partial\theta}{\partial y}, \tag{8}$$

$$\frac{\partial\theta}{\partial t}=\frac{\partial^2\theta}{\partial x^2}+\frac{\partial^2\theta}{\partial y^2}-\frac{\partial\psi}{\partial y}\frac{\partial\theta}{\partial x}+\frac{\partial\psi}{\partial x}\frac{\partial\theta}{\partial y}+S(x,y), \tag{9}$$

where the Darcy-Rayleigh number is given by

$$\mathrm{Ra}=\frac{\rho_0(\rho C)g\beta KL^3Q}{k^2\mu}, \tag{10}$$

and where $S(x,y)$ is a local heat source centred at $(x,y) = (x_c, y_c)$ which, given that $S = q'''/Q$ must satisfy

$$\int_0^{\infty}\int_0^{\infty} S(x,y)\,dx\,dy = 1. \tag{11}$$

When the plume is situated on the horizontal bounding surface at y=0, we use

$$S = \frac{c}{2\pi} e^{-c((x-x_c)^2+y^2)}, \tag{12a}$$

but when it is well above this surface we use

$$S = \frac{c}{\pi} e^{-c((x-x_c)^2+(y-y_c)^2)}. \tag{12b}$$

We use the value c=2 here.

The statement of the problem is completed by the boundary conditions. For the case of a single plume, the flow is bounded by surfaces at $x = 0$ and $y = 0$ with the porous medium contained in the quarter plane, $x, y \geq 0$. Each surface is a streamline and both are assumed to be insulated. Therefore, we set

$$\psi = 0, \quad \frac{\partial \theta}{\partial n} = 0 \quad \text{on } x = 0 \text{ and } y = 0. \tag{13}$$

Inflow occurs at $x = x_{\max}$, and we set

$$\frac{\partial^2 \psi}{\partial x^2} = \theta = 0 \quad \text{on} \quad x = x_{\max}. \tag{14}$$

Outflow occurs at the upper surface, and the conditions used here are

$$\frac{\partial \psi}{\partial y} = \frac{\partial \theta}{\partial y} = 0 \quad \text{on } y = y_{\max}. \tag{15}$$

Outflow conditions are not as destructive for convective flows in porous media as they are for the flows of clear fluids. For the present problem it was found that the outflow conditions given by Eq. (15) cause small streamwise oscillations for only a few grid points upstream of the upper boundary which, given that the upper boundary is very far from where plume attachment takes place due to the use of a coordinate transformation, means that the results presented are essentially independent of the outflow conditions given by Eq. (15).

Eqs. (8) and (9) were solved using second order finite differences in space on a nonuniform grid and first order backward differences in time. The accuracy with respect to time is not of importance here since every simulation eventually yielded a steady state solution. The use of backward differences means that the system being solved is fully implicit and, therefore, we employed a Full Approximation Scheme multigrid methodology to the problem, where iterations on each grid were undertaken using the line Gauss-Seidel method. While this complicates the numerical coding, the fact that the method is implicit means that it is possible and indeed desirable to increase substantially the time steps towards the end of the calculation to enhance convergence to the steady state. Therefore, a crude timestep-changing methodology was employed. In many cases we determined steady state solutions on relatively coarse grids, interpolated these solutions onto finer grids and used this as an initial condition – this increased further the rapidity with which highly accurate solutions were obtained. The code used is a modified version of the one described in detail in *Rees* and *Bassom* (1993).

3. *Results*

The present paper is an exploratory work where, despite the complexity of the numerical code, we are solely interested in determining the qualitative nature of plume entrainment. Comments will be made later about planned improvements of the methodology.

In the numerical code we choose not to vary the value of the Rayleigh number from the chosen value of Ra = 200, rather we alter the location of the source. When the source is located at $x_c = d$, then the transformations

$$(x,y) = d(\hat{x},\hat{y}), \quad \psi = \hat{\psi}, \quad \theta = \hat{\theta}, \quad \mathrm{Ra} = \hat{\mathrm{Ra}}\, d, \quad S = \hat{S} d^{-2} \tag{16}$$

mean that Eqs. (8), (9), and (11) are reproduced precisely in the new variables with the source at $\hat{x} = 1$. Therefore, the setting of Ra = 200 and $x_c = d$ is equivalent to setting Ra = 200d and $x_c = 1$. The only difference between the two cases is the size of the spatial region over which the source is defined. The principle reason we followed this route rather than simply increasing the value of Ra is that solutions were obtained much more quickly.

Fig. 1 shows some typical streamlines and isotherms for cases where the source is centred on the axis. We have taken $x_c = 3$, 5, 7, and 9, and, therefore, the effective Rayleigh numbers are $\hat{\mathrm{Ra}}$ = 600, 1000, 1400, and 1800. The streamlines show clearly that fluid is entrained from the far right, turns near the corner, and travels upward in the expected manner. In addition there is a small region of weak recirculation which is bounded by a dividing streamline which may be regarded as 'centreline' of the plume from the point of view of fluid; this will be called the fluid centreline.

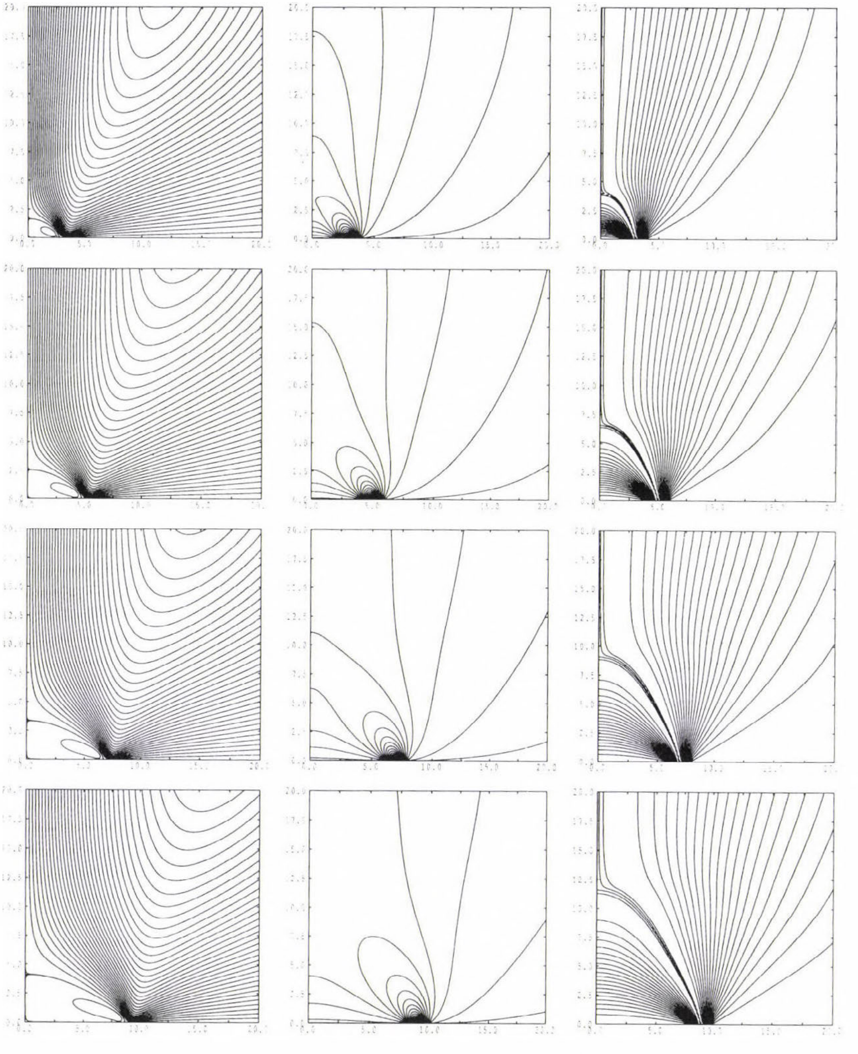

Fig. 1. Streamlines (left), isotherms (centre), and modified isotherms (right) for Ra = 200 with x_c=3, 5, 7, and 9 (from top to bottom) and y_c=0.

We have a situation where buoyancy forces cause the plume to rise, but the plume requires an equal amount of fluid to be entrained from each side for the plume to rise vertically. As the left side of the plume has only a finite amount of fluid (in terms of x) which may be entrained, the plume curves to the left to fulfil its need for fluid to entrain, and it attaches onto the vertical surface thereafter to rise as a wall plume (or, given the boundary conditions, as one half of a standard plume).

It is interesting to see that the point of attachment on the vertical surface (which should be labeled as y_c) is closer to the origin than is the horizontal distance of the source from the origin. *Table 1* shows that this attachment point gradually gets lower as Ra increases. Therefore, the need to entrain fluid appears to be a stronger effect than that due to buoyancy forces, which cause vertical motion.

Table 1. Attachment points for the plume; y_ψ and $\hat{y}_\psi$ correspond to where the dividing streamline joins onto the vertical surface, and y_θ and $\hat{y}_\theta$ to where thermal centreline joins

Râ	y_ψ	$\hat{y}_\psi$	y_θ	$\hat{y}_\theta$
600	1.60	0.53	2.43	0.81
1000	2.50	0.50	6.60	0.94
1400	3.35	0.48	9.10	1.30
1800	4.05	0.45	11.75	1.31

The second column of subfigures in *Fig. 1* shows the corresponding isotherms, but this is not particularly instructive, since the temperature of a free convection line plume in porous media decays roughly as $y^{-1/3}$ as y increases, and this masks the thermal behaviour of the plume that we wish to present. Therefore, the third column of subfigures has been prepared where the temperature at any point has been scaled with respect to the maximum temperature at that value of y. Thus, the contour plots show clearly where the maximum temperature is located and the path taken by this thermal centreline. *Table 1* gives the detailed values of where the thermal attachment point is as a function of Ra, and it is clear that this location (labeled as y_θ) increases slightly as Ra increases. However, we feel that further computation needs to be undertaken on this aspect as the position of the attachment point has not increased greatly between Ra = 1400 and Ra = 1800; it may be that this represents the large-Ra asymptotic limit, or it could presage a lowering of the attachment point following that of the dividing streamline. Further numerical work is needed to determine which of these scenarios is correct.

Fig. 2 shows how the plume reacts to changes in the location of its source, where $x_c = y_c$, or, equivalently, to changes in Ra. Here the source is above the horizontal surface and, therefore, fluid passes beneath the plume in order to feed the entrainment on the left side of the plume. It is important to note that the abscissa and ordinates of the subframes in *Fig. 2* have been scaled in such a way that each represents $0 \le \hat{x}, \hat{y} \le 4$. Given that computations were performed in terms of x and y with the source defined in Eq. (12), the increasing concentration of the isotherms around the source region as x_c increases is a direct consequence of the fact that the source has a diameter of roughly 1 in terms of x and y.

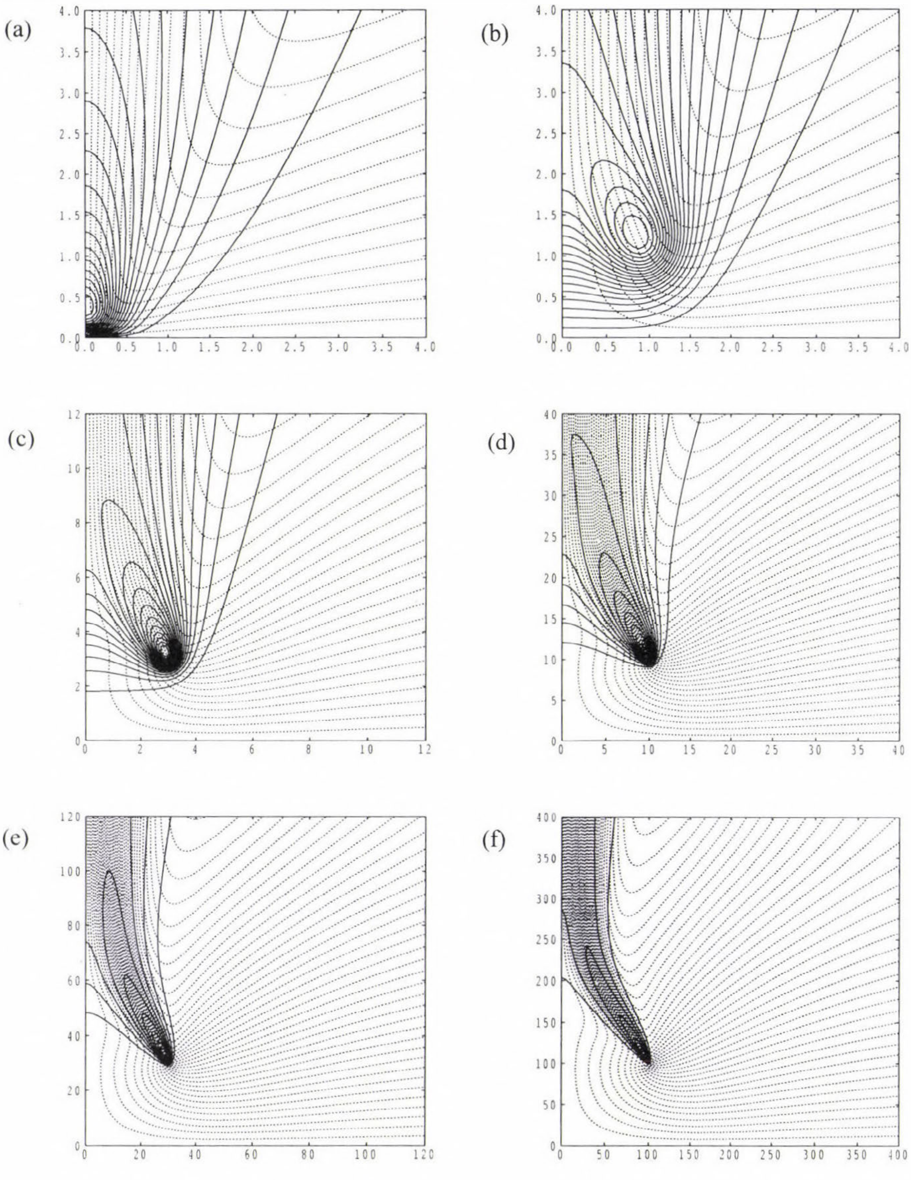

$$\begin{array}{ccc} & 0 & 1 \\ x_{\mathrm{source}} = & 3 & 10 \\ & 30 & 100 \end{array} \quad \Rightarrow \quad \begin{array}{ccc} & 100 & 100 \\ \mathrm{Ra} = & 900 & 10^4 \\ & 9 \times 10^4 & 10^6 \end{array}$$

Fig. 2. Streamlines (dashed) and isotherms (continuous) for Ra = 200 with $x_c = y_c$, where x_c takes the values (a) 0, (b) 1, (c) 3, (d) 10, (e) 30, and (f) 100.

The chief effect of raising the source above $y = 0$ is to delay the attachment of the plume onto the vertical surface. The concept of an attachment point in terms of the streamfunction now no longer exists since there is no recirculation, and the only places where $\psi = 0$ are the two bounding surfaces. However, the concept of thermal attachment still applies, and the presence of a strong upward flow past the plume source means that thermal attachment is delayed substantially. This is seen most clearly in *Fig. 2c* which corresponds to $\hat{\mathrm{Ra}} = 600$, which is the same as the case represented by the first row of *Table 1*. For the sake of comparison we shall define $\hat{y}_\theta$ to be based on the vertical distance between the attachment position and the location of the source: $\hat{y}_\theta = (y_\theta - y_c)/x_c$. As the maximum temperature at any value of y will correspond to that isotherm which has a turning point there, *Fig. 2c* shows clearly that y_θ is well above $y = 9$. Hence $\hat{y}_\theta$ is greater than 2, which is substantially further downstream than the value $\hat{y} = 0.81$ shown in *Table 1*. The attachment point in *Fig. 2d* is close to $\hat{y}_\theta = 3$, which is even greater.

Figs. 3, 4, and *5* show how two plumes interact, and each represents a different type of situation. The computational domain is now a half-plane. *Fig. 3* represents cases where two plumes have sources centred on $y_c = 0$, but where their horizontal locations are $x_c = \pm 4$; therefore, these correspond to cases where $\mathrm{Ra} = 800$ and $\hat{x}_c = \pm 1$. The strength of the right and left hand plumes are given by the expressions given in Eq. (12), but where the right and left hand sides are multiplied by S_r and S_l, respectively. We take $S_r = 1$ and vary S_l between 0 and 1.

Fig. 3a depicts an isolated plume for comparison, while *Fig. 3b* shows that the presence of a weak second source nearby has little effect on the overall flow field and isotherm pattern, except for close to the horizontal bounding surface. We see that the plume generated by the weaker source exists independently for only a small distance above the surface before being absorbed into the main plume. As S_l increases, the left hand plume becomes stronger, and it begins to deflect the main plume towards itself, until, when $S_l = 1$ we are left with a perfectly symmetrical flow pattern.

Fig. 4 represents the same situation as *Fig. 3* except that both sources are placed at $y_c = 4$. The scenario described for *Fig. 3* in the above paragraph also occurs here, apart from the fact that the increased upward flow due to the positioning of the sources allows the weaker plume to exist for longer before being captured by the stronger plume. In this regard the behaviour is similar to that represented by *Fig. 2*.

Finally, two plumes of equal strength, but whose source heights are different, are depicted in *Fig. 5*. In *Fig. 5a* the lower plume is affected very strongly by the flow induced by the upper plume, although the upper plume is hardly affected by the presence of the lower plume, at least in terms of the part it takes. Indeed it is only when the source of the lower plume is as large as $y_c = 0.5$, which is shown in *Fig. 5c*, that the thermal centreline of the combined plume changes from being close to $x = 4$. When $y_c = 0.75$ for the lower plume, the centreline of the combined plume is now very close to $x = 0$, and symmetry is obtained when $y_c = 1$.

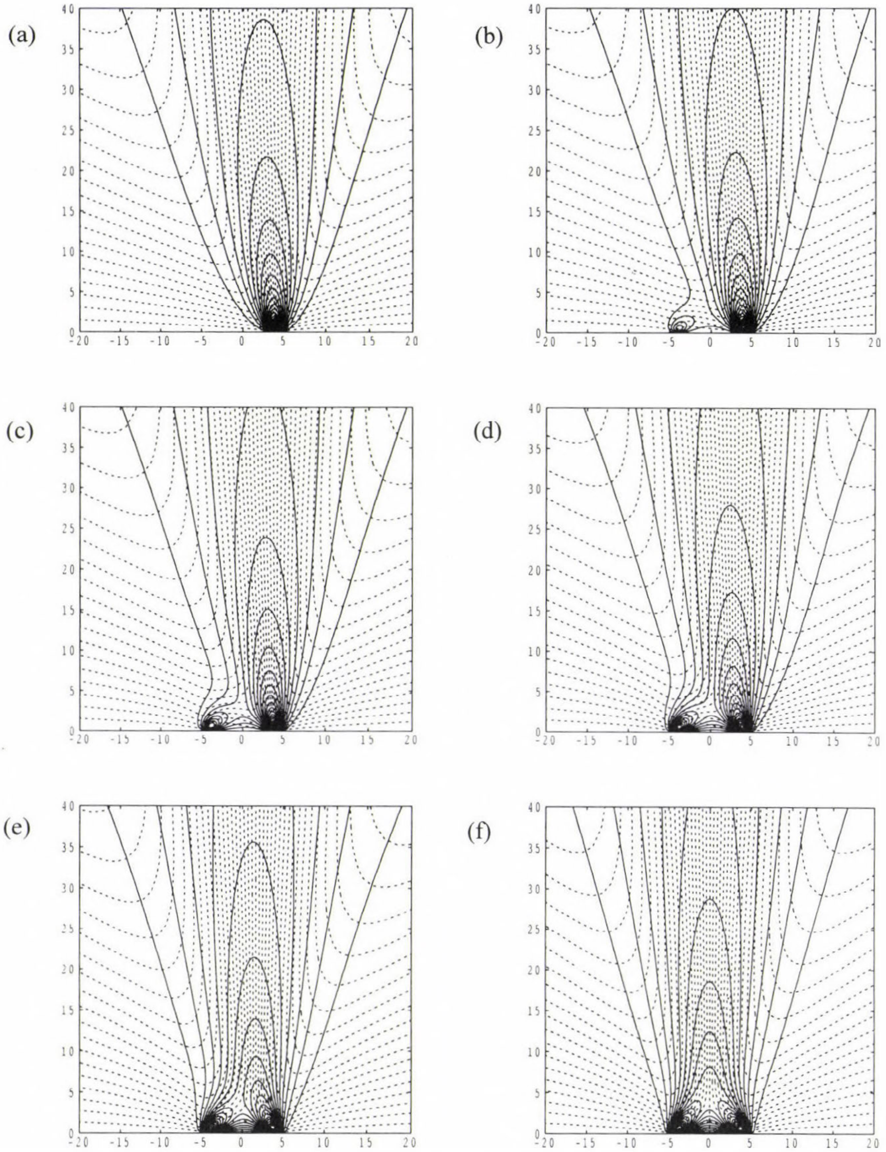

Fig. 3. Streamlines (dashed) and isotherms (continuous) for a situation with two plumes with Ra = 200 and $y_c = 0$. The strength of the right hand plume is S_r, and it is centred at $x_c = 4$. The strengths of the left hand plume are (a) $S_l = 0$, (b) 0.2, (c) 0.4, (d) 0.6, (e) 0.8, and (f) 1. The source of the left hand plume is centred at $x_c = -4$.

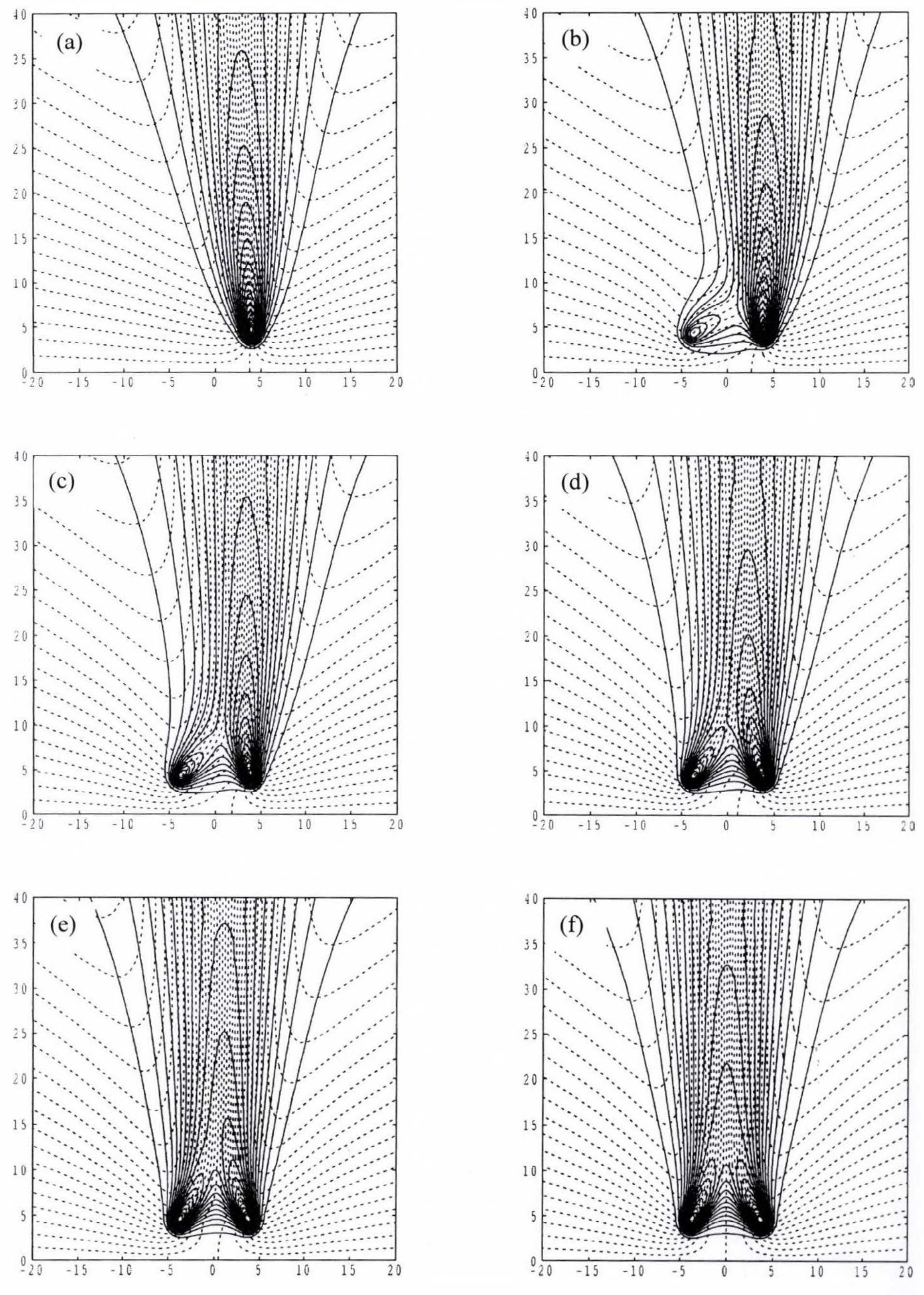

Fig. 4. As Fig. 3 but where the source of each plume is above the lower surface at $y_c = -4$.

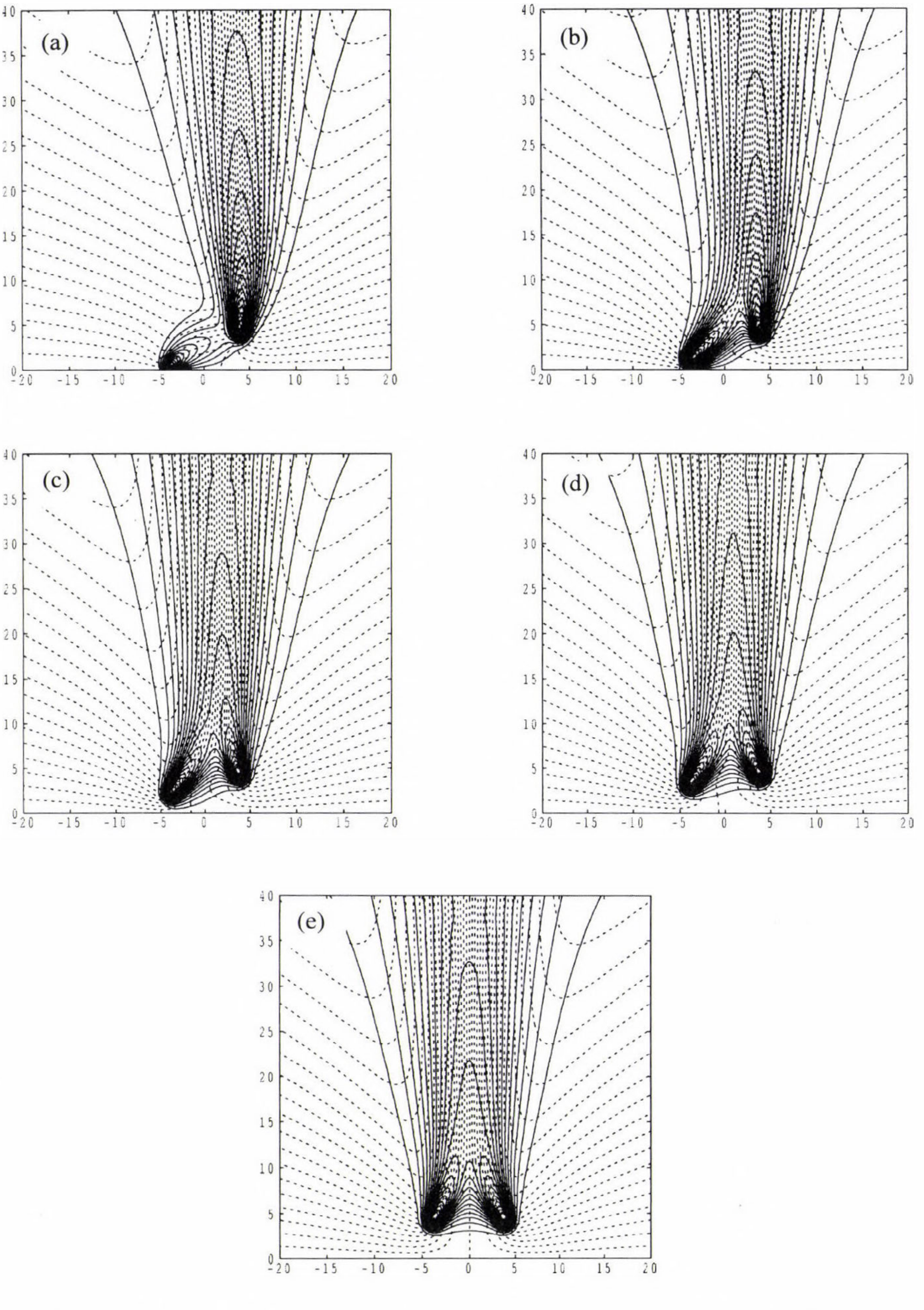

Fig. 5. Interaction of two plumes of equal strength ($S_r = S_l = 1$), where the source of the right hand plume is at $x_c = y_c = 4$, while the source of the left hand plume is at $x_c = -4$ with (a) $y_c = 0$, (b) 0.25, (c) 0.5, (d) 0.75, and (e) 1.

4. Conclusions

The main conclusion of this qualitative paper is that plumes are highly sensitive to their external environment. This was shown analytically by *Bassom et al.* (2000) where plumes in a wedge-shaped domain have a centreline which is straight, but not vertical, in general. In the present numerical study we have found that plumes will exhibit curved centrelines, although, in those cases where a fluid centreline may be defined, the fluid centreline does not coincide with the thermal centreline. In fact, within the parameters covered here, we find that the fluid attachment point descends as Ra increases, while the thermal centreline rises slightly. In addition, the restriction afforded by the placing of a source on a horizontal surface, means that there are substantial differences in both the flow field and the position of the thermal attachment point when the source is raised above the horizontal surface.

When two sources are present, the weaker one or the lower one is assimilated into the stronger one or the upper one, in some cases with little obvious qualitative effect on the latter.

It is our intention to perform further and more detailed computations, but given the sensitivity to domain shape and the need to keep the source region of constant size while the Rayleigh number is increased, it will be necessary to employ more sophisticated coordinate transformations than those employed here. In particular (i) the grid will need to be concentrated near the source region, as the whole flow field depends strongly on this, and (ii) the effective size of the computational domain in terms of the physical variables will need to be very large indeed in order to minimize the effects on the behaviour of the plume of the size and geometry of the computational domain and the inflow and outflow boundary conditions used.

Finally, we believe it to be true that the speed of migration of the plume towards the vertical wall, shown in *Figs. 1* and *2*, will be reduced substantially when point sources are considered. The flow that is induced in the y direction in these cases should provide some of the fluid for entrainment that is necessary to delay attachment.

References

Afzal, N., 1985: Two-dimensional buoyant plume in porous media: high-order effects. *Int. J. Heat Mass Tran. 28,* 2029-2041.

Bassom, A.P., Rees, D.A.S., and *Storesletten, L.*, 2000: Convective plumes in porous media: the effect f asymmetrically placed boundaries. *Int. Comm. Heat Mass Tran. 28,* 31-38.

Gebhart, B., 1979: Buoyancy induced fluid motions characteristic of applications in technology. *Trans. A.S.M.E. J. Fluids Eng. 101,* 4-29.

Harter, T. and *Yeh, T.-C.J.*, 1996a: Stochastic analysis of solute transport in heterogeneous, variably saturated soils. *Water Resour. Res. 32,* 1585-1595.

Harter, T. and *Yeh, T.-C.J.*, 1996b: Conditional stoastic analysis of solute tansport in heterogeneous variably saturated soils. *Water Resour. Res. 32,* 1597-1609.

Kurdyumov, V.N., 2006: Thermal plume induced by line source of heat in asymmetrical environment. *Z. Angew. Math. Phys. 57*, 269-284.
Rees, D.A.S. and *Bassom, A.P.*, 1993: The nonlinear nonparallel wave instability of free convection induced by horizontal heated surface in fluid-saturated porous media. *J. Fluid Mech. 253*, 267-296.
Rees, D.A.S. and *Storesletten, L.*, 2002: Convective plume paths from a line source. *Q. J. Mech. Appl. Math. 55*, 443-455.
Rees, D.A.S., *Storesletten, L.*, and *Bassom, A.P.*, 2002: Convective plume paths in anisotropic porous media. *Transport Porous Med. 49*, 9-25.
Shaw, D.C., 1985: The asymptotic behaviour of a curved line source plume within an enclosure. *I.M.A. J. Appl. Math. 35*, 71-89.
Wooding, R.W., 1963: Convection in a saturated porous medium at large Rayleigh number or Peclet number. *J. Fluid Mech. 15*, 527-544.

IDŐJÁRÁS

Quarterly Journal of the Hungarian Meteorological Service
Vol. 111, No. 2–3, April–September 2007, pp. 123–132

Discussing certain features of the transfer of wave energy in stationary gravity waves and stationary gravity-inertia waves in the atmosphere

Tor Håkon Sivertsen

Norwegian Institute for Agricultural and Environmental Research, Høgskoleveien 7, N-1432 Ås, Norway; E-mail: thsivert@online.no

(Manuscript received in final form January 29, 2007)

Abstract—The topography of Earth influences the movements of parcels of air in the atmosphere. Wind systems blowing across mountain ridges sometimes excite stationary gravity wave systems behind and above ridges with a breadth of about 10 km. The conceptual discussion in this paper is connected to the transport of wave energy in stationary gravity waves and stationary gravity inerta waves, where there are discontinuities in the parameters describing the vertical stratified atmosphere. The discussion is closely connected to two theorems deducted by *Eliassen* and *Palm* (1961) showing that the vertical flux of wave energy is conserved throughout the atmosphere for a great class of systems. But the boundary conditions, used by *Eliassen* and *Palm* (1961) in the gravity wave systems connecting the vertical layers in situations with discontinuities, do not cover all possible physical situations of interest. It is shown how the boundary conditions may be modified to cover most situations of interest.

Key-words: stationary gravity waves, stationary gravity-inerta waves, wave energy

1. Introduction

The influence of the topography on the movements of the parcels of air in the atmosphere is an important theme of dynamic meteorology. In a vertically stratified atmosphere gravity waves or inertia-gravity waves are excited by mountains and mountain ridges on different spatial and temporal scales.

The classical physics of Newtonian mechanics, thermodynamics, and fluid dynamics contains several basic principles, called 'laws of nature', like the conservation of energy, the conservation of mass, the conservation of momentum, and the second law of thermodynamis telling something about the allowed direction of certain physical processes. Sometimes useful results of dynamics are derived, but it is not possible to show exactly how some of the physical laws' are contained in the system of equations.

Examples of this you find in the theory of turbulence. It is not possible to derive theoretically by using the Reynolds equations how the energy and momentum are transferred from the mean flow through the turbulence and to the molecular system, see *Tennekes* and *Lumley* (1987). When using the Navier-Stokes equations, this transfer of energy and momentum is fully described from the flow to the molecular scale. The reason is that the dissipation may be neatly defined, but we have got no theory giving us the components of the Reynold stress tensor.

In this paper certain features of the following concepts are considered: Wave energy of stationary mountain waves, flux densities of wave energy in the horizontal and vertical directions, and reflection of wave energy in the vertical direction. *Eliassen* and *Palm* (1961) did show that the vertical flux of wave energy is conserved throughout the atmosphere in these stationary systems of gravity waves. They also did look theoretically at stratified systems with discontinuities of the parameters in the vertical direction. Below theoretical situations with discontinuities of the mean flow, U is discussed in some details. The theoretical treatment of *Eliassen* and *Palm* (1961) did not cover this physical situation.

2. *The landscape studied and the physical situation considered*

We consider a landscape containing a mountain ridge with a breadth of about 10 km, and the atmosphere is considered stratified in the vertical direction. The landscape and the physical phenomena are modeled in a Cartesian coordinate system with the origin placed under a mountain ridge, the x-axis is normal to the ridge, and the y-axis is parallel with the ridge. The z-coordinate is used to model the height above the (x,y)plane. The fluid-dynamical macrophysical description of the atmosphere is used, by considering the physics to be described by the Navier-Stokes equations, or more precisely by the Euler equations, while the viscosity of the air parcels is not included in this study.

We are using a macrophysical description of the atmosphere. At a moment of time t and at a coordinate point (x,y,z) we have got a parcel of air described by the pressure $p(x,y,z,t)$, temperature $T(x,y,z,t)$, density of the air $\rho(x,y,z,t)$, and wind velocity $\mathbf{v}(x,y,z,t)$. Furthermore, the parcels of air are considered not to exchange heat with the surroundings by conduction or radiation. Also the chemical content of each parcel is considered not to change in time.

We then may consider the thermodynamic processes of each parcel of air as adiabatic. *Eliassen* and *Palm* (1961) is describing the adiabatic process by using the coefficient of piezotropy, γ. In adiabatic thermodynamic processes in the air, the corefficient of piezotropy is given in this manner:

$$\gamma = 1 / C_L^2, \tag{1}$$

where C_L denotes the velocity of sound .

3. *The perturbation equations and the concept of wave energy*

Then we get the mathematical description of the perturbation of the basic flow (only in the (x,z)dimensions):

the horizontal wind velocity is $U(z) + u(x,z)$,

the vertical wind velocity is $w(x,z)$,

the pressure is $p_0(z) + p(x,z)$,

the density of the air is $\rho_0(z) + \rho(x,z)$.

By putting these expressions into the Navier-Stokes equations and the equation of continuity and linearizing, *Eliassen* and *Palm* (1961) obtains the following expression of the wave energy equation:

$$(EU + pu)_x + (pw)_z = -\rho U_z uw, \tag{2}$$

where the indices x and z indicates partial differentiation in x- and z-directions.

$$E = ½\rho_0(u^2 + w^2 + \nu_0{}^2\zeta^2 + \gamma p_0{}^{-2}p^2) \tag{3}$$

is defined as the total wave energy per unit volume. The unit of wave energy is J m^{-3}. ν_0 denotes the Väisälä-Brunt frequency, and $\zeta = \zeta(x,z)$ denotes the vertical displacement of the particles in the disturbed flow.

The wave energy E is made up by

a kinetic part: $½\rho_0(u^2 + w^2)$,

an available potential part: $½\rho_0(\nu_0{}^2\zeta^2)$,

an internal part: $½\rho_0(\gamma p_0{}^{-2}\rho^2)$.

The kinetic part is the kinetic energy connected to the velocity perturbations of the air parcel. The available potential energy is connected to the buoyancy of the air parcel and the distance from the undisturbed equilibrium position. The internal energy is connected to the compressibility of the air parcel.

The horizontal flux density of wave energy is given by the expression $EU + pu$. The vertical flux density of wave energy is denoted by pw, and Eq. (2) is expressing the divergence of wave energy.

If all perturbation quantities tend towards zero as x tends to $\pm\infty$, the following statement is valid concerning the vertical flux of wave energy see *Eliassen* and *Palm* (1961):

$$(1/U)\int pw dx = -\rho_0 \int uw dx. \tag{4}$$

This flux is conserved throughout the atmosphere in systems of stationary gravity waves in the atmosphere on local scales (possible to study by the linearized equations).

4. A situation containing discontinuity of the parameters

We assume that the basic flow, U, the density, ρ_0, or the gradient of the density is discontinuous at a height $z = H$. The kinematic boundary condition is then given by

$$\zeta_1 = \zeta_2 \text{ at } z = H \quad \text{or} \quad (\zeta_1)_x = (\zeta_2)_x \text{ at } z = H . \tag{5}$$

The physical content of this statement is that the vertical displacement, ζ, is the same for the parcels of each side of the surface of discontinuity. The indices 1 and 2 denotes the upper and lower side of a surface of discontinuity.

The linearized vertical velocity is given by $w = U\zeta_x$. Eq. (5) is then transformed into

$$w_1 / U_1 = w_2 / U_2 \quad \text{at} \quad z = H . \tag{6}$$

We get the dynamic boundary condition by requiring that the individual perturbation of the pressure shall be the same on each side of the surface of discontinuity. This condition, linearized, is given by

$$(p_{01})_z \zeta_1 + p_1 = (p_{02})_z \zeta_2 + p_2 \quad \text{at} \quad z = H . \tag{7}$$

By multiplying the right and left sides of Eq. (7) with the right and left sides of the kinematic boundary condition, and integrating along the x-axis we get

$$\int (p_1 w_1 / U_1) dx = \int (p_2 w_2 / U_2) dx . \tag{8}$$

This equation tells us that by using the boundary conditions mentioned, the vertical flux of wave energy is conserved also through the discontinuities of the internal boundaries.

5. Mesoscale mountain waves

We then look at a mountain ridge with a breadth of 100–500 km. This ridge is oriented towards north-south. The Cartesian coordinates x and y are directed eastward and northward, respectively. Pressure p is used as a vertical coordinate. The mountain is situated in an eastward flow, U (p, y). All the physical properties in the atmosphere are functions of y and p, but they are independent of x. The basic flow is in hydrostatic and geostrophic balance.

Behind the mountain ridge we assume the occurrence of a stationary lee wave, which can be described by the linearized equations of motion and continuity. The scale is so large that the flow can be regarded as quasi-static, but the Coriolis parameter, *f*, is assumed to be constant. *Eliassen* and *Palm* (1961) has then shown the following theorem to be valid

$$\frac{\partial}{\partial \text{p}}\left(\frac{\overline{\phi\omega}}{U}\right)+\frac{\partial}{\partial \gamma}\left(\frac{\overline{\phi v}}{U}\right)=0, \tag{9}$$

where

$$\overline{(\,)}=\int_{-\infty}^{\infty}(\,)dx.$$

Here ϕ is the local perturbation of the geopotential, ω is the individual time derivative of pressure, v is the velocity in the y-direction. It is assumed that the perturbation disappears for large positive and negative values of x. $\phi\omega$ and ϕv are the vertical and horizontal components of the flux of wave energy. We use the following notation

$$\frac{\overline{\phi\omega}}{U}=-\frac{\partial\psi}{\partial\gamma}-\psi_y,$$

$$\frac{\overline{\phi v}}{U}=\frac{\partial\psi}{\partial\psi}=\psi_p, \tag{10}$$

where subscripts indicate partial derivatives.

We then define a vector function

$$\mathbf{G}=\mathbf{i}\times\nabla\psi, \tag{11}$$

where

$$\mathbf{i}=\nabla x.$$

The flux of wave energy is then given by

$$\mathbf{F}=U\,\mathbf{G}. \tag{12}$$

ψ is the stream function of the solenoidal vector **F**/U. The curves ψ = constant are the stream functions of the flux of wave energy in the meridional plane. The flux of wave energy in a channel between two adjacent streamlines varies along the channel in proportion to U.

We then assume the occurence of a surface of discontinuity in the atmosphere. Both the density and the basic flow velocity may be discontinuous along this surface.

The slope of the surface is expressed in the formula of Margules, which in pressure coordinates is given by

$$\frac{dp}{dy} = -f\,\frac{(U_1 - U_2)}{\alpha_1 - \alpha_2} = K. \tag{13}$$

The flow is perturbed by the mountain ridge, and it is assumed that the perturbation can be approximated by linear expressions. In this case the particles move along the surface of discontinuity, and it is assumed that the slope of the surface is not affected.

Let $\eta(x, p)$ represent the particle displacement in the y-direction and π the change of pressure for a particle from its upstream value. The displacements in the (y, p)plane are assumed to take place along straight lines. The kinematic boundary condition is given by

$$\frac{\pi_1 - \pi_2}{\eta_1 - \eta_2} = -f\,\frac{U_1 - U_2}{\alpha_1 - \alpha_2} = K, \tag{14}$$

or

$$K\eta_1 - \pi_1 = K\eta_2 - \pi_2, \tag{15}$$

where $\pi_i, \eta_i, (i = 1,2)$ represent the displacement of the particles on each side of the surface of discontinuity which were adjacent upstream.

The requirement, that the geopotential shall vary continuously on the surface of discontinuity, constitutes the dynamic boundary condition. Upstream the boundary condition then is given by

$$\phi_1(y, p) = \phi_2(y, p). \tag{16}$$

Downstream the geopotential on each side of the surface at the point $(y + \eta_1, p + \pi_1)$ is given by

$$\phi_1(y,p) + \phi_{i1}(y,p) = \phi_2(y + \eta_1 - \eta_2, p + \pi_1 - \pi_2) + \phi_{i2}(y + \eta_1 - \eta_2, p + \pi_1 - \pi_2), \tag{17}$$

where $\phi_{ij}\,(y, p), (j = 1,2)$ is the individual change of geopotential for a particle from its upstream value along the streamline (y, p). Thus, the particles at the point $(y + \eta_1, p + \pi_1)$ on each side of the surface downstream come from the points (y, p) and $(y + \eta_1 - \eta_2, p + \pi_1 - \pi_2)$ upstream. The linearized individual perturbation is given by

$$\phi_{ij} = \phi_{jp}\,\pi_j + \phi_{jy}\,\eta_j + \phi_j, (j = 1,2). \tag{18}$$

By using Eqs. (15)–(17) and retaining only the first order terms, we get

$$\phi_2 - \phi_1 + \eta_1(\phi_{2y} - \phi_{1y}) + \eta_1(\phi_{2p} - \phi_{1p}) = 0. \tag{19}$$

We then use the hydrostatic relation, $\phi_p = -\alpha$, and the geostrophic relation, $\phi_y = -fU$, thus, Eq. (19) is alternatively given by

$$\phi_1 - \phi_2 + \eta_1(U_2 - U_1)f + \pi_1(\alpha_2 - \alpha_2) = 0. \tag{20}$$

By noting from Eq. (16) that $f(U_2 - U_1) = K(\alpha_2 - \alpha_1) = 0$ and by using Eq. (15), Eq. (20) becomes

$$\phi_1 - \phi_2 = (K\eta_1 - \pi_1)(\alpha_2 - \alpha_1) = (K\eta_2 - \pi_2)(\alpha_2 - \alpha_1). \tag{21}$$

Using Eq. (15) and multiplying Eq. (20) on each side by $(K\eta_1 - \pi_1)_x = (K\eta_2 - \pi_2)_x$ we get

$$\phi_1(K\eta_1 - \pi_1)_x - \phi_2(K\eta_2 - \pi_2)_x = (K\eta_1 - \pi_1)(K\eta - \pi_1)_x(\alpha_2 - \alpha_1), \tag{22}$$

where α_1 and α_2 are independent of x. Integration along the x-axis then gives

$$K\,\overline{\phi_2\,\eta_{2x}} - \overline{\phi_2\pi_{2x}} = K\,\overline{\phi_1\eta_{1x}} - \overline{\phi_1\pi_{1x}}. \tag{23}$$

We suppose for the sake of argument that there is only one surface of discontinuity in the space. Above the surface we define a vector $\mathbf{G}_2 = \mathbf{i} \times \nabla\Psi_2$ and below the surface a vector $\mathbf{G}_1 = \mathbf{i} \times \nabla\Psi_1$. The surface of discontinuity is (for each value of x) represented in a (y, p)plane by a line. Let $d\mathbf{l}$ denote a vector element of this line.

A vector element of the surface of discontinuity is then defined by

$$d\boldsymbol{\sigma} = \mathbf{i} \times d\mathbf{l}. \tag{24}$$

Since $\mathbf{G}_1$ and $\mathbf{G}_2$ are solenoidal, we have

$$\oint_{\Omega_j} \mathbf{G}j \cdot d\boldsymbol{\sigma}_\mathrm{j} = 0, \quad (j = 1,2). \tag{25}$$

The domains Ω_j, $(j = 1,2)$ are not cut by the surface of discontinuity. The theorem corresponding to this on the surface would be

$$\mathbf{G}_1 \cdot d\boldsymbol{\sigma} = \mathbf{G}_2 \cdot d\boldsymbol{\sigma}. \tag{26}$$

From the preceding we get

$$\mathbf{G}_1 \cdot d\boldsymbol{\sigma} = \mathbf{i} \times \nabla\Psi \cdot (\mathbf{i} \times d\mathbf{l}) = d\mathrm{l} \cdot \nabla \Psi_j = d\psi_j, \quad (j = 1{,}2\ ). \tag{27}$$

If Eq. (26) is valid, then $d\psi_1 = d\psi_2$ on the surface of discontinuity, and it is possible to define a scalar function, the equilines of which are continuous on this surface.

Eq. (13) gives

$$d\psi_j = \psi_{jp} dp + \psi_{jy} dy = (\psi_{jp} K + \psi_{jy})\, dy, \quad (j = 1{,}2). \tag{28}$$

The linearized ω and v are given by

$$\omega = U\pi_x \quad \text{and} \quad v = U\eta_x. \tag{29}$$

Eqs. (10) and (29) give

$$\psi_{jp} = \frac{\overline{\phi_j v_j}}{U_j} = \overline{\phi_j \eta_{jx}}, \quad (j = 1{,}2) \tag{30}$$

$$\psi_{jy} = \frac{\overline{\phi_j \omega_j}}{U_j} = \overline{\phi_j \pi_{jx}}.$$

From Eqs. (28) and (30) we have

$$d\psi_1 = \left(K\overline{\phi_1 \eta_{1x}} - \overline{\phi_1 \pi_{1x}}\right) dy,$$

$$d\psi_2 = \left(K\overline{\phi 2 \eta_{2x}} - \overline{\phi_2 \pi_{2x}}\right) dy. \tag{31}$$

By comparing (31) and (23) we notice that Eq. (23) is equivalent to the assertion $d\psi_1 = d\psi_2$ on the surface of discontinuity.

According to *Eliassen* and *Palm* (1961), the flux of wave energy, $\mathbf{F} = U\mathbf{G}$, in a stationary quasi-static wave in a non-uniform basic current varies between adjacent streamlines, $\psi = \text{constant}$, in proportion to the basic current U. The preceding shows that this is also the case when there is a surface of discontinuity in the atmosphere. Along this surface both the basic flow U and the density ρ may be discontinuous, see also *Sivertsen* (1976).

6. *Fourier-transformation of the equations and the idea of vertical transmission and reflection of wave energy*

The system of linear equations for this stationary situation on local scale is manipulated and we arrive at the following equation for w (the vertical wind velocity):

$$w_{zz} + w_{xx} - l^2(z)w = 0.$$

$l^2(z)$ is called the Scorer-parameter, and with good approximation we get:

$$l^2(z) = {v_0}^2 U^{-2} - U_{zz} U^{-1}.$$

By Fourier-transforming this equation we arrive at the following formula:

$$\hat{w}_{zz} - (l^2 - k^2)\hat{w} = 0,$$

where k is the wave number in this transformation.

In a layered atmosphere, each layer with a constant Scorer-parameter; the analytical solutions in each layer may be linked by the knowledge of the boundary conditions between each layer.

Eliassen and *Palm* (1961) invoked an analogy with the theory of electromagnetism when discussing reflection and transmission of energy in an atmosphere with layers of constant Scorer-parameter. In order to maintain this analogy, they are using something they call 'pure mathematical boundary conditions':

$$w_1 = w_2 \tag{32}$$

and

$$w_{1z} = w_{2z}. \tag{33}$$

Nevertheless, they sometimes violate their own main result, Eq. (4), that the vertical flux of wave energy always is conserved through the atmosphere in a stationary system. Their theory is not valid in situations with discontnuities in the main stream, U.

When using the ordinary kinematical and dynamical boundary conditions Eqs. (6) and (7), we get other results in calculating the coefficient of reflection than according to the analogy with electromagnetism, see *Sivertsen* (1972). When studying other aspects of the phenomenon of stationary gravity waves in the atmosphere, like calculation of the pressure drag on the mountains in a layered atmosphere with discontinuity of the parameters connecting to the different layers, using boundary conditions Eqs. (32) and (33) sometimes will give the wrong results.

References

Eliassen, A. and *Palm, E.,* 1961: On the transfer of energy in stationary mountain waves. *Geofysiske Publikasjoner,* Oslo.

Sivertsen, T.H., 1972: About stationary mountains waves (in Norwegian). *Thesis Master of Science.*University of Oslo.

Sivertsen, T.H., 1976: On the transfer of energy in stationary mountain waves in an atmosphere with discontinuous parameters. *Meteorologiske annaler 7,* No. 3. Det norske meteorologiske institutt, Oslo, 9 pp.

Tennekes, H. and *Lumley, J.L.,* 1987: *A First Course in Turbulence.* MIT Press Cambridge Massachusetts, London, England.

IDŐJÁRÁS

Quarterly Journal of the Hungarian Meteorological Service
Vol. 111, No. 2–3, April–September 2007, pp. 133–148

Internal waves and internal boundary currents

In memoriam Fridtjof Nansen

Yuli D. Chashechkin

Laboratory of Fluid Mechanics,
Institute for Problems in Mechanics of the Russian Academy of Sciences
101/1 prospect Vernadskogo, Moscow, 119526, Russia; E-mail: chakin@ipmnet.ru

(Manuscript received in final form February 5, 2007)

Abstract—Re-reading of books written by Fridtjof Nansen after his great travels and humanitarian feats shows that his precise observations as well as deep thoughts are still rich source of inspiration. He gave clear description of the behavior of this ship *Fram* in dead waters of Siberian seashores and invited Vagn Ekman to clarify the phenomenon in laboratory experiments. Laboratory studies of stratified flows is now performed in many laboratories around the globe. The first part of this paper is a memorial talk of Nansen. In the second part a classification of infinitesimal periodic motions including waves and singular components of motions is presented. Singular solutions describe a set of linear periodic boundary layers. Approximation of a 3D homogeneous fluid results in merging boundary layers and degeneration of the governing equations set. Structure of 2D attached internal waves is visualized numerically.

Key-words: viscous stratified fluids, exact regular singular solutions, periodic motions

1. Introduction — life in the service of science and humanity

Fridtjof Nansen was born in Norway, on October 10, 1861 in aristocratic family. His father, Baldur Fridtjof Nansen, a prosperous lawyer, was a religious man with a clear conception of personal duty and moral principle. His mother, baroness Adelaide Johanna Tekle Isidore Belling formerly Wedel Jarlsberg was a strong-minded, athletic woman. She owned a farmstead near Christiania (now Oslo) where Fridtjof Nansen, together with his brother Alexander and a number of older half-brothers and half-sisters, had a privileged childhood. Mother had introduced children to outdoor life and encouraged them to develop physical skills. Not massively built, F. Nansen was tall, supple, strong, and possessed the physical endurance to ski fifty kilometers in a day and then to win a skiing competition.

Preferring physics and mathematics he, nevertheless, selected zoology to spend more time in the open air, when in 1880 he entered the University of Christiania. Even during student days, in 1882, when, at a tutor's suggestion, he took passage aboard a sealer *Viking* to the Arctic Ocean, he used thermometers, bathometers, and different nets for scientific observations of winds, ocean currents, ice movements, and animal life. He firstly found that warm salty Atlantic waters were placed below cold and fresh Arctic waters and rightly described freezing of polar seas. He landed on a floating iceberg and collected stones. Thinking about the patterns of the frozen in ice ship drift, he recognized that the effect of complex vortex currents caused by the bottom topography dominate, over a wind impact. He wrote extended diaries and published papers about his expeditions in newspapers and scientific journals that were illustrated by his own excellent sketches. After the travel he firmly decided to study cold Arctic Ocean and crossed Greenland icecap on skies.

On his return Nansen was offered the post of curator at the Bergen Museum. During six years he performed intensive laboratory study mostly with the microscope that was a gift of his father. The transition from the rugged days aboard the Arctic sealer to study minute animals through microscopes was productive. He wrote his thesis *The Structure and Combination of Histological Elements of the Central Nervous System* in English language in 1887, accepted by the examining board with a degree of skepticism. He could obtain his doctorate only four days before leaving for Greenland in view of his future dangerous travel. In the course of two years he published abbreviated version of his thesis in four different languages and today his thesis is regarded as a classic. He visited the international biological station in Naples (Italy) in 1886 and was so impressed that recommended to construct similar stations in Norway. The idea was supported and two biological stations were built on Nansen's projects. Constructions were so good that the station in Drobak is still operating today, in the same building.

In 1887 Nansen embarked on the preparations for the journey to cross the Greenland icecap. The six-man expedition was financed by a wealthy Danish businessman A. Gamel and Nansen himself. The expedition started in June on the east coast and going to the inhabited west coast. The ice drift delays the beginning of the journey as it took 12 days to row to land in open boats instead of expecting 2–3 hours. Nansen, still only 27 years of age, had led his team firmly and finally reached the west coast in late September. Throughout the journey the team made careful records of meteorological conditions when the temperature fell to 50 °C below zero. Data were analyzed later by the known meteorologist H. Mohn (1835–1916). No boats were due to leave Greenland until the following spring, so Nansen spent the enforced winter in Greenland studying the Inuits and returned to Norway in May 1889. After the expedition he published many articles and books, like *The First Crossing of Greenland* (1890) and *Eskimo Life* (1891).

Meanwhile, he started planning an another great expedition by ship over the Polar Sea hoping to reach the North Pole. He read a lot of lectures in different countries discussing his plans and construction of the ship. When – in 1892 – he outlined his plan for a North Pole expedition in the Royal Geographic Society of London, he met a lot of criticism and opposition by the most experienced Arctic explorers. But the idea received a great support in Norway. The Storting (the Norwegian Parliament) granted a large part of the necessary expenses, subscriptions from the King, private individuals and own payment of Nansen provided the rest.

The primary task was to build a ship that could withstand the pressure of the ice. Nansen collaborated with famous shipbuilder Colin Archer to design it. The government provided by the best oak and timber for the ship construction from the state stock. The hull of the vessel *Fram* was made exceptionally strong, and her lines below the waterline were far rounder than customary. As a result, when the pack became jammed hard together, the ship slipped free and was lifted clear instead of being crushed.

In June 1893 the *Fram* left Christiania with provisions for six years and fuel oil for eight. Nansen believed the trip would take from two to three years. After having sailed the nothern Siberian coast, the expedition reached the area around New Siberian Islands where the *Fram* had been frozen fast in the drifting ice. However, it became evident soon, that the ship root was too far from the North Pole. Then Nansen with Hjalmar Johansen left the *Fram* on February 1895 to ski to the North Pole with dog sledges. Despite the incredible difficulties they reached 86°14'N when the drifting ice and lack of food forced them to turn back. The travelers had no idea of *Fram's* whereabouts, so they decided to spend the winter in Franz Josef Land, and they survived in a stone hut by shooting walruses and polar bears. After the long winter they started to go to south, and by an incredible stroke of luck, they met a British expedition, headed by Frederick George Jackson, which took them back to Norway. Just after Nansen had arrived in Norway, the *Fram* came in, too. Nansen described the history of the expedition in a two-volume work *Farthest North* (1897). The successful outcome of the North Pole expedition made Nansen a national hero and gave him a world-wide reputation.

The most important results of Nansen's *Fram* expedition were

- the discovery of the deep Arctic Ocean completely devoid of islands,
- the confirmation of the existence of the trans-polar current,
- existence of intermediate warm and salty waters,
- thickening pack ice from below due to freezing of melting fresh water.

Furthermore, Nansen recognized that the *Fram* and the ice pack drifted approximately 30° to the right of the wind direction. This fact he interpreted as the effect of the Earth's rotation, which laid the concept for the Ekman spiral and the foundation for the modern wind-driven ocean circulation. Nansen descibed in details the misterious "dead water" phenomen which the *Fram* met in Bergen fjord and Siberian coast waters. Scientific results of expedition were published in a six volumes collection of papers. Later Nansen decided to hand the *Fram* over to Roald Amundsen for an expedition to the South Pole. Nansen and Captain Otto Sverdrup shared their rich experience on ship motion in ice with the Russian Admiral S.O. Makarov, who decided to built the first large icebraker with iron hull .

As a scientist, Nansen was much aware of the need for precise and exact measurements. Leaving the ship in March 14, 1895 he wrote in a letter to Sverdrup: "Besides foods, weapons, clothes, and equipment, take off scientific materials, diaries, and collections, but not so heavy, ...photos and plates… It is good to take off Oderman's densimeter for measuring of sea water density…". Later Nansen found that some of the oceanographic measurements on the *Fram* were not of sufficient precision. He wrote: "I understood that future studies in physical oceanography would have small impact or even no sense if they will not produced by more exact methods than current methods or used before". At that time, when densimeters were the most precise instruments in physical oceanography, Nansen exchanged his experience of methods of calibrations with the known Russian oceanographer Admiral S.O. Makarov (1848–1904), who made round-the-world expedition on the corvette *Vityaz* (1886–1889, 903 days of travel and 526 days of sailing and steaming) and wrote the famous book *Vityaz and the Pacific Ocean*. Nansen was able to remarkably improve methods and instruments, and he invented the bottle for sampling ocean water at various depths and different types of current meters. He supported the international cooperation in oceanography, and he was one of the founding fathers of the International Council for the Exploration of the Sea (ICES) in 1902.

Nansen's books were soon translated into Russian (first in 1897) making his name extremely popular. He was honored by the Prince Konstantin Gold Medal of the Russian Geographic Society in 1897. He visited Russia first in 1898, when he was awarded by the State Stanislav insignia and was elected Honor Member of St. Petersberg Academy of Science.

The success of the *Fram* expedition stimulated Norwegians to act for state independence, and Nansen involved himself in the political debates. He played an important role in the actions in 1905 when the union with Sweden was dissolved and Norway declared its full independence. Reportedly, he was also secretly requested to become either president or king but declined both offers, on the grounds that he was "a scientist and explorer". However, he played a personal part in bringing to the vacant Norwegian throne the Danish Prince Carl, who took the Norwegian name Haakon VII and was appointed as Norway's first ambassador in London.

After two years in London, he returned to scientific work for some years and had some good years studying the oceanography of the Norwegian Sea and the way of formation of bottom water in the Greenland Sea. His results were published jointly with Professor B. Helland-Hansen in the classic book *The Norwegian Sea*.

In 1913 he traveled to Siberia and Far East with a diplomat I.G. Loris-Melikov and the deputy of the State Duma (Parliament), S.V. Vostrotin from Tromsoe to Krasnoyarsk. They followed the only working way from Far East to Europe up to the still mouth of the river Enisey on a cargo ship *Correct*, then up along the river Enisey on a motor boat to Krasnoyarsk. Then he took a rail car and went to Vladivistok on the just constructed Transsiberian railway, where one of the stations was named by him. The Eastern Siberian railroad is the longest continuous railway of the world. His impressions of the environment, common people life, and seeing of future development of these extended but almost unhabitated lands are expressed in his excellent book *Into the country of Future (Fremtidens Land) – Great North Marine way from Europe to Asia through Kara Sea* with a supplement *Shipping in Kara Sea*. The book contains right prognosis of future economic development of this outermost land and was reprinted in Russia (*Nansen*, 1992).

The further life of Fridtjof Nansen is an illustration of his deep thinking, efficiency, and humanism. He did save the lives of millions of people. In 1917–1918 Nansen negotiated in Washington, USA an agreement for a relaxation of the blockade of the allies to permit shipments of essential food to neutral Norway.

In June 1921 the Council of the League of Nations, spurred by the International Red Cross and other organizations, instituted its High Commission for Refugees and asked Nansen to administer it. For the stateless refugees under his care Nansen invented the "Nansen Passport", a document of identification, which was eventually recognized by fifty-two governments. In the nine-year life of this office, Nansen ministered to hundreds of thousands of refugees – Russian, Turkish, Armenian, Assyrian, Assyro-Chaldean – utilizing the methods that were to become classic.

A heavy drought in the Russian grain growing areas in 1921 brought famine to millions of people. Nansen responded on appeal of Maxim Gorky and opened in Moscow Kremlin an office of the International Russian Relief Executive. But his appeals to the League of Nations for funds to finance the work met deaf ears. As Nansen was sure that even a small food parcel can save a life, he appealed to common people and succeeded in raising finances. Norwegian pensioners, peasants, and charity organizations collected 3,225,295 Norwegian crowns, and the government added 770,000 crowns to this sum. Nansen was proud that the small populated Norway gave more for struggle with famine in Russia than great states. Although this amount was not sufficient to save all of the starving people and many of them died, thousands received help and survived, particularly in Ukraine and the Volga districts (the figures quoted are ranging from 7 to 22 millons). Nansen was made an honorary member of the Moscow Soviet and honored by Thanking Letter of the Russian Supreme Soviet. Together with Maxim Gorky he wrote the book *Russia and Peace* (Russland og freden), where he defended Lenin's harsh methods and argued that they were necessary in order to build up the country.

In recognition of his work for refugees and the famine-stricken, the Nobel Committee in Oslo decided to honor Fridtjof Nansen with the 1922 Nobel Prize for Peace. A Danish publisher, Christian Erichsen, presented him with the same sum. Half of the total amount Nansen spent to create two agricultural stations: one in the Saratov region and the second in Ukraine. Idea of machinery stations and rural agricultural institutes was reborn in the 1930's, when kolkhoses replaced the individual rural economy.

Nansen arranged an exchange of about 1,250,000 Greeks living on Turkish land for about 500,000 Turks living in Greece, with appropriate indemnification and provisions. Nansen's fifth great humanitarian effort was to save the remnants of the Armenian people from extinction. He drew up a political and financial plan for creating a national home for the Armenians in Erivan, which was not accepted by the League of Nations. By personal efforts he settled later some 10,000 Armenians in Erivan and 40,000 in Syria and Lebanon. Impressed by Armenian history and fortune, Nansen wrote the books *Armenia and the Middle East* (1927), *Along Armenia* (1929), and *Across Caucas to Volga*, and the made money-raising tours in USA for the Armenian people.

During all these years Nansen remained interested in Arctic studies. He initiated the creation of the Aeroarctic Society, was elected as its Permanent President in 1924, and took part in the Second Aeroarctic Congress in St. Petersburg in 1928. In 1930 he planned to take part in an Arctic expedition on the dirigible balloon *Count Zeppelin* when he died from a heart attack on May 13, 1930. Nansen was buried on May 17, on the national celebration day of Norway.

The world lost a great humanist, scientist, traveller, and writer. The memory of his humanitarian actions is still alive in different countries and especially in Russia in the hearts of the descendants of millions of saved people.

2. *Discovery of internal waves*

Although mathematical studies of waves on an interface between fluids of different densities was initiated by *Stokes* (1847), physical significance of the phenomenon as well as their existence inside a continuously stratified fluid were not recognized up to the *Fram* expediton. The pioneering paper of *Rayleigh* (1880), containing the definition of buoyancy frequency was not properly written up to the late twentieth of the next century, when *Väisälä* (1925) and *Brunt* (1927) rediscovered this principle parameter for a stratified atmosphere.

Nansen gave a picturesque descriprion of the "dead water" (*Ekman*, 1906) and later interpreted the semidiurnal variation of the ocean temperature as the manifestation of internal waves. The deepness of his understanding is illustrated by a letter to the Russian polar explorer Barony E.V. Tall, in which he recommended to register the lost of the ship velocity, to measure thickness of upper fresh layer, and to measure the difference in salinities below the the ship and under the boat which is towed on different distances from the ship

(*Pasetskii*, 1986). He discussed the problem with V. Bjerknes, who asked his former student to model the "dead water" phenomenon in a laboratory. Nansen provided money for organizing the experiment, Bjerknes found a grant for the work, Ekman performed a comprehensive study of forces acting on the model of *Fram* and visualized the patterns of waves on the interface. Unfortunately, the resulting paper (*Ekman*, 1906) did not receive continuation up to the late fifties of the last century, when *Lighthill* (1978) started to study anisotropic waves and collected theoreticians and experimenters for cooperative studies on the internal waves in a continuously stratified liquid. Results were also applied for qualitative explanation of mysterious phenomena like "turbulence of the clean sky" caused by overturning of internal waves, "mountain lee waves" in the atmosphere and waves behind moving vehicles in the ocean. The number of work increased greatly and setups for internal waves modeling were created in diffent countries. As the results of the studies based of different approaches were in general in agreement while not fitting completely, the classification of infinitesimal periodic motions was done (*Chashechkin* and *Kistovich*, 2004) and its results were used for construction of exact solutions of some inernal wave generation problems (*Chashechkin et al.*, 2004; *Bardakov* and *Chashechkin*, 2004).

3. Classification of infinitesimal periodic motions

Periodic motions are studied on rotating with angular velocity Ω spherical planet with the gravity field characterized by gravity acceleration g. The density profile $\rho(z)=\rho_o\exp(-z/\Lambda)$ is defined by the total salinity $S=\Sigma S_n$ that is of concentration of dissolved or dispersed matter S_n and is characterized by a scale $\Lambda=(d\ln\rho(z)/dz)^{-1}$ and frequency $N=\sqrt{g/\Lambda}$ of buoyancy, which can be supposed to be constant and by $N_c=\sqrt{(N^2c_s^2-g^2)/c_s^2}$ where c_s is sound velocity. Disturbances of density $\rho=\rho(p,S_n,|\mathrm{v}|)$ depend on velocity $\mathbf{v}=(u,\mathrm{v},w)$ pressure p, and S_n.

The set of governing equations in the linear approximation has the form

$$
\begin{aligned}
&\frac{\partial\bar\rho}{\partial t}-\frac{\mathrm{w}}{\Lambda}+\nabla\cdot\mathbf{v}=0,\quad \frac{\partial\bar S}{\partial t}-\frac{\mathrm{w}}{\Lambda}-\kappa\Delta\bar S=0\\
&\frac{1}{c^2}\frac{\partial\bar p}{\partial t}-\frac{\mathrm{w}g}{c^2}+\nabla\cdot\mathbf{v}+\kappa\Delta\bar S=0\\
&\frac{\partial \mathrm{u}}{\partial t}=-\frac{\partial\bar p}{\partial x}+2\Omega\left(\mathrm{v}\sin\varphi-\frac{1}{\sqrt2}\mathrm{w}\cos\varphi\right)+\nu\Delta\mathrm{u}+\left(\mu+\frac{\nu}{3}\right)\frac{\partial}{\partial x}\nabla\cdot\mathbf{v}\\
&\frac{\partial \mathrm{v}}{\partial t}=-\frac{\partial\bar p}{\partial y}+2\Omega\left(\frac{1}{\sqrt2}\mathrm{w}\cos\varphi-\mathrm{u}\sin\varphi\right)+\nu\Delta\mathrm{v}+\left(\mu+\frac{\nu}{3}\right)\frac{\partial}{\partial y}\nabla\cdot\mathbf{v}\\
&\frac{\partial \mathrm{w}}{\partial t}=-\frac{\partial\bar p}{\partial z}+\sqrt2\Omega(\mathrm{u}\text{-}\mathrm{v})\cos\varphi+\nu\Delta\mathrm{w}+\left(\mu+\frac{\nu}{3}\right)\frac{\partial}{\partial z}\nabla\cdot\mathbf{v}-\bar\rho g
\end{aligned}
\tag{1}
$$

where $\bar{\rho}$, $\bar{p}$, $\bar{S}$ are the pressure minus hydrostatic pressure, medium-density perturbation normalized to the density at the reference level $z=0$, and normalized on salinity profile perturbation, φ is the latitude of the observation point, and ν and μ are the first and second kinematic viscosities.

In particular cases the set (1) had to be supplemented by initial and no-slip and no-flux boundary conditions $\mathbf{v} = \mathbf{I}_n \cdot \mathbf{n} = 0$ where $\mathbf{n}$ is local normal to the contact solid boundary Σ. In the present study the scale of stratification is large and dissipative coefficients of kinematic viscosity ν and salt diffusion κ_s are small. Axis z of the Cartesian coordinate frame (x, y, z) is directed to zenith and the x- and y-axes are taken so that the corresponding projections of the angular velocity are equal to each other.

For periodic flows $\mathbf{v} = \mathbf{v}_0 \, \mathrm{f}_p(\mathbf{k}, \omega)$, $P = P_0 \, \mathrm{f}_p(\mathbf{k}, \omega)$, $\rho = \rho_0 \, \mathrm{f}_p(\mathbf{k}, \omega)$ where $\mathrm{f}_p(\mathbf{k}, \omega) = \exp(i\mathbf{kr} - i\omega t)$ with real positive frequency ω and wave vector $\mathbf{k} = (k_x, k_y, k_z)$, the general solution of to system Eq. (1) can be written as a superposition of elementary waves

$$A = \sum_j \int_{-\infty}^{+\infty} \int_{-\infty}^{+\infty} a_j(k_x, k_y) \exp\left(i\left(k_{zj}(k_x, k_y) z + k_x x + k_y y - \omega t\right)\right) dk_x dk_y, \tag{2}$$

where A is a velocity component, pressure, or density. The summation must be performed over **all** roots of the dispersion equation that are obtained from the condition of non-trivial solvability of the equation set Eq. (1). Coefficients $a_j(k_x, k_y)$ are defined from the boundary conditions. For stationary periodic waves, frequency ω is fixed, and the dispersion equation describes the relation between the wave number components that is expressed $k_{zj}(k_x, k_y)$ for given k_x and k_y values and has a form

$$\begin{aligned} &D_\kappa \{\omega D_\nu(k)\left[\omega D_\nu(k)\tilde{D}_\nu(k) + 2\sqrt{2}\omega\Omega(k_x - k_y)\cos\varphi\right] \\ &- \omega D_\nu(k) N^2\left[D_\nu(k) + i(\mu + \nu/3)k_\perp^2\right] + \\ &+ 4\omega\Omega^2\left[N^2 \sin^2\varphi - \omega\left(D_\nu(k) + i(\mu + \nu/3) f^2(k)\right)\right] + \\ &+ \frac{\kappa c^2 k^2}{\Lambda} \times \left[\omega k_z D_\nu^2(k) - 2\sqrt{2}\omega\Omega^2 f(k)\sin\varphi - iD_\nu(k)\left(gk_\perp^2 + \sqrt{2}\omega\Omega(k_y - k_x)\cos\varphi\right)\right]\Big\} = 0, \end{aligned} \tag{3}$$

where $\tilde{\nu} = 4\nu/3 + \mu$, $k^2 = \Sigma k_i^2$, $k_\perp^2 = k_x^2 + k_y^2$, $f(k) = \left(k_z \sin\varphi + (k_x + k_y)\cos\varphi\right)/\sqrt{2}$, $D_\nu(k) = \omega + i\nu k^2$, $\tilde{D}_\nu(k) = \omega + i\tilde{\nu}k^2$, $D_\kappa(k) = \omega + i\kappa k^2$.

The power of the singularly perturbed dispersion equation (the leading, k^8, term involves a small factor $\nu^2 \tilde{\nu} \kappa$) defines the number of roots. When all dissipative coefficients equal to zero, Eq. (3) becomes a second order equation. So two of eight roots of Eq. (3) are regular in dissipative factors and describe propagating waves. The remaining six roots characterize the set of singular components including coexisting boundary layers. The question what components of motions propagate in the fluid body (only regular or regular and singular components which looks like interfaces in a fluid interior) is still open. The boundary of domains of propagating waves with the real frequency ω existence depends on the ratio of wave and intrinsic rotation and buoyancy frequencies, the compressibility of the medium, and the geometry of the problem.

Solutions of Eq. (3) are further analyzed in the spherical coordinate system (k,Ψ,Θ) introduced in the wave number space (k_x,k_y,k_z) by the relations $k_x = k\sin\Theta\cos\Psi$, $k_y = k\sin\Theta\sin\Psi$, $k_z = k\cos\Theta$. Regular in dissipative factors solutions are written in a power series

$$k_z^{(r)} = k_0 + \sum_{i,j,k=0}^{\infty} b_{ijk}\,\kappa^i \nu^j \mu^k . \tag{4}$$

In the zero approximation all kinetic coefficients in Eq. (4) are equal to zero and solution for k_0 has a form

$$\begin{aligned}
&k_0 = \frac{\beta \pm \sqrt{\beta^2 - 4\alpha\gamma}}{2\alpha};\ \alpha = c^2\left(N_c^2\sin^2\theta - \omega^2 + 4\Omega^2F^2\right)\\
&\beta = 2\sqrt{2}\omega\Omega g\left(\sin\psi - \cos\psi\right)\cos\theta\cos\varphi;\\
&\gamma = \omega^2\left(\omega^2 - N^2\right) + 4\Omega^2\left(N^2\sin^2\theta - \omega^2\right)
\end{aligned} \tag{5}$$

and the domain of existence of propagating waves of frequency ω is defined by condition $\beta^2 - 4\alpha\gamma \ge 0$ and determined by the inequality

$$\begin{aligned}
&2\omega^2\Omega^2g^2\sin^2\theta\cos^2\varphi\left(\sin\psi - \cos\psi\right)^2 \ge\\
&\ge \frac{c^2\left(4\Omega^2\left(N^2\sin^2\varphi - \omega^2\right) - \omega^2\left(N^2 - \omega^2\right)\right)}{N_c^2\sin^2\theta - \omega^2 + 4\Omega^2F^2}.
\end{aligned} \tag{6}$$

More detailed calculations show that complete regular solution at the first approximation can be written as sum $k_z^{(r)} = k_0 + k_1$ that is phase correction term depends on diffusivity only. Boundaries of frequency ranges depend on many factors, such as the ratio of wave and intrinsic rotation and buoyancy frequencies, the compressibility of the medium and geometry of the problem.

4. Singular components of periodic motions

Singular components are analyzed on the plane whose direction of the normal is defined by the above mentioned angles ψ and θ in local coordinate frame. Solution of the dispersion equation is a function, describing the dependence of the normal component of the wave number k_n on two components, which are parallel to the plane. Approximate form of the dispersion equation, Eq. (3), defining only the main parts of the singular solutions in the local coordinate frame is

$$\begin{aligned}&\omega\kappa\nu^2 k_n^6 - i\nu\left[\omega^2\nu - \kappa\left(\left(N_c^2 - N^2\right)\sin^2\theta - 2\omega^2\right)\right]k_n^4 + \\ &+\omega\left[\nu\left(N_c^2\sin^2\theta - 2\omega^2\right) + \kappa\left(\left(N_c^2 - N^2\right)\sin^2\theta - \omega^2 + 4\Omega^2F^2\right)\right]k_n^2 - \\ &-i\omega^2\left(N_c^2\sin^2\theta - \omega^2 + 4\Omega^2F^2\right) = 0\end{aligned} \tag{7}$$

There are no components of wave number, which are parallel to the contact plane in Eq. (7). Thus near the contact surface only solenoidal motions exist with $\operatorname{div}\mathbf{v} = 0$. Eq. (7) has three solutions with respect to variable k_n^2

$$\begin{aligned}&k_{n\kappa}^2 = -\frac{\omega}{\kappa}\left[1 + \varepsilon\frac{N^2\sin^2\theta}{\omega^2} - \varepsilon^2\frac{N^2\sin^2\theta\left(N_c^2\sin^2\theta - \omega^2\right)}{\omega^4}\right], \\ &k_{n\nu\pm}^2 = \frac{1}{\nu}\left[\omega_\pm - \omega + \varepsilon\frac{N^2\sin^2\theta}{\omega^2}\frac{N_c^2\sin^2\theta - \omega^2}{N_c^2\sin^2\theta - 2\omega\omega_\pm}\right]\end{aligned} \tag{8}$$

where $\varepsilon = \kappa/\nu = Sc^{-1}$ is the inverse Schmidt number (typically in a real fluid $\varepsilon << 1$) and

$$\omega_\pm = \frac{N_c^2\sin^2\theta}{2\omega}\left[1 \pm \sqrt{1 + \frac{16\omega^2\Omega^2F^2}{N_c^4\sin^2\theta}}\right]. \tag{9}$$

Solution $k_{n\kappa}^2$ in Eq. (8) describes density boundary layer of a thickness $\delta_\kappa \approx \sqrt{2\kappa/\omega}$. The two other expressions $k_{n\nu\pm}^2$ in Eq. (9) describe two different viscous boundary layers with transverse scales $\delta_{\nu\pm} \approx \sqrt{2\nu/|\omega_\pm - \omega|}$. All three singular components exist at the same time and their relative thickness depends upon parameter ε. When the rotation frequency is small $\Omega << N_c^2 \sin\theta / 4\omega F$ the viscous boundary layers have essentially different thickness as in this case $\omega_+ \approx N_c^2 \sin^2\theta/\omega$, $\omega_- \approx 4\omega\Omega^2 F^2 / N_c^2$ and $\delta_{\nu+} = \delta_N \sqrt{2\omega^* / \left|N_c^2 \sin^2\theta - \omega^2\right|}$, $\delta_{\nu-} = \delta_N \sqrt{2/\omega^* \left|1 + 4\Omega^2 F^2 / N_c^2\right|}$, where $\delta_N = \sqrt{\nu/N}$ is universal microscale. One of the velocity boundary layers with the thickness $\delta_{\nu+}$ is defined by viscosity, buoyancy frequency and compressibility effects. Parameters of the second layer with thickness $\delta_{\nu-}$ additionally depend upon the rotation frequency Ω. In high frequency limit ($\omega^2 >> N_c^2 \sin^2\theta$) thickness of both boundary layers tends to the Stokes scale $\delta_{\nu+} \approx \delta_\nu \approx \sqrt{2\nu/\omega}$.

Taking compressibility into account and disregarding rotation effects ($\Omega = 0$), we conclude from Eq. (6) that propagating three-dimensional acoustic gravity waves exist in two frequency bands $\omega \le N_c$ and $\omega \ge N$. At the low frequency ($\omega \le N_c$) they exhibit the properties of internal gravity waves. Their properties for $\omega \ge N$ approach the isotropic sound. Simultaneously with waves, two types of boundary layers with the characteristic thickness

$$\delta_{St} = \delta_N \sqrt{2/\sin\Theta_\omega}, \quad \delta_i = \delta_N \, 2\sin\Theta_\omega \Big/ \left|\sin^2\Theta - \sin^2\Theta_\omega\right|, \tag{10}$$

where $\delta_N = \sqrt{\nu/N}$, $\Theta_\omega = \arcsin(\omega/N)$, are formed on rigid boundaries. The first of them is similar to the periodic Stokes flow in a homogeneous fluid (*Stokes*, 1847), and the second, whose parameters depend both on the buoyancy frequency N and on the speed of sound c, is specific for stratified media. The universal microscale $\delta_N = \sqrt{\nu/N}$ is common for both boundary layers. The thicknesses of the boundary layers also depend on the slopes of the waves and bounding surfaces.

The frequency band $\omega_- < \omega < \omega_+$ of the existence of inertial gravity waves in stratified rotating incompressible media is limited by the values

$$2\omega_\pm^2 = N^2 + 4\Omega^2 \pm \sqrt{\left(N^2 + 4\Omega^2 \cos 2\varphi\right)^2 + 16\Omega^4 \sin^2 2\varphi},$$

which depend on the latitude of the observation point. Simultaneously with 3D inertial gravity waves, there are two types of boundary layers with the scales

$$\delta_{b\pm} = \delta_N \sqrt{\frac{2}{\left|\omega_\pm - \omega^*\right|}}, \quad \omega_\pm = \frac{\sin^2\Theta}{2\omega^*}\left[1 \pm \sqrt{1 + \frac{16\omega^2\Omega^2F^2}{N^4 \sin^4\Theta}}\right] \quad \omega^* = \frac{\omega}{N}. \tag{11}$$

Inertial acoustic waves in homogeneous fluid (N = 0) coexist with two separated boundary layers with the thickness

$$\delta_{b\pm} = \sqrt{\nu/\Omega|F \pm \cos\Theta_\omega|}\ , \tag{12}$$

where $\Theta_\omega = \arccos(\omega/2\Omega)$ is the slope of the propagation lines of the inertial acoustic waves to the horizon. One of these waves with thickness δ_{b+} is an analogue of the known Ekman layer. Periodic flows have the properties of inertial and acoustic waves for $\omega << \Omega$ and the opposite case, respectively.

Three-dimensional acoustic waves in a homogeneous fluid ($N = \Omega = 0$) are characterized by the dispersion $\omega^2 = k^2\left(c^2 - i\omega(4\nu/3 + \mu)\right)$. In this case two sets of boundary layers are joined in the united doubly degenerate Stokes layer with the thickness $\delta_b = \sqrt{2\nu/\omega}$. Perturbations within this layer are transverse with zero divergence of the velocity; i.e., the fluid within it behaves as incompressible.

From the form of the dispersion of three-dimensional periodic perturbations in a homogeneous incompressible fluid, $k^2\left(\omega + i\nu k^2\right)^2 = 0$, when $(N = \Omega = \nabla \cdot \mathrm{u} = 0)$, it follows that this medium is free of developed propagating waves. Doubly degenerated viscous boundary layer consisting of two periodic Stokes flows with thickness $\delta_b = \sqrt{2\nu/\omega}$ is formed on the rigid oscillating boundary. It means that classical 3D Navier–Stokes equations both for compressible and incompressible fluids form ill-posed problem due to merging of boundary layers. The degeneration of Navier–Stokes equations for homogeneous fluids is removed by specific boundary conditions abolished one of the boundary layers (2D or axial-symmetric problems).

5. Attached internal waves past horizontally moving strip

Calculation of periodic waves beams show that singular components manifest itself near the contact rigid surface as set of boundary layers and inside the wave beam as fine components with their intrinsic spatial and temporal scales (*Chashechkin et al.*, 2004). Here attached internal waves produced by a horizontally moving strip are discussed as example of 2D Navier–Stokes equations exact solution. In this case both the boundary conditions and governing equations are linearized.

In the simplest case when the source of disturbances is uniformly moving horizontal strip the set of governing equations, Eq. (1), is transformed into standard internal wave equation for stream function Ψ defining components of velocity $u_x = \partial\Psi/\partial z$, $u_z = -\partial\Psi/\partial x$

$$\left[\frac{\partial^2}{\partial t^2}\left(\frac{\partial^2}{\partial x^2} + \frac{\partial^2}{\partial z^2}\right) + N^2\frac{\partial^2}{\partial x^2} - \nu\frac{\partial}{\partial t}\left(\frac{\partial^2}{\partial x^2} + \frac{\partial^2}{\partial z^2}\right)^2\right]\Psi = 0 \tag{13}$$

with no-slip boundary conditions at the plane and on the strip of length a

$$\left.\frac{\partial\Psi}{\partial z}\right|_{z=0}=U\,\vartheta\left(x+\frac{a}{2}-Ut\right)\vartheta\left(\frac{a}{2}+Ut-x\right),$$
$$\left.\frac{\partial\Psi}{\partial x}\right|_{z=0}=0. \tag{14}$$

and attenuation of all disturbances at infinity.

The solution of Eq. (13) is represented as the Fourier integral expansion:

$$\Psi(x,z,t)=\int_{-\infty}^{\infty}e^{-i\omega t}\int_{-\infty}^{\infty}\left[A_w(\omega,k)e^{ik_w(\omega,k)z}+B_i(\omega,k)e^{ik_i(\omega,k)z}\right]e^{ikx}\,dk\,d\omega \tag{15}$$

The roots of the dispersion equation, corresponding Eq. (13) are

$$\omega^2\left(k^2+k_z^2\right)-N^2k^2+i\omega\,\nu\left(k^2+k_z^2\right)^2=0 \tag{16}$$

and include both regular in viscosity (corresponding to waves)

$$k_w^2(\omega,k)=-k^2+\frac{i\omega}{2\nu}\left[1-\sqrt{1+\frac{4i\nu k^2N^2}{\omega^3}}\right],$$

and singular in viscosity characterizing boundary layers

$$k_i^2(\omega,k)=-k^2+\frac{i\omega}{2\nu}\left[1+\sqrt{1+\frac{4i\nu k^2N^2}{\omega^3}}\right].$$

Substitution of Eq. (15) into the boundary conditions Eq. (14) leads to a system of algebraic equations for spectral component of amplitude

$$A_w(w,k)=-A_i(\omega,k)=\frac{iU}{\pi k\left(k_w-k_i\right)}\sin\frac{ka}{2}\delta(\omega-kU). \tag{17}$$

Substitution of the solution of Eq. (17) into Eq. (15) and integration give the resultant expression for the stream function

$$\Psi(x,z,t) = \frac{iU}{\pi} \int_{-\infty}^{\infty} \frac{1}{k} \sin\frac{ka}{2} e^{ik(x-Ut)} \frac{e^{ik_w(kU,k)z} - e^{ik_i(kU,k)z}}{k_w(kU,k) - k_i(kU,k)} dk. \quad (18)$$

From Eq. (18), it follows that the field of lee waves is transient ahead and stationary behind the source in the local reference frame (*Bardakov* and *Chashechkin*, 2004).

Visualization of exact solution, Eq. (18), for the vertical component of velocity and vorticity by the modified method of isopleths makes it possible to reveal not only the complete structure of transient leading and stationary attached internal waves, but also details of the fine structure of the boundary layer. Wave perturbations near the plate are more contrasting for the horizontal velocity than for the vertical one (*Fig. 1*). Moreover, the number of perturbation peaks in a single wave field turns out to be different for different wave components (one peak band for the horizontal component and two bands for the vertical one). The phase surface slope to the horizon is characterized by local frequency values.

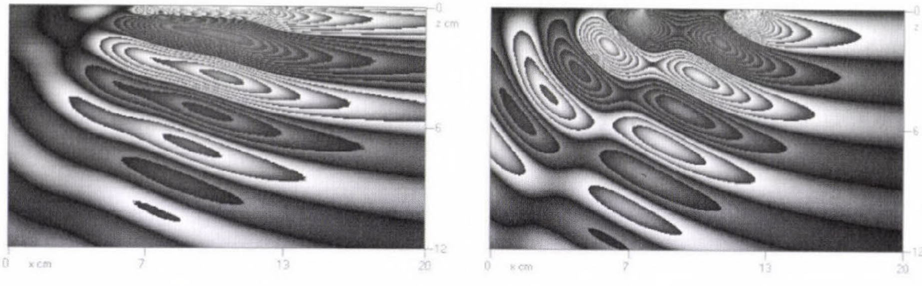

(a) (b)

Fig. 1. Pattern of attached internal waves for horizontal (a) and vertical (b) components of velocity. Bright points on upper horizontal line indicate edges of the strip moving from left to right (T_b = 6.28 s, a =5.5 cm, U = 1 cm/s, λ = 6 cm, Fr = 0.18, Re = 550).

The detailed structure of the module of field velocity within the boundary layer is shown as a magnified continuous-tone image in *Fig. 2*. Both leading and trailing edges of the plate incorporate singular perturbations with the vertical velocity oriented at first toward the fluid and, then, toward the plate. The edge singularities of the horizontal velocity are much less prominent. The thickness of Prandtl's boundary layer (with a typical length scale of $\delta_u = \nu/U$) monotonously increases with distance from the leading edge the same way as in laminar flow of a homogeneous liquid. The boundary layer is detached from the trailing edge into the liquid. The complicated structure of boundary layers at a horizontally moving plate indicates that it is impossible to model the formation of attached internal waves near a real obstacle in terms of a set of singular mass or force sources.

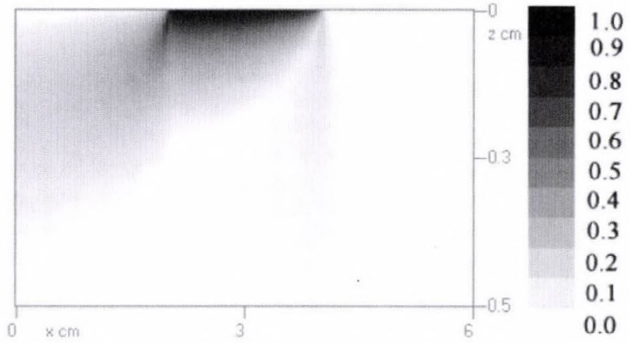

Fig. 2. Module of field velocity within the boundary layer on the strip (T_b = 14 s, a = 2 cm, U = 1 cm/s, λ = 14 cm, Fr = 1.12, Re = 200.

The complex structure of a calculated flow pattern indicates that even on the strip a drag is produced due to emission of waves and viscous lost of energy. Calculated flow pattern fit in laboratory experiments when sensitive Schlieren instrument and markers are used for flow observation.

6. Conclusion

Analysis of complex questions put by F. Nansen shows that internal wave fields have a complex structure and include transient and attached waves and boundary singularities. Therefore, molecular effects play an important role in a stratified flow fine structure formation. Presented classification of 3D periodic motions in fluids generalizes classical Stokes scheme for the wave and accompanying periodic boundary layer. Two different types of viscous boundary layers on rigid boundaries supplement all kinds of waves. The first of them is similar to the periodic Stokes flow, the second one has no analogue in homogeneous fluid. Diffusivity effects are resposible for the formation of new kinds of boundary layers.

In the general case, the dynamics of hydrodynamic systems is determined by nonlinear interaction between all structural elements of flows including both regular (waves, vortices) and singular types (boundary layers and singular components in a fluid interior). In particular, variations in thickness and nonlinear interactions of boundary layers make the generation of internal waves possible even in the cases when the direct excitation is forbidden by the linear theory. Owing to large vorticity, interacting boundary layers may be effective generators of vortex motions. Instruments for experimental studies of fluid dynamics must resolve the fine structure of the smallest elements of flows.

Acknowledgements—The work is supported by the Russian Foundation for Basic Research (Grant 05-05-64090).

References

Bardakov, R.N. and *Chashechkin, Yu.D.*, 2004: Calculation and visualization of two-dimensional joined internal waves in viscous exponentially stratified fluid. *Atmospheric and Oceanic Physics 40*, 470-482.

Brunt, D., 1927: The period of simple vertical oscillations in the atmosphere. *Q. J. Roy. Meteor. Soc. 53*, 30-32.

Chashechkin, Yu.D. and *Kistovich, A.V.*, 2004: Classification of Three-Dimensional Periodic Fluid Flows. *Doklady Earth Science 397*, 667-681.

Chashechkin, Yu.D., Vasiliev, A.Yu., and *Bardakov, R.N.*, 2004: Fine structure of Beams of Three-Dimensional periodic internal wave. *Doklady Earth Sciences 397A*, 816-819.

Ekman, V.W., 1906: On dead water: Being a description of the so-called phenomenon often hindering the headway and navigation of ships in Norwegian Fjords and elsewhere and an experimental investigation of its etc. *The Norwegian North Polar expedition 1893–1896. Scientific Results* (ed.: *F. Nansen*). Vol. 5, 1-152.

Lighthill, J., 1978: *Waves in Fluids*. University Press, Cambridge.

Nansen, F., 1992: Into the country of Future – Great North Marine way from Europe to Asia through Kara Sea (*Fremtidens Land*) (in Russian). Krasnoyarsk, kn. Izdat.

Pasetskii, V.M., 1986: *Fridtjof Nansen* (in Russian). Nauka, Moscow, 336 pp.

Rayleigh, Lord, 1980: Investigation of the character of the equilibrium of an incompressible heavy fluid of variable density. *Proceeding of the London Mathematical Society*. 1883. Vol. 14, 170-177 (Papers V.2, 200).

Stokes, G.G., 1847: On the theory of oscillatory waves. *Transactions of Cambridge Philosophical Society 8*, 441-455. (*Mathematical and Physical Papers 1*, 1880. University Press, Cambridge, 197-229).

Väisälä, V., 1925: Über die Wirkung der Windschwankungen auf die Pilotbeobachtungen. *Soc. Sci. Fenn. Commentat. Phys.-Math. 2*, 19-37.

IDŐJÁRÁS

Quarterly Journal of the Hungarian Meteorological Service
Vol. 111, No. 2–3, April–September 2007, pp. 149–159

A new model for boundary layer flows interacting with particulates in land surface on complex terrain

Kirill Karelsky, Arakel Petrosyan* and **Igor Smirnov**

*Space Research Institute of the Russian Academy of Sciences, Profsoyuznaya 84/32, Moscow 117997, Russia; E-mail: *apetrosy@iki.rssi.ru*

(Manuscript received in final form January 29, 2007)

Abstract—This paper presents a model describing three-dimensional atmospheric flows with solid particles or aerosols. The model uses the Nigmatulin equations for two-phase atmosphere, which describes lifted atmosphere by ideal gas equations with variable equation of state. The Godunov numerical method based on solution of the one dimensional initial discontinuity decay problem on an interface of two cells of computational grid is applied in this work.

Key-words: boundary layer, Curant-Friedrichs-Levy condition, discontinuity decay problem, Godunov method, grid-scale function, Nigmatulin equations, scheme viscosity, single-velocity model, relaxation, two-phase atmosphere

1. Introduction

In the present work a new physical model of transport of atmospheric impurities (solid particles or heavy gases) by the wind in regions over non-homogeneous or variable in time surfaces is realized. This task is very important for solving the problems linked with preservation and optimal using of the nature. It is necessary to discuss fundamental difficulties, which prevent constructive solution of this problem. Essentially this task can be divided into two subtasks:

- Description of an atmospheric flow in planetary boundary layers under non-homogeneous and/or non-stationary conditions.
- Prediction of the space-time distribution of transported particulates concentration.

* Corresponding author

Well-known traditional theories of boundary layers are applied to atmospheric flows along plane, homogeneous, and stationary surfaces. Along such ideal surfaces, atmospheric boundary layer is also horizontally homogeneous and it is in state of equilibrium. The problem of impurity transport reduces to solving the equation of passive scalar for turbulent flow in boundary layer in this simple situation. However, concentration of particulates or external factors can be beyond the limits of applicability of the passive scalar approximation (*Barenblatt* and *Golitsin*, 1974). In these cases the full system of thermo-hydrodynamic equations of boundary layer with parameterization of sub-grid scale turbulent flows in large eddy simulations method or in Reynolds averaged equations approach fails. Non-homogeneity of the Earth surface and its variations in time change the picture of the flow considerably. When flowing around various obstacles (mountains, buildings, and street canyons), the flow may change both dramatically and gradually. Usually, different space-time variations of planetary surface may appear simultaneously. In such situations it is impossible to create an adequate model of turbulent boundary layer.

The complicated topology of flows in such complex terrain may change the character of the impurity. In such a situation the initially passive impurity may be transformed into active one (affecting the hydrodynamic flow). A well-known example, which should be mentioned, is the origination of dust vortexes (devils) in domains with valleys. Moreover, an initially homogeneous cloud of particulates is transforming to complex non-homogeneous structure. Such structure includes regions with high concentration of impurities, which have its own dynamic behavior. As a result, besides the possibility of changing of impurity character, which was stated above, we face the necessity to analyze the interaction of such formations with the entire cloud of particles, and to predict duration of their life.

In the present work we develop the method describing the transport of particulates in atmospheric boundary layer over complex surface. This method is directed to overcome the difficulties of traditional methods, described above. Besides, it practically expands the opportunity of predictions of transportation of solid particles onto cases when it is impossible to use the approximation of passive scalar or in changes of impurity character in particular domains of cloud. Our model also permits to analyze phenomena, which are driven by complex topology of the flow above obstacles and can describe processes on interface between cloud of solid particles and pure atmosphere. In our model we use Nigmatulin equations (*Nigmatulin*, 1987) describing two-phase medium "gas-particles" by equations of ideal gas with variable equation of state. Effective equation of state for such medium depends upon characteristic size and concentration of spherical particles, and in the limit of absence of solid phase it is converted to usual equations of the ideal gas. Practically, the task to analyze the transport of particles in the atmosphere is reduced to solving equations of ideal gas with variable in space and time equations of state.

It provides the opportunity of describing the loaded and pure atmosphere by the same set of equations with different thermodynamic properties. In fact it means that this system of equations can be applied for modeling the boundary of clouds of solid particles and pure atmosphere. The use of the system of equations of ideal gas with a variable equation of state provides a direct dependence of hydrodynamic flow velocity upon the concentration of solid phase. Practically, it means that there is a possibility of overstepping the limits of applicability of passive impurity approximation.

The main idea of the suggested method is to use the non-viscous equations for modeling the transport of solid particles near a complex surface (*Kulikovskii et al.*, 2001). For free atmospheric flows the Reynolds number, which characterizes the ratio of inertial force to viscosity force in hydrodynamic equations, is very large. That is why nonlinear inertial terms exceed significantly the molecular viscosity terms. The opposite situation appears for atmospheric flows near a surface, where viscosity mechanisms play the main role.

Flows in a viscous atmosphere with arbitrarily small viscosity coefficient have to satisfy non-slip conditions, which demand the full velocity of flow on solid surface to be zero. Undoubtedly, the hypothesis of Prandtl is satisfied (*Schlichting*, 1955). This means that the terms describing dissipation of energy in atmospheric flows are comparable with inertial force for a wide range of conditions in a layer boundering a solid surface. Thus, according to the Prandtl hypothesis, atmospheric flows, characterized by a high Reynolds number, formate a boundary layer. Within this layer a necessary transition from zero value of wind velocity to finite value on external side of a boundary layer is provided. In this case such values on external side of the boundary layer are very similar to the values that appear in an ideal atmospheric flow (*Zilitinkevich*, 1970). Within this layer, the high gradients of velocity field lead to the situation when viscosity effects are comparable to inertial force effects.

Thus, first we have to conciliate the concept of high gradients of wind in a boundary layer, and second, we have to ignore molecular viscosity in equations of the two-phase atmosphere. In this work we suggest to provide the high wind field gradients by means of the scheme viscosity of the numerical algorithm for modeling phenomena near a surface.

We use Godunov method (*Godunov*, 1976) for numerical solution of equations of the two-phase atmosphere. The main idea of Godunov method is to use the generalized solutions of initial discontinuity decay problem with discretization of impulse, mass, and energy conservation laws in each cell of the computational domain. These solutions include local tangential gaps, which do not appear on outer scales, and none the less provide dissipation of kinetic energy, as it is necessary for flows in a boundary layer. Thus, the structure of the used finite difference scheme provides diffusion of ranges with high entropy on all space coordinates and represents qualitatively effects of molecular viscosity. It should be mentioned that influence of the scheme viscosity is shown more considerably in the situation when boundary layer is loaded with solid particles and in regions with considerable variations of surface relief. In such cases the influence of molecular viscosity also increases in reality. The value of molecular viscosity depends on gradients of sub-grid flows and has a finite limit as the grid of discretisation decreases. Thus, it can be regulated by a choice of the size of the grid. It is clear that for a turbulent flow, the scheme viscosity exceeds one for laminar flows, demonstrating a well-known relation between the turbulent and laminar viscosity.

2. Model of the effective ideal gas for atmosphere with solid particles

The effects of inhomogeneities seriously complicate the investigations of the processes in the atmospheric boundary layers. If we suppose that the size of particles is much smaller than the characteristic scale of those of atmospheric flows, we may describe macroscopic processes in such atmosphere with averaged parameters. We will use the same mass, impulse, and energy conservation equations for the atmosphere lifted by solid particles as for a single-phase medium. In this case it is necessary to take into account boundary conditions on the interface between the phases.

We suppose that volume concentration of solid phase is small enough. Let α_i $(i = 1,2)$ be the part of particulates volume which is occupied by each phase: $\alpha_1 + \alpha_2 = 1$ $(\alpha_i \geq 0)$. Hence, $\alpha_2^2 \leq 1$. The solid phase is represented by spherical particles of the radius a. In our model ρ_1^0 and ρ_2^0 are the density of the atmosphere and the solid particles, respectively, n is the number of particles of dispersed phase in a unit volume of particulates. Thus, according to our assumption, we have $\alpha_2 = \frac{4}{3}\pi a^3 n$, $\alpha_1 = 1 - \alpha_2$. Weights of phases in a unit volume of the atmosphere are denoted as $\rho_i (i = 1,2)$, and $\rho_1 = \rho_1^0 \alpha_1$, $\rho_2 = \rho_2^0 \alpha_2$, $\rho = \rho_1 + \rho_2$. We ignore the effects of inertia for moving solid particles, their interactions and collisions, and the process of subdivision and sticking of particles. Viscosity and heat-conduction of fluid and solid phase do not appear in the macroscopic transport of impulse and energy. The values of viscosity and heat-conduction are needed only to describe processes in inter-phases interaction. It allows using non-slip boundary conditions near the solid surface to find parameters of the fluid phase. The density of the atmosphere with solid particles is much less than the density of the substance of solid particles.

Under these conditions the atmosphere with solid particles allows hydrodynamic description. If velocities, $\mathbf{v}$, and temperatures of these phases are equal to each other, we can describe such impurity by equations of nonviscous and non-heat-conducting medium of ideal gas. For three-dimensional atmosphere, these equations can be written as:

$$\begin{aligned}
&\frac{\partial\rho}{\partial t}+\frac{\partial(\rho v_x)}{\partial x}+\frac{\partial(\rho v_y)}{\partial y}+\frac{\partial(\rho v_z)}{\partial z}=0,\\
&\frac{\partial(\rho v_x)}{\partial t}+\frac{\partial(p+\rho v_x^2)}{\partial x}+\frac{\partial(\rho v_x v_y)}{\partial y}+\frac{\partial(\rho v_x v_z)}{\partial z}=0,\\
&\frac{\partial(\rho v_y)}{\partial t}+\frac{\partial(\rho v_x v_y)}{\partial x}+\frac{\partial(p+\rho v_y^2)}{\partial y}+\frac{\partial(\rho v_y v_z)}{\partial z}=0,\\
&\frac{\partial(\rho v_z)}{\partial t}+\frac{\partial(\rho v_x v_z)}{\partial x}+\frac{\partial(\rho v_y v_z)}{\partial y}+\frac{\partial(p+\rho v_z^2)}{\partial z}=0,\\
&\frac{\partial e}{\partial t}+\frac{\partial(e+p)v_x}{\partial x}+\frac{\partial(e+p)v_y}{\partial y}+\frac{\partial(e+p)v_z}{\partial z}=0.
\end{aligned}\tag{1}$$

Here e is the total energy per unit volume of mixture: $e=\rho(\varepsilon+\frac{v_x^2+v_y^2+v_z^2}{2})$, $\varepsilon(\rho,p)$ is the internal energy determined by the equation of state. In accordance with Nigmatulin's model (*Nigmatulin*, 1987), rheology of mixture can be described by the equation of state of ideal gas with the effective gas constant R:

$$\varepsilon=cT,\ p=\rho RT,\quad \text{where } R=x_1R_1,\ c=x_1c_1+x_2c_2,\ x_i=\rho_i/\rho,\ x_1+x_2=1,$$

R and R_1 are the specific ratios of atmosphere gas mixture and solid particles, respectively, and c, c_1, c_2 are the heat capacities of the atmospheric gas mixture and solid phase under constant pressure accordingly. Thus, to close the system Eq. (1), we add a complimentary equation of change of mass of solid particles:

$$\frac{\partial\rho_2}{\partial t}+\frac{\partial(\rho_2 v_x)}{\partial x}+\frac{\partial(\rho_2 v_y)}{\partial y}+\frac{\partial(\rho_2 v_z)}{\partial z}=0.\tag{2}$$

The described model of the atmosphere with solid particles is especially useful for modeling processes near a solid surface, because it formally coincides with classic hydrodynamic equations of ideal gas with the recalculated adiabatic index γ (*Ovsyannikov*, 1981): $\gamma=(c+R)/c\le\gamma_1$, and with the recalculated velocity of sound wave: $C_s=\sqrt{\frac{\gamma p}{\rho}}=C_{1s}\sqrt{\frac{\gamma x_1}{\gamma_1}}\le C_{1s}$. The formal coincidence of the equations of clear and lifted atmosphere provides a possibility of modeling nonstationary processes of the particle transport in the atmosphere and motion of dust clouds. In particular, it allows to investigate stability and dynamics of the propagation of a dust cloud and its boundary.

The main limitation of the model is related to ignoring the two-speed effects due to relative motion of the solid phase. It is interesting that the decreasing of the size of solid particles and retaining the same parameters of the atmosphere naturally result in a decrease of relaxation time of velocity and temperature of each phase. If characteristic time scale of the investigated flow is much smaller than the velocity inter-phase relaxation time, we can use a one-speed scheme. According to *Nigmatulin* (1987), for small characteristic Reynolds numbers (Re_1, $2 \leq 1$), describing the atmospheric stream flow over the individual particle, the relaxation time is determined only by viscosity of flowing phase μ_1, by the size and density of the particles substance $\rho_2^{\ 0}$: $t_1 = \dfrac{2a^2 \rho_2^{\ 0}}{9\mu}$. In the other limit case of high Reynolds numbers (Re_1, $2 \geq 50$), the relaxation time is determined by the density of the ambient atmosphere phase $\rho_1^{\ 0}$, its flow velocities v_0, and the velocities of particles v_2: $t_2 = \dfrac{16a}{3} \dfrac{\rho_2^{\ 0}}{\rho_1^{\ 0}} \dfrac{1}{|\upsilon_0 - \upsilon_2|} << t_1$.

3. *Computational method*

To build the finite difference scheme, we use a cubic orthogonal grid with constant step. Initially we have calculation domain size (X + 2) (Y + 2) (Z + 2) with given cell size L. The internal part of the calculation region has the size XYZ and is filled with gas and solid particles with arbitrary initial conditions.

Internal part of the calculation region is surrounded by a layer of gas with arbitrary boundary conditions. We suppose that boundary cells are "infinite" – if any part of the ambient gas or gas with solid particles flow in or flow out from the cell, the thermodynamic parameters of the boundary conditions do not change. Inside of any internal cell, all thermodynamic parameters are isotropic through one time step.

Procedure of digitization of the computational domain consists of putting the space grid with constant step on this domain. In this case, for a cell, which contains elements of relief we set in the following criterion:

- If a volume filled with gas is less than one half of the total volume of the cell, we suppose that this cell completely consists of relief, otherwise we suppose that this cell is completely filled by gas or gas with admixture. In latter case, values of thermodynamic parameters for all cells are supposed to be equal to thermodynamic parameters in real range.

Calculation of all thermodynamic parameters in studied region is carried on the base of integral form of the equations, which in this case looks as follows:

$$
\begin{aligned}
&\oiiint \rho_1 dxdydz + \rho_1 v_x dydzdt + \rho_1 v_y dxdzdt + \rho_1 v_z dxdydt = 0,\\
&\oiiint \rho_2 dxdydz + \rho_2 v_x dydzdt + \rho_2 v_y dxdzdt + \rho_2 v_z dxdydt = 0,\\
&\oiiint \rho_1 v_x dxdydz + (p + \rho_1 v_x^2) dydzdt + \rho_1 v_x v_y dxdzdt + \rho_1 v_x v_z dxdydt = 0,\\
&\oiiint \rho_1 v_y dxdydz + \rho_1 v_x v_y dydzdt + (p + \rho_1 v_y^2) dxdzdt + \rho_1 v_y v_z dxdydt = 0,\\
&\oiiint \rho_1 v_z dxdydz + \rho_1 v_x v_z dydzdt + \rho_1 v_y v_z dxdzdt + (p + \rho_1 v_z^2) dxdydt = 0,\\
&\oiiint e dxdydz + (e + p) v_x dydzdt + (e + p) v_y dxdzdt + (e + p) v_z dxdydt = 0.
\end{aligned}
\tag{3}
$$

Suppose that the integration can be implemented on any close surface in four-dimensional space (x,y,z,t). We consider integrals in expressions of Eq. (3) as surface integrals of the second type, i.e., as integrals on oriented surface. Using the mean theorem we obtain the following equations:

$$
\begin{aligned}
&R_1^* = R_1 + \frac{\tau}{S}(R_1^{(1)} v_x^{(1)} - R_1^{(3)} v_x^{(3)} + R_1^{(2)} v_y^{(2)} - R_1^{(4)} v_y^{(4)} + R_1^{(5)} v_z^{(5)} - R_1^{(6)} v_z^{(6)}),\\
&R_2^* = R_2 + \frac{\tau}{S}(R_2^{(1)} v_x^{(1)} - R_2^{(3)} v_x^{(3)} + R_2^{(2)} v_y^{(2)} - R_2^{(4)} v_y^{(4)} + R_2^{(5)} v_z^{(5)} - R_2^{(6)} v_z^{(6)}),\\
&R_1^* v_x^* = R_1 v_x + \frac{\tau}{L}((P^{(1)} + R_1^{(1)} v_x^{(1)^2}) - (P^{(3)} + R_1^{(3)} v_x^{(3)^2})),\\
&R_1^* v_y^* = R_1 v_y + \frac{\tau}{L}((P^{(2)} + R_1^{(2)} v_y^{(2)^2}) - (P^{(4)} + R_1^{(4)} v_y^{(4)^2})),\\
&R_1^* v_z^* = R_1 v_z + \frac{\tau}{L}((P^{(5)} + R_1^{(5)} v_z^{(5)^2}) - (P^{(6)} + R_1^{(6)} v_z^{(6)^2})),\\
&E^* = E + \frac{\tau}{L}((E^{(1)} + P^{(1)}) v_x^{(1)} - (E^{(3)} + P^{(3)}) v_x^{(3)} + (E^{(2)} + P^{(2)}) v_y^{(2)},\\
&\qquad - (E^{(4)} + P^{(4)}) v_y^{(4)} + (E^{(5)} - P^{(5)}) v_z^{(5)} - (E^{(6)} + P^{(6)}) v_z^{(6)}).
\end{aligned}
\tag{4}
$$

The obtained formulas have simple physical meaning and they determine the stream of flowing phase and solid particles, impulse, and energy through a plane surface. In the set of equations of Eq. (4) symbols with superscripts are used to denote the values of thermodynamic parameters at corresponding sides of the cell. Symbols with asterisk denote the values of parameters inside the cells after time τ.

Starting from the initial conditions, our task consists of computing the value of all parameters inside the computational domain after a fixed time τ. Common computation scheme of the single time step, i.e., transition from the state of task on time moment t_0 to the state on time moment $t_0 + \tau$, in general consists of three parts:

- We have to compute the values of thermodynamic parameters on all sides of all cells in our computational domain, as a solution of the corresponding Riemann problem.
- It is necessary to find the maximum value of time step τ, which satisfies the Courant-Friedrich-Levy condition of stability (*Rogdestvenskiy* and *Yanenko*, 1987).
- Finally, we have to compute the values of thermodynamic parameters inside all cells in our computational domain at the next time step, which guaranties the stability of computation.

To finish the description of this method, we describe an algorithm of computation of flux values. The value of hydrodynamic parameters in neighbor cells is assumed to be an initial condition for one-dimension Cauchy problem for two infinite domains of gas. The concentration of dispersion phase in each of the gases is constant during one step of time and accordingly, effective value of polytrophic constant also stays constant during a computation step of time. Thus, our task is to solve the initial discontinuity decay problem for two polytrophic gases with different polytrophic constants. This task is Cauchy problem with constant initial conditions or Riemann problem. The solution of this task is well-known (*Landau* and *Lifshic*, 1988; *Kochin et al.*, 1963; *Billett* and *Toro*, 1997).

4. Modeling results

To illustrate the capabilities of the developed theory, we have carried out numerical computations. These model computations are directed to show main effects, described by the model. We have created a computer code, which computes the problem with any complex relief. It demonstrated strong influence of admixture on the character of flow and formation of the boundary layer due to scheme viscosity on non-homogeneous surface. The computations are carried out for two different types of obstacles and for conditions characteristic for earth winds: the wind velocity is 10 m/s, the pressure is 100 000 Pa, the tdensity of medium and density of admixture are equal to 1.2 kg/m^3 and 0.01 kg/m^3, accordingly. In all cases, the size of the computational domain is chosen in such a way, that the number of cells within the relief or obstacles is about 10% of all cells in the computational domain. Boundary conditions are the following:

- Non-slip condition on solid surface,
- Constant values of stream on boundaries far from obstacle.

Nontrivial influence of particulates (which was taken to be SiO_2, i.e., sand in the experiments) has been obtained and graphically shown in the following figures of distribution of impurity and velocity field. As *Figs. 1* and *2* show, in the region of particulates, there is a zone with increasing and decreasing, horizontal component of the velocity compared to the average value. This fact is explained by the influence of admixture, because admixture has an active influence on forming boundary layer. *Figs. 1* and *2* show two-dimension visualization of moving steam of admixture over different kind of reliefs. Digits mean:

1. stream of particulates,
2. elements of relief,
3. wind direction,
4. domain of turbulence.

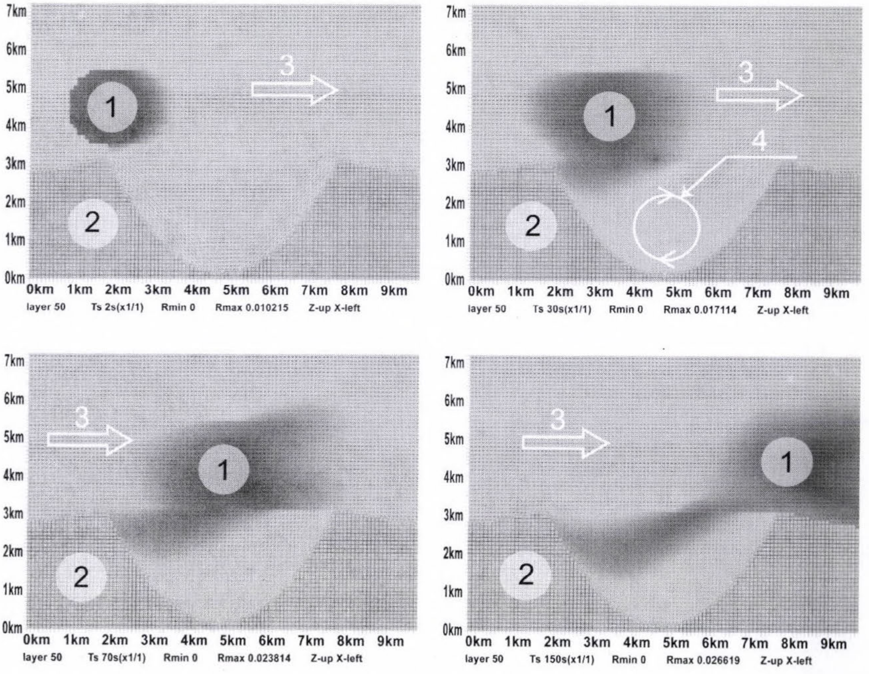

Fig. 1. Dynamics of the particulate cloud moving over a "crater". Tcomp = 2, 30, 70, 150c.

Fig. 3 shows the profiles of the x-component of the velocity at the different grids of computational domain near a surface. It clearly represents the gradients of wind velocity due to scheme viscosity.

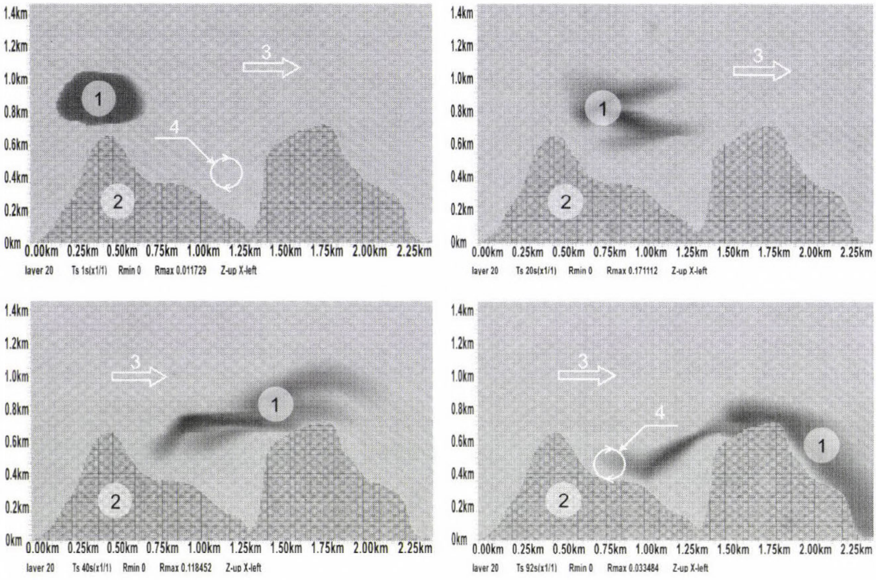

Fig. 2. Dynamics of the particulate cloud moving over "mountains". Tcomp = 1, 20, 40, 92c.

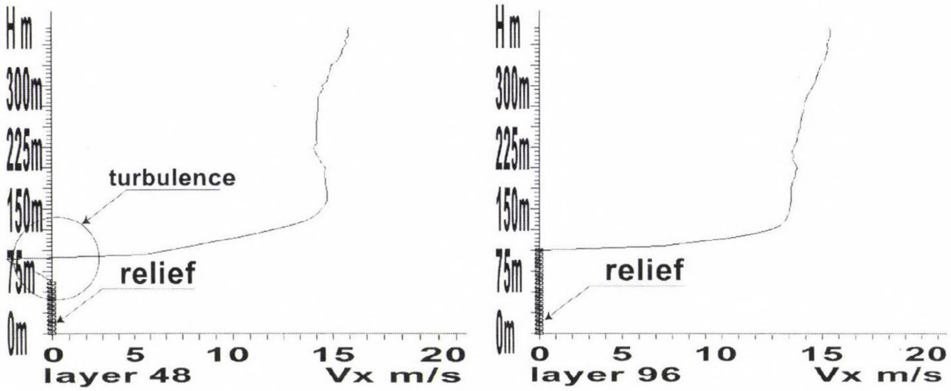

Fig. 3. Profile of the x-component of the velocity (v_x) in different layers.

5. Conclusions

At present work a three-dimension model of transport of solid particles and aerosols near a solid surface is proposed. This model is based on two main physical ideas:

- Description of two-phase atmospheric flows on the base of Nigmatulin equations (equations for perfect gases with renormalized equation of state),
- Use of the Godunov method, which has a scheme viscosity, for numerical solution of model equations.

The main advantage of our model the possibility of modeling of two-phase atmospheric flows in a range, where the vertical scale of inhomogeneousness is much higher than the horizontal scale. This is because of using initial fluid equations in integral form, and the idea of scheme viscosity provides good conditions for the stability of computations. As usual, in this case traditional modeling methods as LES and method based on Reynolds averaging face difficulties due to the modeling of turbulence in fractional grids, and these methods are still in the beginning of development. We will provide results of such computations with our method in subsequent papers. We showed, the that presence of two mechanisms of scheme viscosity in the created algorithm, namely, presence of homogeneities of surface and gradients of concentration of solid admixture, allows reproducing dynamic transport of admixture in boundary layer.

References

Barenblatt, G.I. and *Golitsin, G.S.*, 1974: On the local structure of developed dust storms. *J. Atmos. Sci. 31.*

Billett, S.J. and *Toro, E.F.*, 1997: WAF-Type schemes for multidimensional hyperbolic conservation laws. *J. Comput. Phys.*

Godunov, S.K., 1976: *Numerical Solve Multidimensional Tasks of Gas Dynamics*. Nauka, Moscow.

Kochin, N.E., *Kibel, I.A.*, and *Rose, N.V.*, 1963: *Theoretical Hydromechanics*. Phismatgis, Moscow.

Kulikovskii, A.G., *Pogorelov, N.V.*, and *Semenov, A.U.*, 2001: *Mathematic Questions of Numerical Solve of Hyperbolic Systems of Equations*. Phismatlit, Moscow.

Landau, L.D. and *Lifshic, E.M.*, 1988: *Theoretic Physics*. Nauka, Moscow.

Nigmatulin, R.I., 1987: *Dynamics of Multiphase Medium*. Nauka, Phismatlit, Moscow.

Ovsyannikov, L.V., 1981: *Lectures by Base of Gas Dynamics*. Nauka, Moscow.

Rogdestvenskiy, B.L. and *Yanenko, N.N.*, 1978: *Systems of Quasylinear Equations and Their Application in Gas Dynamics*. Nauka, Moscow.

Schlichting, H., 1955: *Boundary-Layer Theory*. McGraw-Hill, New York.

Zilitinkevich, S.S., 1970: *Dynamics of the Atmospheric Boundary Layer*. Gidrometeoizdat, Leningrad.

IDŐJÁRÁS
Quarterly Journal of the Hungarian Meteorological Service
Vol. 111, No. 2–3, April–September 2007, pp. 161–169

Numerical simulation of cross-flow ventilation of farm buildings in a cold, windy coast climate

Thomas K. Thiis, **Willy K. Jeksrud**[†] and **Andreas S. Flø**

*Department of Mathematical Sciences and Technology,
Norwegian University of Life Sciences,
P.O. Box 5003, N-1432 Ås, Norway; E-mail: thomas.thiis@umb.no*

(Manuscript received in final form February 2, 2007)

Abstract—New demands in farming industry in Norwegian sub-arctic regions has caused a need for larger animal buildings. To minimize the cost of the buildings, they are built without insulation. Uninsulated animal buildings in cold climates raise many new engineering challenges. One challenge is to maintain the animal welfare. Because of the lack of insulation, the walls of the buildings are exposed to a high risk of condensation. This is met with a high ventilation rate to remove the excess moisture. The present study is performed on a farm on the coast in northern Norway. Numerical simulations of cross-flow ventilation for animal housing are performed for several wind directions and different openings. Both the internal and external air movements are simulated in the same simulation domain. The ventilation openings in the walls are varied to assure that the animals are not exposed to draught in periods of cold weather and high wind speed. The study results in a graph showing the relationship between wind velocity, temperature, and porosity of the walls of the building.

Key-words: cross-flow ventilation, numerical simulations

1. Introduction

Animal welfare of cattle has been studied by several authors. A useful parameter for assessing animal exposure to climate is the Lower Critical Temperature (LCT). "LCT is the temperature below which the animal will increase its rate of heat production above normal in order to maintain a constant body temperature" (*Gregory*, 1995). LCT varies according to wind speed, the condition of the coat of the animal, and the feeding level. For cattle LCT is reported in *Table 1* (*Holmes* and *Sykes*, 1984)

Table 1 presents the air velocity in two steps, 0.3 m/s and 3.9 m/s, for dry cattle. This is usually the condition of the cattle in the houses in the study. The upper threshold value is probably also an upper practical limit inside the animal building. If the air velocity should exceed 3.9 m/s, a number of other problems would arise, such as flying debris or dust. In this study, the preferred air velocity inside the animal housing is therefore set to maximum 3.9 m/s in 0.7 m height.

Table 1. Lower critical temperatures (°C) for cattle (*Holmes* and *Sykes*, 1984)

	Maintenance feed				**2 × Maintenance feed**			
	Dry coat		**Wet coat**		**Dry coat**		**Wet coat**	
Wind speed [m/s]	**0.3**	**3.9**	**0.3**	**1.1**	**0.3**	**3.9**	**0.3**	**1.1**
Calves with 40 kg liveweight								
Coat depth 2 cm	9	17	16	24	-9	4	3	16
Adults with 400 kg liveweight								
Coat depth 2 cm	-2	7	6	16	-19	-13	-14	1
Coat depth 3 cm	-7	3	2	11	-36	-20	-22	-5

The climate in Norway varies from cold to polar climate according to the Köeppen climate classification index. The wind climate is also very different in the costal areas compared to the interior of the country. The combination of cold climate and the large moisture emission from the cattle increase the risk of condensation of water on the cold interior surfaces of the animal building. This risk increases even further when the buildings are built without insulation, which is the case for several new animal buildings in Norway. To avoid condensation on interior surfaces, the ventilation rate of the building must be high. To avoid the installation cost of a ventilation system, parts of the walls of the buildings are made permeable, thus the ventilation of the buildings is driven by the wind. The internal climate and the comfort of the animals are thus directly linked to the surrounding climate. The local-scale climate is therefore an important design criterion in the design of new animal buildings. The large differences in local climate will introduce a variety of climate-adapted designs.

Computational Fluid Dynamics (CFD) is a well-known tool determining climate loads on building constructions. It has been used in studies of driving rain, blowing snow, and natural ventilation. *Shklyar* and *Arbel* (2004) performed a study of flow pattern inside and around greenhouses utilizing a similar approach as in the present study.

The indoor temperature should not fall below the LCT at the given feeding level and indoor air velocity. One can assume that the animal coat is dry when the animals are indoors. For high ventilation rates one can also assume that the outside and inside air temperatures are equal. However, measurements of indoor air temperature together with outside air velocity shows that for lower ventilation rates, there is a close correlation between the indoor/outdoor temperature difference and the wind velocity.

1.1. *The building in the study*

The building in the study is 29 meters long and 18 meters wide. Inside the building, there is a section consisting of the milking area, which is ventilated separately and not included in the calculations. There is also a 1.4 meters high fence dividing the building in two long rows, where the cattle can walk freely around. The longest outer walls of the building consist of a permeable, slotted wall from the eaves and 1 m down. The rest of the wall is non permeable to air. *Fig. 1* shows a sketch of the building.

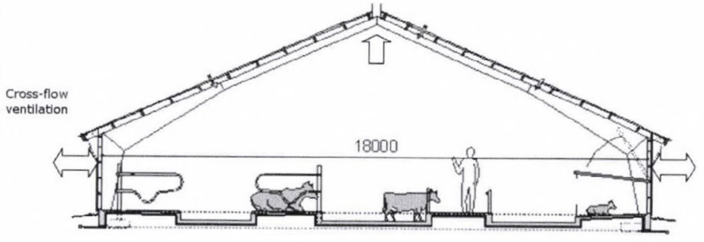

Fig. 1. Section of the building in the study.

2. *Methods*

2.1. *Numerical method*

To simulate the air flow around and inside the building, a general-purpose finite volume CFD code was applied. The CFD code solves the well-known incompressible, time averaged Navier-Stokes equations.

The standard k-ε turbulence model is used to close the equations. The turbulence model is known to compute excessive turbulence near the edges of the windward walls, which also can affect the downwind wakes. It is however widely used, and it is capable of producing realistic wind patterns around buildings. The total number of grid cells in the simulations is around 3.6 million with grid refinement near the surfaces.

The simulation of the wind pattern around and inside the building is performed for 12 wind directions: 0, 30, 60, 90, 120, 150, 180, 210, 240, 270, 300, and 330 degrees. These simulations are performed with an inlet wind velocity of 15 m/s at 10 meters height outside the building. It is assumed that the flow pattern inside the building remains independent of the wind velocity. Based on this assumption, the air velocity inside the building is normalized to the wind velocity at 10 meters height. The normalized air velocity is used to determine the indoor air velocity at different wind velocities. To verify that the flow pattern inside the building remains independent of the wind velocity, a range of simulations has been performed with inlet wind velocity varying according to *Table 1*. In these simulations, the permeability of the wall and the wind direction is kept constant. *Fig. 2* shows the numerical simulation domain.

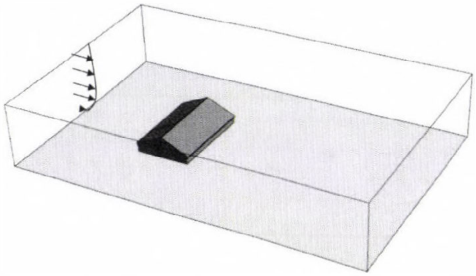

Fig. 2. Numerical simulation domain.

The permeable walls are considered as porous media, and the drag effect is included in the simulations as the source term S_i

$$S_i = C_{R1} u_i - C_{R2} |u| u_i \tag{1}$$

Here C_{R1} and C_{R2} are the linear and quadratic resistance coefficients, respectively. The resistance coefficients are found from solving the flow through the slotted wall with varying slot space, using the CFD solver. *Fig. 3* shows the numerical grid applied in the simulation with 33% porosity, i.e., 33% of the wall is open to air flow.

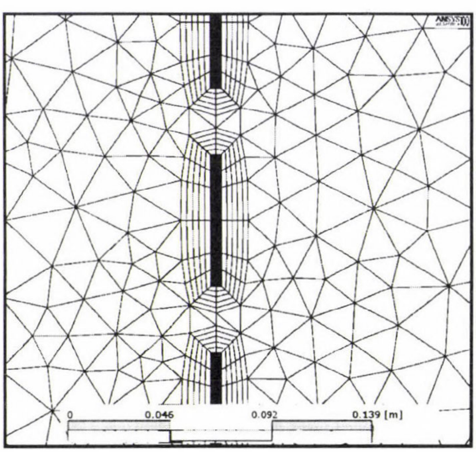

Fig. 3. Numerical grid in the simulation of a 33% slotted wall.

The inlet wind profile follows the logarithmic expression

$$u(z) = \frac{u*}{\kappa} \ln\left(\frac{z}{z_0}\right), \tag{2}$$

where $u(z)$ is the wind speed at height z, z_0 is the roughness of the surface, set to 0.1 m, u^* is the friction velocity set according to *Table 2*, and κ is the von Karman constant, equal to 0.4.

Table 2. Friction velocities used in Eq. (1)

$u(10)$	**5**	**10**	**15**	**25**
$u*$	0.43	0.87	1.30	2.17

The turbulence intensity, i.e., the ratio of the root-mean-square of the turbulent velocity fluctuations and the mean velocity, at the inlet boundary is set to 5%. The outlet boundary is continuative, meaning that the normal derivatives of all quantities are set to zero. On the wall surface boundaries,the boundary conditions are set to "no-slip", i.e., the velocity at the surface is zero. The lateral and top boundaries of the simulation domain have symmetry conditions.

2.2. Permeable wall

To avoid excessive use of grid cells, the slotted walls were modeled as permeable walls with a pressure drop. The pressure drop over slotted walls of different porosity was found simulating the air flow trough the wall, using the CFD solver. The fraction of the wall open to flow and the air velocity were varied to produce the velocity-dependent pressure loss curves. *Miguel* (1998) used a similar procedure on physical measurements of the pressure loss over insect screens.

A section of 3.4 meters of the permeable wall was simulated to minimize any eventual end effects. An example of the numerical grid used in the 33% porosity wall simulation is shown in *Fig. 3*.

3. Results and discussion

3.1. Pressure loss in permeable wall

Fig. 4 shows the results of the simulations of pressure loss in the slotted wall at different air velocities and different porosities. The resistance coefficients used in Eq. (1) are found from these simulations and is shown in *Table 3*.

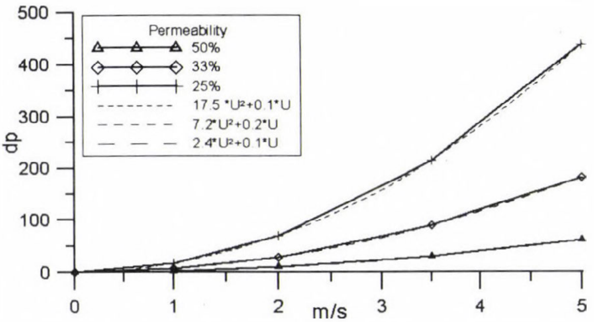

Fig. 4. Pressure loss in slotted walls with different porosity.

Table 3. Linear and quadratic resistance coefficients used in Eq. (1)

50%		33%		25%	
C_{R1}	C_{R2}	C_{R1}	C_{R2}	C_{R1}	C_{R2}
17.5	0.1	7.2	0.2	2.4	0.1

3.2. *Air flow around and inside the building*

It is assumed that the air inside the building is well mixed and the inside temperature equals to the outside temperature. The air velocity inside the building has a large spatial variability. Therefore, a residential zone is defined, where the climatic conditions should be better than outlined in *Table 1*. The residential zone, where the cattle rests, is indicated in *Fig. 5a* with three lines positioned 0.7 meters above the floor. *Fig. 5b* shows the air velocity along these lines for different wind velocities and a 50% porosity of the wall section.

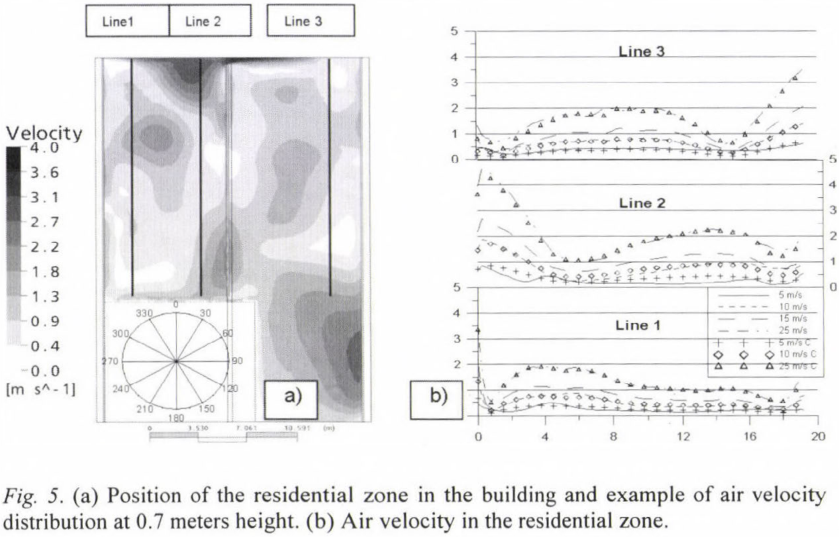

Fig. 5. (a) Position of the residential zone in the building and example of air velocity distribution at 0.7 meters height. (b) Air velocity in the residential zone.

Fig. 5b also shows the validation of the assumption, that the indoor air velocity is independent of the outdoor wind velocity. Points marked with letter C indicate the predicted air velocity along the lines when 15 m/s is used as reference velocity. The correlation between the simulated and predicted velocity with 15 m/s as basis is very good for 25 m/s and 10 m/s, and somewhat poorer for 5 m/s. This means that the indoor flow pattern is nearly independent of the wind velocity, and that it is adequate to use only the simulation with a velocity of 15 m/s at 10 meters height to assess other wind velocities as well.

Fig. 6 shows the maximum allowed wind velocity at 10 meters height outside of the building, above which the air velocity in the residential zone exceeds 0.3 m/s. An interesting feature of the results is that the air velocity in the residential zone is closest to the outdoor wind velocity, when the wind direction is normal to the shorter walls of the building. The reason for this is that the wind velocity is increasing near the upwind edges of the building, and this high speed jet is reattached near the middle of the building with an angle up to 90 degrees. This jet creates a wind environment inside the building, which is poorer than in the case of a wind direction perpendicular to the long wall.

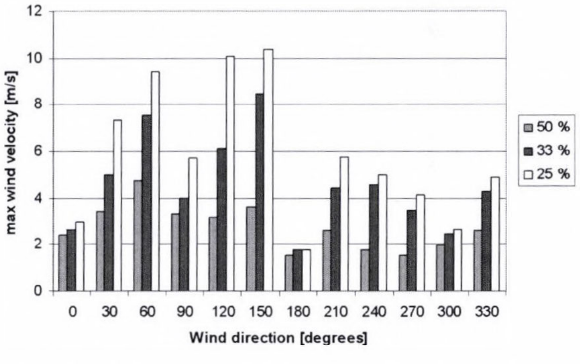

Fig. 6. The maximum allowed wind velocity at 10 meters height.

When the wind direction is normal to the long wall (90° an 270°), the air jet coming trough the air vents is directed above the cattle, driving a low-velocity recirculation flow in the residential zone. When the wind direction is normal to the gable wall, the vortices encircling the building provide a different direction to air entering the building. Air is entering trough the ridge and the sides of the building and a lot of the air is directed towards the floor. As a result, despite the lower air exchange rate for wind directions 0° and 180° found by *Shylar* and *Arbel* (2004), the animal comfort is lower than for wind approaching normal to the longer walls (90° an 270°).

Fig. 7 shows the wind pattern around the building in the case of wind approaching the shortest walls. A similar graph, as showed in *Fig. 6*, is produced for the 3.9 m/s threshold given in *Table 1*. Combining the two graphs produces *Fig. 8*, which shows the allowed combinations of wind velocity (u_{10}), porosity of the wall, and outdoor temperature (T) for wind direction 270°. This is the predominant wind direction at the site, therefore, it is regarded as a "design wind direction". The figure can be used to assess, which porosity the wall should have, based on climatic data.

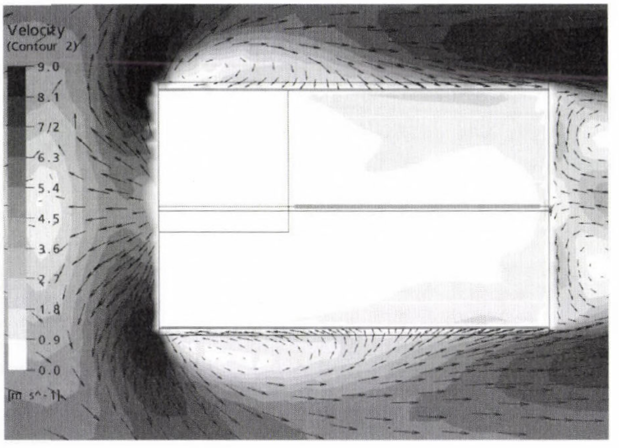

Fig. 7. Exterior wind vectors around the building, and wind velocity contours outside and inside the building.

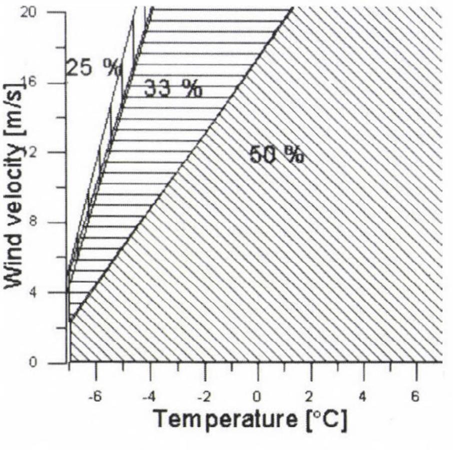

Fig. 8. Allowed combinations of wind velocity, porosity of the wall, and outdoor temperature for wind direction 270°.

4. Conclusions

The method outlined in the paper is capable of calculating the porosity needed to maintain a satisfactory animal comfort in a naturally ventilated animal building with permeable walls. The indoor wind velocity in the animal residential zone is strongly dependent on the outdoor wind direction. This is because the building itself modifies the air-flow pattern creating zones with high and low wind velocities. In some cases the permeable walls are placed in such high velocity zones, which will decrease the indoor animal comfort. This is the reason why the indoor animal comfort is poorest when the wind approaches the shorter walls in the present building design. The knowledge of this mechanism should be included in future designs of naturally ventilated animal buildings.

References

Gregory, N.G., 1995: The role of shelterbelts in protecting livestock: A review. *New Zeal. J. Agr. Res. 38*, 423-450.

Holmes, C.W. and *Sykes, A.R.*, 1984: Shelter and climatic effects on livestock. In *Shelter Research Needs in Relation to Primary Production* (ed.: *J.W. Sturrock*). Water and Soil Misc. Publ. No. 59, 19-35.

Miguel, A.F., 1998: Airflow through porous screens: from theory to practical considerations. *Energ Buildings 28*, 63-69.

Shklyar, A. and *Arbel, A.*, 2004: Numerical model of the three-dimensional isothermal flow patterns and mass fluxes in a pitched-roof greenhouse. *J. Wind Eng. Ind. Aerod. 92*, 1039-1059.

IDŐJÁRÁS

Quarterly Journal of the Hungarian Meteorological Service
Vol. 111, No. 2–3, April–September 2007, pp. 171–183

Surface patterns on thin liquid films, reduced 2D-descriptions. Part I. Perfect fluids

Michael Bestehorn

Department of Theoretical Physics II, Brandenburg Technical University Cottbus, Erich-Weinert-Str 1, 03046 Cottbus, Germany; E-mail: bes@physik.tu-cottbus.de

(Manuscript received in final form February 13, 2007)

Abstract—In this paper we show, how reduced equations for thin fluid layers can be systematically derived from the basic hydrodynamic equations. In this part we consider perfect fluids with zero viscosity. The shallow water equations are derived and extended to the case of a bistable pressure. Numerical solutions show instabilities, coarsening and relaxational behavior versus stationary states. Finally, parametric excitation is included, and a rich spatio-temporal behavior of the surface structures is obtained.

Key-words: hydrodynamic waves, shallow water equations, reduced description

1. Introduction

More or less regularly structured surfaces on fluids or interfaces separating liquids (or a gas and a liquid) are found in nature as well as in technological applications on a large variety of length and time scales. Far from being complete, we mention some examples:

- Water waves caused by wind or sea quakes and land slides (tsunamis) (*Kundu*, 2004; *Faber*, 1995; *Ward* and *Day*, 2001).
- Localized excitations of the surface (solitons), i.e., on shallow water (*Drazin* and *Johnson*, 1989).
- Shear instabilities in clouds or multi-layer systems like the Kelvin-Helmholtz instability or the Rayleigh-Taylor instability (*Kundu*, 2004; *Faber*, 1995; *Chandrasekhar*, 1981).
- Surface deflections in the form of holes or drops of thin fluid films in coating or wetting processes (*Bestehorn* and *Neuffer*, 2001; *Reiter*, 1992).

- Creation and controlled growth of ordered structures in (nano-) technological applications (*Kargupta* and *Sharma*, 2001).
- Biological applications: Behavior of liquid films on leaves or of the tear film on the cornea of the eye; dynamics of thin blood layers; blood clotting.
- Films on the walls of combustion cells.
- Lubrication films in mechanical machines.

Surface patterns may occur due to several mechanisms. One mainly can distinguish between two cases: Patterns excited and organized by some external forces or disturbances (e.g., tsunamis), and those formed by instabilities. The latter may show the aspects of self-organization and will be in the focus of the present contribution (*Haken*, 2004; *Cross* and *Hohenberg*, 1993).

Complicated systems are controlled by a certain set of parameters, which can be accessed from outside. They are named "control parameters". The states of the systems under consideration are described by state variables like temperatures, concentrations, velocity fields, etc. Changing one or more control parameters, the system may reach a certain critical point and an instability may occur. Then the old solution gets unstable and gives way to a qualitatively new behavior. Those instabilities can be regular (periodic) in space and/or time. In that way, new typical length or time scales are created by self-organization (*Haken*, 2004). On the other hand, they can also be homogeneous, stationary, or, the other extreme case, turbulent or chaotic.

The mathematical description of the systems listed above is more or less well known for a long time. Fluid motion is described by the Euler or Navier-Stokes equations, temperature fields by the heat equation, and chemical concentrations by some nonlinear reaction-diffusion equations. The location and spatio-temporal evolution of surfaces or interfaces can be computed by the kinematic boundary conditions, if the velocity of the fluid near the interface is known. All these equations can be coupled and provided with suitable boundary and initial conditions. In that way, rather complicated systems of nonlinear partial differential equations result. Even nowadays, in the age of supercomputers, their further treatment, especially in three room dimensions, remains still a challenge.

On the other hand, solving directly the basic equations, can be considered merely as another experiment. For these reasons, we wish to explore here other methods. In this and in the next contribution we shall describe how to derive reduced 2D descriptions of the fully 3D problems.

2. The shallow water equations

In this section we wish to derive briefly the equations describing the motion of a thin layer of a perfect fluid. They are called *shallow water equations*. Although the derivation is standard (see, for instance, the textbooks (*Kundu*, 2004; *Faber*, 1995; *Bestehorn*, 2006), we wish to present it here, because it serves as a good example of how 2D equations can be found systematically from a 3D basic problem.

2.1. *Potential flow*

We consider an incompressible fluid. Its velocity field $\mathbf{v}(\mathbf{r},t)$ is ruled by the Euler equations and the incompressibility condition:

$$\rho\left[\frac{\partial \mathbf{v}}{\partial t} + (\mathbf{v}\cdot\nabla)\mathbf{v}\right] = -\nabla p + \mathbf{f}\,, \tag{1a}$$

$$\nabla\cdot\mathbf{v} = 0, \tag{1b}$$

where $p(\mathbf{r},t)$ is the pressure, ρ is the (constant) density, and $\mathbf{f}(\mathbf{r},t)$ denotes some external forces like gravity, etc. If the fluid is free of vorticity, $\nabla\times\mathbf{v} = 0$, the velocity can be expressed by a scalar potential $\Phi(\mathbf{r},t)$:

$$\mathbf{v}(\mathbf{r},t) = \nabla\Phi(\mathbf{r},t)\,. \tag{2}$$

From Eq. (1b) we get the Laplace equation:

$$\Delta\Phi(\mathbf{r},t) = 0\,, \tag{3}$$

which determines the velocity field along with suitable boundary conditions.

2.2. *Kinematic boundary conditions*

We assume the surface to vary on a large lateral scale compared to the liquid depth. In addition it should be writable as a (smooth) function $h(x,y,t)$. If the fluid moves, the location of the surface is changed according to the *kinematic boundary condition* (*kbc*) (*Fig. 1*):

$$\partial_t h = \mathbf{n}\cdot\mathbf{v} = (1+(\nabla h)^2)^{-1/2}(v_z - v_x\partial_x h - v_y\partial_y h) \approx v_z - v_x\partial_x h - v_y\partial_y h,$$

or, in terms of the potential

$$\partial_t h = \partial_z\Phi - \partial_x\Phi\partial_x h - \partial_y\Phi\partial_y h\,. \tag{4}$$

Here, $\mathbf{v}$ (and Φ) have to be evaluated at the surface $z = h$, and a small surface slope $(\nabla h)^2 << 1$ is assumed. Inserting Eq. (2) into the Euler equations Eq. (1a) and evaluating them at the surface lead to the other *kbc*:

$$\partial_t \Phi|_{z=h} + \frac{1}{2}(\nabla\Phi)^2{}_{z=h} = -g(h-h_0) - \frac{p(h)}{\rho}, \tag{5}$$

where we consider a constant gravity field in z-direction as external force, and a certain given pressure $p(h)$ at the surface that will be specified later.

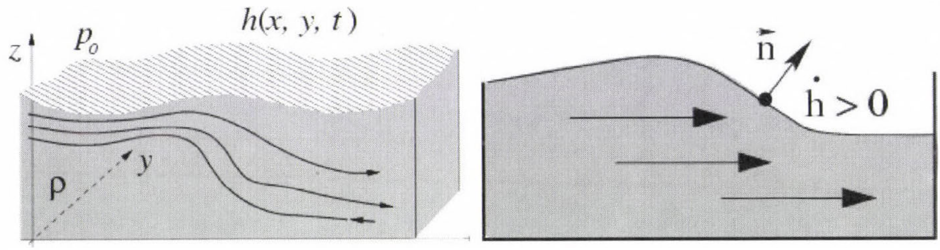

(a) **(b)**

Fig. 1. (a) An (incompressible) fluid with a free and deformable surface located at $z = h(x,y,t)$, on which a constant external pressure p_0 is applied. (b) The location of a certain point of the surface changes if the fluid is in motion.

2.3. Scaling and small parameter

The crucial point in the derivation of the reduced equations is the different scaling used for the vertical and horizontal coordinates. Let h_0 be the uniform depth of the motionless layer and ℓ a certain horizontal length scale (wave length, spatial extension of a front, etc.), then we introduce the dimensionless variables

$$x = \tilde{x}\ell,\ y = \tilde{y}\ell,\ z = \tilde{z}h_0,\ t = \tilde{t}\tau, \tag{6}$$

and

$$h = \tilde{h}h_0, \qquad \Phi = \tilde{\Phi}\frac{\ell^2}{\tau}, \tag{7}$$

where τ is a certain time scale that is left arbitrary for the moment. The different length scales define a small parameter

$$\delta = \frac{h_0}{\ell} << 1, \tag{8}$$

which can now be used for a systematic expansion. In the dimensionless quantities the basic equations and boundary conditions read (we drop all tildes):

$$(\delta^2\Delta_2 + \partial_{zz})\Phi = 0\,, \tag{9a}$$

$$\partial_t h - \delta^{-2}\partial_z\Phi\big|_{z=h} = -(\partial_x h)(\partial_x\Phi)_{z=h} - (\partial_y h)(\partial_y\Phi)_{z=h}\,, \tag{9b}$$

$$\partial_t\Phi\big|_{z=h} + G(h-1) = -p(h) - \frac{1}{2}\left((\partial_x\Phi)^2 + (\partial_y\Phi)^2 + \delta^{-2}(\partial_z\Phi)^2\right)_{z=h}, \tag{9c}$$

$$\partial_z\Phi\big|_{z=0} = 0\,, \tag{9d}$$

with $\Delta_2 = \partial_{xx} + \partial_{yy}$ as the 2D Laplacian, and the dimensionless *gravitation number* $G = \dfrac{gh_0\tau^2}{\ell^2}$.

2.4. Laplace equation

The next step is to solve the Laplace equation Eq. (9a), iteratively. Therefore, we expand

$$\Phi(\mathbf{r},t) = \Phi^{(0)}(\mathbf{r},t) + \delta^2\Phi^{(1)}(\mathbf{r},t) + \delta^4\Phi^{(2)}(\mathbf{r},t) + \ldots$$

and find from Eq. (9a) in the zeroth order of δ that

$$\partial_{zz}\Phi^{(0)} = 0\,.$$

Because of the boundary condition, Eq. (9d), this can only be solved if it is independent of z:

$$\Phi^{(0)} = \Phi^{(0)}(x,y,t)\,.$$

In the order δ^2 one then finds

$$\partial_{zz}\Phi^{(1)}(\mathbf{r},t) = -\Delta_2\Phi^{(0)}(x,y,t)\,,$$

which can be integrated twice:

$$\Phi^{(1)}(\mathbf{r},t) = -\frac{z^2}{2}\Delta_2\Phi^{(0)}(x,y,t) + \varphi^{(1)}(x,y,t) \tag{10}$$

with an arbitrary function $\varphi^{(1)}$. Up to the second order one gets

$$\Phi(\mathbf{r},t) = \Phi^{(0)}(x,y,t) + \delta^2\left[-\frac{z^2}{2}\Delta_2\Phi^{(0)}(x,y,t) + \varphi^{(1)}(x,y,t)\right] + O(\delta^4)\,. \tag{11}$$

2.5. The shallow water equations

Inserting Eq. (11) into the two kbc-s, Eqs. (9b)–(9c), and yielding up to the lowest order in δ, the shallow water equations are

$$\partial_t h = -h\Delta_2\Phi^{(0)} - (\partial_x h)(\partial_x \Phi^{(0)}) - (\partial_y h)(\partial_y \Phi^{(0)}), \tag{12a}$$

$$\partial_t \Phi^{(0)} = -G(h-1) - p(h) - \frac{1}{2}\left(\partial_x \Phi^{(0)}\right)^2 - \frac{1}{2}\left(\partial_y \Phi^{(0)}\right)^2. \tag{12b}$$

Now we have reached our goal to derive a 2D system starting from 3D fluid motion. Eqs. (12) constitute a closed system of partial differential equations for the evolution of the two functions $h(x,y,t)$ and $\Phi^{(0)}(x,y,t)$. Using Eq. (11), from the latter one finds the velocity field immediately (up to the order δ^2).

2.6. Numerical solutions

Fig. 2 shows numerical solutions of the shallow water equations, left frame in 1D, right frame in 2D. In 1D, traveling surface waves can be seen clearly, which may run around due to the periodic boundary conditions in x. On the other hand, one can recognize a second wave with a smaller amplitude going to the left hand side. Both waves seem to penetrate each other without further interaction. The reason seems to be the smallness of the amplitude, which results in a more or less linear behavior.

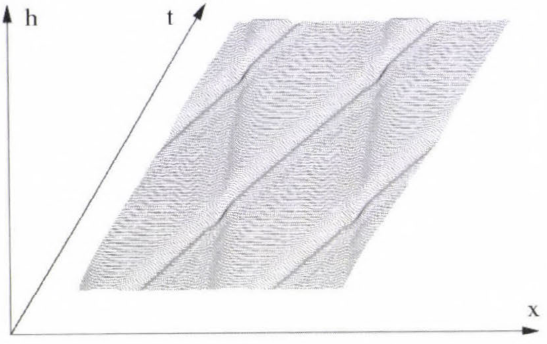

(a)

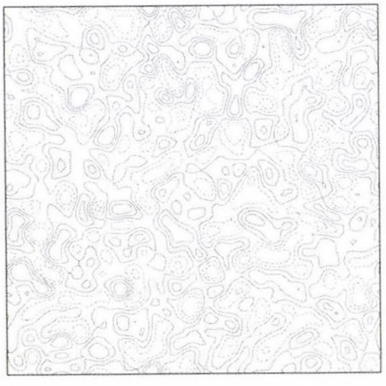

(b)

Fig. 2. Numerical solutions of the shallow water equations. (a) Temporal evolution in one dimension. (b) A snapshot in 2D. Dashed contour lines mark troughs, solid ones correspond to peaks of the sea.

In the 2D frame, a snapshot of the temporal evolution of the surface is presented. The initial condition was chosen randomly. For numerical stability reasons, an additional damping of the form

$$\tilde{\nu}\Delta_2\Phi \tag{13}$$

was added to the right hand side of Eq. (12b) in order to filter out the short wave lengths. This could be justified phenomenologically by friction and in the long time limit it leads to a fluid in rest, if only gravity acts.

3. Instabilities

To see if the flat film $h = 1$ is stable against small perturbations, one may perform a linear stability analysis. To this end it is convenient to introduce the (small) variable

$$\eta(x, y, t) = h(x, y, t) - 1 \tag{14}$$

in Eq. (12) and linearize with respect to η and Φ. The two resulting equations can be combined into one wave equation for η or alternatively for Φ:

$$\partial_{tt}\eta - G\Delta_2\eta = 0, \tag{15}$$

where we have assumed constant surface pressure. A solution of Eq. (15) is provided by

$$\eta \sim e^{\lambda t + ikx},$$

from which one finds the dispersion relation

$$\lambda(k) = \pm i|k|\sqrt{G},$$

for waves traveling with the constant phase velocity $\pm\sqrt{G}$.

3.1. Damped wave equation

Since $\mathrm{Re}(\lambda) = 0$, waves do neither growth nor decay in time, they are marginally stable. This changes if damping according to Eq. (13) is included. Then instead of Eq. (15) one finds a kind of telegraph equation having the dispersion relation

$$\lambda(k) = -\frac{\nu k^2}{2} \pm i|k|\sqrt{G - \nu^2 k^2}.$$

Again waves, now with a slightly smaller phase speed, are the solution, but these waves are all decaying in time (if $k \neq 0$), leading finally to a steady state with a flat surface at $h = 1$. So the initial state is now stable.

3.2. Laplace pressure and disjoining pressure

To discuss Eqs. (12) further, we have to elaborate a little on the dependence of the surface pressure on the depth h.

The length scale of the surface structures is proportional to the depth of the fluid layer. If the films are very thin, we expect to have scales in the range or even well below the capillary length

$$a = \sqrt{\frac{\Gamma}{G\rho}}, \tag{16}$$

where Γ denotes the surface tension. Then one has to take into account the additional pressure, which origins from the curvature of the surface, the so-called *Laplace pressure*. It reads for weakly curved surfaces

$$-q\Delta_2 h, \quad q>0. \tag{17}$$

The dimensionless constant q is linked to the surface tension by

$$q = \frac{h_0 \tau^2}{\ell^4 \rho}\Gamma$$

Thus we have to substitute $p(h)$ in Eq. (12b) for the expression

$$p = p_0 - q\Delta_2 h, \tag{18}$$

which changes the dispersion relation to that of (damped) capillary waves

$$\lambda(k) = -\frac{\nu k^2}{2} \pm i|k|\sqrt{G + qk^2 - \nu^2 k^2}.$$

Again, no instability with $\mathrm{Re}(\lambda)>0$ can occur.

Now assume, that the pressure p_0 depends also on the absolute value of h in some nonlinear non-monotonic fashion. This can be the case for very thin films, where van der Waals forces between the solid support and the free surface come into play (*Israelachvili*, 1992). But also in thicker films, this should be possible in non-isothermal situations, where the surface temperature and, therefore, the surface tension changes with the vertical coordinate (Marangoni effect).

If we take for instance the polynomial (*Fig. 3a*)

$$p_0 = h(h-1)(h-2) \tag{19}$$

linearization around $h = 1$ leads to the growth rates (*Fig. 3b*)

$$\lambda_{12}(k) = -\frac{\nu k^2}{2} \pm i\left|k^2\right| \sqrt{p'_0 + G + qk^2 - \nu^2 k^2}\,, \tag{20}$$

where

$$p'_0 = \left.\frac{dp_0}{dh}\right|_{h=h_0}$$

and h_0 is the conserved mean thickness of the film. An instability occurs if the expression under the integral can be negative, i.e., for $p'_0 + G < 0$

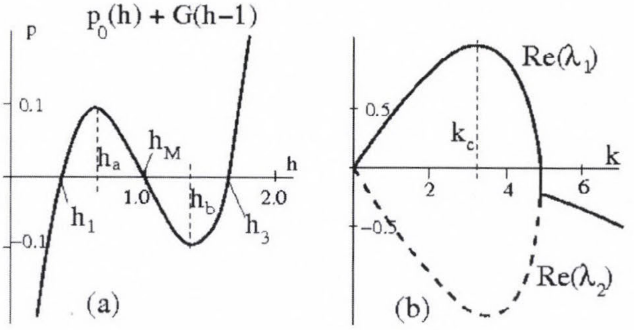

Fig. 3. (a) Non-monotonic generalized pressure with p_0 from Eq. (19). Between the spinodals h_a and h_b, the flat surface is unstable and pattern formation sets in. The binodals h_1 and h_3 follow from a Maxwell construction. (b) Eigenvalues Eq. (20) for the supercritical case.

This corresponds to the region of initial thickness, where the generalized pressure

$$p_0 + G(h-1) \tag{21}$$

has a negative slope (*Fig. 3a*). The two extrema, h_a and h_b are called *spinodals*. For $h_a<h_0<h_b$ the flat film is unstable with respect to infinitesimally small perturbations. The points h_1 and h_2 (the *binodals*) can be found for a general form of the pressure from a Maxwell construction. For the special form of Eq. (19) they coincide with the zeros of Eq. (21). Films having an initial depth in the two regions $h_1 < h_0 < h_a$, $h_b < h_0 < h_3$ are meta-stable. A finite disturbance is necessary to bring the system to an absolutely stable state, that consists of a structured surface. In these regions, pattern formation by nucleation is expected.

Fig. 4 shows a numerically determined time series of a random dot initial condition. The mean thickness h_0 was chosen in the unstable region on the right hand side of the Maxwell point h_M of *Fig. 3a*. The formation shows clearly traveling waves in the linear phase, followed by coarsening to a large scale structure, in this case to one big region of depression, or a hole. This hole gets more and more symmetric, while the velocity decays due to the friction term. Finally, a steady state of a circular big hole remains.

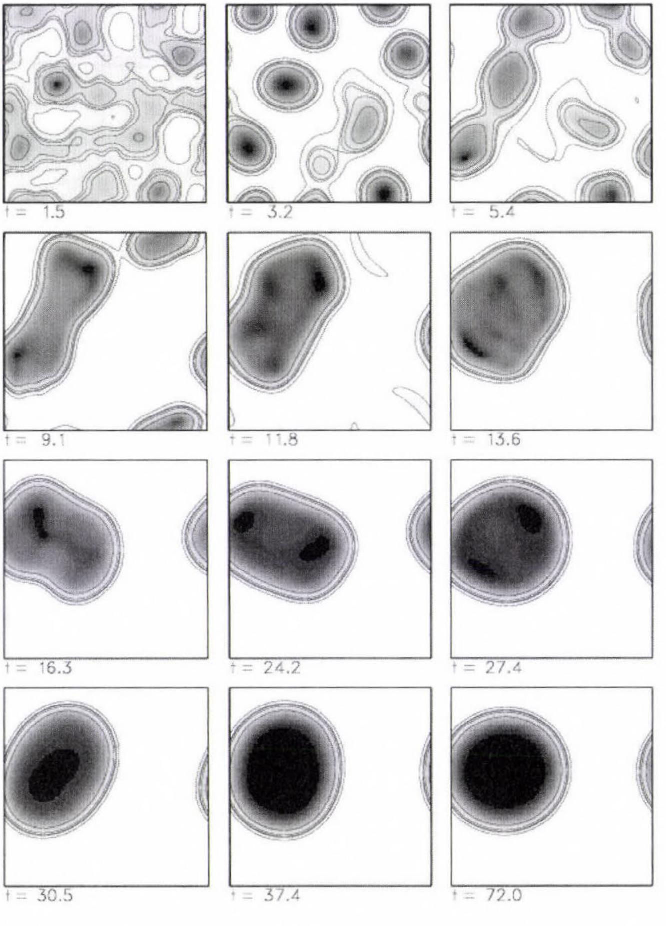

Fig. 4. Time series from a numerical solution of Eq. (12) with damping Eq. (13) and bistable pressure (Eqs. (18), (19), and (21)). Coarsening dominates the non-linear evolution, and eventually, a stationary circular region of surface depression (a hole) remains. Parameters: G=0.5, $\mathbf{v}$=0.02, q=0.01, h_0=1.3. Periodic boundary conditions in both horizontal directions have been used.

3.3. *Parametric excitation of a thin bistable fluid layer*

One way to replace the energy lost by a damping according to Eq. (13) is to accelerate the whole layer periodically in vertical direction. This was done first in an experiment by Michael Faraday in 1831. He obtained regular surface patterns mostly in the form of squares (*Faraday*, 1831).

Faraday patterns can be seen as a solution of the shallow water equations, if the gravity constant G is modulated harmonically (*Bestehorn*, 2006):

$$G(t) = G_0 + G_1 \cos(\Omega t). \tag{22}$$

A linear stability analysis leads to the Mathieu equation (now with $v=q=p_0=0$) (*Abramowitz* and *Stegun*, 1972):

$$\partial_{\tilde{t}\tilde{t}}\,\eta + (b^2 + 2a\cos(2\tilde{t}))\,\eta = 0 \tag{23}$$

with

$$b^2 = \frac{4G_0 k^2}{\Omega^2}, \qquad a^2 = \frac{2G_1 k^2}{\Omega^2}, \tag{24}$$

and the rescaled time $\tilde{t} = t\Omega/2$. The flat film is unstable if frequency and amplitude fall into certain domains, the so-called *Arnold tongues* (*Fig. 5*). There one usually finds squares for not too supercritical values.

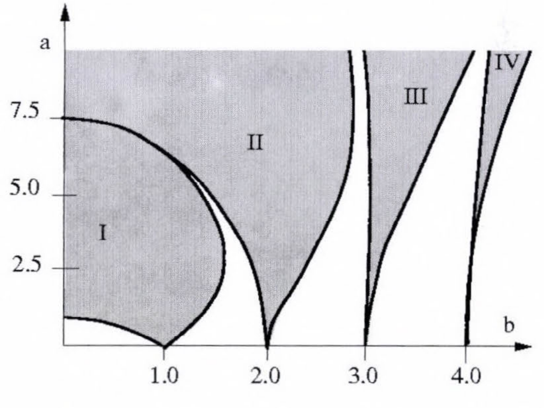

Fig. 5. The stability chart of the Mathieu equation (Eq. (23)) without damping, Arnold tongues. In region I, the pattern oscillates with the half of the driving frequency Ω.

Instead of presenting these results, we finally show a numerical solution of the full equations with v, q, p_0 having the same values as above, but now with an additional periodic excitation (*Fig. 6*). Coarsening is still present, but now oscillating drops emerge in the form of stars. No time stable structure is found in the long time limit.

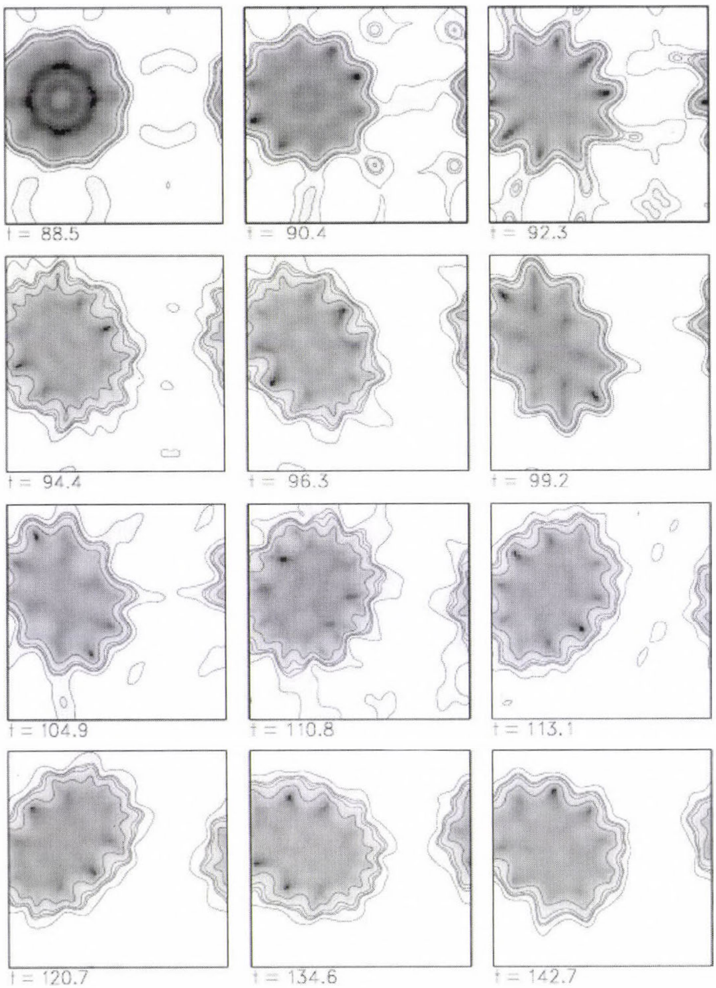

Fig. 6. Continuation of the series of Fig. 4, but with additional parametric excitation according to Eq. (22), switched on at t=72. Instead of stationary patterns, pulsating stars are found.

References

Abramowitz, M. and *Stegun, I.A.*, 1972: *Handbook of Mathematical Functions*. Dover, New York.

Bestehorn, M., 2006: *Hydrodynamik und Strukturbildung*. Springer, Berlin.

Bestehorn, M. and *Neuffer, K.* , 2001: Surface patterns of laterally extended thin liquid films in three dimensions. *Phys. Rev. Lett. 87,* 046101.

Chandrasekhar, S., 1981: *Hydrodynamic and Hydromagnetic Stability*. Dover, New York.

Cross, M.C. and *Hohenberg, P.C.*, 1993: Pattern formation outside equilibrium. *Rev. Mod. Phys. 65,* 851-860.

Drazin, P.G. and *Johnson, R.S.*, 1989: *Solitons: An Introduction*. Cambridge University Press.

Faber, T.E., 1995: *Fluid Dynamics for Physicists*. Cambridge University Press.

Faraday, M., 1831: *Philos. Trans. R. Soc. London 121,* 319 pp.

Haken, H., 2004: *Synergetics. Introduction and Advanced Topics*. Springer, Berlin.

Israelachvili, J.N., 1992: *Intermolecular and Surface Forces*. Academic Press, London.

Kargupta, K. and *Sharma, A.*, 2001: Templating of thin films induced by dewetting on patterned surfaces. *Phys. Rev. Lett. 86,* 4536.

Kundu, M.P.K., 2004: *Fluid Mechanics*. Academic Press.

Reiter, G., 1992: Dewetting of thin polymer films. *Phys. Rev. Lett. 68,* 75-85.

Ward, N. and *Day, S.*, 2001: Cumbre Vieja Volcano – Potential collapse and tsunami at La Palma, Canary Islands. *Geophys. Res. Lett. 28,* 3397.

IDŐJÁRÁS

Quarterly Journal of the Hungarian Meteorological Service
Vol. 111, No. 2–3, April–September 2007, pp. 185–198

Surface patterns on thin liquid films, reduced 2D-descriptions. Part II. Viscous fluids

Michael Bestehorn

Department of Theoretical Physics II, Brandenburg Technical University Cottbus, Erich-Weinert-Str 1, 03046 Cottbus, Germany; E-mail: bes@physik.tu-cottbus.de

(Manuscript received in final form February 13, 2007)

Abstract—We show how a reduced equation describing the spatio-temporal evolution of the surface of a thin viscous liquid film can be systematically derived from the basic hydrodynamic equations. This equation is called thin-film equation. A special form of the interaction between free surface and solid substrate of the film, that has attractive long range and repelling short range properties, is discussed. The formation of holes, drops (spinodal dewetting), as well as nucleation is demonstrated.

Key-words: thin film instabilities, wetting, surface patterns

1. Introduction

In this contribution, we wish to study pattern formation of the surface of thin viscous films. In thin or ultra-thin films, fluid motion described by the velocity field $\mathbf{v}(\mathbf{r},t)$ is usually very slow, and the whole layer can be considered as a boundary layer, where viscous forces are much larger than inertial forces. For that case it is sufficient to consider the Stokes equation

$$\eta\nabla^2 \mathbf{v}=\nabla P, \tag{1}$$

where η denotes the viscosity of the fluid. Again we assume the fluid to be incompressible:

$$\nabla \cdot \mathbf{v}=0. \tag{2}$$

Further, we restrict us to the case that external terms have a potential, which can be included into the "generalized" pressure: $P = p + U$.

Surface patterns of thin liquid films on a solid support were studied during the last decade in numerous experimental and theoretical contributions (*Rehse et al.*, 2001; *Rockford et al.*, 1999; *Oron et al.*, 1997; *Pototsky et al.*, 2004; *Reiter*, 1992; *Reiter et al.*, 1999; *Jacobs et al.*, 1998; *Colinet et al.*, 2001). Most of the theoretical works is based on an interface equation, often called thin film equation, describing the location $z=h(x,y,t)$ of the free surface of the liquid (*Oron et al.*, 1997; *Vrij*, 1966; *Pismen* and *Pomeau*, 2000; *Bestehorn* and *Neuffer*, 2001). This equation can be derived from Eqs.(1)–(2) using the lubrication approximation, what we shall work out next.

2. *The thin film equation*

2.1. The lubrication approximation

For the sake of simplicity, we shall restrict the derivation of this section to one spatial dimension, say x. The final result will be given also in 2D (for more details see in *Oron et al.* (1997)). As above, the aim is to find an equation for the surface location $h(x,t)$ of the liquid. Such an equation is already provided by the kinematic boundary condition:

$$\partial_t h = v_z|_h - v_x|_h \partial_x h. \tag{3}$$

To compute v_z at the surface $z=h$, one integrates the continuity equation, Eq. (2) with respect to z and finds with the bottom boundary condition $v_z(z=0)=0$, that

$$\int_0^{h(x,t)} \partial_x v_x dz + v_z|_h = 0.$$

Extracting the derivative from the integral yields

$$v_z|_h = -\partial_x \int_0^{h(x,t)} v_x dz + v_x|_h \partial_x h,$$

and inserting into Eq. (3), the desired equation for $h(x,t)$ is

$$\partial_t h = -\partial_x \int_0^{h(x,t)} v_x dz, \tag{4}$$

or in two horizontal dimensions it is

$$\partial_t h = -\nabla_2 \cdot \int_0^{h(x,y,t)} \mathbf{v}_H dz\,, \tag{5}$$

where $\mathbf{v}_H = (v_x, v_y)$ denotes the horizontal velocity components.

To close the equation, it is necessary to compute v_x (or $\mathbf{v}_H$) as a function of h. This can be done by solving the Stokes equation. It reads, using the same scaling as in Part I,

$$(\delta^2 \partial_{\tilde{x}\tilde{x}} + \partial_{\tilde{z}\tilde{z}})\tilde{v}_x = \partial_{\tilde{x}} \tilde{P}\,, \tag{6a}$$

$$\delta^2 (\delta^2 \partial_{\tilde{x}\tilde{x}} + \partial_{\tilde{z}\tilde{z}})\tilde{v}_z = \partial_{\tilde{z}} \tilde{P}, \tag{6b}$$

with dimensionless velocity and pressure:

$$v_x = \tilde{v}_x \frac{\ell}{\tau}, \qquad v_z = \tilde{v}_z \frac{d}{\tau}, \qquad P = \tilde{P} \frac{\eta}{\delta^2 \tau},$$

where we use now d instead of h_0 for the uniform depth of the layer at rest. In the limit $d/\ell = \delta \to 0$, it follows from (6b), that

$$\partial_{\tilde{z}} \tilde{P} = 0 \qquad \text{or} \qquad \tilde{P} = \tilde{P}(\tilde{x})\,.$$

Thus, one can integrate Eq. (6a) twice over $\tilde{z}$ and finds with the no-slip condition $\tilde{v}_x(\tilde{x}, 0) = 0$, that

$$\tilde{v}_x(\tilde{x}, \tilde{z}) = f(\tilde{x})\tilde{z} + \frac{1}{2}(\partial_{\tilde{x}} \tilde{P}(\tilde{x}))\tilde{z}^2, \tag{7}$$

with a function $f(\tilde{x})$, which can be determined by the boundary conditions. To this end we consider a constant surface tension. Then the horizontal component of the surface stress has to vanish at the free surface:

$$\eta \partial_z v_x |_{z=h} = 0.$$

Inserting Eq. (7) leads to $f(\tilde{x}) = -(\partial_{\tilde{x}} \tilde{P})h$. Substituting everything into Eq. (4) and integrating by $\tilde{z}$ finally yields (all tildes omitted)

$$\partial_t h = -\partial_x \left[-\frac{h^3}{3} \partial_x P \right], \tag{8}$$

or in two dimensions

$$\partial_t h = -\nabla_2 \cdot \left[-\frac{h^3}{3} \right] \nabla_2 P. \tag{9}$$

This is the basic equation for the evolution of the surface of a thin film in the lubrication approximation. It is called the *thin film equation.*

2.2. Laplace pressure and gravity

To discuss Eq. (9) further, one has to express the pressure as a function of the depth:

$$P = P(h),$$

as we shall do now. To include the influence of gravity, one adds the gravity potential ($\rho g\, z$) to the pressure and evaluates it at the surface $z=h$. In the scaling of Eq. (9), the total pressure then reads

$$P = p_0 + G(h-1) \tag{10}$$

with the *gravitation number*

$$G = \frac{d^3 g \tau}{\ell^2 \nu}.$$

If the films are very thin, we expect to have a surface structure with a length scale in the range of or even well below the capillary length

$$a = \sqrt{\frac{\Gamma}{G\rho}}, \tag{11}$$

where Γ denotes the surface tension. Then one has to take into account the additional pressure, which origins from the curvature of the surface. Therefore, we add the *Laplace pressure* to P which reads for weakly curved surfaces

$$-q\Delta_2 h, \quad q>0. \tag{12}$$

The constant q is linked to the so-called capillary number C and follows from scaling as

$$q = \Gamma \frac{\tau d^3}{\ell^4 \eta} = \delta^2 / C .$$

Thus for $P(h)$ we have to substitute the expression

$$P = p_0 + G(h-1) - q\Delta_2 h \tag{13}$$

in Eq. (9), which yields

$$\partial_t h = \nabla_2 \cdot \left[\frac{h^3}{3} \nabla_2 (Gh - q\Delta_2 h) \right]. \tag{14}$$

The stability of a flat surface with thickness h=1 is examined by introducing small deviations:

$$h(x, y, t) = 1 + \eta(x, y, t),$$

and linearizing with respect to η:

$$\partial_t \eta = \frac{1}{3} \left(G\Delta_2 \eta - q{\Delta_2}^2 \eta \right). \tag{15}$$

Assuming plane waves with exponential behavior in time:

$$\eta \sim e^{\lambda t + ikx},$$

one finds the growth rate for the dispersion relation:

$$\lambda = -\frac{1}{3}(Gk^2 + qk^4).$$

Obviously, λ is always real, and for positive G and q and finite k it is always less than zero. Thus the flat film is always stable, both gravity and Laplace pressure act stabilizing.

However, this can be changed if the system is put "upside down", leading to negative G. In the experiments this can be realized by fixing a thin film on the underside of a horizontal plane (*Fig. 1*, left frame). Gravity is now destabilizing for all wave vectors, which have a length less than the cut-off (*Fig. 1*, right frame):

$$k_0 = \sqrt{-\frac{G}{q}},$$

a value that can be expressed by the capillary length a, already defined in Eq. (11), if one goes back to dimensional values:

$$k_0 = \sqrt{\frac{g\rho}{\gamma}} = \frac{1}{a}.$$

The numerical solution of the full Eq. (14) is not very instructive. In the first phase, periodic instabilities with $k \approx k_c$ occur and grow until h takes zero values. Physically this corresponds to a rupture of the film, beyond which the thin film equation cannot be used.

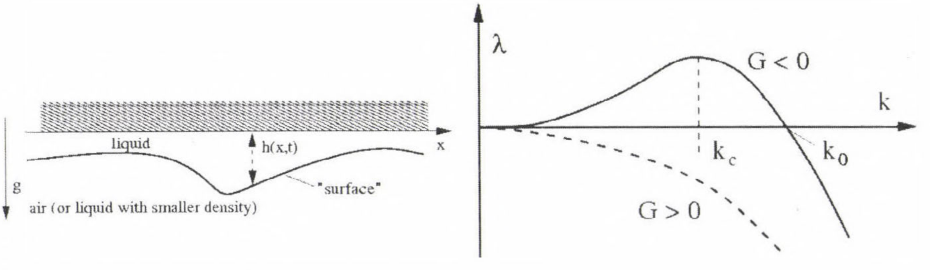

Fig. 1. Left: Sketch of a thin liquid film fixed under a solid plane. The plane surface is unstable due to gravity forces. Fingers are formed and finally the film ruptures.

Right: Growth rates of periodic disturbances of the plane surface with wave number k. The situation shown in the left frame corresponds to the solid line $G<0$ in the right ones. Waves having a wave number $k<k_0$ grow exponentially, the mode with $k=k_c$ has the largest growth rate (most dangerous mode). For $G>0$, the flat film is always stable.

2.3. The disjoining pressure and ultra-thin films

Another instability mechanism is encountered in very thin (ultra-thin) films, where the thickness is some 100 nm or even less. Then, van der Waals forces between free surface and solid substrate can no longer be neglected (*Israelachvili*, 1992).

The van der Waals force depends on the distance between the surface and support, which is the depth h. One can show that it is proportional to h^{-4}. It can be taken into account by adding the interaction potential

$$\Phi(h) = \frac{A_H}{h^3},$$

to the generalized pressure, Eq. (13), where A_H is the *Hamaker constant.* The function Φ is called *disjoining pressure.* If we neglect gravitation for the moment (it plays no role in ultra-thin films), the expression for the total pressure reads

$$P = p_0 + \frac{A_H}{h^3} - q\Delta_2 h. \tag{16}$$

If $A_H>0$, the pressure increases with decreasing depth and an instability may occur. Mathematically this corresponds to the condition (prime means derivative with respect to h):

$$P' = \Phi' < 0,$$

which is the case if $A_H>0$. The flat film is unstable for all initial depths, if the Hamaker constant is positive. As in the case of the Rayleigh-Taylor instability, the dynamics starts with the formation of periodic surface structures followed by a rupture.

On the other hand, there can also exist a repelling force between the surface and substrate, which is modeled taking $A_H<0$ and stabilizes the flat surface. Normally, attractive and repelling forces have different ranges. Usually, the repelling force is short range, the attractive is long range. Then, the initially "thick" film can be unstable due to the attraction, but rupture can be avoided by repulsion. In this way completely dry regions cannot exist, but the substrate remains always covered by an extremely thin film (some nm), called *precursor film*.

The complete expression for such an attractive/repulsive disjoining pressure may read

$$\Phi(h) = \frac{A_n}{h^n} - \frac{A_m}{h^m}, \qquad m>n,$$

with the two positive Hamaker constants A_n and A_m. Different models were discussed in *Oron et al.* (1997) in detail. We shall restrict us here to the "Lennard-Jones potential", which results for $n=3$ and $m=9$. Examining the derivative of Φ shows that layers which have a depth bigger than

$$h_a = \left(\frac{3A_9}{A_3}\right)^{1/6}$$

are always unstable. Especially arbitrarily thick films are unstable in this model. This is of course not realistic and has its reason in the neglect of the gravitational force in Eq. (16). If this is also included, one finds, instead of Eq. (16),

$$P = p_0 + \frac{A_3}{h^3} - \frac{A_9}{h^9} + G(h-1) - q\Delta_2 h. \tag{17}$$

The lower and upper stability bounds h_a, h_b for the depth are then solutions of the polynomial

$$Gh^{10} - 3A_3h^6 + 9A_9 = 0,$$

or they can be taken graphically from *Fig. 2*.

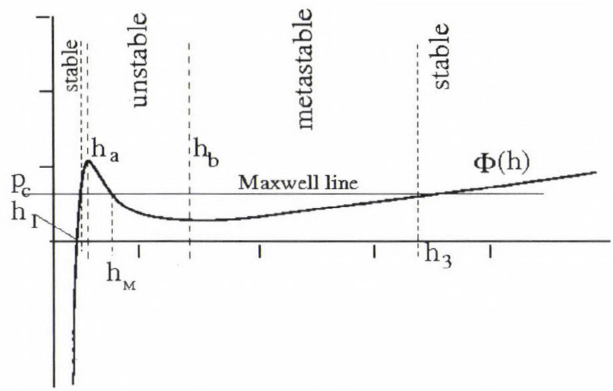

Fig. 2. Disjoining pressure including gravitation, A_3=3, A_9=1, G=0.1. The region of unstable films is bounded by h_a and h_b. The critical pressure (depth), P_c (h_M), where drops turn into holes, is determined by a Maxwell construction (see Section 3.3.1.).

3. *Spinodal de-wetting*

If a thin liquid film is exposed to a non- or partially wetting substrate, a small perturbation is sufficient to destabilize the flat surface. The fluid then bubbles and many small drops are formed. This phenomenon can be seen for instance if rain falls on a waxed cloth or a well polished car roof. Such a process is called *spinodal de-wetting* and can be described in the frame of Eq. (9) if the disjoining pressure has a negative slope for a certain region of the initial depth h (*Bestehorn* and *Neuffer*, 2001).

3.1. Thin film equation

For the following study we take an attracting/repelling disjoining pressure discussed in the last section (Eq. (17)):

$$\Phi(h) = \frac{A_3}{h^3} - \frac{A_9}{h^9} + Gh\,.$$

This, inserted into Eq. (9), yields the thin film equation:

$$\partial_t h = -\nabla_2 \cdot \left[-\frac{h^3}{3} \nabla_2 (\Phi(h) - \Delta_2 h) \right]. \tag{18}$$

Note that we put $q=1$. This is possible by a suitable choice of τ and δ. We shall come back to this issue in more detail below.

3.2. Normal form

Instead of further examining Eq. (18), we first wish to convert it to a more convenient form, showing the canonical form of a type $\mathrm{II_s}$ instability (*Cross* and *Hohenberg*, 1993). It will have also the advantage to be easier transformable into a numerical scheme.

To this end we introduce a variable that describes deviations from the average reference (initial) depth h_0 (a conserved quantity):

$$\eta(x,y,t) = h(x,y,t) - h_0\,.$$

Inserting this into Eq. (18), on the right hand side one can separate the linear and nonlinear expressions in η:

$$\partial_t \eta = \frac{1}{3} h_0{}^3 D(h_0) \Delta_2 \eta - \frac{1}{3} h_0{}^3 \Delta_2{}^2 \eta - \nabla_2 \cdot \mathbf{j}_{NL}(\eta) \tag{19}$$

with the nonlinear current

$$\mathbf{j}_{NL}(\eta) = -\frac{1}{3}\left(q_2 \nabla_2 \eta - q_1 \Delta_2 \nabla_2 \eta\right)$$

and the abbreviations

$D(h) = d_h \Phi$, $q_1 = 3h_0{}^2 \eta + 3h_0 \eta^2 + \eta^3$, $q_2 = (h_0 + \eta)^3 D(h_0 + \eta) - h_0{}^3 D(h_0)$.
Both functions q_1 and q_2 vanish as $\sim\eta$. From Eq. (19) it is evident, how the linearized problem looks near h_0. One has just to drop the nonlinear expression $\mathbf{j}_{NL}$ and a linear equation of the form Eq. (15) can be obtained. The same approach used there yields the dispersion relation

$$\lambda = \frac{1}{3} {h_0}^3 (-D(h_0) k^2 - k^4) . \quad (20)$$

An instability occurs if the "diffusion coefficient" D is less than zero. The dispersion relation then has the form of the solid line in *Fig. 1*, right frame. This of course coincides with the reasoning of Section 2.3. An instability occurs, where the slope of the pressure is negative. Numerically one finds, from

$$D(h_0) = 0,$$

the two limits (for the special choice of A_3=3, A_9=1, G=0.1), the so-called *spinodals*

$$h_0^{(1)} = h_a = 1.002, \qquad h_0^{(2)} = h_b = 3.08 .$$

3.3. Numerical solutions

We present solutions of the fully nonlinear Eq. (19) for the parameters of *Fig. 2* and several initial depths h_0 (*Fig. 3*). As initial condition, a random distribution around the average depth h_0 was chosen.

3.3.1. Spatial and temporal scales

In the early stage of the evolution, structures having a length scale of the critical wave length $\Lambda = 2\pi / k_c$ occur, where k_c is the wave number of the fastest growing mode

$$k_c = \sqrt{-\frac{D}{2}} .$$

This can be called "linear phase", since the amplitudes are still small and nonlinearities play no important role. The structure grows on the typical time scale:

$$\tau = \lambda^{-1}(k_c) = \frac{12}{{h_0}^3 D^2} = \frac{12}{{h_0}^3} (\Phi'(h_0))^{-2} ,$$

which is inverse to the square of the slope of the disjoining pressure. This is the reason why pattern formation in thicker films takes much longer (right column in *Fig. 3*). As a consequence, the small scale (linear phase) structures are overlayed by holes created by certain seeds (see also in the next paragraph). After the linear phase, the position of h_0 with respect to the Maxwell point (*Fig. 2*) is decisive. If $h_0 > h_M$, holes are formed, for $h_0 < h_M$, one finds drops. If $h_0 \approx h_M$, maze-like patterns are obtained in the form of bended, rather irregular stripes (*Fig. 3*, middle column). In a last, strongly nonlinear phase, so-called *coarsening* is observed. This is a slow increase of the length size of the structures (holes, drops, or mazes), accompanied by fusion of smaller objects to larger ones. The final structure (long time limit) is often a single entity, one big drop or hole, which is finally time stable. The whole spatio-temporal evolution is transient and can be formulated as a gradient dynamics. The potential plays the role of a generalized free energy reaching its minimum in the steady end state.

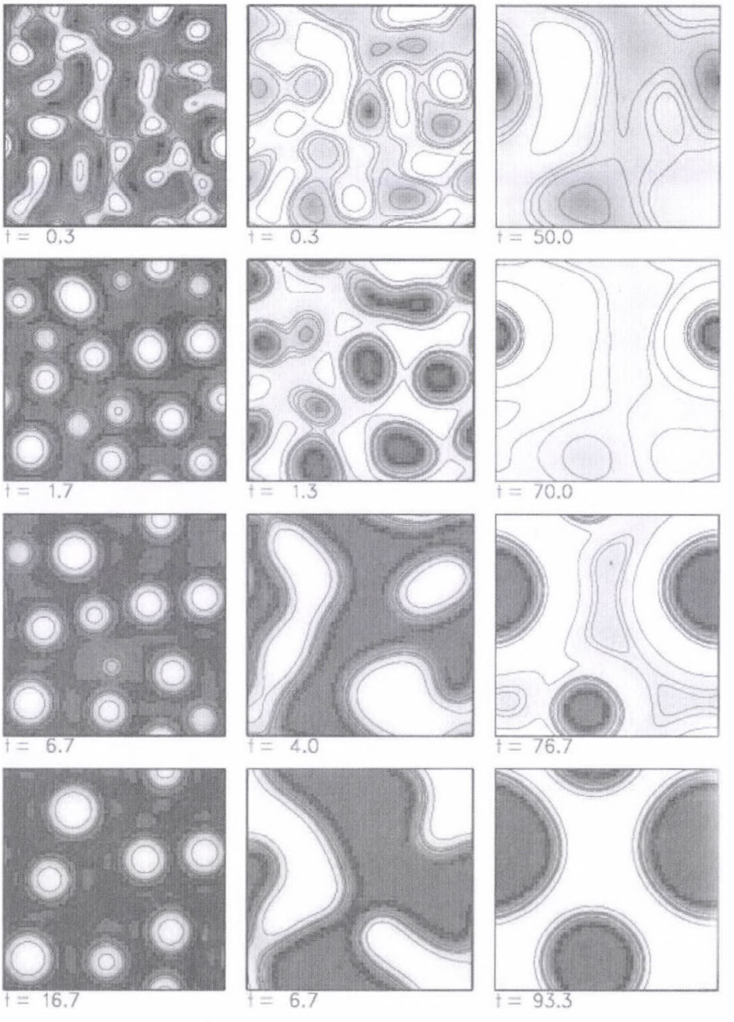

Fig. 3. Time series found by numerical integration of Eq. (19) for h_0=1.2 (left column), 1.862 (middle), and 2.8 (right). Light areas correspond to elevated regions of the surface. Nucleation dominates in the last column.

The critical pressure as well as h_M can be found by a Maxwell construction (*Fig. 2*). One has

$$P_c(h_3 - h_1) = \int_{h_1}^{h_3} \Phi(h)dh\,,$$

with h_1 (h_3) as left (right) intersection of P with the Maxwell line:

$$\Phi(h_1) = \Phi(h_3) = P_c\,.$$

From these three conditions one can determine P_c and the three intersection points by numerical iteration:

$$P_c = 0.647, \qquad h_1 = 0.850, \qquad h_M = 1.862, \qquad h_3 = 6.56.$$

3.3.2. Meta-stable region and nucleation

The flat film is unstable with respect to infinitesimal disturbances, if h_0 is in the region between h_a and h_b. On the other hand, two meta-stable domains exist,

$$h_1 < h_0 < h_a\,, \qquad h_b < h_0 < h_3\,,$$

where the flat film is stable, although the free energy could be lowered by pattern formation. Then, a finite disturbance is necessary, which can be caused by seeds coming for instance from impurities. Such a process is called *nucleation* and can be seen in the right column of *Fig. 3*. There the seeds were provided by the random dot initial conditions, and two holes are formed. Both processes (nucleation and wetting) concur in this region, and it is a question of time scales, which one emerges first. In experiments, the formation of holes by nucleation is seen quite often. The reason is that the meta-stable hole region is much larger compared to that of drops (*Fig. 2*).

3.3.3. Physical values

To get an idea of the spatial and temporal scales of the experiments, one has to rescale to dimensional variables. For the Hamaker constant A_3 this means

$$\widetilde{A}_3 = \frac{\delta^2 \tau}{\eta d^3} A_3\,, \tag{21}$$

where the variables bearing a tilde are non-dimensional (in our simulations, e.g., $\widetilde{A}_3 = 3$). Since we chose q=1, one can determine δ and τ from

$$q = \frac{\tau d^3}{\ell^4 \eta} \gamma = \frac{\delta^4 \tau}{\eta d} \gamma = 1$$

together with Eq. (21):

$$\delta = \frac{1}{d} \left(\frac{A_3}{\gamma \widetilde{A}_3} \right)^{1/2}, \qquad \tau = \left(\frac{\widetilde{A}_3}{A_3} \right)^2 \eta \gamma d^5 .$$

Knowing δ, the horizontal scale ℓ can be specified:

$$\ell = \frac{d}{\delta} = d^2 \left(\frac{\gamma \widetilde{A}_3}{A_3} \right)^{1/2}$$

To compute the scaling, we need values for the Hamaker constant A_3 and for the depth d. From the literature we take the values of *Israelachvili* (1992):

$$A_3 = \frac{0.5}{6\pi} \times 10^{-20} \, J .$$

For the depth of the precursor film h_a this gives about 5.5 nm. Then the depths (water as a working substance) of the runs shown in *Fig. 3* correspond to

$d \approx 7$ nm (left), $\qquad d \approx 10$ nm (middle), $\qquad d \approx 16$ nm (right).

For the time scales we get

$\tau \approx 0.15$ s (left), $\qquad \tau \approx 1$ s (middle), $\qquad \tau \approx 10$ s (right).

This means that the evolution shown in the left column takes about two seconds, the middle one takes seven seconds, and on the right hand side it is 15 minutes. Finally, we mention the horizontal scales:

$\ell \approx 1.4$ μm (left), $\qquad \ell \approx 3.2$ μm (middle), $\qquad \ell \approx 7.5$ μm (right),

corresponding to the horizontal dimensions of the shown areas (64×64 mesh points with distance $\Delta x = 0.5$):

$L \approx 45$ μm (left), $\qquad L \approx 100$ μm (middle), $\qquad L \approx 240$ μm (right).

4. Conclusions

In this and in the preceding paper we showed that it is often sufficient to consider reduced equations instead of the full set of hydrodynamic basic equations (Euler, Navier-Stokes equations). We gave a derivation of such a reduced description for the cases of a perfect fluid as well as of a viscous fluid. The first case leads to the shallow water equations, the latter to the thin film equations. Under both circumstances we studied the influence of a generalized pressure allowing for a bistable depth distribution. In that way the typical coarsening behavior is obtained. For a perfect fluid we add phenomenological damping. The energy lost is balanced by a parametric excitation, leading to very interesting time dependent structures.

References

Bestehorn, M. and *Neuffer, K.*, 2001: Surface patterns of laterally extended thin liquid films in three dimensions. *Phys. Rev. Lett. 87*, 046101.

Colinet, P., Legros, J.C., Velarde, M.G., 2001: *NonlinearDynamics of Surface-Tension-Driven Instabilities*. Wiley-VCH, Berlin.

Cross, M.C. and *Hohenberg, P.C.*, 1993: Pattern formation outside equilibrium. *Rev. Mod. Phys. 65*, 851-860.

Israelachvili, J.N., 1992: *Intermolecular and Surface Forces*. Academic Press, London.

Jacobs, K., Herminghaus, S., and *Mecke, K. R.*, 1998: Thin liquid polymer films repture via defects. *Langmuir 14*, 965.

Oron, A., Davis, S. H., and *Bankhoff, S. G.*, 1997: Long-scale evolution of thin liquid films. *Rev. Mod. Phys. 69*, 931.

Pismen, L.M. and *Pomeau, Y.*, 2000: Disjoining potential and spreading of thin liquid layers in the diffuse-interface model coupled to hydrodynamics. *Phys. Rev. E 62*, 2480.

Pototsky, A., Bestehorn, M., and *Thiele, U.*, 2004: Control of the structuring of thin soft matter films by means of different types of external disturbance. *Physica D199*, 138.

Rehse, N., Wang, C., Hund, M., Geoghegan, M., Magerle, R.., and *Krausch, G.*, 2001: Stability of thin polymer films on a corrugated substrate. *Eur. Phys. J. E4*, 69.

Reiter, G., 1992: Dewetting of thin polymer films. *Phys. Rev. Lett. 68*, 75.

Reiter, G., Sharma, A., Casoli, A., David, M.-O., Khanna, R., and *Auroy, P.*, 1999: Thin film instability induced by long-range forces. *Langmuir 15*, 2551.

Rockford, L., Liu, Y., Mansky, P., Russell, T.P., Yoon, M., and *Mochrie, S.G.*, 1999: Polymers on nanoperiodic, heterogeneous surfaces. *Phys. Rev. Lett. 82*, 2602.

Vrij, A.,1966: Possible mechanism for the spontaneous repture of thin free liquid films. *Discuss. Faraday Soc. 42*, 23.

IDŐJÁRÁS

Quarterly Journal of the Hungarian Meteorological Service
Vol. 111, No. 2–3, April–September 2007, pp. 199–208

Input data representativeness problem in plant disease forecasting models

Lalić Branislava[1*], **Dragutin T. Mihailović**[1], **Slavica Radovanović**[2], **Jelica Balaž**[1] and **Ana Ćirišan**[1]

[1]*Faculty of Agriculture, University of Novi Sad,*
Dositej Obradović Sq. 8, 21000 Novi Sad, Serbia

[2]*Hydrometeorological Service of Serbia,*
Kneza Viseslava 66, Belgrade, Serbia
E-mails: branka@polj.ns.ac.yu; guto@polj.ns.ac.yu

(Manuscript received in final form February 13, 2007)

Abstract—In this paper, the LAPS surface scheme and the BAHUS biometeorological model are shortly described. LAPS has been applied for within-crown microclimate simulations in an apple orchard at experimental site Rimski Sancevi in the northern part of Serbia. The simulated values of leaf wetness duration, air temperature, and relative humidity within the tree crown are compared with the data measured in the orchard during the 2003 apple growing season. On the basis of biological and meteorological inputs coming from the outputs of either the automatic or the climatological weather station, or LAPS, BAHUS was applied in order to give the messages on occurrence of apple scab and fire blight diseases. BAHUS outputs obtained for the three meteorological input data sets are compared with time and intensity of infections observed in the apple orchard.

Key-words: agrometeorological modeling, SVAT models, data representativeness, diseases forecasting

1. Introduction

The first recorded agrometeorological forecast was made by Réaumur in year 1735 (*Réaumur*, 1735). This pioneer work was related to the forecast of phenological development for several crops based on thermal sum concept. Over almost three centuries, an "army" of scientist coming from different meteorological and agricultural communities has invested a great deal of effort

* Corresponding author

to establish agrometeorology as an applied science. At present level of development, agrometeorology plays the main role in the development of sustainable and economically viable agricultural systems, production and quality improvement, losses and risk reduction, cost decrease, and efficiency increase in the use of water, labor, and energy (*Lalic et al.*, 2005).

Accuracy of agrometeorological modeling depends on: (a) how well the initial observations represent the regional conditions, (b) how homogeneous the regional conditions are, (c) how accurate the observations themselves are, and (d) how sensitive the model is to agrometeorological variables variations (*Lomas*, 1984). In addition, it should be taken into account, how representative certain relations or modeling tools are for particular agroecological conditions, and how uncertainties in the variables will affect the result. More details about the representativeness concept, related to the actual use of measured or calculated parameter value in a numerical model, with an application on documentation system for administration of meteorological parameters at The Norwegain Crop Research Institute, can be found in *Sivertsen* (2005).

The objective of this paper is to emphasise the importance of input data and modeling tools representativeness in providing useful and accurate agrometeorological information. After Section 2, which gives a brief overview of basic agrometeorological techniques, in Section 3, the LAPS surface scheme (*Mihailovic*, 1996; *Mihailovic* and *Kallos*, 1997) and BAHUS biometeorological model (*Mihailovic et al.*, 2001; *Lalic et al.*, 2003) for predicting the occurrence of some frequent plant diseases are described shortly. In Section 4, the observations are presented and compared with the results of the following simulations: (a) orchard microclimate simulation provided using the LAPS scheme and (b) plant diseases occurrence prediction obtained using BAHUS model run with the three different types of meteorological data (gathered at an apple orchard, measured at the meteorological station in the vicinity of the orchard, and simulated by the LAPS scheme). Section 5 summaries the concluding remarks.

2. Agrometeorological modeling techniques and data representativeness

Last decades of the 20th century were denoted by increasing development of modeling tools and techniques in all areas of research and technology. No industry is built before a model is conceived where the controls of all its production processes are known (*Dourado-Neto et al.*, 1998). In agrometeorology, modeling is the art of predicting the vegetation dynamics, crop yield and production, disease and pest appearance, drought development, pasture and animal production, fish catches, and meteorologically induced post-harvest losses (*Gommes et al.*, 1996). Since an agrometeorological model attempts to simulate plant/animal-soil-weather interaction in a quantitative way, it needs the information and data on the most important factors that relate agricultural production response to its environment, i.e., model inputs. These inputs mainly consist of different biological, meteorological, soil, and management data.

After passing through the "modeling" part of the model, the inputs are converted into a number of outputs. All procedures incorporated into the "modeling" part are based on either empirical relations or parameterized scientific laws. If a variable of interest could be achieved as a result of parameterization (the intensity of canopy evaporation, soil moisture and temperature, horizontal and vertical runoff, the intensity of within canopy deposition, the rate of nitrogen movement, etc.), then the accuracy of modeling strongly depends on the representativeness and the accuracy of forcing data. Particularly, if the chosen variable represents the statement of atmosphere at a certain point and the mathematical formulation of the process of interest is well known, then the output information for this point is as accurate as the input data are. For that purposes, the SVAT model is an irreplaceable part of an agrometeorological model providing a link between the underlying surface and the atmosphere with the strong background focused on the parameterization of environmental fluid dynamics and physiological processes. Depending on the time and space scales of the agrometeorological model, the included SVAT schemes range in complexity from a simple bucket model as used by *Manabe* (1969) to the vertically complex models, such as BATS (*Dickinson et al.*, 1986), SiB (*Sellers et al.*, 1986) and LAPS (*Mihailovic*, 1996; *Mihailovic* and *Kallos*, 1997). The current improvement of the SVAT models is related to the incorporation of sub-grid scale heterogeneity (*Famiglietti* and *Wood*, 1994; *Liang et al.*, 1994; *Mihailovic et al.*, 2005) and to the improvement of plant physiological processes parameterization (*Wang* and *Jarvis*, 1990) increasing the complexity and the number of model parameters (*Dourado-Neto et al.*, 1998). In this way, the SVAT model becomes more sophisticated but, from the point of view of agrometeorological models, its effectiveness decreases.

On the other hand, if the model output is a result of application of empirical relation (appearance of some phenological phases, crop yield, disease and pest appearance), then the accuracy of the agrometeorological modeling depends on the representativeness of forcing data and on the applied formula. Typically, meteorological elements appearing in empirical relations are not defined precisely enough. Moreover, it is not obvious, where the reference level is placed and whether the data are related to within or above the canopy air space. For example, term "air temperature" (without any other comments) in meteorology assumes that it is the temperature of the air at 2meters above the non-vegetated ground. Yet, the outside meteorological community rules are not so strict, and this term could be also related either to the temperature of air surrounding the plant, bacteria, or insects, or to the air temperature above canopy. Additionally, it is a well-known fact, that empirical relations are representative only of agroecological conditions similar to those for which they are defined in the first place. It assumes that particular relation could not be extrapolated without the adjustment for conditions different from those of its origin.

3. Short descriptions of LAPS scheme and BAHUS model

In order to reconsider the representativeness of different meteorological datasets in agrometeorological forecasting, surface scheme LAPS and biometeorological model BAHUS have been used.

LAPS scheme. This SVAT model describes mass, energy, and momentum transfers between the land surface and the atmosphere. The model is designed as a software package that can be run as part of an environmental model or as a stand-alone one. LAPS includes modeling of the land surface and atmosphere interaction under processes divided into three sections: subsurface thermal and hydraulic processes, bare soil transfer processes, and canopy transfer processes. They are: the interaction of vegetation with radiation, evaporation from bare soil, evapotranspiration including transpiration and evaporation of intercepted water and dew, conduction of soil water through the vegetation layer, vertical water movement in the soil, surface and subsurface runoff, heat conduction in the soil, and momentum transport within and above the vegetation. A single layer "sandwich" approach for canopy is chosen for the physical and biophysical parameterization. The scheme has seven prognostic variables: three temperature variables (foliage, soil surface, and deep soil), one interception storage variable, and three soil moisture storage variables. For the upper boundary conditions the following forcing variables are used: air temperature, water vapor pressure, wind speed, short wave and long wave radiation, and precipitation at a reference level within the atmospheric boundary layer. The surface fluxes are calculated using resistance representation. The soil module is designed as a three-layer model, which is used to describe the vertical transfer of water in the soil. LAPS uses the morphological and physiological characteristics of the vegetation community for deriving the coefficients and resistances that govern all the fluxes between the surface and atmosphere. More details and descriptions can be found in *Mihailovic* (1996) *Mihailovic* and *Kallos* (1997), while the review of the new approaches was reported at the „Workshop on Environmental Fluid Mechanics as Elements in Agrometerological Modeling" (*Mihailovic* and *Lalic*, 2006).

BAHUS model. It is a biometeorological model conceptualized for providing the messages of occurrence of plant diseases and the proper time for pesticide application (*Mihailovic et al.*, 2001; *Mihailovic et al.*, 2002). Components of this model are: (1) input module – providing meteorological and biological data that are representative of a selected area, (2) modeling module – consisting of empirical relations and conditions related to the disease appearance and intensity of infection, and (3) output module – giving the following messages: the risk of infection, the duration of incubation period, the time of the first symptoms, etc. Depending on the method selected in the modeling module, following meteorological data should be provided by the input module: maximum air temperature, minimum air temperature, mean daily temperature, actual values of temperature, relative humidity, precipitation, and the duration of leaf wetness. Since in the literature (indicated bellow) used for developing each diseases routine, there is no precise information about the reference level related to the meteorological variables, it was supposed, in all calculations, that these variables describe conditions within the crown air space. In the modeling module, the BAHUS uses method defined by *Mills* (1944), later modified by *Jones et al.* (1980), based on air temperature, relative humidity, and the duration of leaf wetness in order to describe the intensity of apple scab infection. Requirements for fire blight blossom infection defined by *Steiner* (1990) are incorporated in Degree-day (*Mills*, 1955) and MARYBLIGHT methods (*Steiner* and *Lightner*, 1992). These methods are based on accumulation of degree-days (DD) and degree-hours (DH), which are defined as a number of degrees over the base temperature during one day and one hour, respectively (*Zoller* and *Sisevich*, 1979; *Mills*, 1955). For a particular forecasting day model outputs are: (i) the intensity of apple scab infection ranged as none, weak, medium, and strong infection, and (ii) for a fire blight blossom infection event with a description of risk as none, low, moderate, and high infection. Let us note that this module also produces other outputs, but for the purpose of this paper we have selected the aforementioned ones.

4. Numerical experiment

In the numerical experiment, appearance of fire blight and apple scab diseases, during the 2003 apple growing season in Serbia, was forecasted by the BAHUS model, that is its the first run with real data (*Lalic et al.*, 2003). In that purpose, three sources of meteorolopgical data were used: (i) a data set measured by an ADAS mini weather station placed in the apple orchard, (ii) a data set measured on the weather station Rimski Sancevi in the vicinity of apple orchard ($\approx$ 1 km), and (iii) a data set obtained as a result of the simulation of apple orchard microclimate using the LAPS scheme. In the further text these data sets are denoted by DS1, DS2, and DS3, respectively. The main idea of using these three different data sets is to explore its representativeness for apple orchard disease forecasting. As a first step in this numerical experiment, the LAPS scheme was run on hourly basis to provide simulated values of leaf wetness duration, air temperature, and relative humidity within the tree crown. Obtained results compared with *in situ* measured data illustrate that LAPS can provide an accurate simulation of daily variation of within-crown air temperature and relative humidity (*Figs. 1* and *2*). Some deviations between the simulations and measurements are seen only for extreme values of variables. Regarding leaf wetness duration, results presented in *Fig. 3* show that, for the particular period, LAPS simulates two wet periods, while the ADAS station registered only one. After short inspection of the data related to precipitation, it becomes absolutely clear that there are two wet periods, but the first one (April 24 and 25) was caused with such a small amount of precipitation (0.4 mm and 0.1 mm) that leaf wetness sensor placed within the tree crown did not become wet. On the other hand, LAPS recognized these rain episodes like sources of leaf wetness.

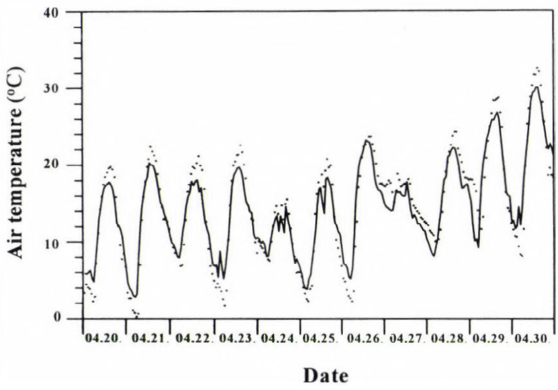

Fig. 1. Within-crown air temperature, measured by the ADAS weather station (dots) and simulated using the LAPS model (line), during the last decade of April 2003.

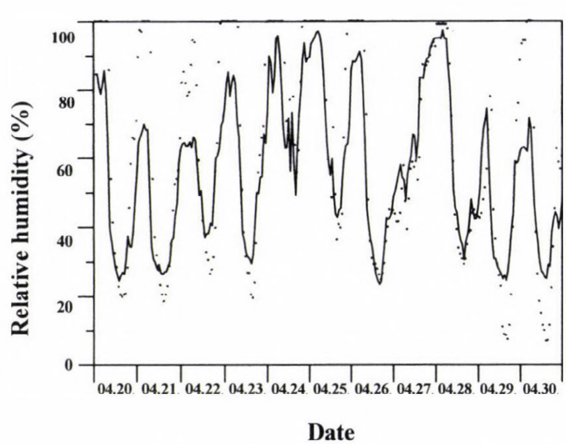

Fig. 2. Within-crown relative humidity, measured by the ADAS weather station (dots) and simulated using the LAPS model (line), during last decade of April 2003.

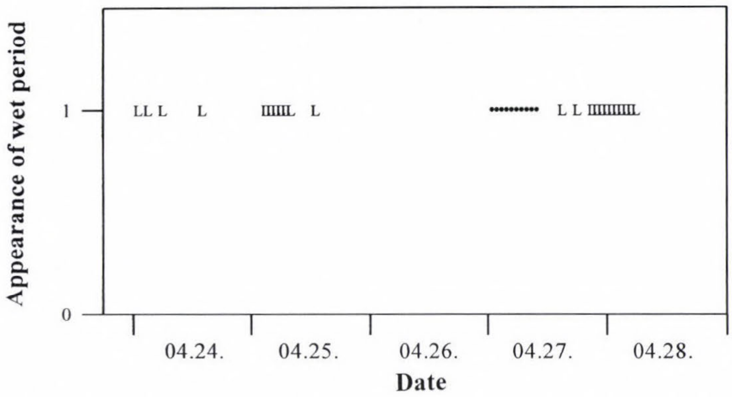

Fig. 3. Appearance of wet period, measured by the ADAS weather station (dots) and simulated using the LAPS model (L), during the last decade of April 2003.

From April 21st, when flowering and the accumulation of degree days (DD) and degree hour (DH) units started, the indicators for *Erwinia amylovora* development, as well as the leaf wetness necessary for releasing the *Venturia inaequalis* ascosporic, were pursued. Accumulated DH units and related epiphytic infection potential (EIP) representing possibility of fire blight blossom infection are calculated using the above mentioned data sets. The results presented in *Table 1* indicate that, in all cases, the infection practically starts on April 29 since there are small differences in EIP among methods in the range of error of measurements. However, the appearance and intensity of apple scab infection are too complex and cannot be described with only two parameters. For that reason, in *Table 2* only critical days and expected intensity of infection are presented. Obviously, in all cases, April 27 is the critical day for apple scab infection appearance with small differences in expected infection intensity. Following the information that comes from phytopathologists, the results presented in *Table 1* and *Table 2* correspond to the observed fire blight blossom appearance and the intensity of apple scab infection in the apple orchard at Rimski Sancevi.

Table 1. Accumulated DH and epiphytic infection potential (EIP) calculated using DS1, DS2, and DS3 data sets (days without DH accumulation are omitted)

Date	DS1		DS2		DS3	
	DH (°C)	EIP	DH (°C)	EIP	DH (°C)	EIP
04. 27	0.5	0.5	31.8	35.3	35.4	31.9
04. 28.	38.2	34.4	27.5	24.8	27.6	24.9
04. 29.	117.1	105.5	109.5	98.6	109.7	98.9
04. 30.	246.5	222.1	248.6	224.0	249.0	224.3

Table 2. Intensity of apple scab infection calculated using DS1, DS2, and DS3 data sets (days, when leaves were dry, are omitted)

Date	DS1	DS2	DS3
04. 24	no infection	no infection	no infection
04. 25	no infection	no infection	no infection
04. 26	no infection	no infection	no infection
04. 27	weak infection	weak infection	moderate infection

5. *Concluding remarks*

In this paper, the LAPS scheme has been applied for apple orchard microclimate simulations. The BAHUS biometeorological model was used in order to forecast appereance of blossom fire blight and apple scab infection in an apple orchard during the 2003 growing season at the experimental site Rimski Sancevi. Three meteorological input data sets coming from automatic weather station, climatological weather station, as well as the LAPS scheme were used in order to compare the BAHUS outputs with the observations and to explore the representativeness of these meteorological inputs for the purpose of disease forecasting.

The obtained results indicate that, sometimes significantly, the differences between DS1, DS2, and DS3 data sets are not considerable in disease forecasting. This situation is strongly affected by the non-sophisticated nature of the prognostic methods incorporated into a BAHUS model and could be taken as an advantage till differences between forecasted and observed time of infection is one or two days. Yet, for larger differences it is obvious, that the applied method is too simplified, avoiding factors and processess strongly affecting the disease development. Consequently, in the absence of *in situ* measurements, the data measured at a weather station in the vicinity of orchard or simulated using the LAPS scheme could be used as meteorological inputs for the BAHUS model, at the present level of sophistication.

However, it is hard to balance the appetite for commonly available input data with internal complexity of the method. Even *in situ* measurements could not guarantee accurate agrometeorological forecast, if they are not harmonized with the applied modeling techniques. Therefore, it is of the utmost importance, that the agrometeorological model is followed by a list of incorporated processes and a precise documentation of parameters and variables used, see *Sivertsen* (2005). From that particular point one can try to provide data sets and parameters as realistic as possible. In the near future, a realistic challenge of the operational use of agrometeorological models will be the extended availability of data from different sources like weather stations, weather radars, satellite, and tools for integrating the data ought to be developed. In order to integrate data from different sources, it is important to document the data thoroughly.

References

Dickinson, R.E., Henderson-Sellers, A., Kennedy, P.J., and *Wilson, M.F.,* 1986: Biosphere-Atmosphere Transfer Scheme (BATS) for the NCAR Community Climate Model. *NCAR Tech. Note TN-275_STR*, Boulder, Co., 72 pp.

Dourado-Neto, D., Teruel, D.A., Reichardt, K., Nielsen, D.R., Frizzone, J.A., and *Bacchi, O.O.S.,* 1998: Principles of crop modeling and simulation II. The implications of the objective in model development. *Sci. Agric., Piracicaba, 55 (Número Especial),* 51-57.

Famiglietti, J.S. and *Wood, E.F.,* 1994: Application of Multi-Scale Water and Energy Balance models on a Tallgrass Prairie. *Water Resour. Res. 30,* 3079-3093.

Gommes, R., Bernardi, M., and *Petrassi, F.,* 1996: Agrometeorological Crop Forecasting. *Environment and Natural Resources Service (SDRN), FAO Research, Extension and Training Division*, 23 pp.

Jones, A.L., Lillevik, S.L., Fisher, P.D., and *Stebbins, T.C.,* 1980: A microcomputer-based instrument to predict primary apple scab infection periods. *Plant Dis. 64,* 69-72.

Lalic, B., Mihailovic, D.T., Balaz, J., and *Koci, I.,* 2003: Prediction of occurrence of plant diseases using the coupled atmosphere-land surface models. *Sixt European Conference on Applications of Meteorology*, September 15-19, Rome (Italy), Abstracts, 13 p.

Lalic, B., Koci, I., and *Mihailovic, D.T.,* 2005: Agrometeorological modeling – powerful tool of modern agriculture. *Proc. of the International Conference on Sustainable Agriculture and European Integration Processes*. 19-24 September 2004. *Savremena poljoprivreda 54,* 312-317.

Liang, T., Lai, H., and *Chen, N.,* 1994: When Client/Server isn't enough: Co-ordinating Multiple Distributed Tasks. *IEEE Computer, Vol. 27,* No. 5. 73-79.

Lomas, J., 1984: CAgM Report No. 22. Chairman of a Working Group of CAgM. Agrometeorological Services in Developing Countries. 35 pp.

Manabe, S., 1969: Climate and the ocean circulation 1. the atmospheric circulation and the hydrology of the earth's surface. *Mon. Weather Rev. 97*, 739-774.

Mihailovic, D.T., 1996: Description of a land-air parameterization scheme (LAPS). *Global Planet. Change 13,* 207-215.

Mihailovic, D.T. and *Kallos, G.,* 1997: A sensitivity study of a coupled-vegetation boundary-layer scheme for use in atmopsheric modeling. *Bound.-Lay. Meteorol. 82,* 283-315.

Mihailovic, D.T., Koci, I., Lalic, B., Arsenic, I., Radlovic, D., and *Balaz, J.,* 2001: The main features of BAHUS – biometeorological system for messages on the occurrence of diseases in fruits and vines. *Environ. Modell. Softw. 16,* 691-696.

Mihailovic, D.T., Eitzinger, J., Koci, I., Lalic, B., Arsenic, J.I., and *Balaz, J.,* 2002: Biometeorological system BAHUS for predicting the occurrence of plant diseases and ensuring their efficient control. *Int. Workshop on Environmental Risk Assessment of Pesticides and Integrated Pesticide Management in Developing Countries,* Kathmandu, Nepal, 6-9 November. *Landschaftsökologie und Umweltforschung 38*, 120-129.

Mihailovic, D.T., Rao, S.T., Alapaty, K., Ku, J.Y., Arsenic, I., and *Lalic, B.,* 2005: A study on the effects of subgrid-scale representation of land use on the boundary layer evolution using a 1-D model. *Environ. Modell. Softw. 20*, 705-714.

Mihailović, D.T. and *Lalic, B.,* 2006: Land-Air Parameterisation Scheme (LAPS) as a Component in Agrometeorological Modelling. Abstracts of *Workshop on Environmental Fluid Mechanics as Elements in Agrometeorological Modelling.* June 6-9, Ås (Norway).

Mills, W.D., 1944: Efficient use of sulfur dusts and sprays during rain to control apple scab. *N.Y. Agric. Exp. Stn. Ithaca Bull. 630*, 4 pp.

Mills, W.D., 1955: Fire blight development on apple in western New York. *Plant Dis. Rep. 39,* 206-207.

Réaumur, R.A.F., 1735: Observation du thermometre, faites to Paris pendant l'année 1735, comparées avec celles qui ont été faites sous la ligne, to the l'Isle of France, to Alger et en quelques-unites of in the l'Amérique isles. *Mém. Acad. give Sci., in the 545,* Paris.

Sellers, P.J., Mintz, Y., Sud, Y.C., and *Dalcher, A.,* 1986: A simple biosphere model (SIB) for use within general circulation models. *J. Atmos. Sci. 43*, 505–531.

Sivertsen, T.H., 2005: Discussing the scientific method and a documentation system of meteorological and biological parameters. *Phys. Chem. Earth 30*, 35-43.

Steiner, P.W., 1990: Predicting apple blossom infection by *Erwinia amylovora* using the Maryblyt model. *Acta Horticulturae 273*, 139-148.

Steiner, P.W. and *Lightner, G.W.*, 1992: MARYBLYT: A Predictive Program for Forecasting Fire Blight Disease in Apples and Pears. *University of Maryland, Version 4.0.*

Wang, Y.P. and *Jarvis, P.G.*, 1990: Description and validation of an array model. MAESTRO. *Agr. Forest Meteorol. 51*, 257-280.

Zoller, B.G. and *Sisevich, J.*, 1979: Blossom populations of Erwinia amilovora in pear orchards vs. accumulated degree hours over 18.3 Celsius, 1972-1976. *Phytopatology 69,* 1050 p.

IDŐJÁRÁS

Quarterly Journal of the Hungarian Meteorological Service
Vol. 111, No. 2–3, April–September 2007, pp. 209–220

An essay on modeling problems of complex systems in environmental fluid mechanics

Dragutin T. Mihailović[1*] and **Igor Balaž**[2]

[1]*Faculty of Agriculture, University of Novi Sad,*
Dositej Obradović Sq. 8, 21000 Novi Sad, Serbia; E-mail: guto@uns.ns.ac.yu

[2]*Scientific Computing Laboratory, Institute of Physics,*
P.O. Box 57, 11001 Belgrade, Serbia

(Manuscript received in final form January 29, 2007)

Abstract—In this essay we point out the current problems in the modeling of complex biophysical systems, particularly in environmental fluid mechanics, which requires quite new methodological and mathematical approaches. We give a short overview of some epistemological attitudes arisen from the 20th century onwards, which have converged on establishing of endophysics. Then, we generally discuss the establishment of the relations between the two different kinds of reasoning (causal and inferential) by pointing out a possibility of using two-state (teleological) model in modeling of complex systems. Using an example from environmental fluid mechanics, i.e., solving the energy balance equation for the Earth-atmosphere interface, we show that uncertainties can occur in predictions because of non-linear relations in the system under consideration.

Key-words: environmental fluid mechanics, endophysics, complex systems, modeling, epistemology, non-linear processes, deterministic chaos, teleological dynamics

1. Introduction

Regardless of the word "balance" being used either globally or locally in any given context, it is undoubtedly the keyword in the increasing number of environmental problems. The underlined sketch is a proper introduction to the question: Why are the environmental problems in the focus now? One particular answer can be found in the hierarchy of the main scientific problems of the 21st century, as seen by the community mostly consisting of physicists. According to them, in the 21st century the world of the scientific community will be occupied by the problems linked to superconductivity, quantum teleology, and

* Corresponding author

environmental problems that are primarily expressed through the problem of climate changes. A unique characteristic of these problems is their close connection with the questions of different aspects of the existence of individual human being, i.e., the questions of technological capability, origin of the consciousness and survival on the Earth. This is the first time in the history of science, when the environmental problems take the place at the front of the sciences. The question, why it is happening now and why it will go on happening in the future, could be answered by the well known fact, that in the scientific as well as in other worlds the main "drama of event" takes place at the interface between either two media or two states (*Mihailovic,* 2006).

The field of environmental sciences is abundant with various interfaces, and it is the right place for application of new fundamental approaches leading towards better understanding of environmental phenomena. We defined the environmental interface as an interface between the two either abiotic or biotic environments, which are in a relative motion exchanging energy through biophysical and chemical processes and fluctuating temporally and spatially regardless of its space and time scale. To our mind, this definition broadly covers the unavoidable multidisciplinary approach in environmental sciences and also includes the traditional approaches in sciences, that are dealing with the environmental space less complex than any one met in reality. The wealth and complexity of processes at this interface determine that the scientists, policy-makers, and the public, as it often seems, are more interested in a possibility of non-linear dislocations and surprises in the behavior of the environment than in a smooth extrapolation of current trends and a use of the approaches close to the linear physics. To overcome the current situation we have to do the following: (a) to establish a way in approaching non-linear physics and the non-linearity in describing the phenomena in environmental sciences, and (b) to solve or, at least, understand the problem of predictability. These two problems are *par excellence* problems of the methodology. Their successful solving will help us to avoid the current problems in mathematical, biophysical, and chemical interpretation of the nature, as well as in design of corresponding software. The environmental discipline that will be under consideration in this essay is the environmental fluid mechanics dealing with a broad range of environmental problems, which are, for example, picturesquely described and defined in *Cushman-Roisin et al.* (2006). Because of the thought behind this essay, this definition will be given in detail.

All forms of life on earth are immersed in a fluid, either the air of the atmosphere or the water of a river, lake, or ocean; even soils are permeated with moisture. So, it is no exaggeration to say that life, including our own, is bathed in fluids. A slightly closer look at the situation reveals further, that it is the mobility of fluids that actually makes them so useful for the maintenance of life, both inside and outside living organisms. For example, it is the flow of air through our lungs that supplies oxygen to our blood stream. The forced air flow created by our respiration, however, is not sufficient. Namely, without atmospheric motion around us, we would sooner or later choke to death with the carbon dioxide exhaled by ourselves. Likewise, most aquatic forms of life rely on the natural transport of water for their nutrients. Our industrial systems, which release pollution on a continuing basis, would not be permissible in the absence of transport and dilution of nearly all emissions by ambient motions of air and water. In sum, natural fluid motions in the environment are vital, and we have a strong incentive to study the naturally occurring fluid flows, particularly those of air in the atmosphere and of water in all its streams, from underground aquifers to surface flows in rivers, lakes, estuaries, and oceans.

The study of these flows has received considerable attention over the years, and several distinct disciplines have emerged: meteorology, climatology, hydrology, hydraulics, limnology, and oceanography. Whereas the particular objectives of each of these disciplines, such as weather forecasting in meteorology and design of water-resource projects in hydraulics, encourage disciplinary segregation, environmental concerns compel experts in those disciplines to consider problems that are essentially similar: the effect of turbulence on the dispersion of a dilute substance, the transfer of matter or momentum across an interface, the flow in complex geometries, the rise of a buoyant plume, and the impact of flow over a biotic system. The common points encourage interdisciplinarity to a degree, that it is increasing in proportion to the acuteness of our environmental problems. This overlap between various disciplines concerned with the environmental aspects of natural fluid flows has given rise to a body of knowledge, that has become known as environmental fluid mechanics.

This short essay aims just to point out the current problems in modeling of complex biophysical systems, particularly in environmental fluid mechanics, that require quite new methodological and mathematical approaches.

2. A short overview of some epistemological points from the 20th century onwards

Until recently, discussions about scientific truth were filled with numerous metaphysical assumptions. They usually converged at one question (more or less explicitly stated): "How can we reach objective truth about natural processes?" However, during the 20th century, this question first became less important and then gradually disappeared from the epistemological scene as a relict from the age of naive realism. Now, in contemporary epistemology of science, it is well established that there is a fundamental difference between phenomenon and noumenon. Therefore, the object of scientific analysis cannot be the nature by itself, but only highly constructivistic products, i.e., conceptually embedded sets of observer's experiences. Accordingly, scientific theories are now understood as logical instruments of organization of human thought, through which we can interpret and organize experimental laws (*Nagel,* 1961). Also, since they have constructivistic character, their relation to the nature should not be considered through the vocabulary of logic; they are not truth statements and they are not logical derivatives of observed facts, but only sets of rules and guiding principles for analysis of empirical facts (*Nagel,* 1961). Therefore, in the development of a scientific theory, it is not a problem to make approximations that can never reach reality. It is inevitable. But believing that relations of abstractions are exactly the same as relations in nature can be very problematic. Firstly, it can usually become a source of unfruitful debates about the "true" nature of the nature. Secondly, from such a perspective it is impossible to see and analyze the consequences of the interface perspective, where the observer is within the universe he observes.

A clear example of both mentioned problems can be found in the development of the contemporary physics. At the very beginning of the 20th century, Pierre Duhem asserted that physical theories are not simple (straightforward) reflexions of natural processes, but rigorous logical systems, which operate with abstract symbols and which are connected with nature through system of measurements and scales (*Duhem,* 1906). Such approaches put forward the process of encoding of natural processes into the domain of formal systems, as the first and crucial step in the development of a physical theory. However, in his opinion, a pattern of encoding depends almost entirely on the previously accepted theories. Therefore, empirical observations cannot be separated from the current state of affairs in a given scientific discipline, since theoretical assumptions determine what will be observed, how it will be observed, and how results will be interpreted. Although Duhem's approach can be characterized as conventionalism, his contribution to the general trend of development of thought in theoretical physics remains immense.

Few decades later, the explosive growth of quantum mechanics raised some fundamental questions about the status of observation in physics, and how our measurement procedures can affect the observed physical properties ("measurement problem"). In short, Einstein, opposing the Copenhagen interpretation of physical properties of quantum systems, claimed that under ideal conditions, observations reflect the objective physical reality (*Einstein et al.,* 1935). On the other hand, Bohr asserts that in quantum mechanics the measured quantum system and the measuring macroscopic apparatus cannot be considered as separate within a scope of scientific consideration. In other words, the physical properties of quantum systems are essentially dependent on the applied experimental apparatus. One of the most famous moments of the debate is now well-known as Einstein-Podolsky-Rosen paradox (*Einstein et al.,* 1935). In the short paper they showed, that if the quantum mechanic description of reality is complete, then the non commutable operators corresponding to two physical quantities can have simultaneous reality. In other words, quantum mechanics is inconsistent with the reduction of the wave-packet postulate. Later, Bell (*Bell,* 1964) revealed, that the EPR paradox stands only under the set of supplementary assumptions, among which there is the assumption of locality. Moreover, within quantum mechanics there is no need to accept them all. Although it can look like a closing chapter in the debate on "measurement problem", this question evolved from the limited scope of quantum mechanics and took a more general form: "how the observations are affected by the fact that the observer is within the universe he observes?". This is certainly not a new question in the history of human though, but (until recent partial attempts) in the natural sciences it never gets a formal explanation. In philosophy, after Kant, it is one of the elementary topics, in developmental psychology Piaget clearly demonstrated, that elementary categories of human thought are construed during one's development, and how externality of cognitive entities is re-structured in accordance with its functional purposes through the process of assimilation of external changes with the operative schematism of that entity (*Piaget,* 1973a; *Piaget,* 1973b), and finally, in the world of logic and formal systems, Gödel shook the scientific community with his proof of incompleteness of formal systems (for extensive discussion see *Nagel* and *Newman,* 1958; *Rosen,* 1991). Now, in the natural sciences this problem is finally recognized and dispersed attempts of its formal treatment fall under the umbrella of discipline called endophysics. This term was originally suggested by David Finkelstein in personal communication with Otto Rössler. Later, it was comprehensively elaborated in details by *Rössler* (1998), although his *magnum opus* is loaded with inconsistencies.

We see the outside world, i.e., the world of phenomena (*ambience*) from the observer's perspective (its inner world). In the ambience there are *systems* of different level of complexity and their *environments*. A system in the ambience is a collection of precepts while whatever lies outside, like the component of a set, constitutes the environment. The fate of science lies in the fact that it is focused on the system (*Rosen*, 1991). Furthermore, to anticipate something, the system gets described by *states* (determined by observations), while the environment is characterized through its effects on the system. The trend in contemporary science and mathematics is to try to dispense with extralinguistic referents entirely and replace them with purely syntactic structures, that only recognize and manipulate the symbols out of which the propositions are built. This process is called *formalization* (*Kleene,* 1952). The crucial thing to bear in mind is that both theory and any formalisation of it are the systems of *entailment*. It is the *relation* between them, or more specifically, the extent to which these schemes of entailment can be brought into congruence. That is of primary interest. The establishment of such congruences is the essence of the *modeling relation* (*Rosen,* 1991). In the precise sense, the incompleteness theorem of Gödel asserts that formalization, in which each entailment is a syntactic entailment, is too poor in entailment to be congruent with the number theory, no matter how we try to establish such a congruence. This kind of situation is termed complexity (*Rosen,* 1977). In this light, Gödel's theorem says that the number theory is more complex than any of its formalizations. Following the message and the fundamental consequences of this theorem, we call the complex system such a system that is more complex than its any formalization.

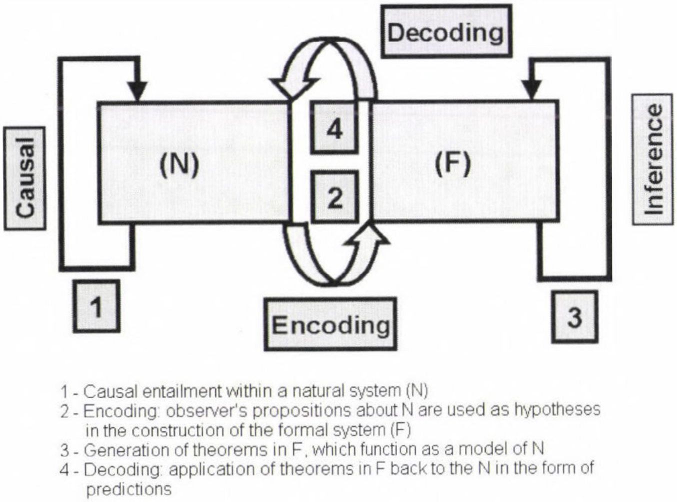

Fig. 1. Schematic diagram representing both (i) comparison of two formalisms F_1 and F_2, and (ii) modeling relation when we have given a natural system N, and a formal system F.

Fig. 1 schematically depicts a comparison of two formalisms F_1 and F_2. To compare two formalisms we need to make two dictionaries. The first of them, which translates from F_1 to F_2, is an *encoding* dictionary while the other, translating from F_2 back to F_1, is a *decoding* dictionary. Let us note, that we do not require any relation at all between them. If we find the encoding and decoding for which the diagram of *Fig. 1 always commutes*, in such a case, we have in fact brought at least a part of the inferential machinery of F_1 into congruence with a corresponding part of the inferential machinery of F_1. We will then say that F_2 is a *model* of F_1, or equivalently, that F_1 is a *realization* of F_2. Also we can say that a *modeling relation* exists between the two inferential structures. We can use the inferential structure of the model to study its realization, to *predict,* in effect, from the encoded hypothesis (via the pathway 2 + 3 + 4 in the diagram in *Fig. 1*), theorems of F_1 from theorems in F_2. In mathematics, there are a lot of procedures of formal modeling of one kind of inferential structure into another. It seems that the category theory comprises, in fact, the general theory of formal modeling, the comparison of different modes of inferential or entailment structures.

Fig. 1 also schematically depicts a modeling relation, when a natural system N and a formal system F are given. As before, the two arrows represent the respective entailment structures; inference in formalism F, causality in N. Now, the two established dictionaries provide an encoding of the phenomena of N into the propositions of F and a decoding of the propositions of F back to the phenomena in N. As we said before, there are two paths in the diagram: (1) and (2) + (3) + (4). According to *Rosen* (1991), the first of them (the path (1)) represents a causal entailment within N (what an observer, simply sitting and watching what happens in, will see). The arrow (2) encodes the phenomena in N into the propositions in F. In this route we must use these propositions as hypothesis, on which the inferential machinery of the formal system F may operate (denoted by the arrow (3)). It generates theorems in F, entailed precisely by the encoded hypotheses. Finally, we have to decode these theorems back into the phenomena of N, via the arrow (4). At this point, the theorems become *predictions* about N. Then the formal system F is called a *model* of the natural system N, if we always get the same answer, regradless of the fact, whether we follow path (1) or path (2) + (3) + (4).

Finally, in this section we cannot avoid the question of time in the modeling relation. A usual approach in physics is that the present state is strictly a result of its evolution from the past. However, recently it has been shown that some phenomena in the real world can be explained, if we accept that the *present state* of a system is defined by its *past*, in the sense that the past determines the possible states that are to be considered, and by its *future*, in the sense that the selection of a possible future state determines the effective present state (*Nedeljkovic* and *Nedeljkovic,* 2003a; *Nedeljkovic* and *Nedeljkovic,* 2003b among others); regarding that a concise and illustrative differentiation between causal and teleological dynamics is given by *Van Loocke* (2002). According to them, in a large part of the present-day physics, the fundamental physical laws are compatible with the teleological as well as with the causal dynamics (the term 'causal' is used in the restricted sense of 'governed by influences from the past'). Considering a system that is characterized by a set of variables $x_i(t)$ ($I = 1,\dots, n$), where t is the time variable, he makes a differentiation between the causal and the teleological dynamics by the following definitions:

(1) A system behaves causally and deterministically if there is a law that determines the values of $x_i(t)$ given the values of $x_i(t-1)$ at the previous time step.

(2) A system behaves causally and non-deterministically, if there is a law that produces the probability distributions for possible values of $x_i(t)$ giving the probability distributions for possible values of of $x_i(t-1)$ at the previous time step.

(3) A system is teleological and deterministic if there is a law that determines the values of $x_i(t)$ giving the values of $x_i(t+1)$ at the next time step.

(4) A system is teleological and non-deterministic, if there is a law that produces the probability distribution for possible values of $x_i(t)$ giving the probability distributions for possible values of $x_i(t+1)$ at the next time step. We will not further speculate with the question about time. This is just a short reminder for the environmental fluid mechanics community that, in the modeling of complex biophysical processes, we should bear in mind a possibility of using two-state (teleological, *Nedeljkovic* and *Nedeljkovic,* 2003a) models.

3. An example of modeling at the Earth-atmosphere interface

There is still no information available in the environmental fluid mechanics literature about the application of the methods and approaches of the endophysics as mentioned in Section 2. Recently *Sivertsen* (2005) discussed the hypothetico-deductive principle, bearing in mind an observer who looks at the ambience representing the biological world. More precisely, he was dealing with a biological system reacting to the atmospheric environment through meteorological parameters. The outcome of the discussion in this paper, which is an extension of the work in *Sivertsen* (2004), is a proposal of a documentation system for the quantitative meteorological and biological parameters, either measured or the parameters derived by model calculation. Undoubtedly, a growing demand for modeling of more complex systems in environmental fluid mechanics will shift the attention towards the endophysics and the methods of modeling of the complex systems. In this section, we will give an example of the modeling at the Earth-atmosphere interface. In particular, we will point out some uncertainties, which can occur in prediction, because of the non-linear relations in system under consideration.

Environmental fluid mechanics modelers base their calculations on mathematical models for simulation and prediction of different processes, which are exclusively non-linear, describing relevant quantities in the field of consideration. Many investigators, for example *Boccaletti et al.* (2000), have proved that complex dynamical evolutions lead to chaotic regime. Finite precision computer realizations of non-linear models give unrealistic solutions, because of the deterministic chaos, a direct consequence of round-off error growth in iterative numerical computations, which doubles on average for each iteration of iterative computations. Round-off error propagates to the mainstream computation and gives unrealistic solutions for different geophysical models, which incorporate thousands of iterative computations in longer-term numerical integration schemes (*Selvam* and *Fadnavis,* 1998). Also, in solving of the model partial differential equations, depending on numerical procedure, the problem of sensitivity to initial conditions may occur. Namely, a small "tuning" of initial conditions may lead the numerical model to instability, if the system is a chaotic one. The aforementioned instabilities can be generated in temporal fluctuations on all space-time scales ranging from turbulence to climate. These kinds of uncertainties take place preferably at the interface between two mediums in geophysical space (*Mihailovic et al.,* 2001). The land-atmosphere interface is a suitable area for the occurrence of irregularities in the temporal variation of some geophysical quantities. Here we will analyze the occurrence of deterministic chaos in the surface temperature obtained by solving the energy balance equation, which describes the exchange of energy at the land-atmosphere interface.

Solar radiation provides almost all of the energy received on the surface of the Earth. Some of the radiant energy is reflected back to space. The Earth also radiates, in the thermal waveband, some of the energy received from the sun. The quantity of the radiant energy remaining on the earth surface is the net radiation R_n (the net radiation energy available on the surface, when all inward and outward streams of radiation have been considered). The net radiation drives certain physical processes important to us. The energy balance may be expressed as

$$C_g \partial T_g / \partial t = R_n - H - \lambda E - S - PS - M \,, \qquad (1)$$

where C_g is the surface heat capacity, T_g is the surface temperature, S is the flux heat out of the soil, H is the flux of sensible heat between the surface and air, λE is the flux of sensible heat between the surface through vaporization (evaporation) of water condensation, PS is the energy fixed in plants photosynthesis, and M is the energy involved in a number of miscellaneous processes as respiration and heat storage in the crop canopy. Eq. (1) is applicable on the scale of a single plant or cropped field, explaining how energy is provided to warm up the soil crop and to evaporate water. The equation is not less valid on the global scale, explaining how energy is provided to the continents and oceans, where vast quantities of heat and vapor are delivered to or extracted from the atmosphere (*Rosenberg et al.,* 1983). Neglecting terms M and PS, which have much smaller values comparing to other terms, leads us to the equation (*Mihailovic* and *Lalic,* 2006)

$$C_g \partial T_g / \partial t = R_n - H - \lambda E - S \,, \qquad (2)$$

that is more appropriate for further analysis. In the resistance representation, the last equation gets the form

$$C_g \partial T_g / \partial t = C_R (T_g - T_r) - C_L [E(T_g) - e_r] - C_H (T_g - T_r) - C_D (T_g - T_r), \quad (3)$$

where the symbols introduced have the following meaning: C_R is a constant in the net radiation term (*Bhumralkar,* 1975; *Holtslag* and *van Ulden,* 1983), T_r is the air temperature at the reference level, C_L is the water vapor transfer coefficient, $E(T_g)$ is the saturated water vapor pressure at the surface temperature, e_r is the water vapor pressure at the reference level, C_H is the heat transfer coefficient, and C_D is the coefficient of conduction. To solve Eq. (1) numerically, for simplicity we use the foreword difference scheme, as it is usual in environmental fluid mechanic modeling, which has the form

$$T_g^{\,n+1} = T_g^{\,n} + \Delta t F^n / C_g, \quad (4)$$

where F^n is the right hand side term of Eq. (1) at the *n*th time step, while Δt is the time step. Because Eq. (1) is a non-linear partial differential equation, it could be expected that its solution exhibits not only periodic but even chaotic behavior under some conditions. One set of those conditions leading to chaotic behavior of the surface temperature is considered in *Mihailovic* (2006). Under those conditions, Eq. (3) can be written as

$$\partial \xi / \partial t = [a_c - C_L b E(T_r) / C_g] \xi - [C_L b^2 E(T_r) / 2C_g] \xi^2, \quad (5)$$

where $a_c = C_R - C_H - C_D$ and $\xi = T_g - T_r$, while $b = 0.06337$ J °C^{-1} is a constant for temperatures around 20 °C (*Hrigan,* 1978), which occurs in expanding the expression for $E(T_g)$ in Taylor's series. If we write Eq. (5) in the finite difference form, we reach the equation having the form

$$\xi_{n+1} = A_1(C_g)\xi_n - A_2(C_g)\xi_n^2, \quad (6)$$

where the symbols introduced have the following meaning $A_1(C_g) = (C_R - C_L b E(T_r) \Delta t / C_g) + 1$ and $A_2(C_g) = C_L^{\,2} b E(T_r) \Delta t / (2C_g)$. Eq. (6) is one form of the so-called logistic equation. As a non-linear equation, it can produce a chaotic solution for some values of A_1 and A_2. It is very interesting to analyze Eq. (6), in the ($\lambda_L, \Delta t$) phase space, for different values of A_1 and A_2. Here we define the Lyapunov exponent λ_L for this equation, which has a single degree of freedom ξ depending on discrete "time" n. It has the form

$$\lambda_L = \lim_{n \to \infty} (1/n) \sum_{j=1}^{n} \ln \left| F'(\xi_n) \right|, \quad (7)$$

where $F(\xi) = A_1(C_g)\xi - A_2(C_g)\xi^2$.

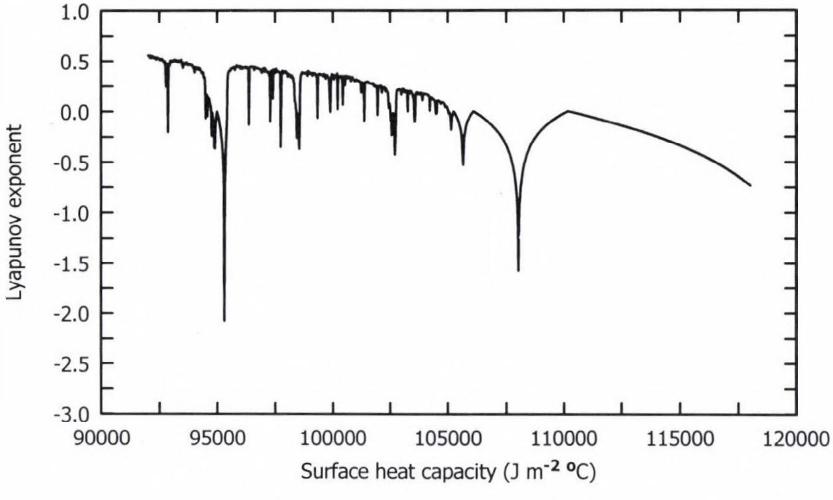

Fig. 2. Dependence of Lyapunov exponent λ_L on soil surface heat capacity C_g (*Mihailovic*, 2006).

Fig. 2 depicts the changes of exponent depending on the variation of the surface heat capacity. It is seen from this figure, that the considered dynamical system, i.e., the soil-atmosphere interface, mostly exhibits chaotic behavior manifested through the positive value of λ_L, while the soil surface heat capacity takes the values from the 92,500–107,500 J m^{-2} °C^{-1} interval. Outside of this interval the considered system is stable, since the Lyapunov exponent takes the negative values. This example points out, that the way to the phenomenon of N via the arrow (4) in *Fig. 1* is not a simple one, even in the case of a relatively simple model. In other word, that attempt is methodologically difficult in the non-linear world.

Acknowledgements—The research work described in this paper has been funded by the Serbian Ministry of Science and Environmental Protection under the project "Modeling and numerical simulations of complex physical systems", No. ON141035 for 2006-2010. The authors would like to thank *Mr. Nebojsa Vukov* for proofreading of the paper.

References

Bell, J.S., 1964: On the Einstein Podolsky Rosen paradox. *Physics 1,* 195-200.

Bhumralkar, C.M., 1975: Numerical experiments on the computation of ground surface temperature in an atmospheric general circulation model. *J. Appl. Meteorol. 14*, 1246-1258.

Boccaletti, C.M., Grebogi, C., Lai, Y-C., Mancini, H., and *Mazaret, D.*, 2000. The control of chaos: Theory and applications. *Phys. Rep. 329*, 108-109.

Cushman-Roisin, B., Gualtieri, C., and *Mihailovic, D.T.*, 2006: *Introduction*. In *Fluid Mechanics Processes at the Environmental Interfaces* (eds.: *C. Gualt*ieri and *D.T. Mihailovic*). Taylor and Francis, London (in press).

Duhem, P. 1906: *The Aim and Structure of Physical Theory* (in Serbian). Izdavacka knjizarnica Zorana Stojanovica, Novi Sad, 2003, 271 pp.

Einstein, E., Podolski, B., and *Rosen, N.,* 1935: Can quantum-mechanical description of physical reality be considered complete? *Phys. Rev. 47,* 777-780.

Holtslag, A.A and *van Ulden, A.P.,* 1983: A simple scheme for daytime estimates of the surface fluxes from routine weather data. *J. Appl. Meteorol. 22,* 517-529.

Hrigan, A.H., 1978: *Fizika atmosfery* (in Russian), *Tom 2.* Gidrometeoizdat, Leningrad, 319 pp.

Kleene, S.C., 1952: *Introduction to Metamathematics.* van Nostrand, New York.

Mihailovic, D.T., 2006: Chaotic time fluctuations of surface temperature occurring in the ecological modeling from local to global scale. Plenary Talk on *Ecological problems of our days – from global to local scale: Vulnerability and adaptation,* 30 November – 1 December, Keszthely (Hungary). CD ROM. Internet: http://www.georgikon.pate.hu/tanszekek/Meteor/programfuzet.htm.

Mihailovic, D.T., Kapor, D.V., Lalic, B., and *Arsenic, I.,* 2001: The chaotic time fluctuations of ground surface temperature resulting from energy balance equation for the soil-surface system. *Abstracts of the 26th General Assembly of European Geophysical Society,* 20-25 March, Nice (France).

Mihailović, D.T. and *Lalic, B.,* 2006: Land-Air Parameterisation Scheme (LAPS) as a component in agrometeorological modeling. Invited lecture on *Workshop on Environmental Fluid Mechanics as Elements in Agrometeorological Modelling,* 6-9 June, Ås (Norway).

Nagel, E., 1961: *The Structure of Science: Problems in the Logic of Scientific Explanation.* Harcourt, Brace World, inc. New York, 618 pp.

Nagel, E. and *Newman, J.R.,* 1958: *Gödel's Proof.* New York University Press, New York, 128 pp.

Nedeljković, Lj.D. and *Nedeljkovic, N.N.,* 2003a: Rydberg-state reionization of multiply charged ions escaping from solid surfaces *Phys. Rev. A 67,* 032709.

Nedeljković, Lj.D. and *Nedeljkovic, N.N.,* 2003b: Reconstruction of the past in quantum teleology of the ion - surface interaction. *Fifth General Conference of Balkan Physical Union.* Vrnjačka Banja, Serbia and Montenegro, August 25-29.

Piaget, J., 1973a: *Introduction to Genetic Epistemology. 1) Mathematical thought* (in Serbian). Izdavacka knjizarnica Zorana Stojanovica, Novi Sad, 1994, 322 pp.

Piaget, J., 1973b: *Introduction to Genetic Epistemology. 2) Physical thought* (in Serbian). Izdavacka knjizarnica Zorana Stojanovica, Novi Sad, 1996, 318 pp.

Rosen, R., 1977: Complexity as a systems property. *Int. J. Gen. Systems 3,* 227-232.

Rosen, R., 1991: *Life Itself: A Comprehensive Inquiry into the Nature, Origin, and Fabrication of Life.* Columbia University Press, New York, 285 pp.

Rosenberg, N.J., Blad, B.L., and *Verma, S.B.,* 1983: *Microclimate: The Biological Environment.* John Wiley & Sons, New York, 528 pp.

Rössler, O.E., 1998: *Endophysics: The World as an Interface.* World Scientific Publishing Co. Pte. Ltd., Singapore, 204 pp.

Selvam, A.M. and *Fadnavis, S.,* 1998: Signatures of a universal spectrum for atmospheric interannual variability in some disparate climatic regimes. *Meteorol. Atmos. Phys. 66,* 87-112.

Sivertsen, T.H., 2004. Invitation to conceptual discussions concerning the scope of the scientific method and classification systems of meteorological phenomena and meteorological parameters. *Selected papers of the International Conference "Fluxes and Structures in Fluids".* St. Petersburg, Russia, 23–26 June 2003. Moscow. IPM RAS, 6 p.

Sivertsen, T.H., 2005: Discussing the scientific method and a documentation system of meteorological and biological parameters. *Phys. Chem. Earth 30,* 35-43.

Van Loocke, Ph., 2002: Deep teleology in artificial systems. *Mind. Mach. 12,* 87–104.

GUIDE FOR AUTHORS OF *IDŐJÁRÁS*

The purpose of the journal is to publish papers in any field of meteorology and atmosphere related scientific areas. These may be

- research papers on new results of scientific investigations,
- critical review articles summarizing the current state of art of a certain topic,
- short contributions dealing with a particular question.

Some issues contain "News" and "Book review", therefore, such contributions are also welcome. The papers must be in American English and should be checked by a native speaker if necessary.

Authors are requested to send their manuscripts to

Editor-in Chief of IDŐJÁRÁS

P.O. Box 39, H-1675 Budapest, Hungary

in three identical printed copies including all illustrations. Papers will then be reviewed normally by two independent referees, who remain unidentified for the author(s). The Editor-in-Chief will inform the author(s) whether or not the paper is acceptable for publication, and what modifications, if any, are necessary.

Please, follow the order given below when typing manuscripts.

Title part: should consist of the title, the name(s) of the author(s), their affiliation(s) including full postal and e-mail address(es). In case of more than one author, the corresponding author must be identified.

Abstract: should contain the purpose, the applied data and methods as well as the basic conclusion(s) of the paper.

Key-words: must be included (from 5 to 10) to help to classify the topic.

Text: has to be typed in single spacing with wide margins on one side of an A4 size white paper. Use of S.I. units are expected, and the use of negative exponent is preferred to fractional sign. Mathematical formulae are expected to be as simple as possible and numbered in parentheses at the right margin.

All publications cited in the text should be presented in a *list of references*, arranged in alphabetical order. For an article: name(s) of author(s) in Italics, year, title of article, name of journal, volume, number (the latter two in Italics) and pages. E.g., *Nathan, K.K.*, 1986: A note on the relationship between photo-synthetically active radiation and cloud amount. *Időjárás 90,* 10-13. For a book: name(s) of author(s), year, title of the book (all in Italics except the year), publisher and place of publication. E.g., *Junge, C.E.*, 1963: *Air Chemistry and Radioactivity*. Academic Press, New York and London. Reference in the text should contain the name(s) of the author(s) in Italics and year of publication. E.g., in the case of one author: *Miller* (1989); in the case of two authors: *Gamov* and *Cleveland* (1973); and if there are more than two authors: *Smith et al.* (1990). If the name of the author cannot be fitted into the text: (*Miller*, 1989); etc. When referring papers published in the same year by the same author, letters a, b, c, etc. should follow the year of publication.

Tables should be marked by Arabic numbers and printed in separate sheets with their numbers and legends given below them. Avoid too lengthy or complicated tables, or tables duplicating results given in other form in the manuscript (e.g., graphs)

Figures should also be marked with Arabic numbers and printed in black and white in camera-ready form in separate sheets with their numbers and captions given below them. JPG, GIF, or XLS formats should be used for electronic artwork submission.

The text should be submitted both in manuscript and in electronic form, the latter on disks or in e-mail. Use standard 3.5" MS-DOS formatted diskette or CD for this purpose. MS Word format is preferred.

Reprints: authors receive 30 reprints free of charge. Additional reprints may be ordered at the authors' expense when sending back the proofs to the Editorial Office.

Information on the last issues: http://www.met.hu/Journal-Idojaras.php

Published by the Hungarian Meteorological Service

Budapest, Hungary

INDEX: 26 361

HU ISSN 0324-6329

IDŐJÁRÁS

QUARTERLY JOURNAL
OF THE HUNGARIAN METEOROLOGICAL SERVICE

CONTENTS

****

http://www.met.hu/Journal-Idojaras.php

VOL. 111 * NO. 4 * OCTOBER – DECEMBER 2007

IDŐJÁRÁS

Quarterly Journal of the Hungarian Meteorological Service

Editorial Office: P.O. Box 39, H-1675 Budapest, Hungary or
Gilice tér 39, H-1181 Budapest, Hungary
E-mail: bozo.l@met.hu or *antal.e@met.hu*
Fax: (36-1) 346-4809

Subscription by

mail: IDŐJÁRÁS, P.O. Box 39, H-1675 Budapest, Hungary;
E-mail: bozo.l@met.hu or *antal.e@met.hu*; *Fax: (36-1) 346-4809*

IDŐJÁRÁS

Quarterly Journal of the Hungarian Meteorological Service
Vol. 111, No. 4, October–December 2007, pp. 221–237

Sensitivity of severe convective storms to soil hydrophysical characteristics: A case study for April 18, 2005

Ákos Horváth[1*], **Ferenc Ács**[2] and **István Geresdi**[3]

[1]*Hungarian Meteorological Service,*
Vitorlás u. 17, H-8600 Siófok, Hungary; E-mail: horvath.a@met.hu

[2]*Department of Meteorology, Eötvös Loránd University,*
P.O. Box 32, H-1518 Budapest, Hungary, E-mail: acs@elte.hu

[3]*University of Pécs, Institute of Environmental Science,*
Ifjúság útja 6, H-7624 Pécs, Hungary; E-mail: geresdi@gamma.ttk.pte.hu

(Manuscript received in final form October 30, 2006)

Abstract—The effect of soil hydraulic properties on formation of severe thunderstorms was investigated by a mesoscale numerical model (Penn State – NCAR MM5). A comparative case study was made to analyze, how two different sets of soil hydrophysical properties, which refer to the same soil texture, affect the convective available potential energy (CAPE), updraft velocity, and precipitation field.

It was found that MM5 simulates adequately the formation and development of severe convective storms. Results of the numerical experiments also show that application of the Hungarian soil hydraulic properties results in formation of more intensive thunderstorm with shorter lifetime than the application of the soil hydraulic properties of the USA. It is shown that application of these site specific soil parameters is important, especially for correct simulation of processes at the meso-γ scale (2–20 km). Further tests are needed to quantify and understand the interrelationships between soil processes and storm events.

Key-words: severe convective storms, soil hydrophysical properties, MM5, Hungary

1. Introduction

Convection refers primarily to atmospheric motions in the vertical direction. The fuel for rising air parcel is the heat energy contained in it. This heat energy can be derived from Earth's surface as sensible heat and from the release of latent heat of condensation and latent heat of fusion. Rising bubbles of hot air, often

---

* Corresponding author

called thermals, form cumulus clouds in a relatively stable air mass. Rising of thermals in an unstable atmosphere form thunderstorms, which produce heavy rain and hail accompanied by lightning, thunder, and gusty winds. Recently, much more attention is paid to these atmospheric phenomena also in Hungary, because of the caused floods (*Horváth*, 2005a) and wind damages (*Horváth*, 2004, 2005b).

Thunderstorms and convective rainfall are investigated by radar observation (e.g., *Bringi et al.*, 1986; *Höller et al.*, 1994), radiosonde networks (e.g., *Findell* and *Eltahir*, 2003a, 2003b), surface observations (e.g., *Eltahir* and *Pal*, 1996), instrumented airplanes (e.g., *Sinkevich* and *Lawson*, 2005; *Lawson* and *Cooper*, 1990), and by using numerical models (e.g., *Schär et al.*, 1999; *Chen* and *Dudhia*, 2001).

The processes result in formation of severe convective storms are affected by characteristics of both the atmosphere and the land surface. The atmospheric influence is significant via triggering, instability, and interaction between the cloud and environmental air. Storms and precipitation can be triggered by both the upper air disturbances (e.g., *Benjamin* and *Carlson*, 1986; *Lanicci et al.*, 1987; *Findell* and *Eltahir*, 2003c) and the boundary wind convergence (e.g., *Pielke et al.*, 1991a, 1991b; *Avissar* and *Liu*, 1996). Effect on entrainment upon convection and convective precipitation has been analyzed in many aspects (e.g., *Clarke*, 1990; *Betts*, 1992; *Betts et al.*, 1994). The effect of atmosphere near to the surface on convection and convective precipitation has also been studied. Importance of correct calculation of equivalent potential temperature near to the surface was proved by *Eltahir* and *Pal* (1996), *Crook* (1996), *Früh* and *Wirth* (2002). Numbers of papers have been published also about land-surface effects on cloud formation. *Pielke* (2001) discussed and showed the sensitivity of cumulus convective rainfall to the land-surface energy and moisture budgets. The energy and moisture budgets of land-surface are determined by both the land use and the hydraulic properties of soil-vegetation system. The effect of land use and landscape heterogeneity upon cumulus convection was studied by *Segal et al.* (1989), *Rabin et al.* (1990), *Chang* and *Wetzel* (1991), *Li* and *Avissar* (1994), *Chen* and *Avissar* (1994a). The relationship between the Bowen ratio and the deep cumulus convection was discussed by *Segal et al.* (1995). Similar discussions but focusing on the available moisture in the soil-vegetation system is presented by *Segal et al.* (1989), *Chen* and *Avissar* (1994b), *Grasso* (2000), *Pan et al.* (1996).

The purpose of this study is to analyze the sensitivity of convective storms to hydraulic properties of soil-vegetation system. Hydraulic properties of soil-vegetation system are affected by soil hydrophysical properties (*Ács*, 2005). Soil hydrophysical properties depend strongly upon soil texture (*Clapp* and *Hornberger*, 1978; *van Genuchten*, 1980). In meteorological applications, it is assumed that soil texture does not depend upon geographical location (e.g., *Mölders*, 1999; *Mölders* and *Rühaak*, 2002; *Schädler*, 1990). Nevertheless, this assumption is doubted by the number of researchers. Note that *Hodnett* and *Tomasella* (2002) showed, that there is remarkable difference between the characteristics of the same soil texture in the case of temperate and that of tropical soils. The purpose of this study is to prove the sensitivity of formation of convective clouds on soil characteristics by a comparative analysis. In the case study, a convective storm event occurred on April 18, 2005, in the north-eastern part of Hungary (in the vicinity of the settlement Tiszaroff) was investigated. Simulations were made by using both the USA and Hungarian soil data by the Penn State – NCAR MM5 modeling system (fifth-generation meso-scale model). The results obtained are also compared to the surface accumulated precipitation data.

2. Model description

2.1. General characteristics of the MM5 model system

The numerical simulations were made by Version 3 of the MM5 (NCAR-PSU Mesoscale Model) (*Dudhia*, 1993). In the model, a terrain-following sigma coordinate system is applied. The predictive variables are: pressure perturbation, the three momentum components, temperature, specific humidity, and the mixing ratio of the different type of hydrometeors (cloud water, cloud ice, rain, snow, and graupel particles). For this study, the model is integrated with horizontal resolutions of 6 km, and with 26 vertical levels. The partial differential equations system is solved by using a relaxation lateral boundary condition and a radiation upper boundary condition.

2.2. Convection and cloud physics parameterization

Grell's scheme (*Grell et al.*, 1994) is applied for parameterization of convection based on rate of destabilization or quasi-equilibrium, simple single-cloud scheme with updraft and downdraft fluxes and compensating motion determining heating/moistening profile. Explicit bulk microphysical scheme with five different types of hydrometeors was used to simulate the formation of cloud and precipitation elements (*Reisner et al.*, 1998). The hydrometeors are: cloud water, cloud ice, rain, snow, and graupel particles. Collision coalescence process between different type of hydrometeors, furthermore, diffusion of vapor, freezing of liquid elements, and melting of ice particles were simulated. Equation of conservation was not only solved for the mixing ratios of hydrometeors but for the number concentration of cloud ice as well.

2.3. PBL scheme and land-surface model

The planetary boundary layer (PBL) is described by the non-local PBL scheme based on *Troen* and *Mahrt* (1986). Compared with other non-local or high-order closure schemes, this PBL scheme proved to be more efficient, because it needs less computer capacity. Land-surface processes are simulated by OSU LSM (Oregon State University Land-surface Model). It is based on the coupling of Penman's potential evaporation approach (*Penman*, 1948) modified by atmospheric stratification effect (*Mahrt* and *Ek*, 1984), the multi-layer soil model (*Mahrt* and *Pan*, 1984), and the single-layer canopy model (*Pan* and *Mahrt*, 1987). Actual evapotranspiration is simulated by using the so-called β-approach based on the moisture availability concept: β depends upon both the land-surface and the atmospheric characteristics (see Eqs. (15) and (13) in papers of *Chen* and *Dudhia* (2001) and *Chen et al.* (1996), respectively). Canopy resistance is formulated after *Jarvis* (1976) using relative stomatal conductivity formulae of *Noilhan* and *Planton* (1989). Atmospheric stratification is simulated by applying the Monin-Obukhov similarity theory (*Oncley* and *Dudhia*, 1995). Recently, as in our simulations too, surface exchange coefficients for heat and moisture are given by using lookup tables. Surface skin temperature (T_{skin}) of combined vegetation-ground layer is calculated by a linearized surface energy balance equation (see, for instance, Eq. (4) of *Sridhar et al.*, 2002). This simple equation has to be solved by numeric iteration technique for the implicit relationships between T_{skin} and surface energy balance components. Soil moisture and temperature are calculated by Richards' and heat flow equations, respectively. A more extensive description of these processes can be found, for instance, in papers of *Chen* and *Dudhia* (2001) and *Sridhar et al.* (2002).

3. Data and numerical experiments

3.1. The synoptic situation

Initial condition fields applied for numerical experiments are obtained from the ECMWF analysis and surface and upper air observations. ECMWF analysis of basic state variables (temperature, humidity, wind, geodynamical height) on mandatory levels up to 100 hPa at 12:00 UTC on April 18, 2005 are considered as first guess data. Surface synoptic information and some sounding data are smoothed to the first guess using Cressman scheme. Boundary conditions are given by the ECMWF forecasts. According to data, the initial surface (1st soil layer) soil moisture field can be characterized as relatively dry.

The weather of the investigated day was determined by a slowly moving cyclone with center situated above the eastern part of the Carpathian Basin. In lower layers of the cyclone (850 hPa) moist and warm air mass was drifted above the basin, meanwhile on higher levels (500 hPa) cold advection occurred, causing convective instability. During afternoon several thunderstorms were formed, and some of them caused flash floods in the mountains of the north-eastern regions of Hungary. During the day many convective storms were also observed over the plane regions. Detailed description of the synoptic situation is presented by *Horváth* (2005a).

Because the storms were formed both over flat and mountainous regions, this case offers a good opportunity to investigate how the soil hydrophysical characteristics affect the cloud formation at different geographical conditions.

3.2. Land-surface characteristics and parameter specification

The region, where the formation and development of the thunderstorms was investigated, is a relatively flat area along the river Tisza. According to the MM5 dataset, the vegetation characteristics in this region for April are as follows: The vegetation type is "cultivations", the green vegetation fraction is 0.6–0.7, the minimal stomatal resistance is 40 s m^{-1}, the albedo is 0.19, the roughness length is 0.075 m. The leaf area index (LAI) is prescribed, but the vegetation fraction is estimated on the basis of NDVI (Normalized Difference Vegetation Index). Details concerning the specification of vegetation parameters are described in the work of *Chen* and *Dudhia* (2001).

According to the soil data set of the MM5 model, clay loam is the prevailing soil texture in the region investigated. It has to be noted that there are also sandy loam patches here. Soil hydrophysical properties (saturated soil moisture content θ_S, saturated soil water retention Ψ_S, saturated water conductivity K_S, pore size distribution index b, field capacity soil moisture content θ_f, and wilting point soil moisture content θ_w) referring to all 12 soil textures are given in *Table 1*. Of course, these parameters refer to the soil characteristics of the USA. The same parameters were determined for Hungarian soils using the works of *Nemes* (2003) and *Fodor* and *Rajkai* (2005). The corresponding soil hydrophysical properties are presented in *Table 2*.

It is obvious that there are remarkable differences between the USA and Hungarian parameters. Let us take a look to the values of pore size distribution index b. For finer soil textures in the USA, b values are larger than the corresponding Hungarian b values. Clay loam soil texture is of interest to us. pF-curves ($\log|\Psi(\mathrm{cm}\ H_2O)|$ as the function of relative/scaled soil moisture content) and soil water conductivity functions for the USA and Hungarian clay loam are presented in *Fig. 1*. The figure shows, that there are large differences between the USA and Hungarian $K(\Psi)$ functions. The Hungarian $K(\Psi)$ is about 2 orders of magnitude larger than the USA $K(\Psi)$, independently of the value of Ψ (*Fig. 1b*).

Table 1. USA soil parameters used in the MM5 model. Symbols: θ_S = saturated soil moisture content, Ψ_S = saturated soil water retention, K_S = saturated water conductivity, b = pore size distribution index, θ_f = field capacity soil moisture content, and θ_w = wilting point soil moisture content

Soil texture	θ_S (m^3 m^{-3})	Ψ_S (m)	K_S (m s^{-1})	b	θ_f (m^3 m^{-3})	θ_w (m^3 m^{-3})
Sand	0.339	0.069	$4.60 \cdot 10^{-5}$	2.79	0.236	0.010
Loamy sand	0.421	0.036	$1.41 \cdot 10^{-5}$	4.26	0.283	0.028
Sandy loam	0.434	0.141	$5.23 \cdot 10^{-6}$	4.74	0.312	0.047
Silt loam	0.476	0.759	$2.81 \cdot 10^{-6}$	5.33	0.360	0.084
Silt	0.476	0.759	$2.81 \cdot 10^{-6}$	5.33	0.360	0.084
Loam	0.439	0.355	$3.38 \cdot 10^{-6}$	5.25	0.329	0.066
Sandy clay loam	0.404	0.135	$4.45 \cdot 10^{-6}$	6.66	0.314	0.067
Silty clay loam	0.464	0.617	$2.04 \cdot 10^{-6}$	8.72	0.387	0.120
Clay loam	0.465	0.263	$2.45 \cdot 10^{-6}$	8.17	0.382	0.103
Sandy clay	0.406	0.098	$7.22 \cdot 10^{-6}$	10.73	0.338	0.100
Silty clay	0.468	0.324	$1.34 \cdot 10^{-6}$	10.39	0.404	0.126
Clay	0.468	0.468	$9.74 \cdot 10^{-7}$	11.55	0.412	0.138

Table 2. Hungarian soil parameters used in the MM5 model. Symbols: θ_S = saturated soil moisture content, Ψ_S = saturated soil water retention, K_S = saturated water conductivity, b = pore size distribution index, θ_f = field capacity soil moisture content, and θ_w = wilting point soil moisture content

Soil texture	θ_S (m^3 m^{-3})	Ψ_S (m)	K_S (m s^{-1})	b	θ_f (m^3 m^{-3})	θ_w (m^3 m^{-3})
Sand	0.409	0.420	$3.26 \cdot 10^{-5}$	1.14	0.189	0.001
Loamy sand	0.414	0.450	$2.52 \cdot 10^{-5}$	2.43	0.233	0.017
Sandy loam	0.425	0.610	$1.14 \cdot 10^{-5}$	3.97	0.283	0.099
Silt loam	0.458	1.010	$2.73 \cdot 10^{-6}$	4.33	0.333	0.068
Silt	0.464	3.190	$2.00 \cdot 10^{-6}$	3.54	0.328	0.072
Loam	0.424	1.530	$4.58 \cdot 10^{-6}$	4.06	0.296	0.064
Sandy clay loam	0.430	0.340	$7.98 \cdot 10^{-6}$	5.18	0.311	0.063
Silty clay loam	0.436	5.680	$6.20 \cdot 10^{-7}$	4.18	0.338	0.093
Clay loam	0.430	4.170	$3.05 \cdot 10^{-6}$	4.05	0.306	0.083
Sandy clay	0.500	0.890	$4.58 \cdot 10^{-6}$	3.58	0.340	0.055
Silty clay	0.453	11.760	$1.05 \cdot 10^{-6}$	4.06	0.340	0.113
Clay	0.499	14.930	$8.00 \cdot 10^{-7}$	3.97	0.378	0.130

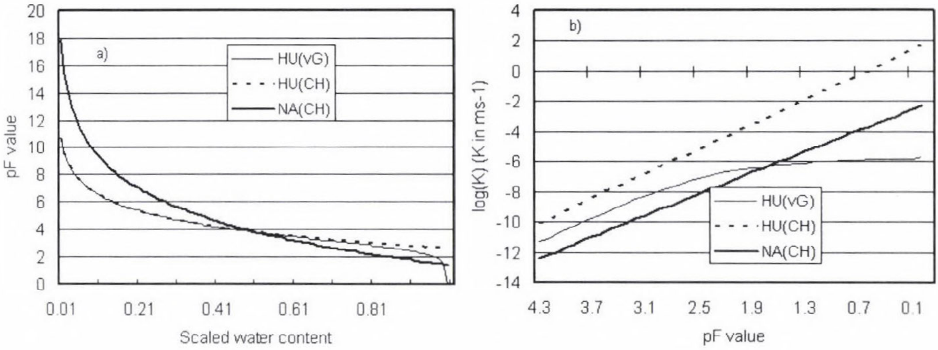

Fig. 1. Soil water retention (given as pF value) as a function of scaled water content (a), and soil water conductivity curves of clay loam for the USA and Hungarian soil data (b). Symbols: HU(vG) = Hungarian soil data, *van Genuchten*'s (1980) parameterization, HU(CH) = Hungarian soil data, *Clapp* and *Hornberger*'s (1978) parameterization, and NA(CH) = USA soil data, *Clapp* and *Hornberger*'s (1978) parameterization.

3.3. Numerical experiments

Since the differences between the USA and Hungarian soil parameters are rather large, numerical experiments are performed for both the USA and Hungarian soil parameters. Although some observations show that the soil texture applied in the MM5 data set is not appropriate for use in Hungary, only soil hydrophysical parameters were changed, the area distribution of soil texture was not modified. In the following, results obtained using USA soil parameters will be briefly referred to as US results, and results obtained using Hungarian soil parameters will be briefly referred to as HU results.

4. Validation, comparison, and discussion

4.1. Validation of the simulated 24 hours precipitation fields

Predicted field of the 24 hours accumulated precipitation is presented in *Fig. 2b*. The calculated data agree well with observations, which were created from rain gauge network 06:00 UTC observations on April 19, 2005 (*Fig. 2a*). Thunderstorms moved from northeast to southwest left significant "tracks". Most of the precipitation measured on the eastern part of Hungary fell between 12:00 and 18:00 UTC on April 18 allowing comparison of modeled and observed precipitation data. The precipitation track starting from the north-eastern part of Hungary can be well identified on the simulated field (*Fig. 2b*). A weaker precipitation field (denoted by P3 in *Fig.* 2b) in the southeast region of Hungary can be identified as part of a south-eastern track. The north-eastern precipitation system (denoted by P1 in *Fig. 2b*) was forced by mountains, therefore, it was much heavier than the thunderstorms in the south-eastern track (denoted by P3 in *Fig. 2b*). In the middle of the track, near to the region of the Tisza Lake, thunderstorms were formed and moved over the flat areas of the Great Hungarian Plain (denoted by P2 in *Fig. 2b*). In this region, the influence of soil hydrophysical properties upon the evolution of thunderstorms is not suppressed by mountains forced convection. Note that MM5 reproduced not only the formation and development of thunderstorms on the Great Hungarian Plain, but also the flash flood event (*Horváth*, 2005a) in the mountainous area (denoted by P4 in *Fig. 2b*).

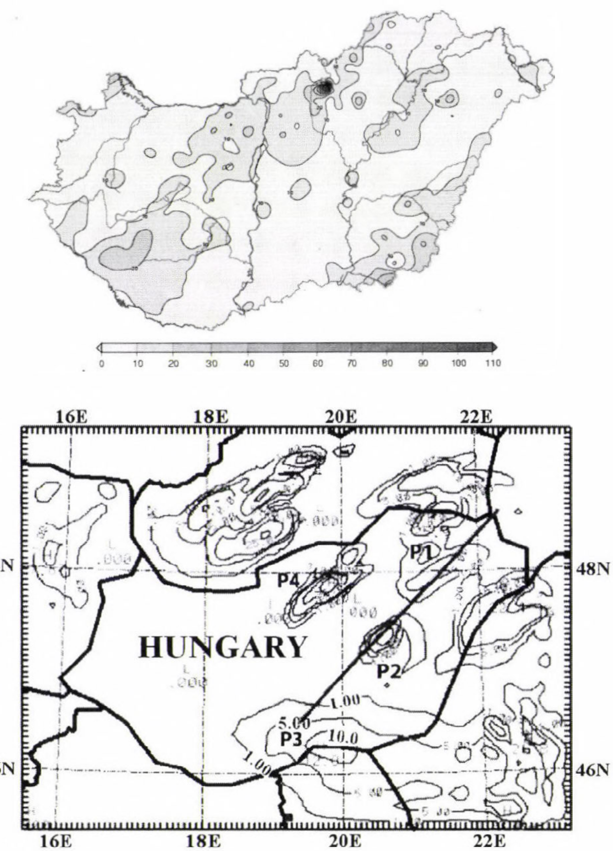

Fig. 2. Observed 24 hours cumulated precipitation measured at 06:00 UTC on April 19, 2005 (up), and the same field simulated by the MM5 model (down). The straight line indicates the position of the vertical cross section displayed in *Fig. 7*. The symbols P1, P2, P3, and P4 denote different precipitation systems. On the east of the river Danube, the precipitation fell mostly between 12:00 and 18:00 UTC of April 18. The calculation was made by using the USA soil data.

4.2. Comparison of surface available energy fields

The surface available energy, A_e (latent plus sensible heat flux) is an important forcing factor in evolution of thunderstorms. It affects their intensity and dynamics. Areal distribution of A_e at 18:00 UTC for the US and HU cases is shown in *Fig. 3*. While in the HU case A_e is generally negative (about from −10 to −50 W m^{-2}), in the US case positive A_e values (up to 50 W m^{-2}) are prevailing. This difference can explain why new convective clouds are formed in the US case at 18:00 UTC, and why the thunderstorms start to be dissipated in the HU case at the same time. These results show that thunderstorm dynamics in the US and HU cases are rather different.

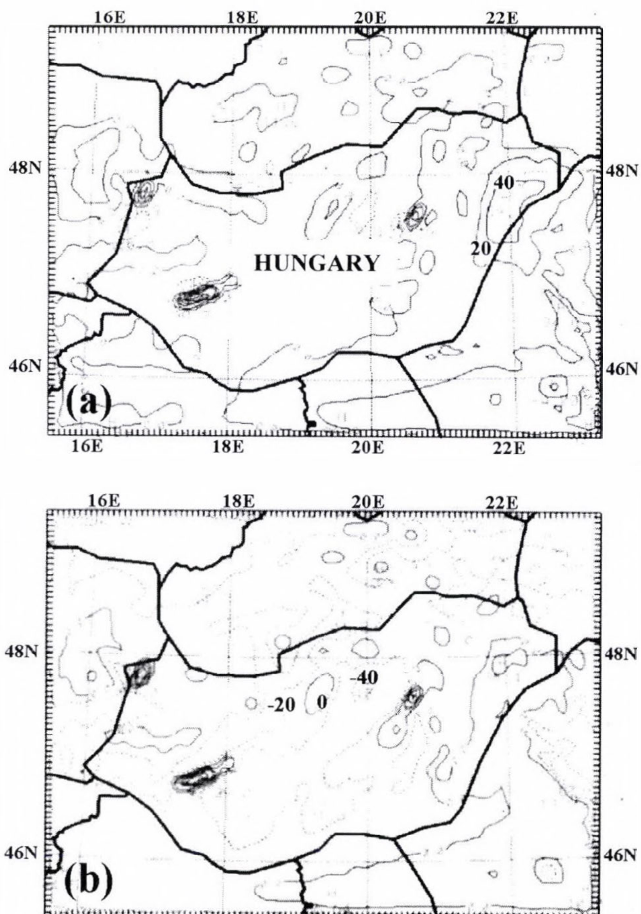

Fig. 3. Computed surface available energy fields obtained by the MM5 modeling system using the USA (a) and Hungarian (b) soil parameters at 18:00 UTC.

4.3. *Comparison of convective available potential energy fields*

The fields of convective available potential energy (CAPE) are analyzed to investigate the convective energy of thunderstorm. *Fig. 4* shows that there are no significant differences between the US and HU CAPE fields at the beginning of the integration time (15:00 UTC). In both cases, larger CAPE values (the highest values are between 500–700 Jkg^{-1}) could be found in the eastern part of Hungary (close to the river Tisza), than in the mountainous region of north Hungary. This shows that the development of thunderstorms above the walley of the river Tisza was more affected by the value of CAPE than above the mountainous region, where the presence of hills contributes to the formation of intensive thunderstorms.

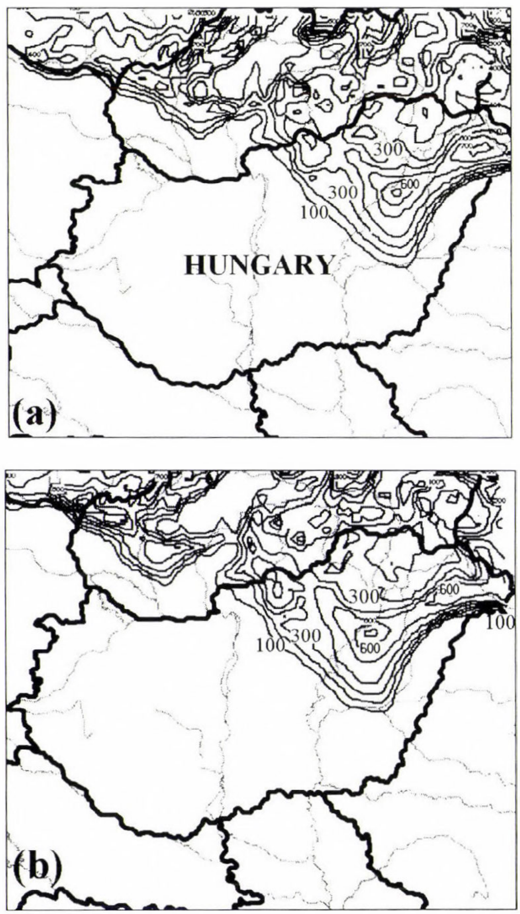

Fig. 4. Calculated convective available potential energy fields obtained by using the USA (up) and Hungarian (down) soil parameters at 15:00 UTC.

Although the difference between the CAPE fields of the HU and US cases was negligible at the beginning of the calculation, by the end of the integration, differences between the US and HU CAPE fields becomes more significant. While in the HU case the energy has already been used up by thunderstorms (*Fig. 5b*) by the end of the simulation, in the US case high CAPE values of 500 J kg^{-1} (*Fig. 5a*) could be observed over a large region. This also unequivocally shows, that the thunderstorms in the HU case are more intensive and developing faster than the ones in the US case.

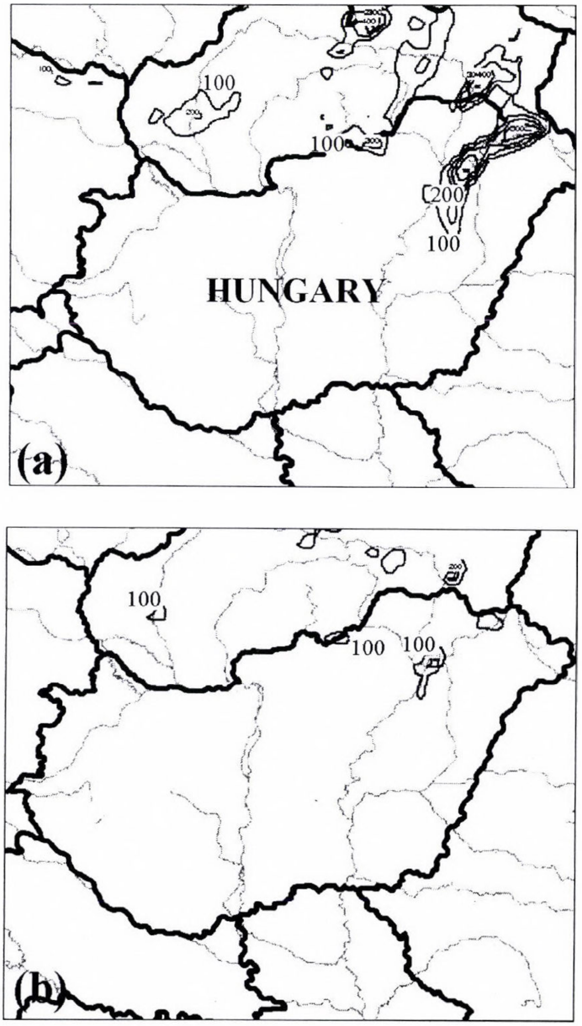

Fig. 5. As in *Fig. 4*, but at 18:00 UTC.

4.4. *Comparison of vertical velocity fields at 925 hPa height*

The transfer of heat and vapor between the surface and the convective clouds occurs in the planetary boundary layer (PBL). One of its important characteristics is the vertical velocity (w) at the level of 925 hPa (about 100 m above the surface level). *Fig. 6* shows the vertical velocity fields (w) values for both the US and HU cases at 17:00 UTC. While negative values mean descending motion, positive values represent ascending motion. In the US case, the boundary line between the ascending and descending regions is going from northwest to southeast. In spite of this, in the HU case the same boundary line is going from southwest to northeast. The thunderstorm in the HU case is much closer to Tiszaroff, than the thunderstorm in the US case. While this difference is remarkably considerable at meso-γ scale (2–20 km) (see *Orlanski*, 1975), it is negligible at meso-β scale.

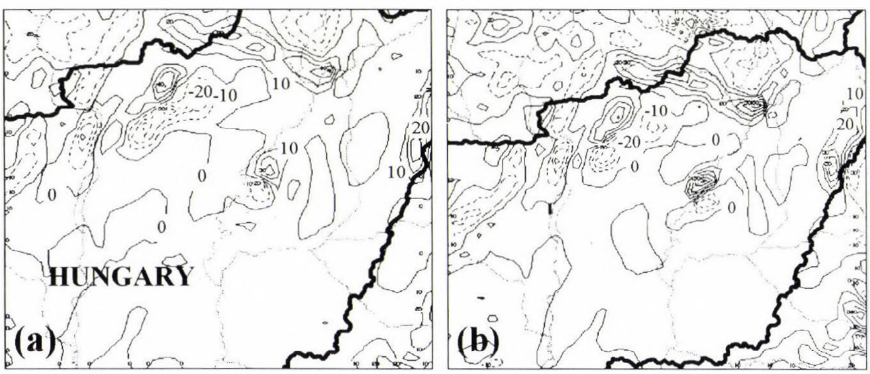

Fig. 6. Vertical velocity fields at the 925 hPa level obtained by using the USA (a) and Hungarian (b) soil parameters at 17:00 UTC. The continuous and dashed lines mean upward and downward direction, respectively. The vertical velocity components are given in cm s^{-1}.

4.5. *Comparison of vertical velocities in clouds*

Two dimensional representation of vertical velocities in clouds (w_{CL}) along the line presented in *Fig. 2b* at 16:00 UTC for both US and HU cases is shown in *Fig. 7*. Two updraft regions could be recognized. The first region, going from southwest to northeast is in the vicinity of Tiszaroff. The second one is close to Tiszalök. The first region seems to be more intensive comparing to the second one. The largest velocity is about 4 m s^{-1}. (It has to be noted, that the updraft velocity in the real thunderstorm must have been about 10 m s^{-1} in about a few km wide region. The much smaller calculated updraft velocity is the consequence of the crude horizontal resolution of 6 km.) While in the US case, the region where the updraft velocity is larger than 4 m s^{-1} is located in a shallow layer between 600–560 hPa, in the HU case the same region is in a deeper layer between 700–480 hPa. It is also obvious, that the thunderstorm close to Tiszaroff is deeper and more intensive in the HU case than in the US case.

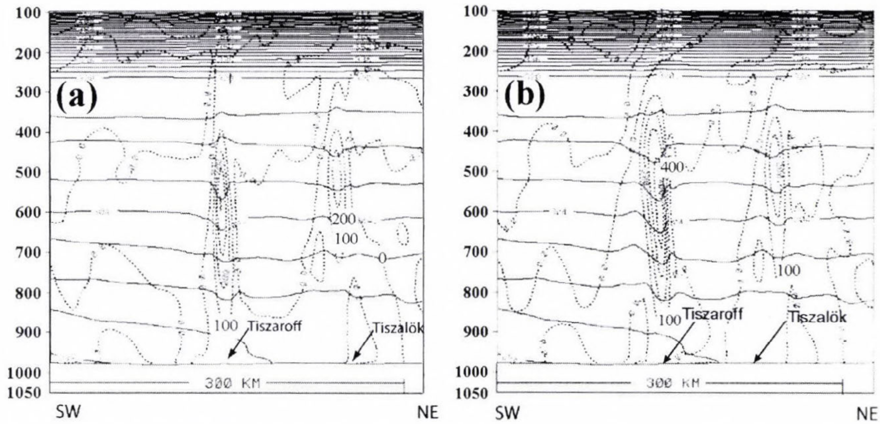

Fig. 7. Simulated vertical velocity fields along the line indicated in *Fig. 2b* using the USA (a) and Hungarian (b) soil parameters at 16:00 UTC. The positions of the settlements mentioned in the text are denoted in the figures. The direction of the cross-section is also shown. Dotted lines denote the isolines for vertical velocity component in cm s^{-1}. Solid lines denote the potential temperature.

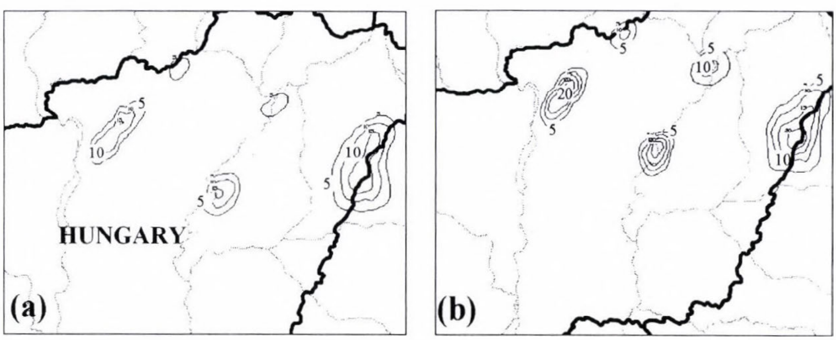

Fig. 8. 15 minutes cumulated precipitation fields obtained by the MM5 modeling system at 18:00 UTC using the USA (a) and Hungarian (b) soil parameters.

4.6. Comparison of precipitation fields at 18:00 UTC

The change of the soil hydrophysical characteristics also affects the precipitation field. Simulated fields of 15 minutes accumulated precipitation at 18:00 UTC for the US and HU case are presented in *Fig. 8*. It is noticeable, that precipitation is somewhat more intensive for the HU than for the US case. This is valid not only for the region close to Tiszaroff but also for the region close to Tiszalök.

5. Conclusions

In this study, the impact of soil hydrophysical properties upon the formation and development of severe convective storms is investigated. Analysis is performed modeling a convective storm event on April 18, 2005, in the vicinity of the settlement Tiszaroff. The Penn State – NCAR MM5 modeling system was used to make the numerical simulation. The calculation was made by both USA and Hungarian soil data. The sensitivity of the formation and development of the thunderstorms to soil hydrophysical characteristics was investigated by comparison of the results of the US and HU runs. The simulation results were also compared with observations. The results obtained can be summarized as follows:

- The MM5 is an appropriate tool for modeling severe convective storms. Simulated precipitation fields agree well with observations in meso-β scale. Unfortunately, no observation database is available to make the comparison in meso-γ scale.
- The parameters (CAPE, w at 925 hPa level, w_{CL}, and precipitation field) characterizing the thunderstorms are sensitive to changes of soil hydrophysical properties (Ψ_S, K_S, b, θ_S, θ_f, θ_w). Differences are particularly obvious in meso-γ scale.
- Both the intensivity and life time of the thunderstorms depends on the soil hydrophysical properties. Application of Hungarian soil characteristics results in formation of deeper thunderstorms with shorter life time. This difference in the dynamics could be related to the different amount of the accumulated precipitation. In the case of the HU run, the calculated accumulated precipitation was significantly larger than that of in the case of the US run. Due to absence of the data in meso-γ scale, we were not able to verify this difference.

Obviously, further tests are needed. For example, we should have to prove that it is more favorable to use site specific soil parameters than anything else (in this case USA parameters are taken), not only for modeling of land surface processes but also for modeling of severe convective storms. This validation experiment is a task for future.

Acknowledgements—This study is financially supported by the Hungarian Scientific Research Fund OTKA, project number T043010 and by the National Program for Research and Development (project number NKFP3-00022/2005). We thank *Mrs. Hajnalka Breuer* for helping in construction of the figures.

References

Avissar, R. and *Liu, Y.*, 1996: Three-dimensional numerical study of shallow convective clouds and precipitation induced by land surface forcing. *J. Geophys. Res. 101*, 7499-7518.

Ács, F., 2005: On transpiration and soil moisture contentsensitivity to soil hydrophysical data. *Bound.-Lay. Meteorol. 115*, 473-497.

Benjamin, S.G. and *Carlson, T.N.*, 1986: Some effects of surface heating and topography ont he regional severe storm environment, I. Three-dimensional simulations. *Mon. Wea. Rev. 114*, 307-329.
Betts, A.K., 1992: FIFE atmospheric boundary layer budget methods. *J. Geophys. Res. 97*, 18523-18531.
Betts, A.K., *Ball, J.H.*, *Beljaars, A.C.M.*, *Miller, M.J.*, and *Viterbo, P.*, 1994: Coupling between land-surface boundary-layer parameterizations and rainfall on local and regional scales. Lessons from the wet summer of 1993. *Fifth Conference on Global Change Studies*. Am. Meteorol. Soc., Boston, 174-181.
Bringi, V.N., *Rasmussen, R.M.*, and *Vivekanandan, J.*, 1986: Multiparameter radar measurements in Colorado convective storms. Part I: Graupel melting studies. *J. Atmos. Sci. 43*, 2545-2562.
Chang, J.T. and *Wetzel, P.J.*, 1991: Effects of spatial variations of soil moisture and vegetation ont he evolution of a prestorm environment: A case study. *Mon. Weather Rev. 119*, 1368-1390.
Chen, F. and *Avissar, R.*, 1994a: The impact of land-surface wetness heterogeneity on mesoscale heat fluxes. *J. Appl. Meteorol. 33*, 1323-1340.
Chen, F. and *Avissar, R.*, 1994b: Impact of land-surface moisture variabilities on local shallow convective cumulus and precipitation in large-scale models. *J. Appl. Meteorol. 33*, 1382-1394.
Chen, F. and *Dudhia, J.*, 2001: Coupling and Advanced Land Surface-Hydrology Model with the Penn State-NCAR MM5 Modeling System. Part I. Model Implementation and Sensitivity. *Mon. Weather Rev. 129*, 569-585.
Chen, F., *Mitchell, K.*, *Schaake, J.*, *Xue, Y.*, *Pan, H.L.*, *Koren, V.*, *Duan, Q.Y.*, *Ek, M.*, and *Betts, A.*, 1996: Modeling of land surface evaporation by four schemes and comparison with FIFE observations. *J. Geophys. Res. 101*, 7251-7268.
Clapp, R.B. and *Hornberger, G.M.*, 1978: Empirical Equations for Some Hydraulic Properties. *Water Resour. Res. 14*, 601-604.
Clarke, R.H., 1990: Modeling mixedlayer growth in the Koorin experiment. *Aust. Meterol. Mag. 38*, 227-234.
Crook, N.A., 1996: Sensitivity of moist convection forced by boundary layer processes to low-level thermodynamic fields. *Mon. Weather Rev. 124*, 1767-1785.
Dudhia, J., 1993: A non-hydrostatic version of the Penn State-NCAR Mesoscale Model: Validation tests and simulation of an Atlantic cyclone and cold front. *Mon. Weather Rev. 121*, 1493 - 1513.
Eltahir, E.A.B., and *Pal, J.S.*, 1996: Relationship between surface conditions and subsequent rainfall in convective storms. *J. Geophys. Res. 101*, 26237-26245.
Findell, K.L. and Eltahir, *E.A.B.*, 2003a: Atmospheric Controls on Soil Moisture-Boundary Layer Interactions. Part I: Framework Developement. *J. Hydrometeorol. 4*, 552-569.
Findell, K.L. and *Eltahir, E.A.B.*, 2003b: Atmospheric Controls on Soil Moisture-Boundary Layer Interactions. Part II: Feedbacks within the Continental United States. *J. Hydrometeorol. 4*, 570-583.
Findell, K.L. and *Eltahir, E.A.B.*, 2003c: Atmospheric controls on soil moisture-boundary layer interactions: Three-dimensional wind effects. *J. Geophys. Res. 108, No. D8*, 8385, doi: 10.1029/2001JD0015152003.
Fodor, N. and *Rajkai, K.*, 2005: Estimation of Physical Soil Properties and Their Use in Models. *Agrokem Talajtan 54*, 25-40.
Früh, B. and *Wirth, V.*, 2002: The role of surface wet-bulb temperature for subsequent convective rainfall in midlatitudes. *Poster presentation at European Geophysical Society, XVII General Assembly*, April 22-26, Nice, France. [Available as pdf-document on http://www.staff.uni-mainz.de/frueh/publics.html]
Grasso, L.D., 2000: The numerical simulation of dryline formation on soil moisture. *Mon. Weather Rev. 128*, 2816-2834.
Grell, G., *Dudhia, J.*, and *Stauffer, D.*, 1994: A description of the fith generation Penn State/NCAR Mesoscale Model. *NCAR Tech. Note NCAR/TN-398+STR*, 117 pp.
Horváth, Á., 2004: The great storm on November 19, 2004 (in Hungarian). *Légkör XLIX*, No. 4, 6-9.
Horváth, Á., 2005a: Meteorological backround of flooding in Mátrakeresztes on April 18, 2005 (in Hungarian). *Légkör 50*, No. 2, 6-9.
Horváth, Á., 2005b: Meteorological description of the storm on May 18, 2005 (in Hungarian). *Légkör 50*, No. 3, 12-16.

Höller, H., Bringi, V.N., Hubbert, J., Hagen, M., and *Meischner, P.F.*, 1994: Life cycle and precipitation formation in a hybrid-type hailstorm revelaed by polarimetric and Doppler radar measurements. *J. Atmos. Sci. 51*, 2500-2522.

Hodnett, M.G. and *Tomasella, J.*, 2002: Marked differences between van Genuchten soil water-retention parameters for temperate and tropical soils: a new water-retention pedo-transfer function developed for tropical soils. *Geoderma 108*, 155-180.

Jarvis, P. G., 1976: The interpretation of the variations in the leaf water potential and stomatal conductance found in canopies in the field. *Philos. T. R. Soc. B. 273*, 593-610.

Lanicci, J.M., Carlson, T.N., and *Warner, T.T.*, 1987: Sensitivity of the great plains severe-storm environment to soil moisture distribution. *Mon. Weather Rev. 115*, 2660-2673.

Lawson, R.P. and *Cooper, W.A.*, 1990: Performance of some airborne thermometers in clouds. *J. Atmos. Ocean. Tech. 7*, 480-494.

Li, B., and *Avissar, R.*, 1994: The impact of spatial variability of land-surface heat fluxes. *J. Clim. 7*, 527-537.

Mahrt, L. and *Ek, M.*, 1984: The Influence of Atmospheric Stability on Potential Evaporation. *J. Clim. Appl. Meteorol. 23*, 222-234.

Mahrt, L. and *Pan, H.L.*, 1984: A two-layer model of soil hydrology. *Bound.-Lay. Meteorol. 29*, 1-20.

Mölders, N., 1999: Einfache und akkumulierte Landnutzungsänderungen und ihre Auswirkungen auf Evapotranspiration, Wolken- und Niederschlagsbildung. *Wissenschaftlichen Mitteilungen aus dem Institut für Meteorologie der Universität und dem Institut für Troposphärenforschung e. V. Leipzig*. BAND 15, ISBN 3-9806117-4-4. [Available at ELTE, Department of Meteorology, Pázmány Péter sétány 1/A., 1117 Budapest]

Mölders, N. and *Rühaak, W.*, 2002: On the impact of explicitly predicted runoff on the simulated atmospheric response to small-scale land-use changes – an integrative modeling approach. *Atmos. Res. 63(1-2)*, 3-38.

Nemes, A., 2003: Multi-scale hydraulic pedotransfer functions for Hungarian soils. *Ph. D. Dissertation. Wageningen Universiteit.* ISBN 90-5808-804-9. 143 p.

Noilhan, J., and *Planton, S.*, 1989: A simple parameterization of land surface processes for meteorological models. *Mon. Weather Rev. 117*, 536-549.

Oncley, S.P. and *Dudhia, J.*, 1995: Evaluation of surface fluxes from MM5 using observations. *Mon. Weathr Rev. 123*, 3344-3357.

Orlanski, I., 1975: A Rational Subdivision of Scales for Atmospheric Processes. *B. Am. Meteorol. Soc. 56*, 527-530.

Pan, H.L. and *Mahrt, L.*, 1987: Interaction between soil hydrology and boundary-layer developement. *Bound.-Lay. Meteorol. 38*, 185-202.

Pan, Z., Takle, E., Segal, M., and *Turner, R.*, 1996: Influences of model parameterization schemes on the response of rainfall to soil moisture in the central United States. *Mon. Weather Rev. 124*, 1786-1802.

Penman, H.L., 1948: Natural evaporation from open water, bare soil and grass. *Proc. R.. Soc. Lond. A193*, 120-195.

Pielke, R.A., 2001: Influence of the spatial distribution of vegetation and soils on the prediction of cumulus convective rainfall. *Rev. Geophys. 39*, 151-177.

Pielke, R.A., Dalu, G., Snook, J.S., Lee, T.J., and *Kittel, T.G.F.*, 1991a: Nonlinear influnce of mesoscale land use on weather and climate. *J. Clim. 4*, 1053-1069.

Pielke, R.A., Song, A., Michaels, P.J., Lyons, W.A., and *Arritt, R.W.*, 1991b: The predictibility of sea-breeze generated thunder-storms. *Atmosfera 4*, 65-78.

Reisner, J., Rasmussen, R. M., and *Bruintjes, R.T.*, 1998: Explicit forecasting of supercooled liquid water in winter storms using the MM5 mesoscale model. *Q. J. Roy. Meteor. Soc. 124*, 1071-1107

Rabin, R.M., Stadler, S., Wetzel, P.J., Stensrud, D.J., and *Gregory, M.*, 1990: Observed effects of landscape variability on convective clouds. *B. Am. Meteorol. Soc. 71*, 272-280.

Schädler, G., 1990: Numerische Simulationen zur Wechselwirkung zwischen Landoberflächen und atmospherischer Grenzschicht. Wissenschaftliche Berichte des Instituts für Meteorologie und Klimaforschung der Universität Karlsruhe. Nr. 13, ISSN 0179-5619. [Available at ELTE, Department of Meteorology, Pázmány Péter sétány 1/A., H-1117 Budapest]

Schär, C., *Lüthi*, *D.*, *Beyerle*, *U.*, and *Heise*, *E.*, 1999: The Soil-Precipitation Feedback: A Process Study with a Regional Climate Model. *J. Climate 12*, 722-741.

Segal, *M.*, *Garratt*, *J.R.*, *Kallos*, *G.*, and *Pielke*, *R.A.*, 1989: The impact of wet soil and canopy temperatures on daytime boundary-layer growth. *J. Atmos. Sci. 46*, 3673-3684.

Segal, *M.*, *Arritt*, *R.W.*, *Clark*, *C.*, *Rabin*, *R.*, and Brown, *J.*, 1995: Scaling evaluation of the effect of surface characteristics on potential for deep convection over uniform terrain. *Mon. Weather Rev. 123*, 383-400.

Sinkevich, *A.A.*, and *Lawson*, *R.P.*, 2005: A Survey of Temperature Measurements in Convective Clouds. *J. Appl. Meteorol. 44*, 1133-1145.

Sridhar, *V.*, *Elliott*, *R.L.*, Chen, *F.*, and *Brotzge*, *J.A.*, 2002: Validation of the NOAH-OSU land surface model using surface flux measurements in Oklahoma. *J. Geophys. Res., 107, NO. D20*, 4418, doi: 10.1029/2001JD001306.

Troen, *I.*, and *Mahrt*, *L.*, 1986: A simple model of the atmospheric boundary layer: Sensitvity to surface evaporation. *Bound.-Lay. Meteorol. 37*, 129-148.

van Genuchten, *M. Th.*, 1980: A Closed-Form Equation for Predicting the Hydraulic Conductivity of Unsaturated Soils. *Soil Sci. Soc. Am. J. 44*, 892-898.

IDŐJÁRÁS
Quarterly Journal of the Hungarian Meteorological Service
Vol. 111, No. 4, October–December 2007, pp. 239–250

Estimation of surface energy and carbon balance components in the vicinity of Debrecen using Thornthwaite's bucket model

Gábor Szász[1], **Ferenc Ács**[2*] and **Hajnalka Breuer**[2]

[1]*Centre of Agricultural Sciences, University of Debrecen, P.O. Box 36, H-4015 Debrecen, Hungary*

[2]*Department of Meteorology, Eötvös Loránd University, P.O. Box 32, H-1518 Budapest, Hungary, E-mail: acs@elte.hu*

(Manuscript received in final form July 12, 2007)

Abstract—Surface energy and carbon balance components are calculated in the vicinity of Debrecen (Hungary) using extended Thornthwaite's bucket model. Soil water content prediction module of the model is tested and verified against measured data of the Agrometeorological Observatory of the University of Debrecen in the period 1972–1992. Energy and carbon balance components estimated are not verified because of the missing direct measurements.

The annual course of components, sensitivity of components to field capacity soil water content changes, and statistical relationships between some energy, water, and carbon balance components are discussed. Among the results it is worth mentioning the sensitive coupling between field capacity water content, actual evapotranspiration, and net ecosystem exchange. Results obtained are useful in describing Debrecen's regional climate.

Key-words: bucket model; energy-, water- and carbon balance; net ecosystem exchange; field capacity, Debrecen

1. Introduction

The Agrometeorological Observatory of the University of Debrecen is an agrometeorological site where a long time series of measured soil water content data is also available. These data combined with long term measurements of relevant meteorological elements, such as global radiation (Rs) or sunshine

* Corresponding author

duration, air temperature (*T*), and precipitation (*P*) enable us to get an insight into the climatology of energy and carbon balance components of the region.

Debrecen's climate and other environmental characteristics have been analyzed by *Justyák* and *Tar* (1994) using simple data processing. The analysis has been based on measured quantities during the 20th century. A more extensive analysis using different empirical approaches for estimating surface energy balance components was done by *Szász* (2002). In these calculations the quantities were diagnostically estimated using measured soil water content data from the period 1964–1993. Recently, a diagnostic analysis using micro-meteorological methods has been performed by *Ács et al.* (2005). This approach used not only soil water content but also ground surface temperature data. The calculations referred to period 1974–1986. Soil water content data are used for verifying the model. According to the results, there are many limitations in estimating energy balance components.

Monthly mean values of energy balance components can be estimated using the bucket method of *Thornthwaite* (1948), avoiding enormous data processing and all limitations arising from the need to scale up the outputs in time and space. Besides, Thornthwaite's model can be simply extended for estimating actual evapotranspiration and carbon balance components of soil-vegetation system.

On the basis of all these, the aim of this study is to analyze the energy and carbon balance components from climatological point of view. In doing so, we focus on

- verifying the model using long term measurements of soil water content,
- analyzing annual course of energy and carbon balance components,
- testing the sensitivity of energy and carbon balance components to field capacity soil water content changes, and
- analyzing the statistical relationship between the energy, water, and carbon balance components.

In the following, these points are separately discussed after presenting the measurement site, the model, and the data used. At the end, basic conclusions are drawn.

2. *Measurement site*

The Agrometeorological Observatory of the University of Debrecen was established in 1962 at Hajdúhát (47°37'N, 21°36'E; 112 m asl). In the last 40 years period, both main climatic elements and the soil water content were systematically measured. This long time series of soil water content data is the unique characteristic of the Observatory. The history of the Observatory and description of the measurements performed are given in *Szász* (2002).

The climate of Hajdúhát can be characterized as a temperate rainy climate with continental features. The annual mean temperature is 10.1°C, while mean annual precipitation sum is 550 mm. The water table is at a depth of 10 m. The soil type is lime covered with black loam (chernozem). The vegetation is short-cut natural grass.

3. *Model and data*

3.1. Inputs and outputs of the model

The input data are as follows: monthly precipitation (P), air temperature (T), sunshine duration (SSD) and $NDVI$ (normalized difference vegetation index), initial soil water content (Θ_{ini}), geographical latitude and longitude, albedo, and soil hydro-physical properties. Precipitation and temperature refer to the period 1953–2003, $NDVI$ (*Bartholy et al.*, 2004) and sunshine duration data refer to periods 1982–2000, 1971–2000, respectively. It is supposed that surface albedo changes from month to month, but there are no inter-annual changes. Soil hydro-physical properties are taken from *Ács et al.* (2005). The outputs are as follows: soil water content (Θ), potential evapotranspiration (PET), actual evapotranspiration (AET) or latent heat flux (LE), water surplus (S), water lack (D), soil respiration (SR), net primary productivity (NPP), net ecosystem exchange (NEE), radiation balance (R_n), sensible heat flux (H), and ground heat flux (G) (*Fig. 1*).

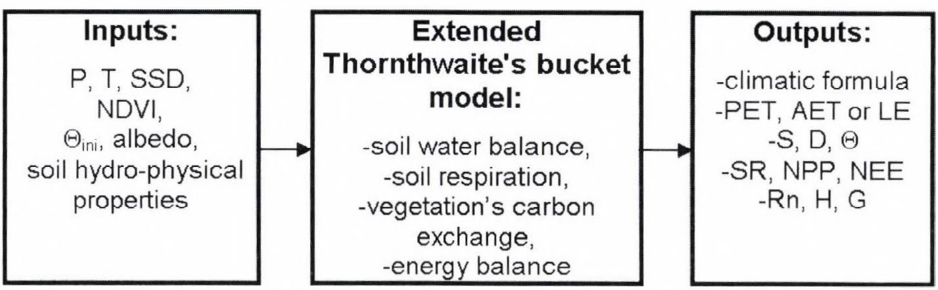

Fig. 1. Inputs and outputs of the extended Thornthwaite's bucket model. Symbols: P = precipitation, T = air temperature, SSD = sunshine duration, $NDVI$ = normalized difference vegetation index, Θ_{ini} = initial value of soil water content, PET = potential evapotranspiration, AET = actual evapotranspiration, LE = actual latent heat flux, S = water surplus, D = water demand, Θ = soil water content, SR = soil respiration, NPP = net primary productivity, NEE = net ecosystem exchange, R_n = net radiation flux, H = sensible heat flux, and G = soil heat flux at the soil surface.

Thornthwaite's bucket model (*Thornthwaite*, 1948) is extended by subroutines for calculating carbon and energy balance components of soil-vegetation system. Soil respiration is calculated according to *Peng et al.* (1998), while *NPP* after *Maisongrande et al.* (1995). The energy balance is calculated according to *Drucza* and *Ács* (2006).

3.2. Bucket model

The most simple soil water content prediction model is the bucket model. Bucket is represented by 1 m deep soil column of 1 m^2 surface which is filled by precipitation and depleted by *AET* and surface runoff. There is no water exchange between the column and the surrounding soil. Soil texture in the column is constant, that is, it has no horizontal and vertical changes.

3.3. Actual evapotranspiration

AET depends upon both the atmospheric conditions and Θ. Atmospheric conditions affect *PET*, while the effect of Θ is taken into account using the so-called β approach. The β function changes between 0 and 1, and it describes the dependence between the ratio *AET/PET* and Θ, that is

$$\frac{AET}{PET} = \beta(\Theta). \tag{1}$$

There are several methods to calculate both *PET* and β. In this study, *PET* is calculated after *Thornthwaite* (1948), while β after *Mintz* and *Walker* (1993).

3.3.1. Thornthwaite's parameterization of PET

Thornthwaite's method (1948) for parameterizing *PET* (mm $month^{-1}$) requires as input only monthly mean air temperature. A newer version of it is proposed by *McKenny* and *Rosenberg* (1993). It is as follows:

$$PET_i = 1.6 \cdot \left(\frac{L_i}{12}\right) \cdot \left(\frac{N_i}{30}\right) \cdot \left(\frac{10 \cdot T_i}{I}\right)^a, \tag{2}$$

where L_i is the average daytime length in hours for the ith month, N_i is the number of days in the ith month, and T_i is the monthly mean air temperature (°C) for the ith month. I is the thermal index calculated as:

$$I = \sum_{i=1}^{12} \left(\frac{T_i}{5}\right)^{1.514} \tag{3}$$

and

$$a = 6.75 \cdot 10^{-7} \cdot I^3 - 7.71 \cdot 10^{-5} \cdot I^2 + 1.792 \cdot 10^{-2} \cdot I + 0.49239. \quad (4)$$

AET's dimensions are equal to *PET*'s dimensions. In energy balance calculations, *LE* (MJ m^{-2} $month^{-1}$) is used instead of *AET* (mm $month^{-1}$).

3.3.2 Mintz and Walker's parameterization of β

Among many parameterizations of β, *Mintz* and *Walker*'s (1993) parameterization is used:

$$\beta(\Theta) = 1 - \exp\left(-6.8 \cdot \frac{\Theta - \Theta_w}{\Theta_f - \Theta_w}\right), \quad (5)$$

where Θ_w is the value of Θ at the wilting point and Θ_f is the one at the field capacity.

3.4. Carbon balance

3.4.1. Soil respiration

Annual sum of soil respiration is parameterized after *Peng et al.* (1998):

$$SR = 7.641 \cdot e^{0.0292 \cdot T} \cdot P^{0.171} \cdot AET^{0.4231}, \quad (6)$$

where P is the annual sum of precipitation, *AET* is the actual evapotranspiration, T is the mean annual air temperature (°C). Note that all relevant climatic elements are taken into account. Monthly sums of *SR* (10^{-3} kg C m^{-2} $month^{-1}$) are estimated after *Raich et al.* (1991) taking the effect of monthly mean air temperature and soil water content into account.

3.4.2. Net primary productivity

NPP is parameterized after *Maisongrande et al.* (1995):

$$NPP = \varepsilon \cdot R_g \cdot 0.5 \cdot NDVI \cdot (1 - r(T)), \quad (7)$$

where ε is the photosynthetic efficiency (10^{-3} kg MJ^{-1}), R_g is the monthly sum of global radiation (MJ m^{-2} $month^{-1}$), and $r(T_i)$ is the respiration of the vegetation expressed as a fraction of *NPP*. ε varies markedly, it depends upon vegetation type and geographical location. In this case, a constant value of $0.55 \cdot 10^{-3}$ kg MJ^{-1} is used.

3.5. Numerical scheme

Among many numerical schemes, a 2nd order implicit scheme was chosen. The set of equations is as follows:

$$\frac{\partial \Theta}{\partial t} = F(\Theta(t)), \tag{8}$$

$$\Theta_{t+1} = \Theta_t + [F_t + F_{t+1}] \cdot \frac{\Delta t}{2}, \tag{9}$$

where

$$F_t = P_t - AET_t, \tag{10}$$

that is

$$\Theta_{t+1} = \frac{\Theta_t + F_t - \frac{1}{2} \cdot \left.\frac{\partial F}{\partial \Theta}\right|_t \cdot \Theta_t \cdot \Delta t}{1 - \frac{1}{2} \cdot \left.\frac{\partial F}{\partial \Theta}\right|_t \cdot \Delta t}. \tag{11}$$

Euler-method has been used in every starting month. To stabilize the scheme, Θ_t has been averaged with new Θ in every time step, so Θ is in the next time step recalculated as:

$$\overline{\Theta}_t = \frac{\Theta_{t+1} + \Theta_t}{2}. \tag{12}$$

4. Results

Analysis is performed according to the points given in the introduction. Firstly, the performance of the bucket model is verified using measured Θ data from the Agrometeorological Observatory of the University of Debrecen, in the period 1972–1992. Then the annual course of simulated energy and carbon balance components is analyzed. Sensitivity of *SR* and *NEE* to Θ_f changes is also discussed. Lastly, statistical relationships between carbon and water balance components in the growing season are considered.

4.1. Verification

Temporal variation of measured and simulated Θ values obtained by the extended Thornthwaite's bucket model is presented in *Fig. 2a*. Agreement between simulated and measured Θ values is acceptable. According to the results, Θ values obtained by Thornthwaite's method are generally higher than the measured ones. Overestimation is especially obvious in the spring. Correlation coefficient obtained is about 0.8.

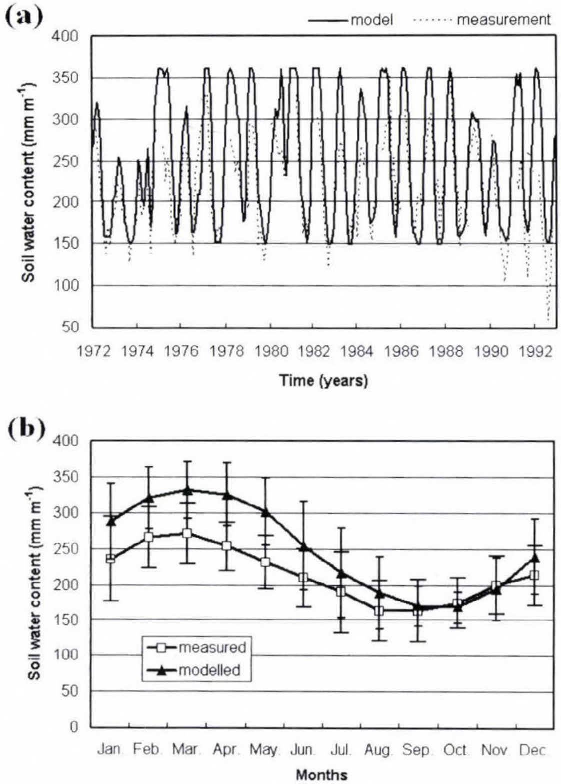

Fig. 2. Temporal variation of simulated and measured Θ obtained by the extended Thornthwaite's bucket model in the time period 1972–1992 (a). Long term mean annual course of simulated and measured Θ and its standard deviations (b).

Comparison of measured and simulated long term (1972–1992) mean annual course of Θ and its standard deviation are presented in *Fig. 2b*. Simulated values are in the scattering region of measured values $\Theta^{mea} - \sigma^{mea} < \Theta^{Thornt} < \Theta^{mea} + \sigma^{mea}$, except from February to May. $\Theta^{Thornt} - \sigma^{Thornt} < \Theta^{mea} < \Theta^{Thornt} + \sigma^{Thornt}$ relationship is also valid excepting spring. It should be said that difference between measured maximum and minimum Θ values changes between 120–260 mm m^{-1}. For modelled Θ values this range is between 80–210 mm m^{-1}.

4.2. Energy and carbon budget components

Long term (1971–2003) mean annual course of energy balance components is presented in *Fig. 3a*. R_n changes between –90 and +380 MJ m^{-2} month^{-1}, *LE* between 0 and 270 MJ m^{-2} $month^{-1}$, while H between –80 and +150 MJ m^{-2} $month^{-1}$. LE is the highest in June because of the precipitation maximum, while it almost vanishes in January, when it amounts only 2 MJ m^{-2} $month^{-1}$. H is quite high in April (about 110 MJ m^{-2} $month^{-1}$), but it is the highest in August (about 150 MJ m^{-2} $month^{-1}$). Note that in October it is still positive (air is warmed by ground surface), but in November it is already negative. March is the month when the effect of the cold winter is over. Then air is usually warmer than the ground surface. Surface is wet ($\beta \approx 1$) but still cold because $R_n \leq LE$. This is obvious from the Bowen-ratio value, which is ~2.0 in this time period. In October, the Bowen-ratio is more than 0.5, which is also a high value for continental conditions. This is caused by macro-circulation effect, which appears regularly in the period September–October. This period is popularly called as 'indian summer'. G is negative in winter months and positive in summer months. Its annual sum is zero.

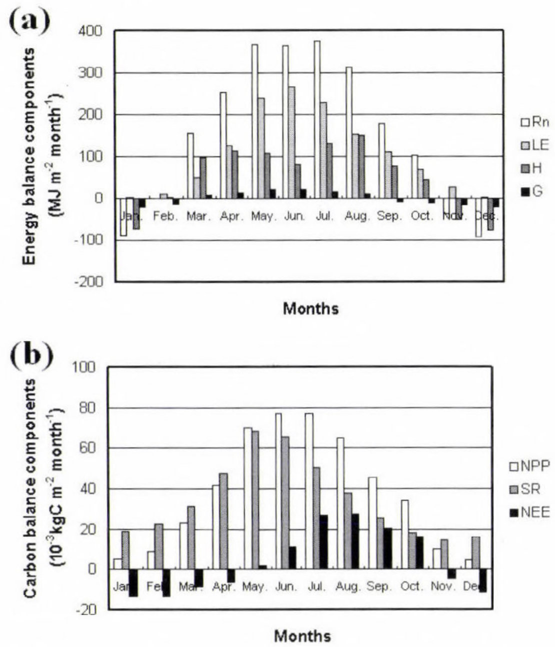

Fig 3. (a) Long term (1971–2003) mean annual course of radiation balance (R_n), latent heat flux (LE), sensible heat flux (H), and ground heat flux (G). (b) Long term (1982–2000) mean annual course of net primary productivity (NPP), soil respiration (SR), and net ecosystem exchange (NEE).

Long term (1982–2000) mean annual course of carbon balance components is presented in *Fig. 3b*. NPP and SR have similar courses, but their relation to each other is variable. This is reflected in NEE values. NPP is the highest in July ($77 \cdot 10^{-3}$ kg C m^{-2} month^{-1}) and the lowest in December ($4 \cdot 10^{-3}$ kg C m^{-2} month^{-1}). *SR* is the highest in May ($68 \cdot 10^{-3}$ kg C m^{-2} month^{-1}). In November it amounts $14 \cdot 10^{-3}$ kg C m^{-2} month^{-1}. Note that *NEE* is negative in the period November–April, while it is positive in the period May–October.

4.3. Sensitivity analysis

Since Θ_f is an important parameter (*Ács*, 2005; *Ács et al.*, 2005) which depends upon soil type and climatic conditions, it is important to know how much it influences the energy and carbon balance components. The sensitivity analysis is performed by increasing/decreasing the Θ_f by ± 10 percent with respect to its Θ_f^r value ($\Theta_f^r = 0.36$ m^3 m^{-3}), which is used in verification tests. These Θ_f changes are not big, in reality Θ_f values can be scattered by about $-45 - +15\%$. Runs performed by $\Theta_f^r = 0.36$ m^3 m^{-3} will be called as 'reference' runs.

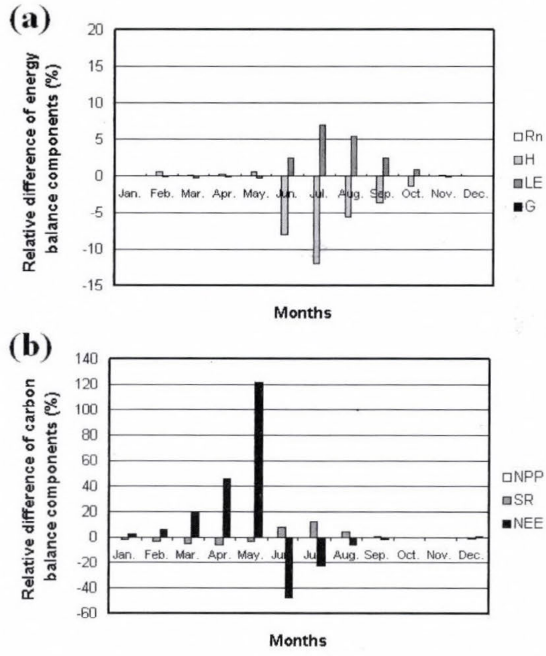

Fig. 4. Annual course of relative difference of energy balance (a) and carbon balance (b) components for $\Theta_f = \Theta_f^r - 0.1 \cdot \Theta_f^r$.

Annual course of relative differences of energy balance components for $\Theta_f = \Theta_f^r - 0.1 \cdot \Theta_f^r$ is presented in *Fig. 4a*. Deviations are small from January to May because of high Θ values (see *Fig. 2b*). In the period June–September, when evapotranspiration is higher than precipitation, Θ becomes important. Since Θ is lower than Θ^r, *LE* obtained is also lower than LE^r. Deviations of *H* in some cases, however, exceed 10 percent as in June and July. In the autumn and winter periods, when *AET* is lower than *P*, relative deviations are small.

The same, but for carbon balance components, is presented in *Fig. 4b.* Relative deviations of *SR* follow the annual course of Θ. From January to April, relative deviations of *SR* with respect to SR^r are over 5 percent. From May to August, relative deviations are negative, in June and July they amount about –10 percent. In autumn, relative deviations are small. Nevertheless, deviations of *NEE* are higher and even reversed to deviations of *SR*. For positive deviations of *SR*, *NEE* deviations are negative and vice versa. In extreme cases, as in April, May, and June, *NEE* deviations amount about –40, +100 and +60 percent, respectively. *NEE* changes are bigger, because *NEE* values are lower than *SR* and/or *NPP* values.

Annual course of relative deviations of energy and carbon balance components for $\Theta_f = \Theta_f^r + 0.1 \cdot \Theta_f^r$ is presented in *Fig. 5a* and *Fig. 5b*, respectively. Relative deviations in absolute value are about the same as in the former case but, courses are opposite. Note that high relative deviations of *NEE* are high again. Summarizing: 10 percent changes in absolute value of Θ_f^r resulted about 5–10 and 50–100 percent changes in absolute values of LE^r and NEE^r, respectively.

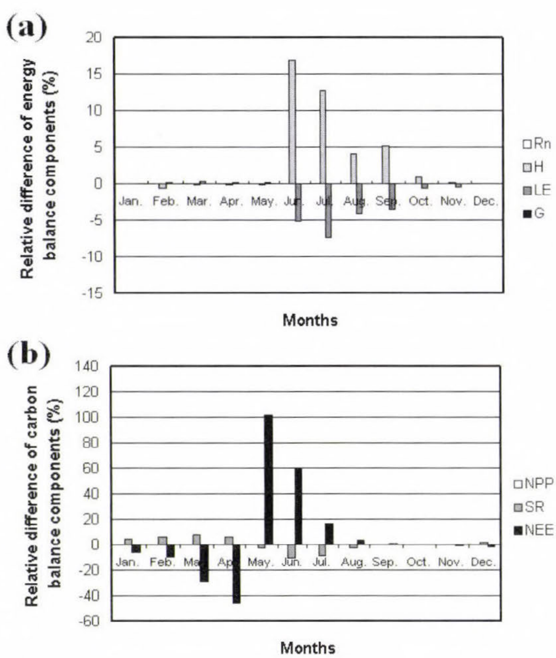

Fig. 5. The same as in Fig. 4a, but for $\Theta_f = \Theta_f^r + 0.1 \cdot \Theta fr$ (a). The same as in Fig. 4b, but for $\Theta_f = \Theta_f^r + 0.1 \cdot \Theta_f^r$ (b).

4.4. Statistical relationships between carbon balance components and environmental factors in the growing season

The period March–November will be called as growing season (GS*)*. This time period is interesting because of the activity of both the soil and vegetation. In this period carbon balance components are significantly changing. There is a strong relationship between *SR* and *H* (see *Fig. 6a*). The correlation coefficient is 0.91. *SR* values are scattered between 300–450 10^{-3} kg C m^{-2} GS^{-1} and sensible heat flux changes between 300–1150 MJ m^{-2} GS^{-1}. Relationship between *NEE* and Θ is presented in *Fig. 6b*. The correlation coefficient is –0.76, that is, *NEE* increases by decreasing of Θ. *NEE* changes between 16 and 160 10^{-3} kg C m^{-2} GS^{-1}. Somewhat stronger relationship exists also between *NEE* and *H* (see *Fig. 6c*). The correlation coefficient is 0.8, that is, *NEE* increases by increasing *H.*

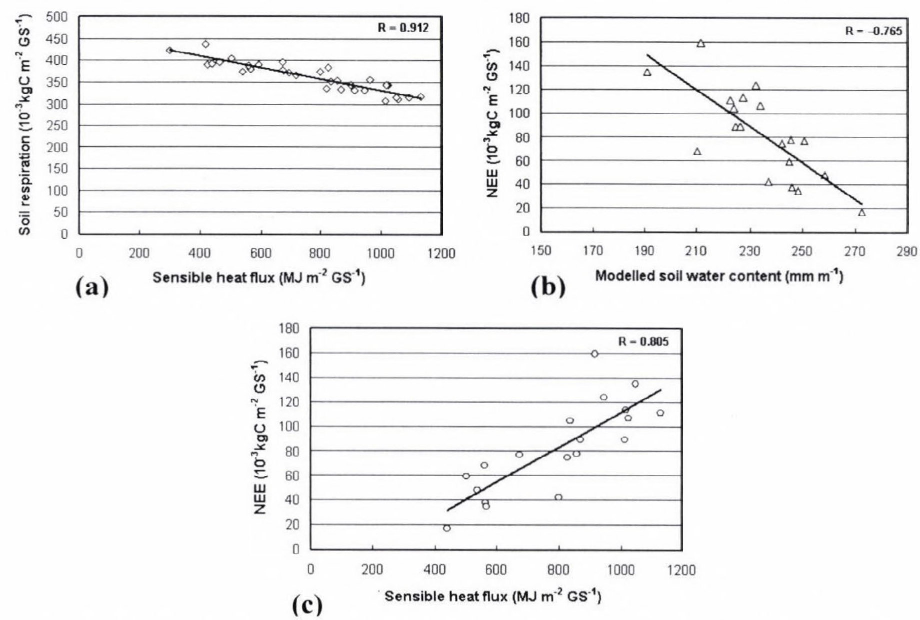

Fig. 6. Statistical relationship between (a) the soil respiration and sensible heat flux, (b) the net ecosystem exchange and precipitation, (c) the net ecosystem exchange and sensible heat flux in the growing season.

5. Conclusions

An extended Thornthwaite's bucket model is applied for estimating surface energy and carbon balance components in the vicinity of Debrecen. Soil water prediction module of the model is verified using measured Θ data from the Agrometeorological Observatory of the University of Debrecen, in the period

1972–1992. There are no verification tests referring to energy and carbon balance components because of the missing direct measurements. Long term mean annual course of energy and carbon balance components is analyzed as well. The sensitivity of *NEE* to Θ_f changes and statistical relationships between energy and carbon balance components in the growing season are considered too.

It is shown that energy balance components are quite influenced in the period September–October (this period is popularly called as 'indian summer'). In this period *Péczely*'s (1961) 12th macro-circulation pattern type is dominating. It is also shown that *AET* and carbon balance components are strongly coupled. Since *AET* is strongly determined by Θ_f, *SR* and/or *NEE* are also sensitive to the changes of Θ_f. In some cases sensitivity of *NEE* to Θ_f could be extremely high. Note that Θ_f is a roughly estimated parameter (*Ács*, 2005). Of course, *NEE* depends not only upon Θ_f, but also upon ε. In our case ε is taken to be 0.55 10^{-3} kg MJ^{-1}. *NEE* values obtained should be treated with caution, because both ε and Θ_f are quite unknown and variable parameters. The model applied does not use any upscaling procedure. Area and time variability of environmental conditions is only implicitly represented by the input data. Thus, model outputs are area and monthly averages, just as the inputs.

References

Ács, F., 2005: On transpiration and soil moisture content sensitivity to soil hydrophiysical data. *Bound.-Lay. Meteorol. 115*, 473–497.

Ács, F., Szász, G., and *Drucza, M.*, 2005: Estimating soil moisture content of a grass–covered surface using an energy balance approach and agroclimatological observations. *Időjárás 109*, 71–88.

Bartholy, J., Pongrácz, R., Barcza, Z., and *Dezső, Zs.*, 2004: Aspects of urban/rural population migration in the Carpathian basin using satellite imagery, 289–313. In *Environmental Change and Its Implications for Population Migration* (eds.: *J.D. Uruh, M.S. Krol*, and *N. Kliot*). Kluwer Academic Publishers, 313 pp.

Drucza, M. and *Ács, F.*, 2006: Relationship between soil texture and near surface climate in Hungary. *Időjárás 110*, 135–153.

Justyák, J., and *Tar, K.*, 1994: *Debrecen's Climate* (in Hungarian). KLTE, Debrecen, Hungary, 160 pp.

Maisongrande, P., Ruimy, A., Dedieu, G., and *Saugier, B.*, 1995. Monitoring seasonal and interannual variations of gross primary productivity, net primary productivity and net ecosystem productivity using a diagnostic model and remotely–sensed data. *Tellus 47B*, 178–190.

Mckenny, M.S. and *Rosenberg, N.J.*, 1993: Sensitivity of some potential evapotranspiration estimation methods to climate change. *Agr. Forest Meteorol. 64*, 81–110.

Mintz, Y. and *Walker, G.K.*, 1993: Global fields of soil moisture and land surface evapotranspiration derived from observed precipitation and surface air temperature. *J. Appl. Meteorol. 32*, 1305–1335.

Péczely, Gy., 1961: Climatological characterization of the macrosynoptic types of Hungary (in Hungarian). *Országos Meteorológiai Intézet Kisebb Kiadványai, 32,* Budapest.

Peng, C.H., Guiot, J., and *van Campo, E.*, 1998. Past and future carbon balance of European ecosystems from pollen data and climatic models simulations. *Global Planet Change 18*, 189–200.

Raich, J.W., Rastetter, E.B., Melillo, J.M., Kicklighter, D.W., Steudler, P.A., and *Peterson, B.J.*, 1991: Potential net primary productivity in South America: Application of a global model. *Ecol. Appl. 1*, 399–429.

Szász, G., 2002: Energy budget between the atmosphere and surface in the vegetation period during 1963–1994. *Időjárás 106*, 161–184.

Thornthwaite, C.W., 1948. An approach toward a rational classification of climate. *Geogr. Rev. 38*, 5–94.

IDŐJÁRÁS
Quarterly Journal of the Hungarian Meteorological Service
Vol. 111, No. 4, October–December 2007, pp. 251–260

A case study on the relationship between radiation intensity and stomatal conductivity in fragmented reedbeds

Angéla Anda[1,*], **Ferenc Horváth**[2], **Anett Boldizsár**[1] and **László Erdei**[2]

[1]*Department of Meteorology and Water, Faculty of Agronomy, Pannon University P.O. Box 71, H-8361 Keszthely, Hungary; E-mail: anda-a@georgikon.hu*

[2]*Department of Plant Physiology, University of Szeged, P. O. Box 654, H-6701 Szeged, Hungary*

(Manuscript received in final form January 19, 2007)

Abstract—Despite the fact that a large number of papers have dealt with the causes of reed die-back, little attention has been paid to the probable effect of environmental factors. Fragmentation is an early sign of die-back and is associated with a considerable change in the environment, particularly in the intensity of radiation. In the present study the relationship between radiation and stomatal conductivity was examined in reeds growing in non-fragmented and fragmented stands on the northern shore of Lake Balaton (Hungary). Hourly measurements were made on the adaxial and abaxial leaf surfaces at every leaf storey of selected shoots on sampling days with the same solar angle in June 1999.

The greater exposure of the fragmented stands to radiation would have been expected to lead to enhanced stomatal conductivity, as plants standing in the lake did not suffer from water deficiency, but this was not the case. The conductivity of plants in the fragmented stand was found to be around 20% lower than that of reeds in a non-fragmented stand, though the direction of the change differed on the two surfaces of the leaves. An intense reduction in conductivity was observed on the adaxial surface and a more moderate increase on the abaxial surface. This discrepancy was greatest at dawn and at a high solar angle. This is thought to be due to adaptation to the stress caused by changes in the environment – more intensive radiation penetration, higher air temperature, reduced humidity – to which the plants in fragmented stands are exposed. Decreased conductivity of fragmented plants results in reduced CO_2 uptake and probably less carbon assimilation as well. This might be one of the reasons leading to reed deterioration of fragmented stands.

A comprehensive analysis of the microclimate of reeds growing in non-fragmented and fragmented stands will be essential if a more detailed picture is to be obtained of changes in stomatal conductivity.

Key-words: fragmented reed, stomatal conductance, radiation relation

[*] Corresponding author

1. *Introduction*

Reeds, one of the most frequent aquatic plants in the Balaton region, play an important role in maintaining the quality of the lake water. The die-back of reeds has become a major problem in the Balaton area in recent decades. In spite of the considerable efforts that have been made to discover the possible reasons for reed decline, the results so far have been modest. It is frequently observed in nature that reedbeds undergo changes in water supply from time to time, becoming temporarily dry or completely inundated with water. However, fragmentation, rather than the continuous variability in the water level, may be the first sign of reed decline. Observations on the die-back of reed stands were published earlier by *Van der Putten* (1997) for reedbeds in central and eastern Europe, and by *Erdei et al.* (2001) for reedbeds in the lake Balaton area. An unusual extent of reed decline, exceeding anything previously recorded, was also observed by *Fogli et al.* (2002) in the Sub-Mediterranean region. *Ostendorp et al.* (2003) attempted to explain the causes of the deterioration of reed stands from 41 lakeshores in central Europe and concluded that lake eutrophication cannot be regarded as the general reason for reed die-back in eastern Europe.

In 1998 the number of fragmented reedbeds isolated from the main stands increased dramatically in Lake Balaton, so tests were made in summer 1999 to determine the difference in radiation intensity compared with that reaching untouched reedbeds and to investigate how fragmented reedbeds, which represent the first symptom of reed die-back, adapt to changes in radiation intensity and related changes in stomatal conductivity. This latter parameter provides direct information on the evapotranspiration of plants standing in water, which is determined solely by the radiation intensity. The results of these observations could contribute to a better understanding of the complex process of reed die-back, and particularly of its relationship to environmental changes.

2. *Materials and methods*

Observations on the radiation intensity in nonfragmented reed stands in Lake Balaton and in fragmented but still viable reedbeds separated from the main stand were carried out in the neighborhood of Balatonfűzfő in June 1999, together with measurements of stomatal activity. The choice of sampling date and place was justified by the increasing number of fragmented reedbeds. At the beginning of the experiment four treatments were distinguished. Reedbeds with a nonfragmented canopy were taken as the control (designated as *E*), while fragments separated from the main stand were classified on the basis of the shoot number. The smallest fragments contained 25–50 shoots, the next category contained around 100 shoots, and the third group consisted of 130–150 shoots. However, as the three groups gave similar responses to the radiation parameters tested, this classification proved unnecessary, so all the fragments were considered as a single treatment (designated as *B*).

The effect of radiation on the stomatal conductivity of reeds in the vegetative phase of development, with an average of 4–10 leaf layers, was recorded on consecutive days in order to eliminate the modifying effect of differences in the solar angle on the relationship between radiation and stomatal conductivity. The investigation of this relationship was favored by the development of fragmented reedbeds, as it allowed the effect of two levels of radiation intensity to be observed simultaneously.

In 1999 a number of cloudy days occurred after June 20, so days were chosen that were uniformly overcast, which meant that there were no great fluctuations in radiation intensity. The completely overcast, "average" sampling day produced from observations made over several days in late June had no previous equal in the literature, except as an explanation for deviations in stomatal activity for brief periods on otherwise bright days. The diurnal variation in stomatal conductance is illustrated by the data of hourly sampling with three repetitions. Parallel with diurnal variation investigations, in contrast to the usual measurements of stomatal conductivity, made on a single, well-illuminated leaf layer, in some cases the present measurement was extended to include all the leaf layers and the conductivity was recorded on both the upper (g_u) and the lower (g_l) epidermis (vertical profiles). According to *Larcher* (2001), the conductivity of the whole leaf (g) can be determined on the analogy of parallel-connected resistances (the reciprocal of conductivity) on the two sides of the leaf. The mean value for each shoot was calculated from the conductivity of all the leaves (series-connected). In vertical profile investigations, in contrast to daily variation, the number of repetitions was ensured not by multiple samplings on a single leaf layer but by measurements on all the leaf layers on the shoot (*Erdei et al.*, 2001). Beside the average values, the coefficient of variation (*CV*, %), and the standard deviation relative to the mean were included in the analysis.

The measurement of radiation was carried out simultaneously with that of stomatal conductivity using a quantum sensor used for the determination of photosynthetically active radiation (*PAR*, μmol s^{-1} m^{-2}). The number of repetitions was the same as in stomatal conductance. The instrument employed was a DELTA T AP4 transient porometer containing sensors for recording both radiation and stomatal conductivity.

3. Results

3.1. Relationship between the radiation and stomatal conductivity

In addition to biological traits, the stomatal conductivity (reciprocal of stomatal resistance) is determined primarily by environmental factors: by the water supplies, representing the hygric component, and by radiation, which provides energy. In the case of reeds standing in water, radiation becomes the primary determinant of stomatal conductivity. The radiation opens the pore in the morning. Later on, when the water is not limiting factor, the higher the radiation intensity, the more opened the stomata. The other abiotic meteorological elements, such as air temperature, air humidity, wind characteristics also affect the movement of the stomata. We have got much less information about the influence, mainly the mechanism of the biotic factors on stomatal behavior. Earlier study on maize showed that diseased plants have higher surface temperature ("fewer") resulted of an increased stomatal resistance referring to decaying the water balance of healthy plants (*Anda*, 1993, 1994). Every factor, biotic or abiotic that increases the stomatal resistance, reduces the input of CO_2 and damages the process of photosynthesis. These disturbances may effect negatively the final production of plants independently on their species, age or phenological phase. In the time of our measurements both the fragmented and nonfragmented reed stands were free from biotic stresses.

The conductivity of healthy and fragmented reedbeds responded differently to variations in radiation intensity (*Fig. 1*). In reedbeds with nonfragmented canopy, *PAR* intensity in excess of 1500 μmol m^{-2} s^{-1} was rarely recorded. Fragmented reedbeds, however, were more open to the environment, so higher *PAR* values were observed, which also allowed examinations to be made over a wider radiation range. For reedbeds with a nonfragmented canopy, the upward slope of the curve describing the relationship between light and stomatal conductivity was steeper above a radiation level of 400 μmol m^{-2} s^{-1} (morning hours) than for fragmented reedbeds, indicating that in a nonfragmented stand the plants responded to unit increase in radiation intensity by greater stomatal opening. The beginning of stomata closure was at 400 μmol m^{-2} s^{-1} light intensity in the time of our experiment.

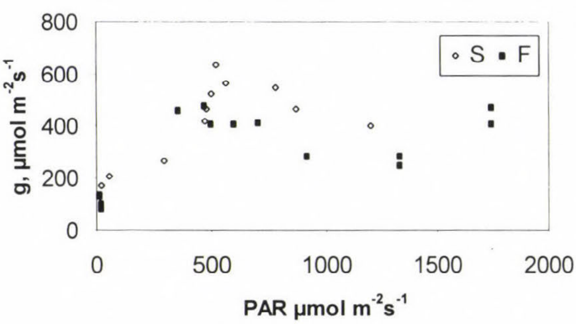

Fig. 1. Relation in photosynthetically active radiation (*PAR*) and stomatal conductance (*g*) of fragmented reed canopy. *S* denotes values for nonfragmented reed stands, *F* denotes values in the fragmented patches. The number of measurements is 24.

The radiation environment of small isolated reedbeds was modified considerably. They received more uniform radiation, but were more exposed to wind and waves than plants within a nonfragmented stand. The modification in the environment and microclimate (radiation penetration, inside air temperature and air humidity, wind) as the result of fragmentation may act as a stress factor, especially at the beginning of the acclimatization period, and may also influence the stomatal conductivity.

Diurnal changes in the stomatal conductivity of nonfragmented reed canopies and fragmented reedbeds in Lake Balaton on bright days were reported by *Erdei et al.* (1998). In agreement with earlier results by this author, the maximum conductivity occurred in both types of reedbeds at around 11 a.m., shortly before the maximum value of radiation (*PAR* = 600–700 μmol m^{-2} s^{-1}). After a transitional decline, possibly associated with stomatal closure at around noon (*Anda* and *Boldizsár*, 2005), there was a further, more moderate increase at radiation values in excess of *PAR* = 1500 μmol m^{-2} s^{-1}.

No difference was observed in the mean stomatal conductivity of each shoot in fragmented reedbeds with different shoot numbers (density). The mean leaf conductivity (recorded on the adaxial and abaxial surfaces) in the fragmented groups decreased by 21% compared with the healthy stand. In fragmented treatments the increase in coefficient of variation was 10%. At low solar angle the difference between the two treatments was less pronounced (13%) (*Fig. 2*). The greater radiation reaching the plants in the more open fragmented stands, which were also more exposed to the wind, while the water supplies were unchanged, would have been expected to cause an increase in stomatal conductivity, while in reality the opposite was observed, probably due to the radical change in the plant environment in the fragmented stands, which can be assumed to be less favorable to the plants than a nonfragmented reedbed. Earlier studies on other plant species demonstrated that environmental stress, whether biotic (fungus, insects, viruses, bacteria) or abiotic (lack of N-fertilizer, water shortage) led to an increase in stomatal resistance (*Anda* and *Lőke*, 1997), i.e., to a reduction in stomatal conductivity.

In fragmented reed difference occurs not only in the magnitude of adaxial and abaxial conductivity, but also in the direction of modification compared with the average value for plants within a reedbed. The reduction in mean conductivity per shoot on the adaxial leaf surface of reed stands was extremely large in the early morning and late afternoon, being around 42–49%. At the same time the conductivity on the abaxial surface of reed stand leaves rose by 14.7–32% (*Fig. 3*). The stomata of the lower epidermis also exhibited greater sensitivity at low solar angle. It should be noted, that this rise in conductivity on the abaxial surface of fragmented reeds was only observed for all leaf zones at certain radiation intensities. One such solar angle was immediately after sunrise at *PAR* = 15–20 μmol m^{-2} s^{-1}, when the difference between the fragmented stands and healthy reedbeds was as much as 150–200%. At high solar angle, with *PAR* values of 1200–1600 μmol m^{-2} s^{-1}, the increase in stomatal conductivity was also substantial (152–173%). At other solar angles there was always one leaf zone in the vertical profile, where the abaxial conductivity of the fragmented reed did not follow the trend for the shoot as a whole.

June 15, 1999

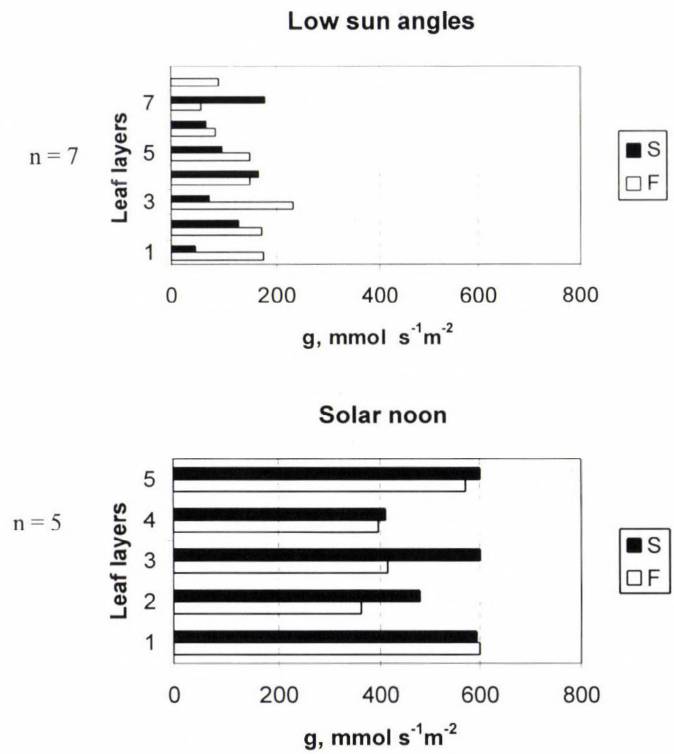

Fig. 2. Vertical profiles of the leaf stomatal conductance (*g*) at low (*PAR*=20 μmol m^{-2} s^{-1}, leaf temperature = 17.7°C) and high solar radiations (*PAR* = 495 μmol m^{-2} s^{-1}; leaf temperature = 23.4°C). *S* denotes the values for healthy stand and *F* is for the fragmented reeds. *n* denotes the number of measurements.

According to earlier observations on the effect of changes in the radiation environment, which can be expected to have been modified in the case of fragmented reeds, factors causing short-term changes deserve the greatest attention. These deviations in radiation induce an acclimatization response in the plants, e.g., a change in leaf thickness, the occurrence of biochemical reactions, or simply a change in leaf movement, etc. (*Larcher*, 2001). Considering the exceptional sensitivity of the stomata to environmental factors, the greater leaf movement caused by the wind in more open stand and the resulting increase in exposure may be sufficient to cause a modification in the stomatal movement.

The higher mean value calculated from the abaxial conductivity recorded for each leaf zone on the shoots of fragmented reeds was characteristic in 94.7% of the total investigations.

In the shoots of healthy reedbeds an increase in conductivity was observed on the abaxial surface compared with the adaxial surface in 43.7% of the cases, though this difference was generally very slight during the day. Even considering the great variability of stomatal conductivity, this difference is noteworthy. The fact, that these changes are masked in some cases in mean stomatal conductivity values, can be explained by the high level of uncertainty caused by point sampling errors. According to *Pearcy et al.* (1991), the measuring error of observations on stomatal activity using a porometer may be as much as 30% or more.

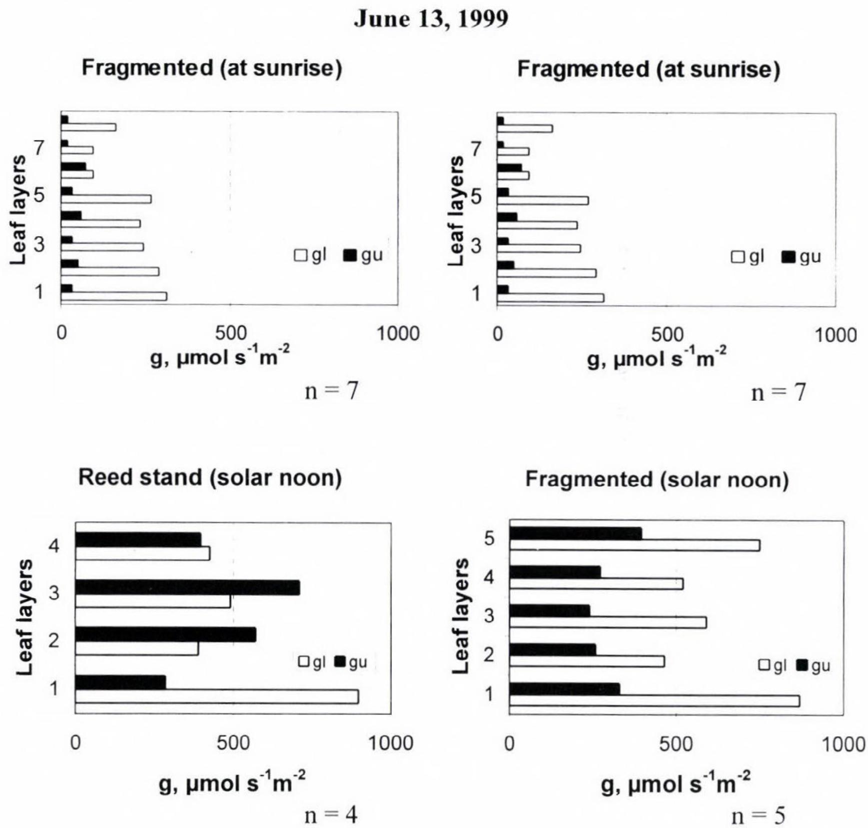

Fig. 3. Vertical profiles of the stomatal conductance on the lower (g_l) and upper (g_u) epidermis. In the time of sunrise *PAR* is 15–50 µmol s^{-1} m^{-2} and leaf temperature is 17.8–18 °C. In the solar noon *PAR* is 1300–1530 µmol s^{-1} m^{-2} and the leaf temperature is 23.4–25 °C. *n* denotes the number of measurements.

3.2. *Stomatal conductivity of reeds on sampling days with even cloud cover*

Irrespective of the plant species, studies on stomatal activity are generally carried out on bright, clear days due to the difficulties encountered during the measurements. Results obtained for healthy and fragmented reedbeds in Lake Balaton were reported by *Erdei et al.* (1998). Due to the variability of the weather, however, it may also be necessary to investigate the stomatal activity when the weather is overcast. This is not possible for all types of cloud cover. In the present study days were chosen, when the cloud cover ensured relatively uniform radiation, allowing the successful measurement of conductivity. The samples were taken at the end of June, during the period immediately following the bright sample days, at the same solar angle. In the early morning hours the reeds were wet, making them unsuitable for measurements, so the diurnal changes are illustrated using values recorded every hour between 10 am and 4 pm. As in the case of values calculated in clear weather, the hourly values are the mean of the conductivity measured on the abaxial and adaxial surfaces.

The stomatal conductivity values recorded on cloudy days were considerably lower than those measured on bright days (*Fig. 4*). The actual value is always determined by the radiation intensity (*PAR*), which fluctuated between 20 and 335 μmol m^{-2} s^{-1} during the observations. The measurements indicated that a *PAR* value of approx. 10–15 μmol m^{-2} s^{-1} is required for the stomata to open, and the lowest conductivity that can be measured is around 25–30 μmol m^{-2} s^{-1}. The change in the cloud cover is revealed by the apparently random stomatal conductivity values, which varied from hour to hour and, despite the low diurnal means 90.6 and 94.7 μmol m^{-2} s^{-1} in nonfragmented reed canopy and fragmented plants, had a relatively high coefficient of variance (*CV* is 68%), half as much again as that found on bright days.

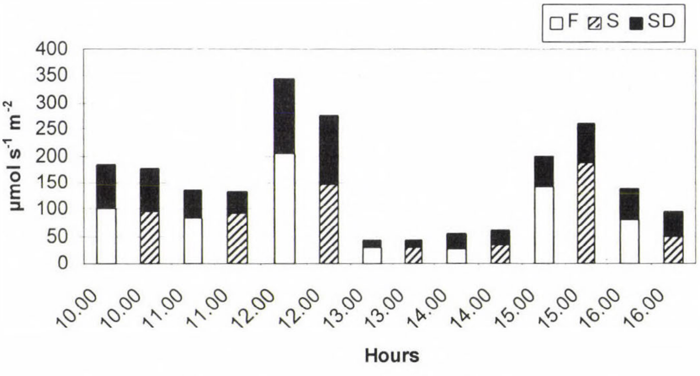

Fig. 4. Daily variation in the stomatal conductance of reed on overcast day. The mean of the measurements in nonfragmented reed stand (*S*) and fragmented treatment (*F*) were 90.6 and 94.7 μmol s^{-1} m^{-2}, respectively. *SD* designates standard deviation.

Unlike the results obtained on bright days, no differences in stomatal conductivity were observed on dull days between the healthy and fragmented reedbeds.

4. *Discussion and conclusions*

The radiation sensitivity of the stomata during the vegetative phase of development differs in healthy and fragmented reedbeds. Reeds in a healthy stand responded to an increase in unit radiation intensity during the morning hours with greater conductivity. Fragmented reedbeds, which were completely open to the elements, were less sensitive to radiation, probably because they had become acclimatized to radiation stress. Stomatal closure followed by renewed stomatal opening was only observed occasionally in fragmented stands at a very high level of radiation. Light intensity measurement within nonfragmented stand was never higher than 1500 $\mu mol\ m^{-2}\ s^{-1}$ in June 1999.

The daily mean leaf conductivity (recorded on the adaxial and abaxial surfaces) in the fragmented groups decreased by 21% compared with the healthy stand. In fragmented treatments the increase in coefficient of variation was 10%. This result was unexpected. For fragmented stands more exposed to radiation, the conductivity should theoretically increase for plants standing in the lake, where water supplies are not a limiting factor. This unexpected phenomenon can probably be attributed to a radical change in the microclimate of the surrounding fragmented stands. For reeds previously growing in a nonfragmented stand, fragmentation inevitably results in intense abiotic stress. In the time of our measurements the fragmented reed was free from biotic stresses.

The direction of difference in stomatal conductivity in fragmented reedbeds differed on the abaxial and adaxial leaf surfaces. While a reduction in conductivity was recorded on the adaxial leaf surface of plants in fragmented stands, an increase was measured on the abaxial surface, compared with plants in nonfragmented stands. At dawn, at low rates of radiation, and at noon, when the radiation was intense, this was true of all the leaf zones. In the intermediate hours changes of opposite sign were observed for some leaf storeys. In daily averages the decreased conductivity of fragmented plants could result reduced CO_2 uptake and carbon assimilation. Among others, disturbance of process of photosynthesis might be one of the reasons leading to reed deterioration of fragmented stands. Our sample day was in the beginning of reed vegetation period (end of June) showing moderate problems in stomatal behavior. Later on this inconvenience intensified in fragmented reed patches, mainly in the following season, ending with complete die-back of plants.

As expected, the mean stomatal conductivity on a sampling day with even cloud cover in late June was lower than in bright weather, with a high coefficient of variance. On cloudy days fragmentation had no influence on trends in the stomatal conductivity of reeds.

The causes of reed die-back in Lake Balaton, which has been detected for some time, are extremely complex. Many scientists attribute the die-back to the simultaneous appearance of a number of unfavorable factors. The present paper was not designed to investigate all the causes, but attempted to shed light on the enhanced sensitivity of fragmented reeds to radiation. The results suggest that complex analysis involving not only radiation but also other factors in the microclimate will be required if we are to understand the changes in stomatal conductivity observed in fragmented reedbeds.

Acknowledgements—This work was supported by the Hungarian Scientific Research Foundation (OTKA T 032524).

References

Anda, A., 1993: Surface temperature as an important parameter of plant stand. *Időjárás 97*, 259-269.

Anda, A., 1994: Infrared thermometry: A new tool in detecting plant diseases (in Hungarian). *Proc. on Forum in Plant Protection*, Keszthely (Hungary), 27 January, 1994.

Anda, A. and *Lőke, Zs.*, 1997: Use of stomatal resistance: Theory and practice. *Annales Geophysicae.* Part II. Supplement II, *15*, p. 288.

Anda, A. and *Boldizsár, A.*, 2005: Transpiration and plant surface temperatures of reedbeds with different watering levels. *Georgikon for Agric. 8*, 39-52.

Erdei, L., Szegletes, Zs., Horváth, F., and *Pécsváradi, A.*, 1998: Changes in ion accumulation, stomatal movements and nitrogen metabolism in clonal fragments of the common reed, Phragmites australis (Cav.) Trin. ex Steudel in the Lake Balaton. In *Proc. of the 11th Congress of the Federation of European Societies of Plant Physiology (FESPP)*. Varna, Bulgaria. *Bulgarian J. Plant Physiol.* (special issue).

Erdei, L., Horváth, F., Tari, I., Pécsváradi, A., Szegletes, Zs., and *Dulai, S.*, 2001: Differences in photorespiration, glutamine synthetase and polyamines between fragmented and closed stands of Phragmites australis. *Aquat. Bot. 69*, 165-176.

Fogli, S., Marchesini, R., and *Gerdol, R.*, 2002: Reed (Phragmites australis) decline in a brackish wetland in Italy. *Mar. Environ. Res. 53*, 465-479.

Larcher, W., 2001: *Physiological Plant Ecology*. Springer Verlag, Berlin-Heidelberg-New York, 513 pp.

Ostendorp, W., Dienst, M., and *Schmieder, K.*, 2003: Disturbance and rehabilitation of Lakeside Phragmites Reeds following an extreme flood in Lake Constance (Germany). *Hydrobiologia*, No.1-3, 687-695.

Pearcy, R.W., Ehleringer, J., Mooney, H.A., and *Rundel, P.W.*, 1991: *Plant Physiological Ecology*. Chapman and Hall, London-New York-Tokyo, 457 pp.

Van der Putten, W., 1997: Die-back of Phragmites australis in European wetlands: An overview of the Research Program on Reed Die-back and Progression (1993-1994). *Aquat. Bot. 59*, 263-275.

④

IDŐJÁRÁS

Quarterly Journal of the Hungarian Meteorological Service
Vol. 111, No. 4, October–December 2007, pp. 261–279

Diurnal course of potential wind power with respect to the synoptic situation

Károly Tar

Department of Meteorology, Faculty of Science, University of Debrecen, P.O. Box 13, H-4010 Debrecen, Hungary; E-mail: tark@puma.unideb.hu

(Manuscript received in final form June 7, 2007)

Abstract—This study is a segment of complex wind energy examinations, which uses statistical methods to analyze the daily mean specific wind power of a month in the period between 1991 and 2000 on seven Hungarian meteorological stations. The properties of monthly average specific wind power can be examined by the definite integral of an approximation function fitting the hourly average of the cubes of wind speed. Certain properties of the approximation function will be analyzed in this paper, mainly its periodicity that may offer implications about the daily course of wind energy. Relations of periodicity of daily course with weather situations are also investigated. Thus, we outline a statistical, stochastic-climatologic model, which could be utilized by energetic systems management in producing electricity from wind energy.

Key-words: average specific wind power, trigonometric polynomials, relative amount of approximation, suddenness and periodicity of the approximation function, weather situations

1. Introduction

In a given term consisting of days (e.g., month, season), the daily average specific wind power is estimated with the definite integral (area under the curve) of a trigonometric polynomial matching the hourly averages of the cubes of wind speeds. In this way, the dependence on the number of measurement times is eliminated, on the other hand, we can investigate the daily courses of wind power: they are the 24-hour and the 12-hour periods in the case of the first two members of trigonometric polynomials. As it is known, the temporal alternation of potential wind power is extremely inconvenient for the operation of electricity, for the power loss must be substituted from other sources. The greatest daily difference may exceed 80% in Germany (*Stróbl,* 2006). For electric energy production those days are advantageous, when the daily (24-hour) course of hourly average wind speed cubes is a simple one with only a single maximum. Days, when the second wave (12-hour period) is random, always have simple daily course with a single maximum. Accordingly, our investigations are applied primarily to the 12-hour period. Only the relationship with the weather situations of the always present whole day period is analyzed in detail.

2. *Objective and database*

The paper discusses a segment of a complex examination, the objective of which is to reveal the inter-dependence of parameters in wind energy in order to outline a statistical, stochastic climatologic model that may be useful in everyday wind energy utilization.

Specific wind power (P_f, in W m^{-2}), is defined as the kinetic energy of the air mass passing through a unit of vertical area in a unit of time. We can calculate it at any given time with the formula

$$P_f = \frac{\rho}{2} v^3, \tag{1}$$

where v is the velocity of wind, ρ is the air density. There are two options to determine the specific wind power of an extended period: either we substitute for the average speed of the period or we add wind power values defined at individual discrete points in time within the period in question. The second option is obviously more realistic. It is problematic, though, that in this case the sum depends on the number of measurement times, as different values are obtained when calculated from wind speeds measured in every hour, in every ten minutes, or at the so called terminal points each day. Although averaging might reduce the dependence on the number of measurement points, it cannot entirely eliminate the problem.

There is a theoretical solution to eliminate this dependence. When the area under the curve of the function describing daily variation in the cubes of wind speeds is multiplied by $\rho/2$, the exact value of every daily specific wind power is obtained. We must use numerical integration, as the necessary function is not analytic on a usual day. We may attempt to determine the average specific wind power falling on a period consisting of days, for instance month, season, or year with an appropriate approximation function.

Hourly wind speed data of ten Hungarian meteorological observatories in the period from 1991 to 2000 required for the energetic examination were provided by the Hungarian Meteorological Service. *Fig. 1* shows the geographical location of the stations. The weather stations in Debrecen, Békéscsaba, Miskolc, and Győr, which are not restricted to wind speed examinations, were relocated (at least once) in the period from 1991 to 2000 of the comprehensive study. The relocation did not caused substantial change in the latitudes or longitudes of any stations concerned, however, increased the elevation in Miskolc and the anemometer height in Békéscsaba. Both heights were changed minimally in Győr. In Debrecen the station relocation caused no significant changes in basic wind statistics as earlier studies showed (*Tar* and *Kircsi*, 2001), unlike Győr, where significant changes can be shown by a simple homogeneity test of the wind data. The reason for this is probably the different environment of the new location. Hence, only the data of those stations are applied, where monthly data series can be regarded homogeneous from January 1991 to December 2001. Thus, anemometric conditions can be considered constant in the following stations: Debrecen, Szeged, Budapest, Pécs, Keszthely, Szombathely, and Kékestető. *Table 1* shows the exact geographical coordinates of the observatories and the height of the wind-gauge above the ground level. We will distinguish lowland (Debrecen, Szeged and Budapest), non-lowland (Pécs, Keszthely, and Szombathely), and mountainous (Kékestető) stations.

Fig. 1. Geographical locations of the meteorological observatories comprising the whole database.

Table 1. Geographical coordinates (φ: latitude, λ: longitude, h: elevation) of the observatories comprising the processed database, and anemometer altitudes (h_a)

Observatory	φ	λ	**h (m)** 1991–2000	**h_a (m)** 1991–2000
Kékestető	47°52'	20°01'	1011	26
		non-lowland		
Szombathely	47°16'	16°38'	219	9
Keszthely	46°46'	17°14'	117	15
Pécs	46°00'	18°14'	201	10
		lowland		
Budapest-Lőrinc	47°27'	19°13'	130	12
Szeged	46°15'	20°06'	83	9
Debrecen	47°30'	21°38'	111	10

3. Determining monthly average specific wind power with an approximation function

Properties of the monthly average specific wind power can be described with the definite integral (area under the curve) of proportional trigonometric polynomial matching the hourly averages of the cubes of wind velocities. An index number for the approximation of the above function is defined, and its spatial variation is analyzed. The conclusions concerning the daily course of wind energy are drawn from the discussion of the suddenness and its relation with the weather situation in the daily and 12-hour waves of the approximation function.

3.1. The method

Wind velocities at discrete measurement times for each day of a specific period are given. The dependence on the number of measurement times is eliminated if a continuous approximation function is found, and the area under its curve can be determined by analytic integration.

Specific wind power falling on a day of a period of time on average is defined as half of the air density multiplied by the area under a function curve that approximates the daily course of the averages of wind speed cubes by measurement time.

The approximation function is

$$f_2(x) = a_0 + \sum_{m=1}^{2}\left(a_m \cos\frac{2\pi m x}{N} + b_m \sin\frac{2\pi m x}{N}\right). \tag{2}$$

It contains the first two members of a Fourier series consisting of trigonometric polynomials, where N is the number of daily measurement times, and $x = 0, 1, 2, ..., N-1$. The so-called residual variance describes the correctness of the approximation or fitting:

$$s_m^2 = s_{m-1}^2 - 0.5A_m^2, \tag{3}$$

where $s_0^2 = s_n^2$, thus, the square of the deviation is

$$A_m = (a_m^2 + b_m^2)^{1/2}, \tag{4}$$

which is the amplitude of the wave m (*Dobosi* and *Felméry*, 1971). It is obvious, though, that s_m^2 depends on the size of the data, and thus, it is not applicable for comparison in this case. For that purpose, the parameter determining the relative amount of approximation is used:

$$s_{0m} = \frac{s_0^2 - s_m^2}{s_0^2}, \tag{5}$$

which might be considered as independent value, thus, it depends not on the magnitude of wind velocities, and it needs not to be corrected for anemometer altitude. s_m^2 values are obviously reduced as the number of approximating polynomials is increased. Let us assume the opposite, when $s_m^2 \approx s_0^2$, that is $s_{0m} \approx 0$. If, however, approximation with Eq. (2) is "perfect", then $s_m^2 \approx 0$, that is $s_{0m} \approx 1$. The closer the s_{0m} falls to 1, the better the approximation function fits the average (*Tar* and *Kircsi*, 2001; *Tar et al.*, 2002).

The primitive of Eq. (2) is

$$F_2(x) = a_0 x + \sum_{m=1}^{2} \left(\frac{a_m}{\alpha_m} \sin \alpha_m x - \frac{b_m}{\alpha_m} \cos \alpha_m x \right), \tag{6}$$

where $\alpha_m = {}^{2\pi m}\!/_N$. Consequently, if we use the time series of the averages of wind speed cubes by measurement times to determine coefficients a_m and b_m, the average specific wind power falling on a day in the period (P_{fmd}) is

$$P_{fmd} = \frac{\rho}{2}[F_2(N-1) - F_2(0)],$$

where

$$T_{ga} = F_2(N-1) - F_2(0) \tag{7}$$

is the area under the curve. The definite integral gives the area under the curve in units determined by the values of x, which depends on the number of measurement times chosen to specify in a day. This fact must be taken into consideration when comparing calculated values.

In the following sections the time series of average wind power falling on a day of a month is described, i.e., the method described above is applied for all the months in the period between 1991 and 2000 at all of the seven stations.

3.2. *Fit of the approximation function*

First the spatial variation of the dimension defined by Eq. (5) is analyzed. *Table 2* contains the most important statistical properties of this parameter. The averages show that the approximation was the best in Szeged and Debrecen, while it was the worst in Keszthely and Pécs. The variability of the parameter, which is indicated by the range, i.e., the difference between the extremities, or by the variation coefficient, appears in the reverse sequence of the previous series in general. Maximum values mainly occur in the spring and summer months, but never in autumn or winter, while the minimum values appear only in winter. The correlation coefficients between s_{02} and the mean monthly wind velocity [v] are also calculated, as it is might be assumed that the goodness-of-fit depends on this velocity. The respective threshold values for significance levels of 0.05 and 0.10 are $|r_{0.05}| \approx 0.1793$, and $|r_{0.10}| \approx 0.1509$ assuming the element number to be $n \approx 120$. The next to the last row in the table shows that stochastic relationship exists everywhere at least on the 0.05 significance level, except for Kékestető.

Table 2. Essential statistical properties of the parameter s_{02} describing the goodness of approximation (v: monthly mean wind velocity)

	Debrecen	**Szeged**	**Budapest**	**Pécs**	**Keszthely**	**Szombathely**	**Kékestető**
Mean	0.77	0.79	0.74	0.68	0.71	0.76	0.76
St.deviation	0.17	0.15	0.18	0.21	0.21	0.17	0.16
Maximum	0.98	0.96	0.95	0.96	0.95	0.96	0.97
Minimum	0.13	0.30	0.10	0.07	0.03	0.13	0.13
Range	0.85	0.66	0.85	0.89	0.92	0.83	0.84
Correlation coefficient (s_{02}, v)	0.2042	0.2408	0.2198	0.2086	0.1863	0.2960	0.1326
> %	63.3	62.5	60.8	61.7	61.0	59.3	64.2

The last row of Table 2 lists the relative frequency in percentage of those parameter values s_{02} that exceed the average. It is the lowest at Szombathely and the highest at Kékestető, a frequency well beyond 50 percent.

There is no observable annual cycle in the appearance of elements exceeding the average due to the small number of cases. If, however, all seven stations are treated together, the values in March and April as well as those in September and October are beyond 10%, representing 43.7% in total. It is remarkable that minimums are found very close to 0 within the extreme values. The absolute minimum is 0.03 which occurred in December 2000 in Keszthely. The absolute maximum is 0.98 which occurred in August 1994 in Debrecen.

3.3. Suddenness of the approximation function

Fourier analysis calls the expected value of amplitudes expectancy (E):

$$E = s_n \sqrt{\frac{\pi}{N}} \; . \tag{8}$$

To decide whether the period N/m of the m wave is random or real, the relation between A_m amplitude and E expectancy is used. In the case when A_m / E is large enough, the probability (p) of random order in the data is low, thus, it can be considered statistically real. In general, $A_m / E > 2$ is acceptable ($p = 0.05$), but in the periodic analysis of time series of meteorological data the wave is considered real, when $A_m / E > 1.5$ ($p = 0.17$) is met (*Koppány*, 1978).

Table 3 shows that the daily wave must not be considered random in 80 to 95% of the cases at the significance level of 0.05 and in 89.2 to 97.5% of the cases at the 0.17 significance level, as it was expected. More interesting is the suddenness of the 12-hour wave, where the ranges in the table are 11.7 to 25% and 29.2 to 57.5%, respectively.

Table 3. Percentages of the reality of the daily and 12-hour waves at significance levels of 0.05 ($A_m/E>2$) and 0.17 ($A_m/E > 1.5$)

%	Debrecen	Szeged	Budapest	Pécs	Keszthely	Szombathely	Kékestető
$A_1/E>2$	95.0	92.5	95.0	80.0	88.3	94.2	91.7
$A_1/E>1.5$	97.5	95.8	95.8	89.2	92.5	97.5	95.0
$A_2/E>2$	12.5	24.2	11.7	25.0	12.5	17.5	17.5
$A_2/E>1.5$	40.0	50.0	38.3	57.5	36.7	40.8	29.2

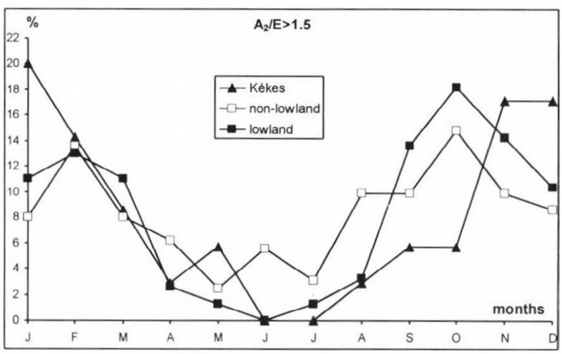

Fig. 2. Monthly frequencies of the reality of the 12-hour wave (p = 0.17).

According to the Introduction, let us take a closer look at the annual variation of the non-random 12-hour waves at the 0.17 significance level. We will examine the monthly distribution of those cases, where A_2 / E is greater than 1.5 according to station types. *Fig. 2* shows the frequency of fulfilled conditions in percentage for every station types. It is clear from the figure that the condition is not realized in June at the lowland stations where the frequency raises above 10% in the autumn and winter months as well as in March. The maximum is in October while the secondary maximum occurs in February. The months for the annual maximum and secondary maximum are the same in the case of non-lowland stations, but the value of the primary maximum reduces in favor of June, when an approximately 6% high tertiary maximum occurs. In Kékestető the yearly course is simpler and smoother: there are two zero minimums in June and July, and a maximum of about 20% in January with large winter values.

We can see that the 12-hour wave of trigonometric polynomials fitted monthly on the average cubes of the hourly wind velocities shows suddenness mainly in the late spring and summer months at the 0.17 significance level, while the frequency of its probable reality increases in the winter, early spring, and autumn months, that is for the major part of the year. Thus, we may expect significant daily alterations of wind energy, its morning and afternoon minimums, as well as its daytime and night maximums (the other way round in the case of Kékestető). There is no circadian change of wind energy in those cases, where the 12-hour wave is random, for they are dominated by the daily cycle with a single maximum around midday. *Fig. 3* illustrates the above, where the hourly average of measured cubes of wind speeds appear by months corresponding to the absolute extreme A_2 / E ratios together with approximate values of waves 1 and 2. The column *b* of the figure clearly shows that at minimal A_2 / E ratio the two waves practically coincide, i.e., the approximation slightly increases including the second random wave.

Fig. 4 shows daily differences in the cases of extreme values in observatory types, they indicate the deviation of the hourly average wind speed cubes from the daily maximum in percentage based on the approximate data. As it follows from the part *a* of *Fig. 4*, if the 12-hour wave is real, there is no great difference between the values of lowland and non-lowland stations. Maximums fall approximately between 65 and 70% on both station types. The daily difference is the lowest in Kékestető, where it raises above 40% only in the early afternoon. According to part *b* of the figure, in the case of a non-dominant, random 12-hour wave, the greatest differences from the daily maximums in the night are over 70% in the average of lowland stations. In Kékestető the differences have a daily maximum over 65% around midday.

Assuming a 0.17 significance level, the frequency of advantageous days for electric energy production from wind is between approximately 43 and 70% in all the seven stations. Kékestető has the most of them with Keszthely, Budapest Debrecen, Szombathely, Szeged, and Pécs following in order. The cases when the daily wave dominates and is accompanied by random 12-hour waves, that is A_1 / E>1.5 and $A_2 / E \leq 1.5$, have not yet been discussed. The number of these cases is expected to be relatively great. Their proportion (to the number of all months) by station types is 63.6% in lowland stations, 58.3% in non-lowland stations without Kékestető and 60.4% with it, while 61.8% in all of the seven stations together.

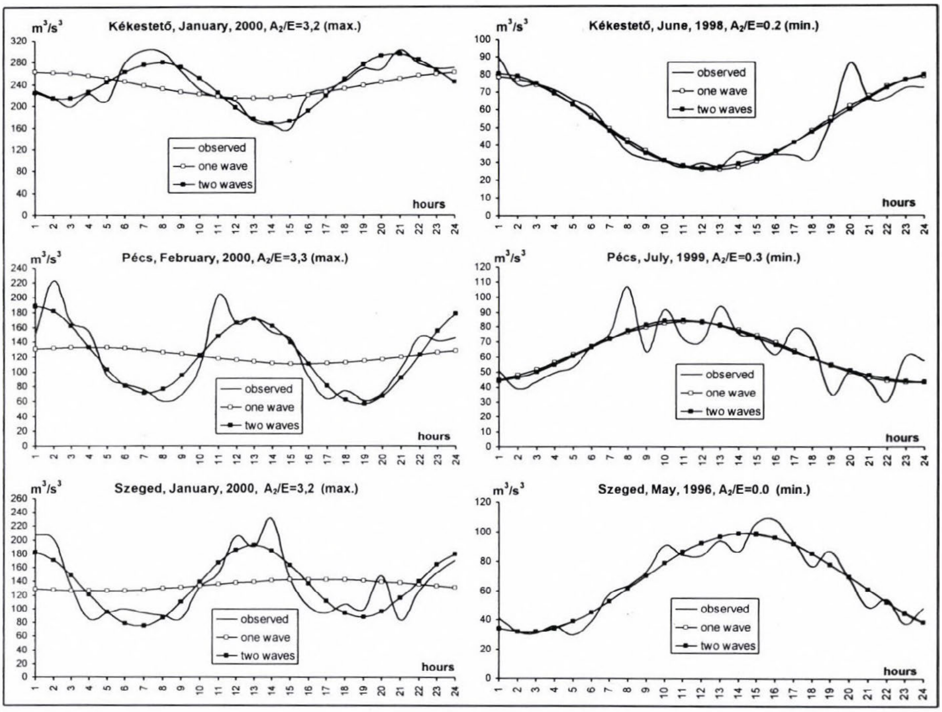

(a) (b)

Fig. 3. Examples for approximation with one and two waves of hourly averages of wind speed cubes (m^3/s^3) in the case of very strong (a) and very week (b) 12-hour periods.

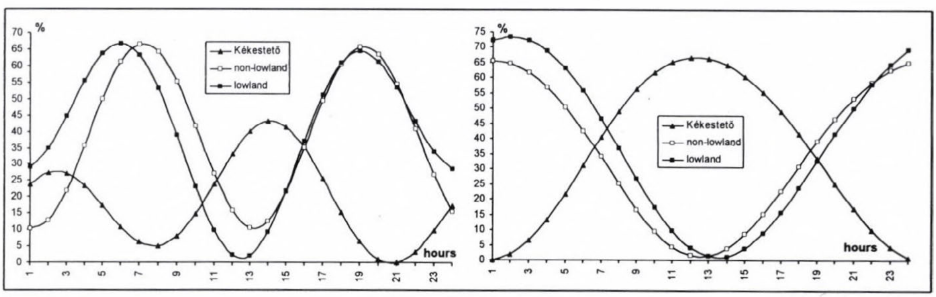

(a) (b)

Fig. 4. Deviation of the average of hourly wind speed cubes from daily maximums in the case of real (a) and random (b) 12-hour wave (from the extreme values of observatory types).

The most favorable days for the system administration are very likely those when there is no significant daily variation. Following from the above, the number of such days must be relatively small. The number of months where the daily average wind power shows neither the daily nor the 12-hour cycle on the 0.17 significance level is altogether 17 days, which is only 2% in the period discussed here.

4. *Relation of the daily course with the weather situations*

Next, we attempt to analyze the interrelation between the reality of the 12-hour period with the weather situations in detail, and to analyze it shortly in the case of daily period. The daily flow conditions with the Péczely's macrosynoptic situations (*Péczely*, 1961, 1983) and with the Hess-Brezowsky macrocirculational types (*Hess* and *Brezowsky*, 1977) are described together with Puskás' weather front types (*Puskás* and *Nowinszky*, 1996; *Puskás*, 2001). Then types, dominate at the seven observation stations in those months, which meet the condition $A_2 / E > 1.5$, is determined.

4.1. Relation between the 12-hour and daily period and Péczely's macrosynoptic conditions

Table 4 summarizes the codes, letter codes, and short descriptions of Péczely's macrosynoptic types (*Péczely*, 1983). It is apparent that both meridional (MN, MS) and zonal (ZW, ZE) type-groups can be created, while central types cannot be grouped. It is also common to gather the types into cyclonic (CG: 1, 3, 4, 6, 7, 13) and anticyclonic (AG: 2, 5, 8, 9, 10, 11, 12) type-groups.

Next, we examine which types and type-groups are dominant in those months when the average daily course of wind energy has real 12-hour periodicity ($A_2 / E > 1.5$). Such dominance is measured with the occurrence of a given type or type-group in percent compared to the number of all occurrences in the month that fulfills the above condition. In Debrecen, for instance, the mCc type if the condition is met occurs on 171 days out of the 457 days within the whole period, thus, its relative frequency is $100 \cdot 171/457 = 34.4\%$.

Fig. 5 displays the frequency of each type in the decade from 1991 to 2000 (*Károssy*, 1993, 1998, 2001). The figure also shows that the days characterized by the zC (zonal–cyclonic) type in the months fulfilling the reality condition occur most frequently at the three station types. According to the figure, zC type is the second rarest condition in the period of our study, as well as in the period from 1971 to 2001 (2.2 and 3.1%, respectively). Its flow is typically directed from west to east, and for the most part it is characterized by windy and changeable weather. As the figure shows, average conditional frequencies do not significantly differ from each other at the lowland and non-lowland stations. On the other hand, the relative frequency at Kékestető rises above 40% only in the case of type zC. The rarest occurrence of the 12-hour period may be expected in the case of AB, AF, and C types: below 40% at the lowland and non-lowland stations, bellow 25% at Kékestető.

Table 4. Codes, letter codes, and short descriptions of Péczely's macrosynoptic types

	Meridional directed types with northern current (MN type-group)	
1	mCc	Hungary lies in the rear of an east-European cyclone
2	AB	anticyclone over the British Isles
3	CMc	Hungary lies in the rear of a Mediterranean cyclone
	Meridional directed types with southern current (MS type-group)	
4	mCw	Hungary lies in the fore part of a west-European cyclone
5	Ae	anticyclone to the east of Hungary
6	CMw	Hungary lies in the fore part of a Mediterranean cyclone
	Zonal directed types with western current (ZW type-group)	
7	zC	zonal cyclone type
8	Aw	anticyclone extending from the west
9	As	anticyclone in the south of Hungary
	Zonal directed types with eastern current (ZE type-group)	
10	An	anticyclone in the north of Hungary
11	AF	anticyclone over the Fennoscandinavian region
	Central types	
12	A	anticyclone over the Carpathian Basin
13	C	cyclone over the Carpathian Basin

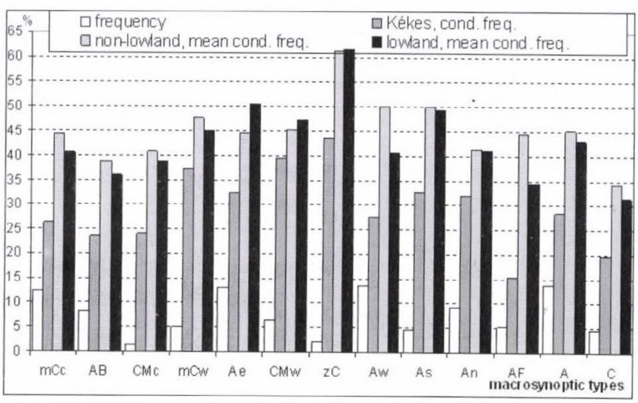

Fig. 5. Frequencies of Péczely's macrosynoptic types in percent of the total number of days of the period studied, and their conditional (A_2/E>1.5) frequency in the presence of real 12-hour periods.

Table 5 shows the frequency of individual macrosynoptic type-groups and their conditional frequency in the presence of 12-hour periods. It is clear that anticyclonic conditions (AG) occur twice as frequently as cyclonic ones, as well as there is a more than 10 percent dominance of meridional (MN + MS) conditions. According to the table, MS types occur most frequently at lowland stations, while types belonging to the ZW group occur most frequently at non-lowland locations, if there is a real 12-hour periodicity. However, the absolute maximum is found at the ZE type-group in Debrecen. According to the same table, cyclonic (CG) and anticyclonic type-groups do not differ significantly in this respect; the greatest difference in their frequency (6.2%) was observable in Pécs.

Table 5. Frequency of individual Péczely's macrosynoptic type-groups and their conditional (A_2/E>1.5) frequency in the presence of real 12-hour periods

A_2/E>1.5	MN	MS	ZW	ZE	CG	AG
Frequency (%)	22.4	24.6	20.4	14.4	32.3	67.7
			Conditional frequency (%)			
Debrecen	62.9	52.9	56.0	65.7	58.5	59.5
Szeged	42.8	57.0	52.2	47.6	48.5	50.2
Budapest	36.6	43.3	39.4	34.9	39.0	38.0
Pécs	54.2	55.5	62.8	60.6	53.3	59.5
Keszthely	34.4	36.6	43.8	29.3	36.0	36.5
Szombathely	37.5	43.9	46.8	37.5	44.4	38.8
Kékes	25.1	35.3	30.5	26.1	30.8	28.2
Mean	41.9	46.4	47.4	43.1	44.4	44.4

As we can see in *Table 3*, the frequency of real daily wave is a long sight larger than the frequency of the 12-hour period. It is located between 80 and 95% on the 0.05 significance level. So we can calculate with a great safety on the appearance of twenty four-hour period in all day. It follows from this, that the conditional frequencies of these do not differ from each other in the various macrosynoptic types and type-groups. For example, we find the next in the different type-groups: the maximum conditional frequency is in the type-group MN in the case of six observatories, the minimum conditional frequency is in the type-group MS in five observatories, there is no maximum or minimum value in the MS and ZW, or MN and ZE type-groups. So the extreme values are in the meridional groups. If only the cyclonic and anticyclonic groups are distinguished (see *Table 5*), we can find that the conditional frequencies are not differ each other significantly on the stations, namely the reality of the whole day wave is independent of these groups.

4.2. Relation between the 12-hour and daily period and the Hess–Brezowsky macro-circulational types

The classification of Hess–Brezowsky macrosynaptic weather types was made with regards to the circulation conditions of the Atlantic-European region and the directions of major frontal zones (*Hess* and *Brezowsky*, 1977). Altogether 29 types (4 zonal, 7 mixed, and 18 meridional) are distinguished and an additional type is defined for the untypical fields. *Table 6* lists the types and groups that can be formed from them according to *Bárdossy* and *Caspary* (1990) and *Bartholy* (2005). We use the daily codes for the period in question from the work of *Gerstengarbe* and *Werner* (2006).

Due to the small size of our database, only the 10 groups distinguished by the main flow direction and three circulation types (zonal, mixed, meridional) were investigated. For easier identification the letters of the circulation types were appended to the beginning of the letter codes of the 10 groups in *Table 6.*

Table 6. List of Hess-Brezowsky major types (GWT)

Major type/groups (GWT)	Main direction of the flow
A. zonal circulation (z)	
West	zW
B. mixed circulation (x)	
Central European high	xHM
Central European low	xTM
Southwest	xSW
Northwest	xNW
C. meridional circulation (m)	
East	mE
South	mS
Southeast	mSE
North	mN
Northeast	mNE

In the next step, type-groups dominating in those months when the average daily course of the wind energy shows real 12-hour periodicity (A_2 / E>1.5) were examined. *Fig. 6* displays the frequency and conditional frequency of each type-group. According to the figure, there are not so much apparent orders as in the case of Péczely's types. The figure leads us to the following conclusion: we can least (somewhat more than 30%) expect the occurrence of the real 12-hour period in the merdional type-group with northeastern main flow direction (indicated as mNE in the figure), while the period will occur most frequently (approximately 50%) in the also meridional, mSE type at the lowland stations.

The absolute maximum occur at the non-lowland stations with the mixed cyclonic type-group (xTM) – almost 2/3 of such days have real 12-hour periods. It is flowed by the zonal west group (zW), where the proportion of real periods is 52%. The absolute minimum (12.5%) is in Kékestető with the meridional NE main flow directional type-group (see above). It is followed by xTM, which is the absolute maximum and the maximum at the non-lowland stations.

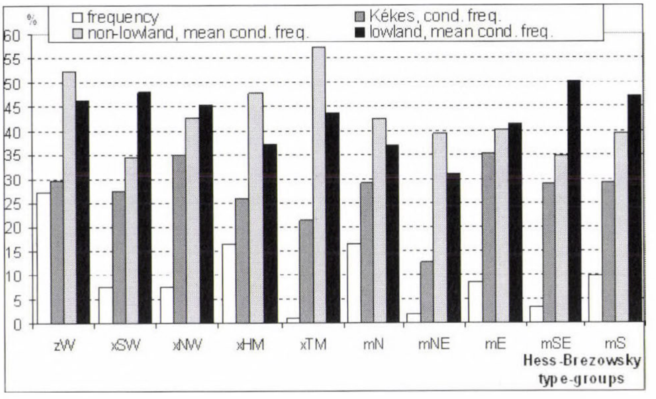

Fig. 6. Frequency of various Hess-Brezowsky macrosynoptic type-groups in per cent of the total number of days of the period studied and their conditional frequency in the presence of real 12-hour periods.

Table 7 contains the frequencies and conditional frequencies of the zonal group and that of the combined mixed and meridional groups. The dominance of the meridional type-group and the northern direction within it is obvious, while it is the anticyclonic group those duffers in the mixed type. The maximum relative frequency falls to Pécs, the minimal one is in Kékestető in all three groups. According to the averages of all stations, the real 12-hour period occurs most frequently in the zonal, while less frequently in the meridional type-group.

The investigation at the 0.05 significance level of reality of daily period shows, that the conditional frequencies reach 100% in the xTM circulation type in four observatories (three lowland stations and Kékestető) and in the mNE type in Debrecen. Investigation by type-groups we find that the maximum or its approximate values are in the mixed (x) group, and the minimum values are in the zonal (z) group.

Table 7. Frequency of various Hess-Brezowsky circulation type-groups and their conditional frequency in the presence of real twelve-hour periods

A_2/E>1.5	Zonal	Mixed	Meridional
Frequency (%)	27.4	32.3	40.3
	Conditional frequency (%)		
Debrecen	44.7	36.6	39.3
Szeged	54.7	48.7	46.9
Budapest	39.0	39.8	36.9
Pécs	64.7	58.3	51.8
Keszthely	45.6	33.8	32.2
Szombathely	46.6	39.7	37.4
Kékes	29.6	28.2	29.6
Mean	46.4	40.7	39.2

4.3. Relation between the 12-hour and daily period and the weather front types

It is well known that frontal passages are accompanied by more or less marked changes in the weather that might be analyzed in details if the weather fronts are classified into different types and the weather characteristics of individual front types are discerned.

The classification of weather fronts may be based on various aspects. *Berkes* (1961) gave 22 front types for the area of Hungary based on detailed air mass analysis by the help of radio probe launches. The front almanac of the Hungarian Meteorological Service uses the same front types. Another, more accurate method of front analysis, which requires a very large database, is the examination of geopotential fields (*Bartholy et al.,* 2006).

Front types based on complicated definitions are rather cumbersome to use in practice, therefore, a simpler front definition method that requires only basic meteorological expertise became necessary. *Puskás* and *Nowinszky* (1996) and *Puskás* (2001) have carried out the classification of fronts passing over Hungary by the help of the synoptic maps for the "Daily Meterorological Reports" of the Hungarian Meteoroligal Service as well as the recorded weather measurement data. *Fig. 7* lists the 9 front types (t1–t9) they have distinguished.

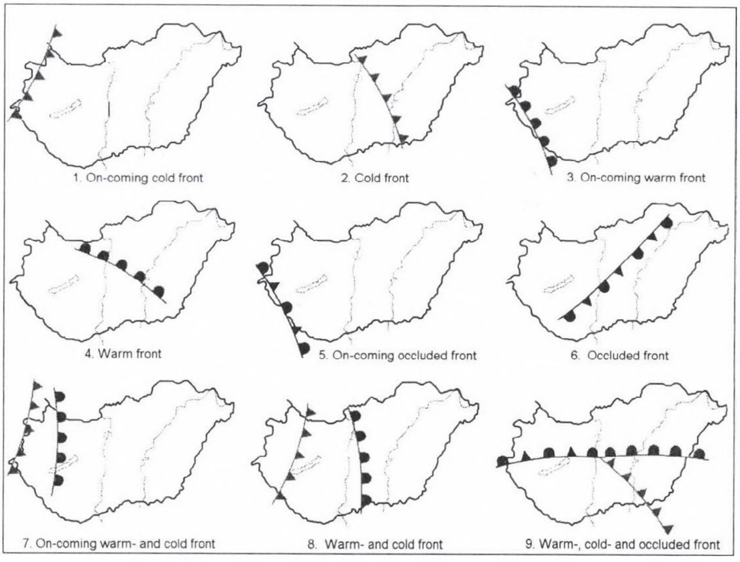

Fig. 7. Weather front types (t1–t9) in Hungary.

Fig. 8 shows the frequency of front types in percent of days with frontal passage. It clearly shows that the most frequent front type is the on-coming cold front (t1) and the rarest type is the simultaneous stationary cold, warm, and occluded front (t9). Cold front types (t1 and t2) occur altogether in 42.3%, warm fronts (t3 and t4) in 28.4%, and both fronts (t7 and t8, without occlusion) in 18.3%, while occluded fronts (t8, t6 and t9) occur in the 10.9% of the cases.

We have examined which front types are dominant in those months when the course of the average daily wind energy shows real 12-hour periodicity. *Fig. 8* also displays the conditional frequency of each type if the condition $A_2 / E \geq 1.5$ is met. This figure allows for some general conclusions to be drawn: there is always warm front (t3 or t7) present at each observation types when local maximums occur. Minimums are always observed in the presence of one of the occluded front types (t5, t6 or t9). The figure shows that real 12-hour periodicity on the whole scale occurs most frequently in the case of two warm front types (t3 and t4). The next probable cases are the approaching warm and cold fronts (t7), while it occurs least frequently in the case of the two occluded front types.

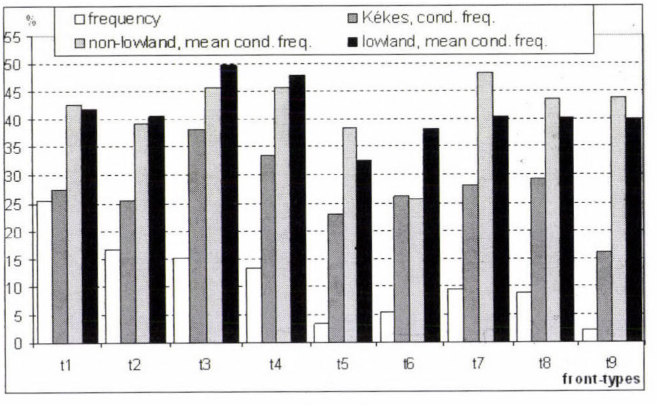

Fig. 8. Frequency of individual front types in percent of the number of days with frontal passage and their conditional frequency in the presence of real 12-hour periods.

If we consider only the days with and without frontal passage (cf. *Table 8*), we may see that the number of days without fronts in the period of our study is more than double of the number of days with frontal passage.

Their conditional frequencies by observation stations and on the average hardly differ, the presence of real 12-hour periodicity is given. Except for Keszthely, this frequency for days with frontal passage is always higher by some tenth % and we find the maximal 3% difference in Szombathely.

The investigation at the 0.05 significance level of reality of daily period shows that the conditional frequencies reach 100% in the t9 type at Debrecen and Kékestető. On the other hand, the maximum values distribute evenly in types t1, t2, t4, t7, t8, and t9, namely they do not occur in types t3, t5, and t6. However, the minimum values are concentrated in t3 type, so the probability of the reality of the daily period is the least in this type. If only the days with and without fronts are distinguished, then the conditional probabilities do not differ each other significantly, namely the reality of the whole day wave is independent of such days.

Table 8. Frequency of days without and with frontal passage in percent of the total number of days of the period studied, and the conditional frequency of days with and without frontal passage in the presence of real 12-hour periods

A_2/E>1.5	Without fronts	With fronts
Frequency (%)	68.7	31.3
	Conditional frequency (%)	
Debrecen	39.8	40.2
Szeged	49.6	49.7
Budapest	38.1	38.7
Pécs	57.3	58.0
Keszthely	36.4	36.3
Szombathely	30.4	33.4
Kékes	28.9	29.3
Mean	40.1	40.8

5. Conclusions

It can be shown by the aid of fitting trigonometric polynomials that the hourly average of wind speed cubes – i.e., the hourly average specific wind power – follows one of three possible daily patterns. Single daily maximal and minimal value occur in the first case, while two daily maxima and minima appear in the second one. In the third case, there is no actual daily pattern, but the hourly values show random fluctuation. Seasonal distribution of the above cases may provide useful information for energetic systems management, when wind power is used to produce electricity:

- The 12-hour period mostly shows randomness in late spring and summer months, the reality of the first (24-hour) wave increases with the randomness of the second one in these months. Thus, we may rather safely assume that diurnal changes of wind energy will follow patterns that are favorable for energetic systems management in spring and summer. The number of most favorable days for the systems management, where there is no significant daily course at all, is few. The frequency of those months when average daily wind power shows neither diurnal nor 12-hour cycles, is only 2% in the period examined.
- In the majority of the observation stations, days that can be characterized as zC (zonal cyclonic) types according to Péczely's classification are the most frequent in those months, where the hourly

average wind power has real 12-hour period. Its flow is typical west to east, characterized mostly by steady wind and changeable weather. We may least expect the occurrence of 12-hour periods in the case of the AB, AF, and C types.

- 12-hour periods occur least frequently in the meridional northeast main flow direction type-group, while they will occur most frequently in zonal west and mixed cyclic type-groups in the case of Hess-Brezowsky classification.
- If we separate the days with or without frontal passage, we find that their frequency by observation stations and on the average hardly differs, the presence of real 12-hour periodicity is proven. Considering the front types, maximum always occurs in the presence of warm front at each stations, while minimum mostly occurs together with an occluded front type. Averages show that real 12-hour periodicity occurs most frequently with warm front types, together with approaching warm and cold fronts, but least frequently with the two occluded front types.

Acknowledgements—The author expresses his gratitude to the Hungarian Meteorological Service for providing the wind data necessary for his research.

References

Bárdossy, A. and *Caspary, H.J.*, 1990: Detection of climate change in Europe by analyzing European atmospheric circulation patterns from 1881 to 1989. *Theor. Appl. Climatol. 42*, 155–1671.

Bartholy, J., 2005: Reconstruction of climatic past of Carpathian Basin and the estimate of the expected tendencies in the future (in Hungarian). *DSc Thesis*, Magyar Tudományos Akadémia, Budapest, Hungary.

Bartholy, J., *Pongrácz, R.*, and *Pattantyús-Ábrahám, M.*, 2006: European cyclone track analysis based on ECMWF ERA-40 datasets. *Int. J. Climatol. 26*, 1517-1527.

Berkes, Z., 1961: Air-masses and front types in the Carpathian Basin (in Hungarian). *Időjárás* 65, 289-293.

Dobosi, Z. and *Felméry, L.*, 1971: *Climatology* (in Hungarian). Tankönyvkiadó, Budapest.

Gerstengarbe, F.-W. and *Werner, P.C.*, 2006: Katalog der Grosswetterlagen Europas (1881-2004). *PIK Report* No. 100. http://www.pik-potsdam.de/publications/pik_reports/reports/pr.100/pr100.pdf

Hess, P. and *Brezowsky, H.*, 1977: *Katalog der Grosswetterlagen Europas*. Berichte des Deutschen Wetterdienst, 113, 15.

Károssy, Cs., 1993: Péczely's classification of macro-synoptic types and catalogue of weather situations (1951-1992). In *Light Trapping of Insects Influenced by Abiotic Factors.* Part I. (ed.: *L. Nowinszky*). Publisher OSKAR, Szombathely, 113-126.

Károssy, Cs., 1998: Péczely's classification of macro-synoptic types and catalogue of weather situations (1992-1997). In *Light Trapping of Insects Influenced by Abiotic Factors.* Part II. (ed.: *L. Nowinszky*). Savaria University Press, Szombathely, 117-130.

Károssy, Cs., 2001: Characterisation and catalogue of the Péczely's macrosynoptic weather types (1996-2000). In *Light Trapping of Insects Influenced by Abiotic Factors.* Part III. (ed.: *L. Nowinszky*). Savaria University Press, Szombathely, 75-86.

Koppány, Gy., 1978: *Long-Range Forecast* (in Hungarian). Tankönyvkiadó, Budapest.

Péczely, Gy., 1961: *Climatic characterization of macro-synoptic types in Hungary* (in Hungarian). Országos Meteorológiai Szolgálat Kisebb Kiadványai 32, Budapest.

Péczely, Gy., 1983: *Catalogue of the macrosynoptic types for Hungary (1881-1983)* (in Hungarian). Országos Meteorológiai Szolgálat Kisebb Kiadványai, 53, Budapest.

Puskás, J., 2001: New weather front types and catalogue for the Carpathian Basin. In *Light Trapping of Insects Influenced by Abiotic Factors.* Part III. (ed.: *L. Nowinszky*). Savaria University Press, Szombathely, 87-118.

Puskás, J. and *Nowinszky, L.*, 1996: Light-trap catch of the turnip moth (Scotia segetum Schiff.) during the time of weather fronts (in Hungarian). *Légkör* XLI., No. 2, 29-32.

Stróbl, A., 2006: Extra load of wind turbines in our electric energy system (in Hungarian). *Magyar Energetika 4*, 33-43.

Tar, K. and *Kircsi, A.*, 2001: A method for calculation of the daily specific wind power (in Hungarian). In *Meteorological Scientific Days — Meteorological Basics of the Atmospheric Resources Utilization* (ed.: *J. Mika*). Országos Meteorológiai Szolgálat, Budapest, 129-137.

Tar, K., Kircsi, A., and *Vágvölgyi, S.*, 2002: Temporal changes of wind energy in connection with the climatic change. In *Proc. of the Global Windpower Conference and Exhibition.* CD-ROM, Paris.

IDŐJÁRÁS

VOLUME 111 * 2007

BUDAPEST, HUNGARY

AUTHOR INDEX

TABLE OF CONTENTS
Papers

SUBJECT INDEX

T

U

V

W

GUIDE FOR AUTHORS OF *IDŐJÁRÁS*

The purpose of the journal is to publish papers in any field of meteorology and atmosphere related scientific areas. These may be

- research papers on new results of scientific investigations,
- critical review articles summarizing the current state of art of a certain topic,
- short contributions dealing with a particular question.

Some issues contain "News" and "Book review", therefore, such contributions are also welcome. The papers must be in American English and should be checked by a native speaker if necessary.

Authors are requested to send their manuscripts to

Editor-in Chief of IDŐJÁRÁS
P.O. Box 39, H-1675 Budapest, Hungary

in three identical printed copies including all illustrations. Papers will then be reviewed normally by two independent referees, who remain unidentified for the author(s). The Editor-in-Chief will inform the author(s) whether or not the paper is acceptable for publication, and what modifications, if any, are necessary.

Please, follow the order given below when typing manuscripts.

Title part: should consist of the title, the name(s) of the author(s), their affiliation(s) including full postal and e-mail address(es). In case of more than one author, the corresponding author must be identified.

Abstract: should contain the purpose, the applied data and methods as well as the basic conclusion(s) of the paper.

Key-words: must be included (from 5 to 10) to help to classify the topic.

Text: has to be typed in single spacing with wide margins on one side of an A4 size white paper. Use of S.I. units are expected, and the use of negative exponent is preferred to fractional sign. Mathematical formulae are expected to be as simple as possible and numbered in parentheses at the right margin.

All publications cited in the text should be presented in a *list of references*, arranged in alphabetical order. For an article: name(s) of author(s) in Italics, year, title of article, name of journal, volume, number (the latter two in Italics) and pages. E.g., *Nathan, K.K.*, 1986: A note on the relationship between photo-synthetically active radiation and cloud amount. *Időjárás 90,* 10-13. For a book: name(s) of author(s), year, title of the book (all in Italics except the year), publisher and place of publication. E.g., *Junge, C.E.*, 1963: *Air Chemistry and Radioactivity*. Academic Press, New York and London. Reference in the text should contain the name(s) of the author(s) in Italics and year of publication. E.g., in the case of one author: *Miller* (1989); in the case of two authors: *Gamov* and *Cleveland* (1973); and if there are more than two authors: *Smith et al.* (1990). If the name of the author cannot be fitted into the text: *(Miller,* 1989); etc. When referring papers published in the same year by the same author, letters a, b, c, etc. should follow the year of publication.

Tables should be marked by Arabic numbers and printed in separate sheets with their numbers and legends given below them. Avoid too lengthy or complicated tables, or tables duplicating results given in other form in the manuscript (e.g., graphs)

Figures should also be marked with Arabic numbers and printed in black and white in camera-ready form in separate sheets with their numbers and captions given below them. JPG, GIF, or XLS formats should be used for electronic artwork submission.

The text should be submitted both in manuscript and in electronic form, the latter on disks or in e-mail. Use standard 3.5" MS-DOS formatted diskette or CD for this purpose. MS Word format is preferred.

Reprints: authors receive 30 reprints free of charge. Additional reprints may be ordered at the authors' expense when sending back the proofs to the Editorial Office.

Information on the last issues: http://www.met.hu/Journal-Idojaras.php

Published by the Hungarian Meteorological Service

Budapest, Hungary

INDEX: 26 361

HU ISSN 0324-6329